Search for the Supersymmetric Partner of the Top Quark with the ATLAS Detector via $\tilde{t}_1 \to t\widetilde{\chi}_1^0$ and $\tilde{t}_1 \to b\widetilde{\chi}_1^{\pm}$ Decays

Francesca Consiglia Ungaro

Physikalisches Institut
Fakultät für Mathematik und Physik
Albert-Ludwigs-Universität Freiburg

January 2015

Search for the Supersymmetric Partner of the Top Quark with the ATLAS Detector via $\tilde{t}_1 \to t\widetilde{\chi}_1^0$ and $\tilde{t}_1 \to b\widetilde{\chi}_1^{\pm}$ Decays

Francesca Consiglia Ungaro

Dissertation

zur Erlangung des Doktorgrades
der Fakultät für Mathematik und Physik der

Albert-Ludwigs-Universität

Freiburg im Breisgau

vorgelegt von

Francesca Consiglia Ungaro

January 2015

Dekan:	Prof. Dietmar Kröner
Referent:	Prof. Dr. Karl Jakobs
Koreferent:	Prof. Dr. Horst Fischer
Tag der mündlichen Prüfung:	10 April 2015

Contents

Introduction

The elementary particles composing matter and their interactions are described by the Standard Model of particle physics.

Its predictions have been confirmed by several experimental evidences, as the discovery of the carriers of the weak interaction, the $W^{\pm}$ and Z^0 bosons [1], at CERN in 1983 [2] [3] [4], and the discovery of the top quark at Fermilab in 1995 [5] [6].

Until very recently, the only missing element of the Standard Model was the Higgs boson. Observing this particle was one of the main motivations to build the LHC, a hadron collider able to accelerate hadrons to unprecedented energies, and its general-purpose experiments, ATLAS and CMS.

On 4th July 2012 it was announced by both experiments the observation of a boson with a mass of about 125 GeV [7] [8]. All its properties measured so far, like spin, parity and coupling strength to bosons and fermions, are in agreement within uncertainties with the predictions of the Standard Model for the Higgs boson. This discovery has been a milestone in the road to understand nature, but there are several theoretical motivations to believe the Standard Model cannot be the ultimate theory of elementary particles.

One of the strongest reasons to expect Physics beyond the Standard Model is to allow for a mechanism protecting the Higgs boson mass against radiative corrections growing quadratically with the energy scale up to which the Standard Model is considered to be valid.

A theory which naturally solves this and other shortcomings of the Standard Model is Supersymmetry. Supersymmetry postulates for each Standard Model particle superpartners, new particles with identical quantum numbers except for the spin, differing by half a unit. The presence of these new particles realises the necessary conditions to stabilise the Higgs boson mass.

Looking for supersymmetric signals has been another strong reason to build the LHC and its experiments ATLAS and CMS.

Several well motivated Supersymmetry models foresee that at least one of the superpartners of the top quark (the lightest stop, symbol $\tilde{t}_1$) should be lighter than the superpartners of the other quarks, with mass in the sub-TeV range and therefore detectable at

the LHC.

In the context of this thesis, two of the first analyses to search for signals of direct stop pair production have been performed, with the data collected by the ATLAS experiment between 2010 and 2012 at a centre-of-mass energy of the proton-proton collisions of 7 TeV and 8 TeV. Different decay modes and different final states have been investigated.

The thesis is structured as follows. Chapter 1 is dedicated to the theoretical foundation. It provides a description of the Standard Model and of its open points. An introduction to Supersymmetry is then provided, with particular focus on the phenomenological aspects. Chapter 2 presents the experimental set-up. An overview of the LHC and of the ATLAS experiment are given first. The remainder of the chapter presents the phenomenology of the proton-proton collisions and the steps to simulate the events produced at the LHC and detected by the ATLAS experiment. Chapter 3 describes the techniques to reconstruct the final state objects starting from the raw data collected by the detector. Chapter 4 gives an overview of the searches for supersymmetric signals performed by the ATLAS collaboration, presents the analysis techniques and the statistical framework to interpret the results. Chapter 5 describes the first analysis performed in the context of this thesis. The search targets direct stop pair production in a mass range close to the top quark mass, ideal to protect the Higgs boson mass from radiative corrections coming from this Standard Model particle. The decay mode $\tilde{t}_1 \rightarrow b\widetilde{\chi}_1^{\pm}$ is considered. The second analysis is described in Chapter 6. The rise of the centre-of-mass energy of the proton-proton collisions resulted in an increase of the ratio between the cross sections of top squark pair production and Standard Model backgrounds, allowing to extend towards higher values the range of accessible stop masses. This chapter is dedicated to the investigation of signals where the decay mode $\tilde{t}_1 \rightarrow t\widetilde{\chi}_1^0$ competes with the decay mode $\tilde{t}_1 \rightarrow b\widetilde{\chi}_1^{\pm}$. Chapter 7 concludes the thesis providing the prospects for future stop searches, to be performed with the data that the ATLAS experiment will collect at the increased centre-of-mass energy of the proton-proton collisions of 13 TeV starting from 2015. The chapter describes a study performed in the context of this thesis to increase the efficiency of the tracking reconstruction algorithm in environments with high density of particles, condition that will characterise many interesting physics processes in the upcoming data-taking, including stop searches.

Chapter 1

The Standard Model of Particle Physics and its Supersymmetric Extension

The Standard Model (SM) of particle physics is at present the most successful endeavour of classifying the particle content of matter and their interactions. It is a *quantum field theory* whose predictions have been largely verified by experiments. However, the SM cannot be considered the ultimate theory, because it presents some known and unsolved problems.

In the SM elementary particles are quanta of fields (Klein-Gordon for spin 0 particles, Dirac for spin 1/2 particles and Proca for spin 1 particles). Their kinematics and dynamics are described by the SM Lagrangian and their properties are represented by *quantum numbers*. In Sections 1.1 - 1.4 of this chapter the basic principles of the SM are reviewed [9] [10] [11]. The properties of both the constituents of matter and of the particles responsible for the fundamental interactions are presented, together with the mechanism giving them mass.

Section 1.5 presents the open points left by the SM, hinting to the need for an extension. Sections 1.6 - 1.7 give an overview of the most promising extension of the SM, Supersymmetry, and of its minimal formulation, the Minimal Supersymmetric Standard Model. Section 1.8 focuses on the phenomenological aspects of the Minimal Supersymmetric Standard Model, allowing to understand the most probable mass spectrum which should be probed by analysing the data of the LHC collected by the ATLAS experiment [13].

1.1 Matter Particles

The constituents of matter are 12 *fermions*, spin 1/2 particles, which can be represented as Dirac spinors. The Lagrangian for a fermion with mass m can be written as:

$$\mathcal{L}_{Dirac} = i\overline{\psi}\gamma^{\mu}\partial_{\mu}\psi - m\overline{\psi}\psi \tag{1.1}$$

where γ^{μ} ($\mu = 0, ..., 3$) are the Dirac matrices, ∂_{μ} ($\mu = 0, ..., 3$) are the space-time derivatives and $\overline{\psi}$ represents the adjoint of the ψ Dirac spinor ($\overline{\psi} = \psi^{\dagger}\gamma^{0}$).

The fermions can be classified in two categories depending on the interactions they undergo: the *leptons* experience *weak* and (if electrically charged) *electromagnetic* interactions, while the *quarks* experience also *strong* interaction. These differences are due to the type of charges or *quantum numbers* each fermion carries. Particles with electric charge different from zero experience the electromagnetic interaction. All the matter particles have weak isospin, and thus experience weak interaction. Quarks are the only matter particles with a colour charge (which can be red, blue or green), and this is why they are the only fermions experiencing strong interaction (more details on fundamental interactions can be found in Section 1.2).

Both quarks and leptons are organised in three generations of increasing mass. A fourth generation of fermions is theoretically possible, but has never been observed and at present is disfavoured by experimental results [14]. The first generation includes the *electron* and the corresponding *electronic neutrino* and has *electron number*, L_e, equals to one. The second generation includes the *muon* and the *muonic neutrino* (*muon number*, L_{μ}, equals to one). The third generation includes the *tau* and the *tauonic neutrino* (*tau number*, L_{τ}, equals to one). In the quark sector in each generation a quark with electric charge 2/3 (up type quark) appears with a quark with electric charge -1/3 (down type quark). Each of the quarks is characterised by a different *flavour* (up, down, charm, strange, top and bottom).

For each of the leptons and the quarks, there is a corresponding *antiparticle*, a particle with same mass but opposite electric, weak and colour charge.

Contrary to leptons, quarks have never been observed as free particles and they bind to form *hadrons*. From the combination of one quark and one antiquark originates a *meson* and from the combination of three quarks originates a *baryon*.

1.2 Fundamental Interactions and Gauge Bosons

In nature there are four known fundamental forces of decreasing strength: *strong*, *electromagnetic*, *weak* and *gravitational*.

The first three forces have been incorporated within the SM, meaning that a quantum

description of them is available and experimentally confirmed. On contrast, a satisfactory quantum description of the gravitational force has not been formulated yet, but its effects are so small at the energy scales of interest that it can be left out without losing predictive power [1].

The fundamental forces of the SM are mediated by the exchange of spin 1 particles, called *gauge bosons*. The carrier of the electromagnetic interaction is a massless particle, the *photon*, with symbol γ. The carriers of the weak interaction are an electrically neutral particle, the Z^0 boson, plus two charged particles, the W^+ and W^- bosons, all with masses different from zero. The strong interaction is carried by eight electrically neutral massless bosons, the *gluons*, with symbol g. A summary of the properties of the mediators of the different interactions can be found in Table 1.1.

Interaction	**Boson**	**Electric charge**	**Mass (GeV)**
Strong	Gluons (g)	0	0
Electromagnetic	Photon (γ)	0	0
Weak	$W^{\pm}$	± 1	80.385 ± 0.015
	Z^0	0	91.1876 ± 0.0021

Table 1.1: *Fundamental interactions and gauge bosons of the Standard Model (values for the masses taken from Ref. [19]).*

1.2.1 The Electro-Weak Sector

U(1) Symmetry and the Electromagnetic Interaction

The Dirac Lagrangian (Equation 1.1) describing a free fermion is invariant under the transformation:

$$\psi \rightarrow \psi' = e^{i\theta}\psi \tag{1.2}$$

that belongs to the group U(1).
In order for this transformation to hold also locally (i.e., having a Lagrangian which is invariant under $\psi \rightarrow \psi' = e^{i\theta(x)}\psi = e^{ie\lambda(x)}\psi$) the derivative appearing in the Dirac Lagrangian has to be modified with the addition of a vectorial field A_μ:

$$\partial_\mu \rightarrow D_\mu = \partial_\mu - ieA_\mu \tag{1.3}$$

[1] The quantum effect of gravity are expected to become relevant at an energy scale of 10^{19} GeV, called Planck scale.

with transformation law $A_\mu \to A'_\mu = A_\mu + \partial_\mu \lambda(x)$. It is possible to add to the resulting Lagrangian a free term for the field A_μ of the form $\frac{1}{4}F^{\mu\nu}F_{\mu\nu}$ without spoiling the U(1) gauge invariance, where $F^{\mu\nu} = \partial^\mu A^\nu - \partial^\nu A^\mu$. The resulting Lagrangian:

$$\mathcal{L}_{QED} = i\overline{\psi}\gamma^\mu \partial_\mu \psi - m\overline{\psi}\psi - \frac{1}{4}F^{\mu\nu}F_{\mu\nu} + e\overline{\psi}\gamma^\mu \psi A_\mu \tag{1.4}$$

describes a Dirac field (representing a fermion) and a vectorial field (that can be interpreted as a photon) interacting with each other with a coupling proportional to the electric charge e. This is the Lagrangian of *quantum electrodynamics, QED*. In order for this Lagrangian to be invariant under U(1) transformations the vectorial field A_μ has to be massless, prohibiting a term of the form $\frac{1}{2}A_\mu A^\mu$.

According to Noether's theorem each symmetry of a Lagrangian is associated with a conserved charge. The charge following from the invariance of the Dirac Lagrangian under a U(1) transformation is the electric charge e of Equation 1.4, which is therefore conserved in electromagnetic interactions.

SU(2) and the Electro-Weak Unification

Similarly to the electromagnetic interaction, also the weak interaction arises from explicitly requiring that a global symmetry of the Lagrangian holds locally.

The Lagrangian for two free Dirac fields can be written in the compact form:

$$\mathcal{L} = i\overline{\psi}\gamma^\mu \partial_\mu \psi - m\overline{\psi}\psi \tag{1.5}$$

if ψ is regarded as a doublet with components ψ_1 and ψ_2 and $m(\psi_1) = m(\psi_2)$.
This Lagrangian is invariant under the SU(2) transformation that relate the two components of the doublet:

$$\psi \to \psi' = e^{i\boldsymbol{\tau}\cdot\boldsymbol{\alpha}}\psi \tag{1.6}$$

where the symbol $\boldsymbol{\tau}$ stands for the Pauli matrices.
To make the symmetry a local property the derivative needs to be modified with the addition of three vectorial fields:

$$\partial_\mu \to D_\mu = \partial_\mu + ig\boldsymbol{\tau}\cdot\boldsymbol{W_\mu} \tag{1.7}$$

where $\boldsymbol{W_\mu} = (W^1_\mu,\ W^2_\mu,\ W^3_\mu)$ are three vectorial fields transforming according to $\boldsymbol{W_\mu} \to \boldsymbol{W'_\mu} = \boldsymbol{W_\mu} + \partial_\mu \boldsymbol{\lambda(x)} + 2g\boldsymbol{\lambda(x)} \times \boldsymbol{A_\mu}$, requiring their own free propagation terms in the Lagrangian which can be written as $\frac{1}{4}\boldsymbol{W^{\mu\nu}}\cdot\boldsymbol{W_{\mu\nu}}$ ($\boldsymbol{W^{\mu\nu}} = \partial^\mu \boldsymbol{W^\nu} - \partial^\nu \boldsymbol{W^\mu} - 2g\boldsymbol{W^\mu} \times \boldsymbol{W^\nu}$).

Including all the terms the SU(2) invariant Lagrangian reads:

$$\mathcal{L} = i\overline{\psi}\gamma^{\mu}\partial_{\mu}\psi - m\overline{\psi}\psi - \frac{1}{4}\boldsymbol{W^{\mu\nu}} \cdot \boldsymbol{W_{\mu\nu}} - g(\overline{\psi}\gamma^{\mu}\boldsymbol{\tau}\psi)\cdot\boldsymbol{W_{\mu}} \tag{1.8}$$

Interpreting the three new vectorial fields W^1_μ, W^2_μ and W^3_μ as the three carriers of the weak interaction W^+ W^- and Z^0 would lead to a prediction which is in contrast with the experimental results, as the weak interaction violates parity [15] [16].

To incorporate this observation in the theory the Lagrangian in Equation 1.8 has to be modified to include only the left-handed component of the doublet:

$$\mathcal{L} = i\overline{\psi}_L\gamma^{\mu}\partial_{\mu}\psi_L - m\overline{\psi}_L\psi_L - \frac{1}{4}\boldsymbol{W^{\mu\nu}} \cdot \boldsymbol{W_{\mu\nu}} - g(\overline{\psi}_L\gamma^{\mu}\boldsymbol{\tau}\psi_L)\cdot\boldsymbol{W_{\mu}} \tag{1.9}$$

The SU(2) transformation in Equation 1.6 has also to be regarded as acting on the left-handed part of the doublet (while leaving untouched the right-handed part), therefore named $\mathrm{SU(2)_L}$. The conserved charge associated with the SU(2) invariance of the Lagrangian is the *weak isospin* $\mathrm{T_3}$. The two components of the doublet ψ_L have weak isospin $\frac{1}{2}$ and $-\frac{1}{2}$ respectively, while ψ_R is a singlet with $\mathrm{T_3} = 0$.

As a consequence of switching from the Lagrangian 1.8 to the Lagrangian 1.9, also the W^3_μ neutral field interacts only with the left-handed component of the doublet of Dirac fields, in contrast with another observation, the evidence that the Z^0 boson couples both with the left and with the right-handed components [17].

This inconsistency can be overcome by considering at the same time the U(1) and the $\mathrm{SU(2)_L}$ invariances of the Lagrangian, obtaining an overall $\mathrm{U(1)_Y \times SU(2)_L}$ which accounts for the unified electro-weak interaction. In contrast to what has been done to build QED, the conserved charge related to the U(1) symmetry is not the electric charge but has to be seen as the *weak hypercharge* (from which the subscript Y), and the compensating vectorial field has to be regarded as a non-physical field B_μ (and not as the photon) which couples to the Dirac field with strength proportional to a constant g' and having free propagation term $\frac{1}{4}B^{\mu\nu}B_{\mu\nu}$. Weak hypercharge and weak isospin are bounded to the electric charge by the relation:

$$Q = T_3 + \frac{Y}{2} \tag{1.10}$$

The overall Lagrangian for the unified electro-weak interaction reads:

$$\begin{gathered}\mathcal{L}_{EW} = -\frac{1}{4}\boldsymbol{W^{\mu\nu}} \cdot \boldsymbol{W_{\mu\nu}} - \frac{1}{4}B^{\mu\nu} \cdot B_{\mu\nu} + \\ \overline{\psi}_L\gamma^{\mu}\left(i\partial_{\mu} - g\frac{1}{2}\boldsymbol{\tau} \cdot \boldsymbol{W_{\mu}} - g'\frac{Y}{2}\right)\psi_L + \overline{\psi}_R\gamma^{\mu}\left(i\partial_{\mu} - g'\frac{Y}{2}\right)\psi_R\end{gathered} \tag{1.11}$$

The physical fields Z_μ and A_μ (respectively the Z^0 boson and the photon) are obtained by the mixing of the neutral fields B_μ and W^3_μ:

$$\begin{aligned} A_\mu &= B_\mu \cos\theta_W + W^3_\mu \sin\theta_W \\ Z_\mu &= -B_\mu \sin\theta_W + W^3_\mu \cos\theta_W \end{aligned} \tag{1.12}$$

where θ_W is the weak mixing angle. Combining these equations with the information coming from Equation 1.10 leads to:

$$e = g\cos\theta_W = g'\sin\theta_W \tag{1.13}$$

The physical charged fields $W^\pm_\mu$ can be obtained from the fields W^1_μ and W^2_μ as:

$$W^\pm_\mu = \frac{1}{\sqrt{2}}\left(W^1_\mu \mp iW^2_\mu\right) \tag{1.14}$$

The net effect of the coupling of the fermions to the charged weak bosons $W^\pm$ is to change their electric and weak isospin charge by a unit.

The coupling of $W^\pm$ to leptons takes place only within the same generation. This is not true for quarks, where the interaction can occur across different generations. It is therefore clear that the mass eigenstates of the quarks are not the weak isospin eigenstates but mixing across generations occurs. The Cabibbo-Kobayashi-Maskawa (CKM) matrix allows to switch from the mass basis to the weak isospin basis and gives the magnitude of the mixing:

$$V_{CKM} = \begin{pmatrix} V_{ud} & V_{us} & V_{ub} \\ V_{cd} & V_{cs} & V_{cb} \\ V_{td} & V_{ts} & V_{tb} \end{pmatrix} = \begin{pmatrix} c_{12}c_{13} & s_{12}c_{13} & s_{13}e^{-i\delta} \\ -s_{12}c_{23} - c_{12}s_{23}s_{13}e^{i\delta} & c_{12}c_{23} - s_{12}s_{23}s_{13}e^{i\delta} & s_{23}c_{13} \\ s_{12}s_{23} - c_{12}c_{23}s_{13}e^{i\delta} & -c_{12}s_{23} - s_{12}c_{23}s_{13}e^{i\delta} & c_{23}c_{13} \end{pmatrix},$$

$$\begin{pmatrix} d' \\ s' \\ b' \end{pmatrix} = \begin{pmatrix} V_{ud} & V_{us} & V_{ub} \\ V_{cd} & V_{cs} & V_{cb} \\ V_{td} & V_{ts} & V_{tb} \end{pmatrix} \begin{pmatrix} d \\ s \\ b \end{pmatrix} \tag{1.15}$$

where $s_{ij} = \sin\theta_{ij}$, $c_{ij} = \cos\theta_{ij}$ (θ_{ij} mixing angles), δ is the phase responsible for the CP violating processes in the SM, and d', s' and b' are the second components of the three doublets composing the weak isospin basis (the first components, u, c and b are the same for both the mass and the weak isospin basis).

The coupling between the fermions and the Z^0 boson occurs only within the same family both for leptons and for quarks, as Flavour-Changing Neutral Currents (FCNCs) are not allowed in the SM and strong experimental limits hold [18].

As already noted in the case of QED, mass terms for the gauge bosons are not admitted. Also explicit mass terms for the fermions break the symmetry. They would have the form $m\overline{\psi}\psi = m\overline{\psi}_R\psi_L + m\overline{\psi}_L\psi_R$ that is not invariant under the $\mathrm{SU(2)_L}$ transformation 1.6, as ψ_L and $\overline{\psi}_L$ transform differently than ψ_R and $\overline{\psi}_R$.

Spontaneous Symmetry Breaking and the Higgs Boson

The gauge bosons which accounts for the electromagnetic and weak interactions must be massless to preserve the $\mathrm{U(1)_Y} \times \mathrm{SU(2)_L}$ gauge invariance.

While the photon is actually massless, the weak bosons are not (see Table 1.1). A mechanism is therefore needed that accounts for the masses of the $W^{\pm}$ and Z^0 bosons without introducing terms explicitly breaking the symmetry. Such a mechanism is the Higgs mechanism, in which mass terms arise from the spontaneous symmetry breaking of a local symmetry.

According to the Goldstone theorem massless scalar bosons appear when spontaneous symmetry breaking of a global symmetry occurs [20] [21]. This can be seen considering a scalar field ϕ with Lagrangian:

$$\mathcal{L} = T - V = \frac{1}{2}\Big(\partial_\mu\phi\Big)^2 - \Big(\frac{1}{2}\mu^2\phi^2 + \frac{1}{4}\lambda\phi^4\Big) \tag{1.16}$$

In order for the potential to be bounded from below $\lambda > 0$. For $\mu > 0$ the vacuum state is trivially $\phi_0 = 0$, therefore no symmetry breaking occurs. For $\mu < 0$ there are two minima located in $\phi = \pm v = \pm\sqrt{\frac{-\mu^2}{\lambda}}$. Choosing a minimum breaks the symmetry, as the potential is symmetric under the substitution $\phi \to -\phi$ while the ground state is not. To obtain a mass term an expansion around the ground state is needed, which can be obtained by substituting ϕ with $\phi(x) = v + \eta(x)$ in Equation 1.16.

With this substitution the Lagrangian reads:

$$\mathcal{L} = \frac{1}{2}\Big(\partial_\mu\eta\Big)^2 - \lambda v^2\eta^2 - \lambda v\eta^3 - \frac{1}{4}\lambda\eta^4 + const \tag{1.17}$$

which describes a scalar field with mass $m_\eta = \sqrt{2\lambda v^2} = \sqrt{-2\mu^2}$ and a self interaction, but there is no sign of a mechanism which could give mass to any other particle possibly appearing in the theory.

In order for the mechanism to account for the masses of other particles, spontaneous symmetry breaking of a local (and not of a global) symmetry should occur.

A Lagrangian of the same type of Equation 1.16 for two scalar fields exhibits U(1) symmetry:

$$\mathcal{L} = \frac{1}{2}\Big(\partial_\mu\phi_1\Big)^2 + \frac{1}{2}\Big(\partial_\mu\phi_2\Big)^2 - \frac{1}{2}\mu^2\Big(\phi_1^2 + \phi_2^2\Big) - \frac{1}{4}\lambda\Big(\phi_1^2 + \phi_2^2\Big)^2 \tag{1.18}$$

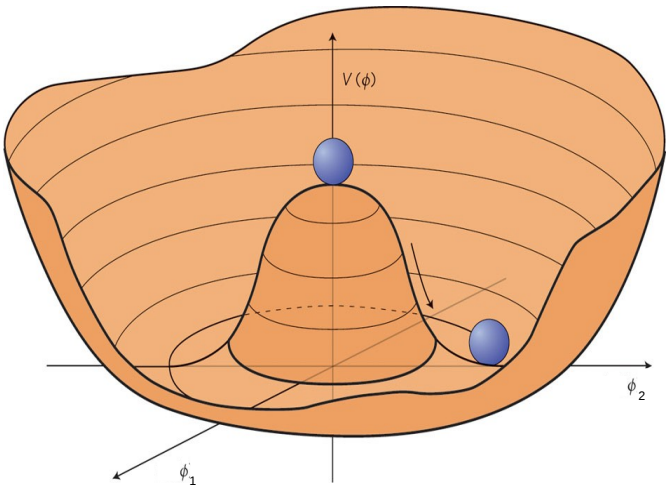

Figure 1.1: *Representation of the Higgs potential.*

In analogy with the one dimensional case, the interesting case is the one with $\lambda > 0$ and $\mu < 0$. The potential shows a continuum of minima on a circle with radius $v = \sqrt{\phi_1^2 + \phi_2^2} = \sqrt{-\frac{\mu^2}{\lambda}}$ (see Figure 1.1).

To make the U(1) symmetry local the introduction of a new vectorial field is needed, following the same procedure adopted to build QED.

The resulting Lagrangian is than expanded around an arbitrary chosen minimum through the substitution $\phi(x) = \sqrt{\frac{1}{2}\Big[v + \eta(x) + i\xi(x)\Big]}$ to obtain:

$$\begin{aligned}\mathcal{L} = &\frac{1}{2}\Big(\partial_\mu \xi\Big)^2 + \frac{1}{2}\Big(\partial_\mu \eta\Big)^2 - v^2\lambda\eta^2 + \frac{1}{2}e^2v^2A_\mu A^\mu \\ &- evA_\mu\partial^\mu\xi - \frac{1}{4}F_{\mu\nu}F^{\mu\nu} + \text{interacion terms}\end{aligned} \tag{1.19}$$

From which it can be seen that the vector field A_μ acquired mass $m_A = ev$ (where e is the electric charge, introduced in the QED Lagrangian in Equation 1.4) and as before $m_\eta = \sqrt{2\lambda v^2}$. Also in this case there is a massless Goldstone boson ξ, that is non physical. It can be eliminated exploiting the U(1) symmetry by choosing a particular gauge which results in a Lagrangian describing a vector boson A_μ interacting with a massive scalar, the Higgs boson. In this way the degree of freedom of the unwanted Goldstone boson is turned into a longitudinal polarization degree of freedom for the vector boson resulting from the fact that it acquired mass.

The real case of interest is the case in which one vector boson (the photon) remains massless and three vector bosons (the mediators of the weak interactions) acquire mass. The suitable Lagrangian showing local $U(1) \times SU(2)$ invariance has the form:

$$\begin{gathered}\mathcal{L}_{Higgs} = \left|\left(i\partial_\mu - g\boldsymbol{T}\cdot\boldsymbol{W_\mu} - g'\frac{Y}{2}B_\mu\right)\phi\right|^2 - V(\phi), \\ V(\phi) = \mu^2\phi^\dagger\phi + \lambda(\phi^\dagger\phi)\end{gathered} \tag{1.20}$$

where

$$\phi = \frac{1}{\sqrt{2}}\begin{pmatrix}\phi_1 + i\phi_2 \\ \phi_3 + i\phi_4\end{pmatrix} \tag{1.21}$$

is a weak isospin doublet with Y=1.

For the case $\lambda > 0$ and $\mu < 0$ the minima are on a manifold where $|\phi|$ satisfies $\phi^\dagger\phi = \sqrt{\frac{-\mu^2}{\lambda}}$.

Once again, mass terms for the gauge bosons arise from substituting in Equation 1.20 the vacuum expectation value ϕ_0 for ϕ:

$$\phi_0 = \frac{1}{\sqrt{2}}\begin{pmatrix}0 \\ v\end{pmatrix} \tag{1.22}$$

The part of the Lagrangian concerning the mass of the bosons is thus:

$$(\frac{1}{2}vg)^2 W_\mu^+ W^{-\mu} + \frac{1}{8}v^2(W_\mu^3, B_\mu)\begin{pmatrix} g^2 & -gg' \\ -gg' & g'^2\end{pmatrix}\begin{pmatrix}W^{3\mu} \\ B^\mu\end{pmatrix} \tag{1.23}$$

The mass of the $W^\pm$ bosons can be read from the first term and is:

$$m_W = \frac{1}{2}vg \tag{1.24}$$

The remaining term is expressed in the non-physical basis W_μ^3 and B_μ.
By expressing the fields in the physical basis Z_μ and A_μ follow:

$$\begin{aligned} m_A &= 0, \\ m_Z &= \frac{1}{2}v\sqrt{g^2 + g'^2}\end{aligned} \tag{1.25}$$

Combining Equations 1.24 and 1.25 with Equation 1.13 follows that

$$\frac{m_W}{m_Z} = \cos\theta_W \tag{1.26}$$

which is an important prediction of the SM built with a Higgs doublet.

The Higgs doublet can be used also to give mass to the fermions by replacing the isospin doublet ϕ with its expansion around a ground state:

$$\phi(x) = \frac{1}{\sqrt{2}}\begin{pmatrix} 0 \\ v + h(x) \end{pmatrix} \tag{1.27}$$

in a Lagrangian coupling ϕ to the fermions without violating the U(1)×SU(2) symmetry:

$$\mathcal{L}_{\text{Yukawa}} = -G_l \bar{L}_L \phi l_R - G_d \bar{Q}_L \phi d_R - G_u \bar{Q}_L \phi_C u_R + \text{h. c.} \tag{1.28}$$

where ϕ_C is the hypercharge conjugate of ϕ, L_L and l_R stand respectively for the leptonic weak isospin doublet and singlet, Q_L, u_R and d_R are the quarks weak isospin doublet and singlets. The left-handed quark doublets have to be intended as expressed in the weak isospin basis, according to Equation 1.15.

The couplings in Equation 1.28 can be interpreted in terms of fermion masses, for example for the electron $m_e = \frac{G_e v}{\sqrt{2}}$. However, the couplings are free parameters and therefore do not give any indication on the values of the masses.

Also the mass of the Higgs boson itself is not predicted. Substituting the field 1.27 in the potential of the Lagrangian 1.20 it is possible to read $m_h = 2v^2\lambda$. While v is fixed by the mass of the gauge bosons, λ is not. The Higgs boson has been recently discovered at CERN by the ATLAS and CMS collaborations [7] [8], and its mass has been measured to be $m_H = 125.36 \pm 0.37(\text{stat}) \pm 0.18(\text{syst})$ GeV by the ATLAS Collaboration [22] and $m_H = 125.03^{+0.26}_{-0.27}(\text{stat})^{+0.13}_{-0.15}(\text{syst})$ GeV by the CMS Collaboration [23].

1.2.2 The Strong Sector

The theory describing strong interactions is called *quantum chromodynamics, QCD* and its formulation closely follows the formulation of weak interactions.

Each quark flavour comes in three colour states (usually chosen to be red, blue and green). The starting point to formulate the theory describing quark dynamics is to consider a Lagrangian containing three Dirac spinors ψ_r, ψ_b and ψ_g.

The Lagrangian has a SU(3) symmetry that can be made local by introducing eight massless vectorial fields $\boldsymbol{G} = (G_1, ..., G_8)$ corresponding to eight gluons.

After simplifying the notation by defining:

$$\psi = \begin{pmatrix} \psi_r \\ \psi_b \\ \psi_g \end{pmatrix} \tag{1.29}$$

and introducing the free terms for each of the vectorial fields, the Lagrangian for QCD reads:

$$\mathcal{L}_{QCD} = i\overline{\psi}\gamma^\mu \partial_\mu \psi - m\overline{\psi}\psi - g_s(\overline{\psi}\gamma^\mu \boldsymbol{\lambda}\psi) \cdot \boldsymbol{G_\mu} - \frac{1}{4}\boldsymbol{G_{\mu\nu}} \cdot \boldsymbol{G^{\mu\nu}} \tag{1.30}$$

where $\boldsymbol{\lambda} = (\lambda_1, ..., \lambda_8)$ are the Gell-Mann matrices and $G^{\mu\nu} = \partial_\mu G_\nu - \partial_\nu G_\mu + g_s f^{abc} G_\mu G_\nu$ (f^{abc} are the structure constants of the SU(3) group).

On contrast to the photon, which is electrically neutral, the eight gluons carry a colour and an anticolour charge. As a consequence, in addition to mediate the strong interaction between a quark (which carries colour) and an antiquark (which carries anticolour), gluons are subject to strong interactions themselves. Self-interactions, as three gluons and four gluons interactions, are admitted by the theory.

1.3 Feynman Calculus

Decay rates and scattering cross sections can be evaluated in a perturbative way by the use of the Feynman calculus. Each perturbative order can be represented graphically with the so-called Feynman diagrams. The left part of Figure 1.2 shows a leading order diagram for a QED scattering process. The distinctive elements of any diagram can be seen: incoming and outgoing particles represented by external lines, the propagators or mediators of the interactions represented by internal lines and vertices at interaction points between external and internal lines.

The order of a diagram can be determined by the number of vertices. Higher order diagrams give smaller contributions to the total scattering cross section and therefore in most of the cases calculations are performed at leading order (LO), at next-to-leading order (NLO), or at next-to-next-to leading order (NNLO). In some cases each order of the expansion is accompanied by large logarithmic corrections. With a procedure called resummation it is possible to account for the dominant and, if needed, sub-dominant logarithmic terms. In this case the calculation is performed at leading logarithm (LL) or next-to leading logarithm (NLL) accuracy [24].

The right part of Figure 1.2 shows an example of higher order contribution to the scattering process: a loop diagram. The propagating photon creates a virtual fermion-antifermion pair which then annihilate. Although the four momentum is conserved at each vertex, the momentum circulating in the loop can have any value. To obtain the amplitude for the process an integration over all momenta is therefore needed, with divergent results.

Figure 1.2: *Examples of Feynmann diagrams for a generic QED scattering process: leading order (left) and one loop vacuum polarization diagram (right).*

The loop diagram can be interpreted as a modification to the propagator and the infinite part can be absorbed in a redefinition of the electric charge. This is the basic idea behind *renormalization*: the measurable quantities (like the electric charge) can be expressed in terms of their *bare* values (the paramenters appearing in the Lagrangian) and the energy scale Q at which the quantity is measured. The *Renormalization Group Equations* (RGE) allow to predict how the values of the physical quantities vary when Q is changed.

The dependence (running) of the QCD coupling constant with the energy scale has important phenomenological consequences. It is described by the function:

$$\alpha_s(Q^2) = \frac{\alpha_s(\mu^2)}{1 + \frac{\alpha_s(\mu^2)}{12\pi}(33 - 2n_f)\log\frac{Q^2}{\Lambda^2}} \tag{1.31}$$

with $\alpha_s = g_s^2/4\pi$, n_f the number of quark flavours and Λ a cut-off scale, experimentally measured to be $\Lambda \approx 200$ MeV.

The behaviour of α_s with the energy scale Q^2 is shown in Figure 1.3. For $Q^2 \leq \Lambda^2$, the magnitude of α_s increases, up to values where perturbative calculations cannot be performed any more and different techniques than the ones described in this section must be adopted. In this regime, quarks and gluons bind to form colourless particles. This property is called confinement. In the energy regime of perturbative QCD, $Q^2 \gg \Lambda^2$, quarks and gluons behave as free particles. This property is called asymptotic freedom [24].

The evolution of the coupling constant of QED with the energy scale Q^2 is described by:

$$\alpha(Q^2) = \frac{\alpha(\mu^2)}{1 - z_f\frac{\alpha(\mu^2)}{3\pi}\log\frac{Q^2}{\mu^2}} \tag{1.32}$$

with $\alpha = g^2/4\pi$, z_f the sum of the squared electric charge of the fermions, and μ a reference energy scale.

On contrast to the coupling constant of QCD, the coupling constant of QED increases with the energy scale. The dependence is mild ($\alpha \approx 1/137$ for $Q^2 \to 0$ and $\alpha \approx 1/128$ for $Q^2 = m_Z^2$), therefore the perturbative regime is respected for all the energy scales of practical use.

1.4 Summary of the Standard Model

The overall SM Lagrangian is obtained by putting together the results obtained in the previous sections and shows an overall $\mathrm{SU(3)_C} \times \mathrm{SU(2)_L} \times \mathrm{U(1)_Y}$ symmetry is referred to in the next sections as the SM gauge group.

The SM Lagrangian has 19 free parameters, that have to be measured experimentally. These are the nine fermion masses (the six quarks and the three charged leptons), the $W^{\pm}$

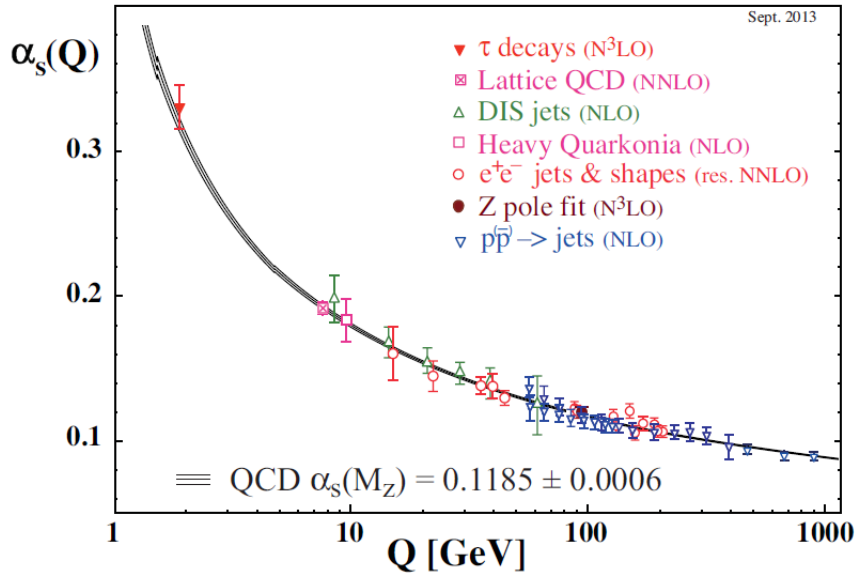

Figure 1.3: *Summary of measurements of α_s as a function of the energy scale Q. The respective level of QCD perturbation theory used in the extraction of α_s is indicated in brackets (NLO: next-to-leading order; NNLO: next-to-next-to leading order; res. NNLO: NNLO matched with resummed next-to-leading logs; N^3LO: next-to-NNLO)* [19].

and Higgs bosons masses, the three interaction strengths (g, g' and g_s), the three mixing angles and the CP-violating phase of the CKM matrix, plus a CP-violating parameter for the strong interactions [2].

In the previous sections the conserved charges associated to each symmetry of the Lagrangian have been reviewed. Electric charge and weak isospin, originated by the U(1) and SU(2) invariances, are conserved by all interactions. Colour charge, originated by the SU(3) invariance, is conserved in the strong interactions and do not play any role in electromagnetic and weak interactions.

If chiral anomalies are neglected, also the *total leptonic number* L_n and the *total quark number* Q_n are conserved. Each lepton has $L_n = +1$, each antilepton $L_n = -1$ and every other particle $L_n = 0$. Similarly for the total quark number, a quark has $Q_n = +1$, an antiquark has $Q_n = -1$ and other particles have $Q_n = 0$. L_n and Q_n are additive quantum numbers, that means that their sum is preserved in the interactions. The *individual lepton numbers* L_e, L_μ and L_τ would be conserved if neutrinos were massless, as they are assumed to be in the SM. Since this assumption is contradicted by the experiments investigating their flavour oscillations [27], a certain degree of violation of the individual lepton numbers is present.

[2] CP violation in the strong sector is allowed by QCD but has never been observed, therefore the quantity parametrizing it (θ_{QCD}) is considered to be approximately zero.

On a phenomenological point of view it is more convenient to consider the *baryon number B* instead of the quark number. The baryon number is 1/3 of the quark number. Baryons are composed of three quarks, therefore have baryon number equal to 1. Mesons are composed of one quark and one antiquark, therefore their baryon number is zero and the number of mesons in a reaction does not have to be conserved.

1.5 Need for an Extension of the Standard Model

Despite the self consistency and the predictive power of the SM have been confirmed by many experimental measurements, it is known that it cannot be considered as the ultimate theory, because it does not explain all aspects of fundamental physics and some unsolved problems remain:

- *Dark matter*:
  The SM provides a description only of the ordinary matter, that, according to the latest results from the Planck mission interpreted in the context of the Standard Model of Cosmology [25] accounts only for 4.9% of the total mass-energy content of the universe. The 26.8% is composed of *dark matter*, a type of matter not experiencing electromagnetic interaction (therefore "dark") but with detectable gravitational effects. The remaining 68.3% is made of *dark energy*, a form of energy responsible for the accelerated expansion of the universe.

- *Unification of the coupling constants*:
  Grand Unified Theories (GUT) postulate the existence of a larger symmetry group containing the SM gauge group ($SU(3)_C \times SU(2)_L \times U(1)$), as e.g. SU(5) or O(10) (see for example Ref. [26]). It follows that the electromagnetic, weak and strong interactions arise from the breaking of this overall symmetry group and therefore there is an energy scale where the coupling constants for the three interactions unify. This is in contrast with the evolution of the gauge coupling constants as predicted by the RGEs, that show crossing points at different energies (see the dashed lines in Figure 1.6).

- *Gravity*:
  As stated in Section 1.2 the description of gravity is not included in the SM, therefore its validity is limited to energy scales below the Planck scale, where gravitational effects can be neglected.

- *Mass of neutrinos*:
  In the SM the neutrino masses are set to zero, but experiments investigating their flavour oscillations contradict this assumption [27]. Understanding what is the cor-

rect way to incorporate neutrino masses in the theory describing the elementary particles is at present an open point.

- *Matter-antimatter asymmetry*:
  The only known parameter accounting for CP violation in the SM is the phase of the CKM matrix, but its magnitude is not large enough to explain the matter-antimatter asymmetry of the universe.

- *Number of free parameters*:
  The SM has a total of 19 free parameters, which seems unnatural for a fundamental theory.

- *Hierarchy problem*:
  The Higgs boson mass can be decomposed in a term representing its bare mass plus a term including all the corrections originated by the virtual effects of each particle coupling to the Higgs field:

$$m_H^2 = m_{H,0}^2 + \delta m_H^2 \tag{1.33}$$

  Figure 1.4 represents a one-loop radiative correction due to a fermion, which can be written as:

$$\delta m_{H,f}^2 = -\frac{|\lambda_f|^2}{8\pi^2}\Lambda^2 + ... \tag{1.34}$$

  with Λ being the energy scale up to which the SM is considered to be valid (needed to regulate the loop integral), and the subscript f which can refer to any of the fermions of the SM. The neglected terms grow at most logarithmically with Λ and are proportional to m_f^2.

  It appears clear that the bare mass and the corrections (that can potentially acquire high values) need to balance in such a way that the result is compatible with the measured Higgs boson mass. This seems very unlikely and unnatural.

1.6 Supersymmetry Algebra

Most of the problems of the SM described in the previous section can be solved if the existence of a further symmetry is postulated. This symmetry, referred to as Supersymmetry (SUSY), relates bosons and fermions. More precisely, a supersymmetric transformation turns a bosonic state into a fermionic state and vice versa, by changing its spin by $\pm 1/2$:

$$Q|\text{boson}>=|\text{fermion}>, \quad Q|\text{fermion}>=|\text{boson}> \tag{1.35}$$

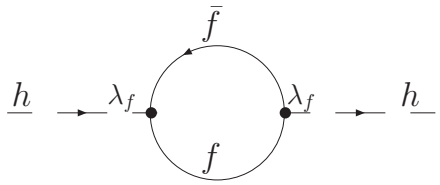

Figure 1.4: *One-loop radiative corrections to the Higgs boson mass due to a fermionic particle and.*

The generator of the SUSY transformation Q must be an anti-commuting spinor. According to the Haag-Lopuszanski-Sohnius extension [28] of the Coleman-Mandula theorem [29][3] the generator Q of the SUSY transformation and its hermitiane conjugate $Q^\dagger$ must satisfy the following algebra (with P^μ being the generator of the translations in space-time):

$$\{Q, Q^\dagger\} = P^\mu \tag{1.36}$$

$$\{Q, Q\} = \{Q^\dagger, Q^\dagger\} = 0 \tag{1.37}$$

$$[P_\mu, Q] = [P_\mu, Q^\dagger] = 0 \tag{1.38}$$

Each particle can be classified in a *supermultiplet*, the irreducible representation of the SUSY algebra. Since the generators of the SM gauge group commute with the SUSY generators, particles in the same supermultiplet have the same quantum numbers (charge, weak isospin and colour). From Equation 1.38 follows that $[P^2, Q] = 0$ ($P^2 = P^\mu P_\mu$), hence particles in the same supermultiplet have the same mass.

The commutation and anticommutation rules in Equations 1.36 - 1.38 imply that in a given supermultiplet there must be the same number of bosonic (n_b) and fermionic (n_f) degrees of freedom. The simplest supermultiplets satisfying the condition $n_b = n_f$ are:

[3]The Coleman-Mandula theorem states that in presence of a mass gap the symmetry group of a 4-dimensional quantum field theory is the direct product of the internal symmetry group and the Poincare group (i.e. no mixing between space-time and internal symmetries is possible). The Haag-Lopuszanski-Sohnius theorem generalises the Coleman-Mandula theorem showing that a supersymmetry algebra can extend the Poincare algebra in a non trivial way (i.e. allowing an interplay between space-time and internal symmetries) if both commuting and anti-commuting symmetry generators are allowed.

- *Chiral* or *matter supermultiplet* containing one Weyl spinor with two helicity states (spin-1/2, $n_f = 2$) and two real scalars each with one helicity state (spin-0, $n_b = 2$).
- *Gauge* or *vectorial supermultiplet* containing a massless spin-1 boson ($n_b = 2$) and a spin-1/2 Weyl fermion ($n_f = 2$).
- If gravity is included, the graviton (spin-2 particle) must have a spin-3/2 superpartner, the *gravitino*.

1.7 The Minimal Supersymmetric Standard Model

The minimal SUSY extension of the SM in terms of new particles is the Minimal Supersymmetric Standard Model (MSSM). In the MSSM to every boson (fermion) of the SM is associated a new fermion (boson) called *superpartner*. The SM particles and their superpartners can be classified in chiral and gauge supermultiplets.

Gauge supermultiplets of the MSSM

The gauge bosons before electro-weak and spontaneous symmetry breaking are massless spin-1 bosons (see Section 1.2.1), therefore they belong, together with their superpartners (the *gauginos*), to chiral supermultiplets. The name of a gaugino is obtained adding the suffix "-ino" to the name of the corresponding gauge boson, thus three *winos* ($\widetilde{W}^+$, $\widetilde{W}^-$, $\widetilde{W}^0$) are associated to the W^+ , W^- and W^0 bosons, the *bino* ($\widetilde{B}^0$) is associated to the B^0 boson[4] and eight *gluinos* ($\widetilde{g}$) are associated to the gluons. A summary of the gauge supermultiplets of the MSSM can be found in Table 1.2.

Chiral supermultiplets of the MSSM

Gauginos must transform in the same way as gauge bosons, hence the transformation rules for the left and the right-handed components of the gauginos must be identical. This implies that quarks and leptons, the fermions of the SM, cannot be placed in gauge supermultiplets (as their left and right-handed components have different transformation properties under the SM gauge group), but must be placed in chiral supermultiplets.

The name of the spin-0 superpartners of the fermions are built adding the prefix "s" (standing for scalar) to the name of the corresponding SM particle (thus, for example, the superpartner of the top quark is called stop). Superpartners of quarks and leptons are also generically called *squarks* and *sleptons* or referred to as *sfermions*. Quarks and leptons are Dirac spinors with a right and a left-handed component, therefore they can

[4] from now on for convenience the W^3 vectorial field defined in Section 1.2.1 has been renamed W^0 while the B^0, W^+ and W^- definitions are left untouched.

Names	spin 1/2	spin 1	$SU(3)_C$, $SU(2)_L$, $U(1)_Y$
gluino, gluon	$\tilde{g}$	g	(**8**, **1** , 0)
winos, W bosons	$\tilde{W}^{\pm}$ $\tilde{W}^0$	$W^{\pm}$ W^0	(**1**, **3** , 0)
bino, B boson	$\tilde{B}^0$	B^0	(**1**, **1** , 0)

Table 1.2: *Gauge supermultiplets in the Minimal Supersymmetric Standard Model and their quantum numbers* [12] .

Names		spin 0	spin 1/2	$SU(3)_C$, $SU(2)_L$, $U(1)_Y$
squarks, quarks	Q	$(\tilde{u}_L \;\; \tilde{d}_L)$	$(u_L \;\; d_L)$	(**3**, **2** , $\frac{1}{6}$)
(×3 families)	$\bar{u}$	$\tilde{u}^*_R$	$u^{\dagger}_R$	($\overline{\mathbf{3}}$, **1**, $-\frac{2}{3}$)
	$\bar{d}$	$\tilde{d}^*_R$	$d^{\dagger}_R$	($\overline{\mathbf{3}}$, **1**, $\frac{1}{3}$)
sleptons, leptons	L	$(\tilde{\nu} \;\; \tilde{e}_L)$	$(\nu \;\; e_L)$	(**1**, **2** , $-\frac{1}{2}$)
(×3 families)	$\bar{e}$	$\tilde{e}^*_R$	$e^{\dagger}_R$	(**1**, **1**, 1)
Higgs, higgsinos	H_u	$(H^+_u \;\; H^0_u)$	$(\tilde{H}^+_u \;\; \tilde{H}^0_u)$	(**1**, **2** , $\frac{1}{2}$)
	H_d	$(H^0_d \;\; H^-_d)$	$(\tilde{H}^0_d \;\; \tilde{H}^-_d)$	(**1**, **2** , $-\frac{1}{2}$)

Table 1.3: *Chiral supermultiplets in the Minimal Supersymmetric Standard Model and their quantum numbers* [12].

be decomposed in two Weyl spinors. Each Weyl fermion has its own superpartner, thus to the left and right-handed components of a lepton (quark) is associated a left and right slepton (squark). For neutrinos, that in the SM have only the left-handed component, this distinction is not made.

The Higgs boson is a spin-0 particle, therefore it also belongs to chiral supermultiplets. Two chiral supermultiplets for the Higgs boson are needed, which are $SU(2)_L$-doublet complex scalar fields (four degrees of freedom each). One supermultiplet has Y=1/2 and the Yukawa couplings necessary to give masses to the up-type quarks and is referred to as H_u, with weak isospin components (H^+_u, H^0_u). The supermultiplet with Y=-1/2 is needed to give masses to the down-type quarks and is called H_d, with components (H^0_d, H^-_d).

The superpartners of the Higgs scalars are called *higgsinos* and are denoted with $\widetilde{H}_u$ and $\widetilde{H}_d$, with components $(\widetilde{H}^+_u, \widetilde{H}^0_u)$ and $(\widetilde{H}^0_d, \widetilde{H}^-_d)$ respectively. Table 1.3 summarises the chiral supermultiplets of the MSSM.

A solution to the hierarchy problem

This newly introduced symmetry provides a solution to the hierarchy problem discussed in Section 1.5.

If terms growing at most logarithmically with the energy scale are neglected, the one-loop radiative correction due to a scalar particle (see Figure 1.5) contributes to the squared

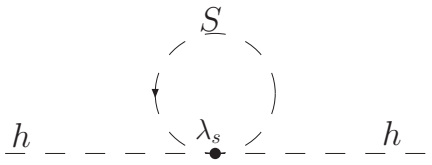

Figure 1.5: *One-loop radiative corrections to the Higgs boson mass due to a scalar particle.*

Higgs boson mass correction with a term:

$$\delta m_{H,s}^2 = \frac{\lambda_s}{16\pi^2}\Lambda^2 \tag{1.39}$$

Supersymmetry introduces two complex scalar fields for each SM fermion. The corrections due to two complex scalar fields given in Equation 1.39 cancel with the correction due to a fermion given in Equation 1.34, if the dimensionless couplings λ_s and λ_f satisfy $\lambda_s = |\lambda_f|^2$.

1.7.1 R-parity

The SUSY Lagrangian extends the SM Lagrangian by including kinetic and mass terms for SUSY particles, interactions among the SUSY particles and between SUSY and SM particles.

As stated in Section 1.4 in the SM gauge invariance and renormalizability impose the conservation of baryon (B) and lepton (L) numbers. In SUSY this is not the case, as it is possible to write terms of the Lagrangian that are gauge invariant and renormalizable but violate either B or L.

The conservation of these quantum numbers is strongly constrained by many experimental results (the strongest being the limit on the lifetime of the proton), implying that either the terms in the Lagrangian violating B and L have very small couplings, or are not admitted. The most natural solution is to impose a new symmetry eliminating the possibility of terms violating B and L. This symmetry is called *R-parity*, a multiplicative quantum number defined as:

$$R = (-1)^{3(B-L)+2s} \tag{1.40}$$

Where s is the spin of the particle considered. As a result, R=1 for SM particles and R=-1 for the SUSY particles [5].
The conservation of R-parity has important phenomenological consequences:

[5]Scenarios where the conservation of R-parity is not assumed are also considered and investigated as part of the Physics program of the ATLAS experiment.

- In collider experiments SUSY particles can only be produced in even numbers (usually two).
- The lightest SUSY particle (LSP) is stable.
- Each SUSY particle other than the LSP can decay only in an odd number of LSPs (usually just one).

1.7.2 Supersymmetry Breaking

If SUSY were an unbroken symmetry, the superpartners would have the same mass as the SM particles, making them very easy to detect. No superpartners have been observed yet, meaning that SUSY must be broken. The way SUSY is broken must be such that it still provides a solution to the hierarchy problem, not to spoil one of the main reasons why SUSY is a promising extension of the SM.

To achieve the scope, even after SUSY breaking the relation between the dimensionless couplings introduced in the previous section must hold. SUSY must therefore be broken in a "soft" way, meaning that the Lagrangian must be composed of two parts:

$$\mathcal{L} = \mathcal{L}_{\text{SUSY}} + \mathcal{L}_{\text{soft}} \tag{1.41}$$

With $\mathcal{L}_{\text{SUSY}}$ containing all the gauge and Yukawa interactions and preserving SUSY, and $\mathcal{L}_{\text{soft}}$ violating SUSY but containing only mass terms and couplings with positive mass dimensions. In this way, the correction of Equation 1.34 continue to cancel with twice the correction of Equation 1.39, and the only residual terms are those growing logarithmically with the energy scale, of the form:

$$\delta m_H^2 \approx m_{\text{soft}}^2 \Big[\frac{\lambda}{16\pi^2} \ln \frac{\Lambda}{m_{\text{soft}}} \Big] \tag{1.42}$$

Using $\Lambda \approx m_p$ (the proton mass) and $\lambda \approx 1$, it turns out that unnatural cancellations between the bare mass and the corrections in Equation 1.33 are not needed if m_{soft} do not exceed the TeV scale, which is an excellent reason to expect the SUSY particles to be produced at the LHC.

There are many different models for SUSY breaking. In most of them it is implemented via a renormalizable interaction between a *hidden sector* (not interacting with the SM) and the SUSY particles of the *visible sector*. The interaction mediating SUSY breaking can be gravity, as for example in the mSUGRA model [30], thus allowing its incorporation in the theory.

In the MSSM, the soft part of the Lagrangian reads:

$$
\begin{aligned}
\mathcal{L}_{\text{soft}}^{\text{MSSM}} = & -\frac{1}{2}(M_3\widetilde{g}\widetilde{g} + M_2\widetilde{W}\widetilde{W} + M_1\widetilde{B}\widetilde{B} + c.c.) \\
& - \widetilde{Q}^{\dagger}\,\mathbf{m_Q^2}\,\widetilde{Q} - \widetilde{L}^{\dagger}\,\mathbf{m_L^2}\,\widetilde{L} - \widetilde{\overline{u}}\,\mathbf{m_{\overline{u}}^2}\,\widetilde{\overline{u}}^{\dagger} - \widetilde{\overline{d}}\,\mathbf{m_{\overline{d}}^2}\,\widetilde{\overline{d}}^{\dagger} - \widetilde{\overline{e}}\,\mathbf{m_{\overline{e}}^2}\,\widetilde{\overline{e}}^{\dagger} \\
& - (\widetilde{\overline{u}}\,\mathbf{a_u}\,\widetilde{Q}H_u - \widetilde{\overline{d}}\,\mathbf{a_d}\,\widetilde{Q}H_d - \widetilde{\overline{e}}\,\mathbf{a_e}\,\widetilde{L}H_d + c.c.) \\
& - m_{H_u}^2 H_u^* H_u - m_{H_d}^2 H_d^* H_d - (bH_uH_d + c.c.)\,.
\end{aligned}
$$

The first line contains M_3, M_2 and M_1, respectively the gluino, wino and bino mass terms. In the second line the squarks and sleptons mass terms $\mathbf{m_Q^2}$, $\mathbf{m_L^2}$, $\mathbf{m_{\overline{u}}^2}$, $\mathbf{m_{\overline{d}}^2}$, $\mathbf{m_{\overline{e}}^2}$ are 3×3 matrices in family space. The third line describes the trilinear couplings between the scalars, with $\mathbf{a_u}$, $\mathbf{a_d}$ and $\mathbf{a_e}$ having mass dimension. The last line are contributions to the Higgs potential coming from SUSY breaking, with $m_{H_u}^2$, $m_{H_d}^2$ and b having squared mass dimension.

While in the Lagrangian of unbroken SUSY all interactions and masses are determined by the gauge transformation properties and by the superpotential, $\mathcal{L}_{\text{soft}}$ has 105 free parameters with no counterparts in the SM.

Reducing the number of free parameters

The number of free parameters in $\mathcal{L}_{\text{soft}}$ can be reduced if the experimental constraints set by SM measurements are considered:

- The strong limits on individual lepton number conservation, as for example the limits documented in Ref. [31], imply that $\mathbf{m_{\overline{e}}^2}$ and $\mathbf{a_e}$ are diagonal or almost diagonal. Off-diagonal terms in $\mathbf{m_{\overline{e}}^2}$ would result in mixing between different slepton flavours, leading to individual lepton number violation. Off-diagonal terms in $\mathbf{a_e}$ would lead to terms mixing left and right-handed slepton components of different flavour, again resulting in individual lepton number violation.

- Experimental limits on $K_0 \leftrightarrow \overline{K}_0$ mixing [32] and to a lesser extent the limits on the amount of $B_0 \leftrightarrow \overline{B}_0$ and $D_0 \leftrightarrow \overline{D}_0$ mixing constrain the magnitude of the admitted off-diagonal terms of the squark mass matrices $\mathbf{m_{\overline{d}}^2}, \mathbf{m_Q^2}, \mathbf{m_{\overline{u}}^2}$ and of the trilinear couplings $\mathbf{a_u}$ and $\mathbf{a_d}$.

- Limits on the electric dipole moments of the neutron and electron [33] constrain CP-violating phases in the gaugino masses and trilinear scalar couplings.

CP violating and flavour changing effects can be avoided if *soft supersymmetry-breaking universality* is assumed:

- Sleptons and squarks mass matrices are flavour blind, that means proportional to a 3×3 identity matrix.

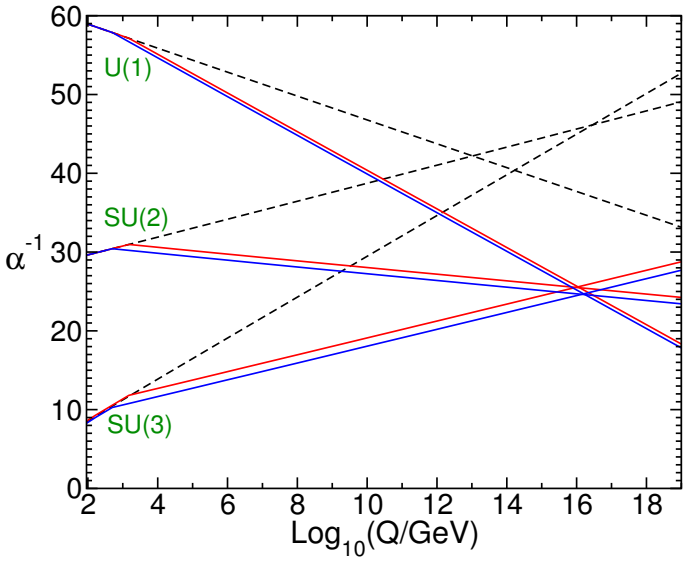

Figure 1.6: *Two-loop renormalization group evolution of the inverse gauge couplings with the energy scale in the SM (dashed lines) and in a MSSM scenario (solid lines)* [12].

- Trilinear couplings are proportional to the corresponding SM Yukawa couplings:

$$\mathbf{a_u} = A_{u0}\mathbf{y_u}, \quad \mathbf{a_d} = A_{d0}\mathbf{y_d}, \quad \mathbf{a_e} = A_{u0}\mathbf{y_e} \tag{1.43}$$

  so that only third generation squarks and sleptons can have large trilinear couplings.

- Soft SUSY breaking parameters do not introduce new complex phases.

Under these assumptions, the number of free parameters reduces from 105 to 15: three real gaugino masses, five real squark and slepton squared mass parameters, three real trilinear couplings, and four Higgs boson mass parameters (one of which can be traded as the known electroweak breaking scale).

Another assumption reducing the number of free parameters is *gaugino universality*. Unlike the SM, in the MSSM the coupling constants of electromagnetic, weak and strong interaction unify at a scale of $M_U = 2 \times 10^{16}$ GeV (see Figure 1.6). It is therefore quite natural to assume that also the gaugino masses unify around M_U, at a value named $m_{1/2}$, from which:

$$\frac{M_1}{g_1^2} = \frac{M_2}{g_2^2} = \frac{M_3}{g_3^2} = \frac{m_{1/2}}{g_U^2} \tag{1.44}$$

implying the mass prediction around the TeV scale:

$$M_3 : M_2 : M_1 \approx 6 : 2 : 1 \tag{1.45}$$

A particular configuration of the MSSM with only five free parameters is called *constrained MSSM* (cMSSM). In the cMSSM model the MSSM is considered to be the low energy limit of a GUT. The trilinear couplings, the gaugino and scalar mass parameters are assumed to unify at common values respectively called A_0, $m_{1/2}$ and m_0, which are three of the five free parameters. The other free parameters are $\tan\beta$ (the ratio of the vacuum expectation values v_u and v_d of the Higgs doublets H_u and H_d) and sign(μ) (the sign of the parameter μ on which Higgs bosons and higgsinos masses depend). In the mSUGRA model the same assumptions are made, therefore the set of free parameters is identical.

1.7.3 Particle Content After Supersymmetry Breaking

The particles listed in Tables 1.2 and 1.3 are not the physical particles of the MSSM.

After electro-weak symmetry breaking, W^0 and B^0 mix to form the physical gauge bosons Z^0 and γ. Similarly, $\widetilde{W}^0$ and $\widetilde{B}^0$ mix to form the *zino* ($\widetilde{Z}^0$) and the *photino* ($\widetilde{\gamma}$). These particles, however, are also not necessarily the mass eigenstates.

In the MSSM Higgs sector there are eight degrees of freedom. Three are needed to give mass to the $W^\pm$ and Z^0 bosons. The remaining degrees of freedom result in five Higgs bosons:

- H^0, h^0 CP-even and electrically neutral (with h^0 lighter by convention)
- A^0 CP-odd and electrically neutral
- $H^\pm$ electrically charged

The mass of h^0 is bounded from above due to its relationship with the Z^0 mass and the vacuum expectation values of the two Higgs fields:

$$m_{h_0} = m_Z^2 \cos 2\beta + ... \lesssim 135 \ \ \text{GeV} \tag{1.46}$$

where the neglected terms are higher order corrections.

This finding is compatible with the mass of the recently discovered Higgs boson and it is not excluded that the particle actually is a SUSY Higgs boson [34] [35]. An interesting case is the *decoupling limit*, in which h^0 reaches its saturation limit and all the other Higgs bosons are much heavier and nearly degenerate in mass. As for the electroweak gauginos, also the five Higgs bosons listed above are not necessarily the mass eigenstates.

Higgsinos and electroweak gauginos have the same quantum numbers and mix to form mass eigenstates. From the mixing of $\widetilde{W}^0$, $\widetilde{B}^0$ and the neutral higgsinos originate two *neutralinos*, $\widetilde{\chi}_1^0$ and $\widetilde{\chi}_2^0$. The lightest mass eigenstate, the $\widetilde{\chi}_1^0$, is usually taken as the LSP. From the mixing of the charged electroweak gauginos and charged higgsinos with the same electric charge originate the *charginos*, again with two mass eigenstates: $\widetilde{\chi}_1^\pm$ and $\widetilde{\chi}_2^\pm$.

Gluinos have colour charge, therefore cannot mix with other gauginos and with higgsinos. If gaugino universality is assumed, they are expected to be much heavier than neutralinos and charginos (see Equation 1.45).

The left and right-handed components of the SM fermions must have the same mass to preserve Lorentz invariance. On contrast, their superpartners do not have to. Under the hypothesis of flavour blind SUSY breaking only third generation squarks and sleptons can have very different masses with respect to first and second generation ones. Furthermore, significant mixing between left and right-handed superpartners can occur. The squared mass matrix for the superpartners of the top quark in the $(\tilde{t}_L, \tilde{t}_R)$ basis is:

$$\mathbf{m}^{\mathbf{2}}_{\tilde{\mathbf{t}}} = \begin{pmatrix} m^2_{Q_3} + m^2_t + \Delta_{\tilde{u}_L} & v(a^*_t \sin\beta - \mu y_t \cos\beta) \\ v(a_t \sin\beta - \mu^* y_t \cos\beta) & m^2_{\tilde{u}_3} + m^2_t + \Delta_{\tilde{u}_R} \end{pmatrix} \tag{1.47}$$

where $\Delta_{\tilde{u}_L}$ and $\Delta_{\tilde{u}_R}$ are contributions to the squared mass matrix due to electro-weak symmetry breaking.

The matrix can be diagonalized to obtain the mass eigenstates $(\tilde{t}_1, \tilde{t}_2)$, with $\tilde{t}_1$ chosen to be the lightest by convention. In a similar way it is possible to determine the mass eigenstates for $(\tilde{b}_1, \tilde{b}_2)$ and $(\tilde{\tau}_1, \tilde{\tau}_2)$. In general, a larger amount of mixing lead to a larger mass splitting between the mass eigenstates and $\tilde{t}_1$ and $\tilde{b}_1$ are very likely to be the lightest squarks because of the effect of the possibly large mixing.

The squarks of the first two generations are very likely to be heavier than the sleptons, because they receive positive radiative corrections from loop involving gluinos.

1.8 Natural Supersymmetry

Despite the reduced number of free parameters of the MSSM Lagrangian when taking into account the constraints coming from SM measurements and the reasonable assumptions on the universality of SUSY breaking, the ensemble of the possible phenomenologies remains wide. A principle that can provide guidance in understanding the most probable mass spectrum for the SUSY particles and therefore help in designing the searches is *naturalness*. In the MSSM, the following tree level relationship holds:

$$-\frac{m^2_Z}{2} = |\mu|^2 + m^2_{H_u} \tag{1.48}$$

To avoid tuning the terms on the right-hand side between each other in order to achieve the correct value on the left-hand side, they must be not too far from the electro-weak scale.

The parameter μ has been introduced in the previous section and directly controls the mass of the higgsinos. The first consequence of requiring low fine tuning in Equation 1.48 is therefore to have light higgsinos.

The masses of stop and gluino correct m_{H_u} respectively at one and two loop level, therefore to keep m_{H_u} reasonably low stop and gluino should not be too heavy. The calculation reported in Ref. [12] shows that the highest stop mass must be below about 700 GeV, the mass of the gluino below about 1.5 TeV and that the separation between the two stop mass eigenstates should not be too high.

Low stop masses imply a low mass also for the left-handed sbottom, as it is bounded to the left-handed stop by SM weak isospin symmetry.

The constraints on all the other SUSY particles are weaker, so their masses can be significantly higher and can be considered decoupled from higgsinos, stops, sbottoms and gluinos. A schematic illustration of a natural SUSY spectrum can be found in Figure 1.7.

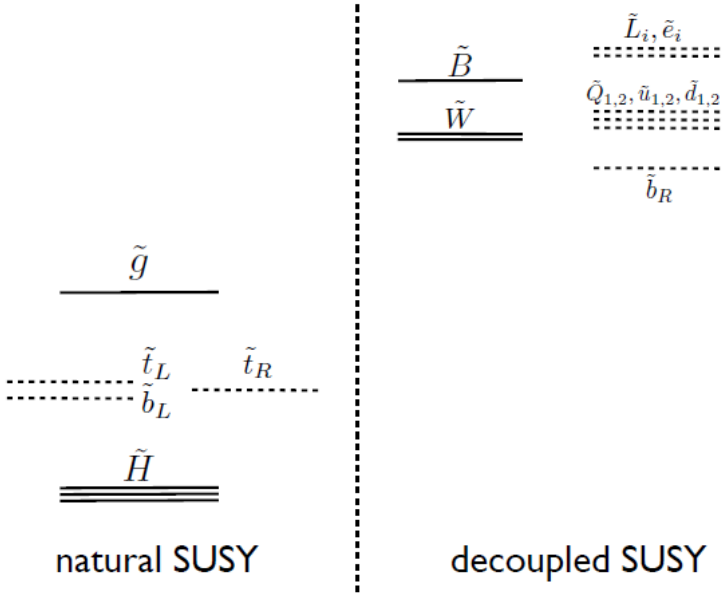

Figure 1.7: *Schematic illustration of the consequences of the naturalness principle on the mass spectrum of the SUSY particles. Natural electroweak symmetry breaking constrains the superpartners on the left to be light. The superpartners on the right can be heavy (M $\gg$ 1 TeV) without spoiling naturalness* [13].

1.8.1 Stop Decay Modes

This thesis focuses on the search for light stops in R-parity conserving models. Different decay modes are possible, depending on different assumptions including the composition of the mass eigenstates in terms of right-left squarks and the mass hierarchy of the SUSY particles involved in the decay chain. A $\tilde{t}_1$ which is mainly $\tilde{t}_R$ has as dominant decay mode $\tilde{t}_1 \to t\widetilde{\chi}_1^0$, as a consequence of the fact that charged weak interactions only couples

to the left-handed part of the SM fermions. For an admixture of $\tilde{t}_R$ and $\tilde{t}_L$ the decay mode $\tilde{t}_1 \to t\widetilde{\chi}_1^0$ is very likely to compete with the decay mode $\tilde{t}_1 \to b\widetilde{\chi}_1^{\pm}$. Under the hypothesis of naturalness the sleptons are decoupled, therefore the $\widetilde{\chi}_1^{\pm}$ decays into a $W^{\pm}$ boson and a $\widetilde{\chi}_1^0$, which is assumed to be the LSP.

The masses of the SUSY particles involved in the decay also play an important role. If the $\tilde{t}_1$ mass is lower than the sum of top quark and $\widetilde{\chi}_1^0$ masses, the decay of the squark into these two particles is not allowed. Under certain particular relations between the masses of the particles other decay modes open up, as for example $\tilde{t}_1 \to c\widetilde{\chi}_1^0$. Figure 1.8 shows a schematic illustration of the most likely $\tilde{t}_1$ decay modes depending on the assumptions made on the other particles involved in the decay.

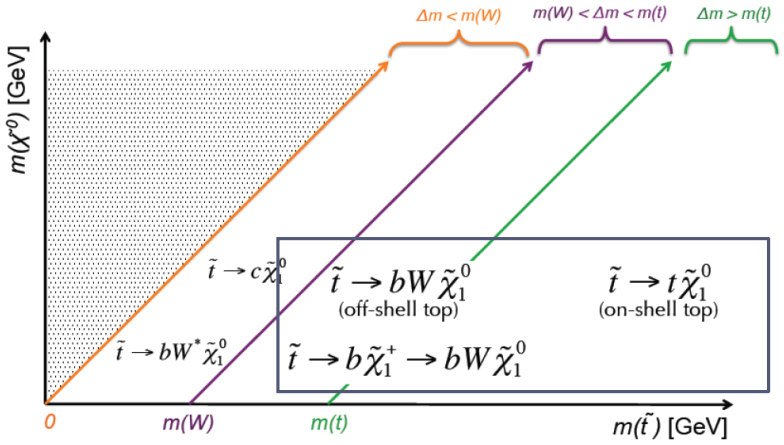

Figure 1.8: *Schematic illustration of the dominant $\tilde{t}_1$ decay modes depending on the masses of the particles involved. Δm is the $\tilde{t}_1 - \widetilde{\chi}_1^0$ mass difference.*

Chapter 2

The ATLAS Experiment

This chapter describes the experimental set-up. The data analysed in this thesis result from the proton-proton collisions generated by the LHC (Large Hadron Collider) [36], described in Section 2.1, and collected by the ATLAS (A Toroidal LHC ApparatuS) experiment [38], reviewed in Section 2.2.

The following Section, 2.3, introduce the physics behind the proton-proton collisions [42], allowing to understand what are the final objects crossing the detector. The simulation of the events produced at the LHC is a crucial tool to understand the detector performance. Section 2.4 is devoted to the explanation of the steps to simulate the proton-proton collisions [55].

2.1 The Large Hadron Collider

2.1.1 Accelerator System

The LHC is a hadron accelerator and collider located at CERN (Conseil Européen pour la Recherche Nucléaire) near Geneva, Switzerland, about 110 m below the surface. It is normally operated with two proton beams, but is also adopted to accelerate and collide lead ions. It was built between 1998 and 2008 and installed in the 26.7 km tunnel that was previously used for the LEP (Large Electron-Positron collider) machine.

The design of the LHC is optimised to reach two goals: high rates of collisions per second in the four chosen interaction points (where four experiments are located), and high centre-of-mass energy of the collisions.

The parameter controlling the first requirement is the *luminosity*, L. The number of events per second N_{event} for a process with cross section σ_{event} generated by the collisions is:

$$N_{event} = L\sigma_{event} \tag{2.1}$$

The beams are composed of packets of protons called *bunches*. For a beam in which the distribution for the density of particles in each bunch can be approximated with a Gaussian function, L is:

$$L = \frac{N_b^2 n_b f_{rev} \gamma_r}{4\pi\epsilon_n \beta^*} F \tag{2.2}$$

where N_b is the number of particles per bunch, n_b is the number of bunches per beam, f_r the revolution frequency, γ_r the relativistic gamma factor for the particles, ϵ_n is the normalised beam emittance (providing a measure of the spread of position and momentum of the particles), β^* is the transverse size of the beam evaluated at the interaction point and F is a reduction factor due to the angle at which the two beams cross.

High values of n_b cause multiple proton-proton interactions in the same bunch crossing, called *in-time pile-up*. The overlap of signals in the detectors from consequent bunch crossings is called *out-of-time pile-up*, and is determined by the detector response time.

Two of the four experiments are general purpose detectors with the same physics goals: ATLAS and CMS (Compact Muon Solenoid) [39]. They aim at a very high peak luminosity, nominally $L = 10^{34}$ cm^{-2}s^{-1} when operated with protons. This requirement excludes the choice of colliding protons with antiprotons and forces instead the use of two proton beams.

The other two experiments require lower luminosity: LHCb (Large Hadron Collider beauty), designed for studying the physics of B-hadrons [40], aims at a peak luminosity of $L = 10^{32}$ cm^{-2}s^{-1}, and ALICE (A Large Ion Collider Experiment), optimised for studying lead-lead interactions [41], aims at a luminosity for the collisions of $L = 10^{27}$ cm^{-2}s^{-1}.

The other important parameter in the LHC design, the centre-of-mass energy of the collisions, depends on the ability to accelerate and maintain the particles on a circular path. The particles are accelerated by 16 radiofrequency cavities lodged in four cylindrical cryomodules keeping them in a superconducting state. The particles are maintained on a circular orbit by the use of 1232 superconducting dipole magnets. For proton beams accelerated at 7 TeV (14 TeV in the centre-of-mass energy of the collisions), the dipoles must generate magnetic fields of 8.33 T. This is obtained keeping them at the extremely low temperature of 1.9 K by the use of a liquid helium cooling system.

The protons circulating in the LHC are obtained by ionising a gas of hydrogen. Before reaching the LHC they are passed through a complex pre-accelerator system. A linear accelerator, the LINAC-2, accelerates them to 50 MeV. From the LINAC-2 the protons pass to the PSB (Proton Synchrotron Booster), where they reach an energy of 1.4 GeV, and then to the PS (Proton Synchrotron), which brings them to 25 GeV. The last pre-accelerator is the SPS (Super Proton Synchrotron), where the protons arrive at an energy of 450 GeV and can then be injected in the LHC.

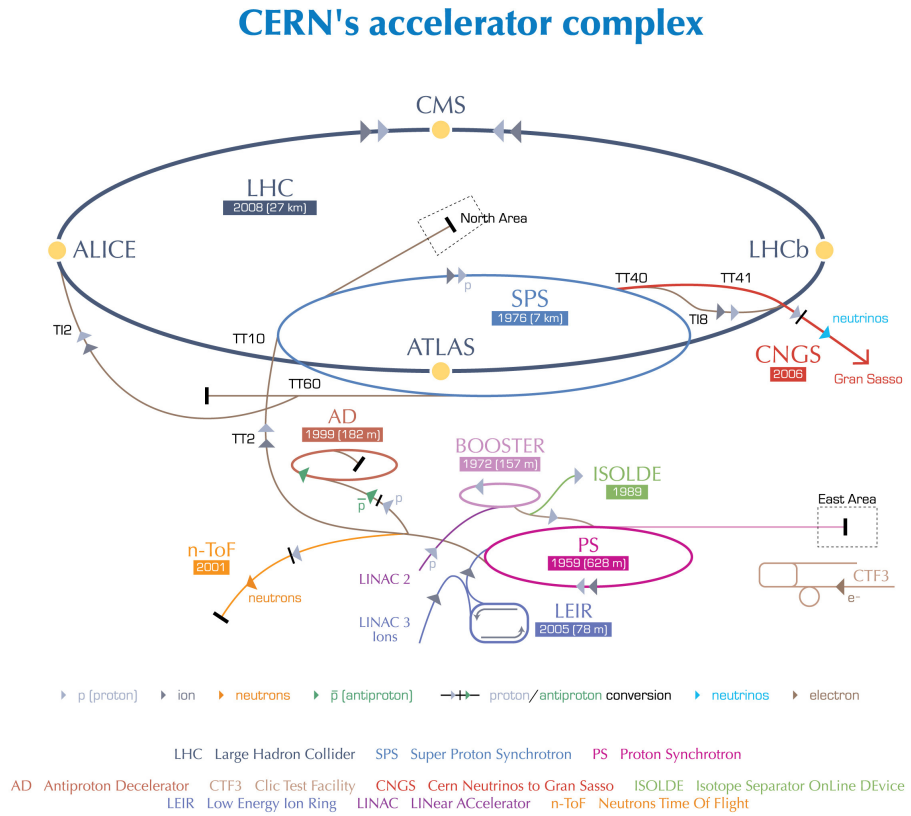

Figure 2.1: *Schematic view of the LHC and its pre-accelerator system and interaction points (in yellow), from Ref. [37].*

A schematic illustration of the pre-accelerator system and of the LHC interaction points at which the four experiments mentioned above are located is shown in Figure 2.1.

2.1.2 Data Taking

The LHC started operating with protons on 10th September 2008. Nine days later a faulty electrical connection caused a liquid helium leak, leading to the damage of 53 magnets. It took about one year to repair them. The LHC was restarted on 10th November 2009, and the first proton-proton collisions at 450 GeV per beam recorded on 23rd November 2009. The centre-of-mass energy was then increased to the intermediate energy of 2.36 TeV, before arriving to 7 TeV. From end of March to beginning of November 2010 and from March to December 2011 the LHC operated at a centre-of-mass energy for the proton-proton collisions of 7 TeV. In between, a run with heavy ions took place. The highest luminosity for this run was reached during 2011, and is $L = 3.65 \times 10^{33}$ cm^{-2}s^{-1}. The bunch spacing was progressively reduced during the data taking, down to a value of 50 ns, and the number of protons per bunch increased. As a result the in-time pile- up grew, the

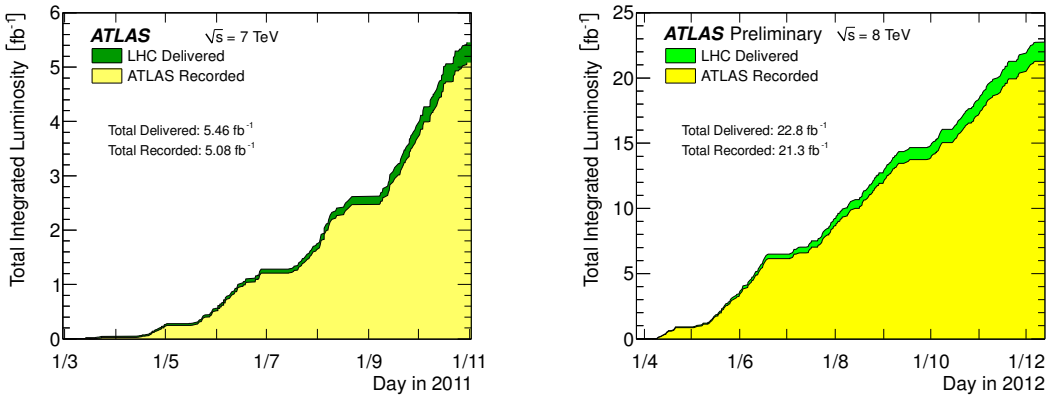

(a) (b)

Figure 2.2: *Cumulative luminosity versus time delivered to (green), and recorded by (yellow) the ATLAS experiment during stable beams and for proton-proton collisions at centre-of-mass energy of 7 (a) and 8 (b) TeV* [43].

number of average interactions per bunch crossing $\langle\mu\rangle$ increased from about 3 to 9.

The luminosity integrated over time is referred to as *integrated luminosity* and allows to evaluate the total number of events produced for a given process. The integrated luminosity delivered to the ATLAS experiment at a centre-of-mass energy of 7 TeV was of about 5.5 fb^{-1}, as shown in Figure 2.2(a).

During 2012 the LHC was operated at a centre-of-mass energy for the proton-proton collisions of 8 TeV, with an average bunch spacing of 50 ns, a peak luminosity of 8×10^{33} cm^{-2}s^{-1} and a $\langle\mu\rangle \sim 20$. The total integrated luminosity delivered to the ATLAS experiments was about 23 fb^{-1} (Figure 2.2(b)) [43].

The design values for the proton-proton collisions centre-of-mass energy of 14 TeV, the bunch spacing of 25 ns and the peak luminosity of 10^{34} cm^{-2}s^{-1} will be probably reached in 2015, when the LHC will restart operating after the first long shut down.

2.2 ATLAS Detector Design

2.2.1 Overview

The ATLAS detector is located about 100 m underground. It has a cylindrical shape, with a length of 44 m and a diameter of 25 m (Figure 2.4 shows a schematic illustration of the experiment).

It has been designed to provide good performance both for precision measurements within the SM and for searches for signals of new physics processes. In order to achieve this, several fundamental requirements have to be fulfilled:

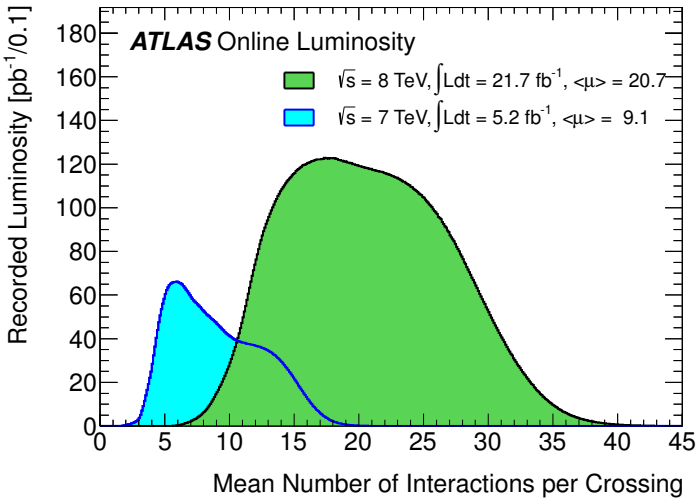

Figure 2.3: *Luminosity-weighted distribution of the average number of interactions per bunch crossing for the 2011 and 2012 data* [43].

- Due to the high collision rate and the intense radiation level, the electronics and sensors need to be fast and resistant to radiations.
- To provide an optimal measurement of the position of the particles the granularity of the detector has to be high.
- The different components of the detector have to be designed to provide a precise identification and measurement of the energy and of the momentum of all final state objects.
- The geometric acceptance has to be as wide as possible, so that momentum conservation in the transverse plane can be exploited to evaluate the magnitude of the momentum of particles leaving the detector without interacting with it (see Section 3.7 for further information).
- An efficient system, called *trigger*, is needed to select events of potential interest.

The design of the detector follows these guiding principles. The ATLAS experiment is composed of different highly segmented layers of sub-detectors that are reviewed in more details in the next subsections.

A convenient coordinate system is the one in which the longitudinal direction z is along the beam line and the x and y axis define the transverse plane. The origin of the axis is chosen to be the nominal interaction point of the protons. The position of an object is usually expressed in terms of (η, ϕ, z) rather than (x, y, z). η is the *pseudorapidity*, $\eta = -\ln(\tan\theta/2)$ with θ the polar angle in cylindrical coordinates, while ϕ is the azimuthal

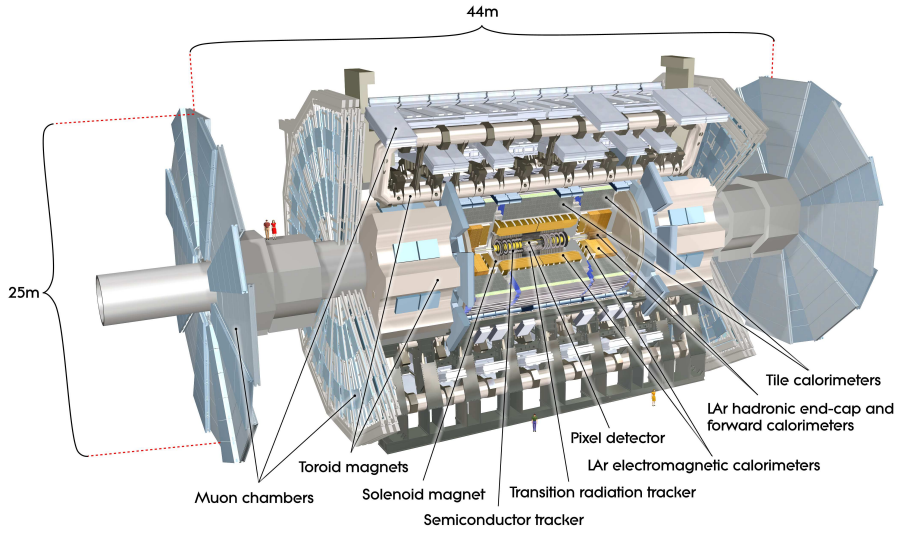

Figure 2.4: *Cut-away view of the ATLAS detector* [38].

angle. To express the distance in the transverse plane between two final state objects the distance $\Delta R = \sqrt{\Delta\eta^2 + \Delta\phi^2}$ is used. An important quantity is the momentum of a particle in the transverse plane, called *transverse momentum*.

2.2.2 Inner Detector

The innermost part of the ATLAS detector is the *Inner Detector* (ID). Its central part, called barrel, is in the region $|\eta| < 2.5$. The coverage is completed by the presence of end-caps at each extremity.

The ID is immersed in a 2 T magnetic field generated by a solenoid. Charged particles originating from the interaction point perform a helical trajectory with a radius that depends on the particle momentum. By the use of the different sub-components of the ID (the *Pixel Detector*, the *Semi-Conductor Tracker* and the *Transition Radiation Tracker*) the path of each particle, called *track*, can be reconstructed. Exploiting the information on the tracks it is possible to measure the position of the primary interaction vertex (and of possible secondary decay vertices), as well as the charged particles momentum.

Pixel Detector

The Pixel Detector is the closest detector to the interaction point and allows a precise measurement of its position and of the position of secondary vertices.
The barrel (covering the region $|\eta| < 2.5$) is composed of three cylindrical pixel layers of radius 5.05, 8.85 and 12.25 cm respectively, while three disks complete the coverage in the forward regions. The majority of the pixels have a size of 50×400 μm, providing a spatial

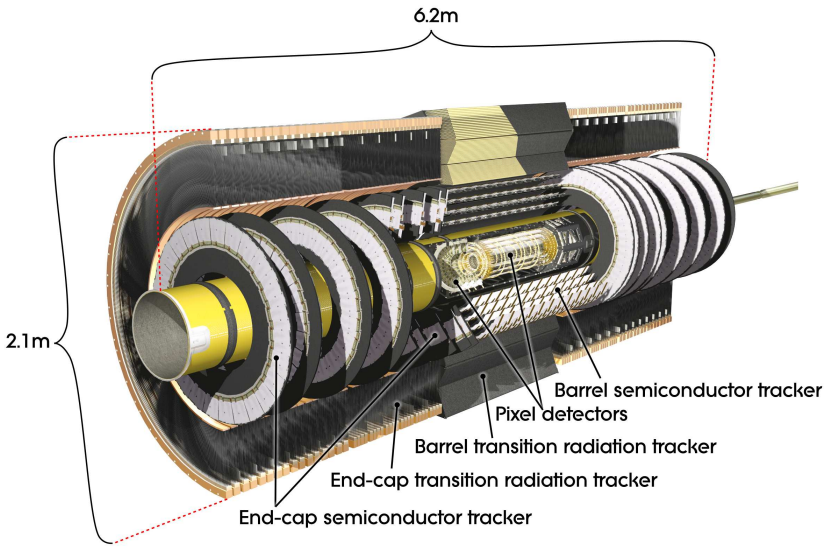

Figure 2.5: *Cut-away view of the ATLAS inner detector* [38].

resolution of 10 μm and 115 μm respectively in the transverse and longitudinal direction.

Semiconductor Tracker

The Semiconductor Tracker (SCT) surrounds the Pixel Detector and completes the precision tracking by providing an average of four additional points per track. It is composed of silicon strips of size 80 μm$\times$64 mm arranged in four layers located respectively at radii of 30.0, 37.3, 44.7, and 52.0 cm from the beam line, respectively. In each of the barrel layers (that as for the Pixel Detector is in the region $|\eta| < 2.5$) the $R-\phi$ measurement is provided by a strip running parallel to the beam line and another strip forming an angle of 40 mrad with the first one. In the end-caps, the strips are organised in nine discs, with a set of strips running radially and another forming a stereo angle of 40 mrad.

Both in the barrel and in the end-caps the intrinsic resolution in the transverse plane is 17 μm, while a resolution of 580 μm is achieved, respectively, in the z direction for the barrel and R direction for the endcaps.

The pixel and the SCT are instrumented with a cooling system, absorbing the heat coming from the electronics.

Transition radiation tracker

The Transition Radiation Tracker (TRT) is located in the outer part of the ID. It extends from a radius of 55.4 cm to 108.2 cm. Straw tubes with a diameter of 4 mm and maximum length of 144 cm provide a large (typically 36) number of hits per track. The TRT provides

information about the position in the $R - \phi$ plane only, with a typical resolution of 130 μm.

In the barrel the drift tubes are parallel to the beam-pipe, while in the end-caps they are arranged radially, divided into nine discs. The TRT works both as a drift-time detector (where the measurement of the position of a particle is derived from the drift-time of the charge) and as a transition radiation detector (with the drift tubes separated by layers of radiating material).

2.2.3 Calorimeter System

The calorimeter system of the ATLAS detector surrounds the ID and covers the region $|\eta| < 4.9$. It provides position and energy measurements of the particles crossing it through their total absorption. The calorimeter is divided into two parts: an electromagnetic calorimeter, designed for measuring electrons and photons, and a hadronic calorimeter, designed for measuring hadrons. Figure 2.6 illustrates the calorimeter system schematically.

Electromagnetic Calorimeter

The electromagnetic (EM) calorimeter is a sampling calorimeter. Copper electrodes are alternated with lead absorbers used as passive material, while liquid-argon is used as active material and fills the gaps between them.

The EM calorimeter covers the pseudorapidity range $|\eta| < 3.2$ and is split in a barrel region ($|\eta| < 1.475$) and in two end-cap regions ($1.375 < |\eta| < 3.2$), each of them housed in its own cryostat. Service cables are located between the barrel and the end-caps, degrading the resolution in the pseudorapidity region $1.37 < |\eta| < 1.52$ which is called *crack region*.

The η region matching the ID is composed of three layers characterised by a particularly fine granularity (starting from a minimum of $\Delta\eta \times \Delta\phi = 0.003 \times 0.025$), while for the region $2.5 < |\eta| < 3.2$ the granularity is coarser ($\Delta\eta \times \Delta\phi = 0.1 \times 0.1$). This system provides a typical relative uncertainty on the energy measurement of $\Delta E/E = 10\%/\sqrt{E} \oplus 0.7\%$, with E the energy (in GeV) of the particle crossing the detector.

An important requirement for a good calorimeter system is to provide good containment, to assure an accurate energy measurement and to limit the punch-through into the muon system (see Subsection 2.2.4). A critical parameter is therefore its depth. The total thickness of the EM calorimeter corresponds to about 9.7 interaction lengths in the barrel and 10 in the end-caps, providing a good containment of the electromagnetic shower.

The EM calorimeter is completed by the presence of a liquid argon layer called *presampler*, placed in front of it and covering the region $|\eta| < 1.8$. The measurement of the energy deposit in the presampler allows to estimate the energy lost by the particles before reaching the EM calorimeter.

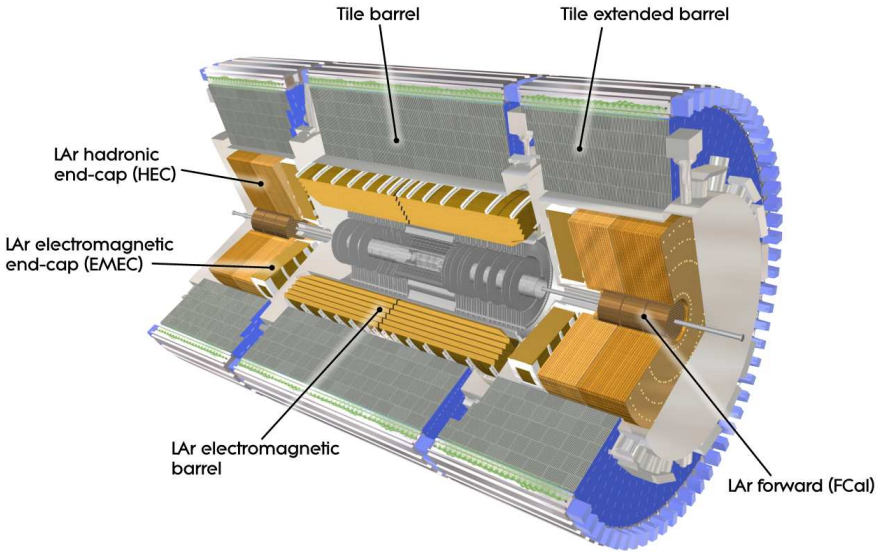

Figure 2.6: *Cut-away view of the ATLAS calorimeter* [38].

Hadronic Calorimeter

The hadronic calorimeter is designed to provide accurate energy measurements of hadrons, its typical energy resolution is $\Delta E/E = 50\%/\sqrt{E} \oplus 0.3\%$. It extends from a radius of 2.28 m to 4.25 m and is composed of scintillator tile calorimeters in the barrel region ($|\eta| < 1.7$) and LAr calorimeters in the end-caps ($1.5 < |\eta| < 3.2$).

- *Tile Calorimeter*
  The tile calorimeter is a sampling calorimeter with steel used as absorbing material and scintillating tiles as active material. It is divided into a barrel ($|\eta| < 1.0$) and two extended barrels ($0.8 < |\eta| < 1.7$). Barrel and extended barrels have three layers, approximately 1.5, 4.1 and 1.8 interaction lengths thick for the barrel and 1.5, 2.6, and 3.3 for the extended barrel. The granularity of the tile calorimeter is $\Delta\eta \times \Delta\phi = 0.1 \times 0.1$ in the first two layers and $\Delta\eta \times \Delta\phi = 0.2 \times 0.1$ in the last layer.

- *Hadronic End-cap Calorimeter*
  The Hadronic End-cap Calorimeter (HEC) exploits the LAr technology of the EM calorimeter, but with copper used as absorbing material. It has two wheels per end-cap located behind the EM calorimeter and shares the same cryostat with it. To reduce the drop in material density at the transition between the different calorimeter systems, it overlaps both with the tile calorimeter and with the forward calorimeter described below. Its granularity ranges from $\Delta\eta \times \Delta\phi = 0.1 \times 0.1$ to $\Delta\eta \times \Delta\phi = 0.2 \times 0.2$

Forward Calorimeter

To ensure a large coverage in pseudorapidity a further calorimeter, the Forward Calorimeter (FCal), covers the region $2.5 < |\eta| < 4.9$. The FCal acts both as electromagnetic and as hadronic calorimeter and is located in the same cryostat as the EM and HEC calorimeter end-caps. It consists of three modules in each end-cap: the first, using copper as absorbing material, is designed to measure the energies of photons and electrons. The other two, using tungsten as absorbing material, measure the energy coming from hadronic interactions. The FCal is approximately 10 interaction lengths deep and its granularity ranges from $\Delta\eta \times \Delta\phi = 0.75 \times 0.65$ to $\Delta\eta \times \Delta\phi = 5.4 \times 4.7$. Energy measurements done with this calorimeter are characterised by low resolution, typically $\Delta E/E = 100\%/\sqrt{E} \oplus 3.1\%$.

2.2.4 Muon System

Muons cross the ID and calorimeter system without being absorbed, therefore a dedicated detector is needed to measure their trajectory and momentum. The outermost part of the ATLAS experiment is devoted to this purpose. A barrel ($|\eta| < 1.0$) and two end-caps ($1.4 < |\eta| < 2.7$) toroid magnets surround the calorimeter, each of them consisting of eight coils located symmetrically around the beam axis. The toroids ensure a magnetic field mostly perpendicular to the muon trajectories, resulting in about 1.5-5.5 Tm of bending power in the range $|\eta| < 1.4$, and approximately 1-7.5 Tm in the region $1.6 < |\eta| < 2.7$.

The tracks of the muons are reconstructed based on position measurements in three layers of chambers. Different types of muon chambers are employed, designed for different functions. Precise measurements are provided by chambers instrumented with Monitored Drift Tubes (MDT) for $|\eta| < 2.7$, while Cathode Strips Chambers are used for larger η. Both technologies are characterised by high resolution but slow response. These chambers are not suitable for trigger purposes, for which Resistive Plate Chambers (RPCs) in the barrel region and Thin Gap Chambers (TGC) in the end-caps are used.

2.2.5 Forward Detectors

Three auxiliary smaller detectors complete the ATLAS experiment.

Two of the three systems are used to determine the luminosity delivered by LHC to the ATLAS experiment. One is LUCID (LUminosity measurement using Cherenkov Integrating Detector), located at 17 m from the interaction point. It detects inelastic proton-proton scattering, and serves as main device for monitoring the online relative luminosity. The other detector is ALFA (Absolute Luminosity For ATLAS). It is located at 240 m from the interaction point and consists of trackers made of scintillating fibres.

The last system is the Zero-Degree Calorimeter (ZDC), used when operating the LHC with heavy ions. It consists of layers of alternating quartz rods and tungsten plates

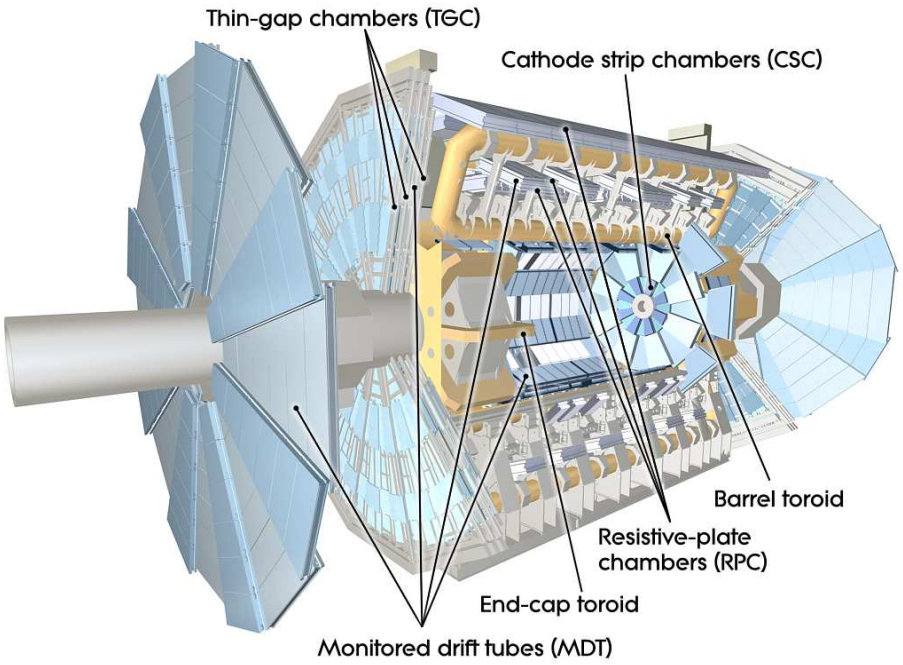

Figure 2.7: *Cut-away view of the ATLAS muon system* [38].

measuring neutral particles in the range $|\eta| \geq 8.2$.

2.3 From Collisions to Final State Objects

2.3.1 Proton-Proton Interactions

The LHC collides protons, that are not elementary particles but composite objects made of *partons*: in a proton there are two up-type quarks and one down-type quark, called *valence quarks*, plus a *see* of other quarks and gluons. The composition of the proton in terms of partons is described by the Parton Distribution Functions (PDFs). The PDFs give the probability of finding a parton that carries a fraction x of the total momentum of the proton for a transferred momentum Q^2.

The dependency of the PDFs on Q^2 can be obtained through the DGLAP (Dokshitzer-Gribov-Lipatov-Altarelli-Parisi) [47] [48] [49] equations. For a quark q carrying a fraction x of the total momentum of the proton, the evolution of $f_q(x, Q^2)$ with Q^2 is given by:

$$\frac{d}{d\log Q^2} f_q(x, Q^2) = \frac{\alpha_s}{2\pi} \int_x^1 \frac{d\xi}{\xi} f_q(\xi, Q^2) P_{qq'}\left(\frac{x}{\xi}, \alpha_s\right) \tag{2.3}$$

where $P_{qq'}$ is the *splitting function*: $\alpha_s P_{qq'}\left(\frac{x}{\xi}, \alpha_s\right)$ is proportional to the probability that the quark q carrying momentum fraction x is originated by a quark q' carrying momentum

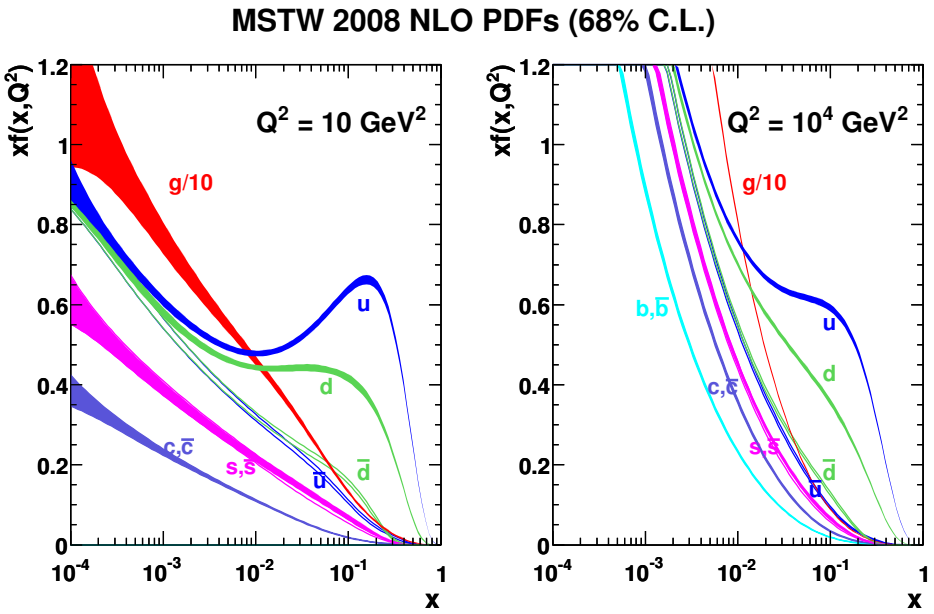

Figure 2.8: *MSTW PDFs evaluated at NLO with* $Q^2 = 10\ GeV^2$ *and* $Q^2 = 10^4\ GeV^2$ [51].

fraction ξ larger than x. Similar equations relate the other quarks, the antiquarks and the gluon.

The dependency of the PDFs on x, on the other hand, cannot be evaluated with perturbative QCD calculations, but have to be derived experimentally. For this purpose, a global fit of the data of processes probing different ranges of x and Q^2 is performed.

PDFs at NLO and NNLO with their uncertainties are provided by the CTEQ (The Coordinated Theoretical-Experimental Project on QCD) [50], MSTW (Martin-Stirling-Thorne-Watt Parton Distribution Functions) [51] and NNPDF (Neural Network Parton Distribution Functions) groups [53], as well as the HERA (Hadron Elektron Ring Anlage) experiment [54], which provided important experimental input through the analysis of the results of electron-proton scattering. For this thesis the latest available PDFs at the time of the data analyses from the CTEQ and MSTW (previously MRST: Martin-Roberts-Stirling-Thorne [52]) groups have been used. As an example, Figure 2.8 shows the PDFs from the MSTW group at two different values of Q^2.

When the collisions take place, the dominating processes are those mediated by strong interaction: soft and hard scattering processes, characterised by low and high transferred momentum, respectively. The cross section for the hard scattering between two partons $\sigma_{ab\to X}$ can be evaluated making use of perturbative QCD calculations at a given order. The overall scattering cross section for the two protons colliding, σ_{AB}, can be obtained through the *factorisation theorem* [44] [45] by weighting the scattering cross section of the

two partons, $\hat{\sigma}_{ab\to X}$, for the PDFs of the protons:

$$\sigma_{AB} = \int dx_a dx_b f_{a/A}(x_a, Q^2) f_{b/B}(x_b, Q^2) \hat{\sigma}_{ab\to X} \tag{2.4}$$

where x_a and x_b are the fraction of the total momentum carried by the partons a and b, Q^2 a large momentum scale characterising the hard scattering, and $f_{a/A}(x_a, Q^2)$ and $f_{b/B}(x_b, Q^2)$ are the proton PDFs.

Q^2 is typically chosen to be the *factorisation scale*, μ_F, the scale distinguishing the soft from the hard regime. The partonic cross section can be wrote in a perturbative expansion in α_s, which is evaluated at the renormalisation scale μ_R. With these changes Equation 2.4 can be rewrote in the form:

$$\sigma_{AB} = \int dx_a dx_b f_{a/A}(x_a, \mu_F^2) f_{b/B}(x_b, \mu_F^2) \times \left[\hat{\sigma}_0 + \alpha_s(\mu_R^2)\hat{\sigma}_1 + ...\right]_{ab\to X} \tag{2.5}$$

The production cross sections as a function of the centre-of-mass energy of the proton-proton collisions for some relevant benchmark processes as evaluated with this procedure are shown in Figure 2.9.

2.3.2 Parton Showers

The factorisation theorem provides a tool to evaluate the hard interaction cross section resulting from the proton-proton collisions. The partons from the hard scattering usually have large momentum, and can produce a shower of secondary partons of lower momenta through processes like gluon splitting ($g \to q\overline{q}$) and gluon emission ($q \to gq$).

The evolution of a parton can in principle be evaluated at a fixed order with perturbative QCD, but the calculation for the full shower is virtually impossible, and there are some processes (collinear emission of a gluon or emission of a gluon of low momentum) leading to divergences.

Alternative approaches to the fixed order calculation are represented by "all-orders" techniques in which the evolution of the parton shower is described making use of splitting functions: the probability of evolving from an energy scale to a lower one without emitting a gluon of energy larger than a given value is parametrised by the Sudakov form factors [46]. The probability is evaluated iteratively on all the secondary partons produced, till the energy scale at which partons combine to form hadrons (see below). The emission of radiation during the evolution of the parton shower and by final state hadrons is called *final state radiation*, in contrast with the emission due to the incoming partons, which is called *initial state radiation*.

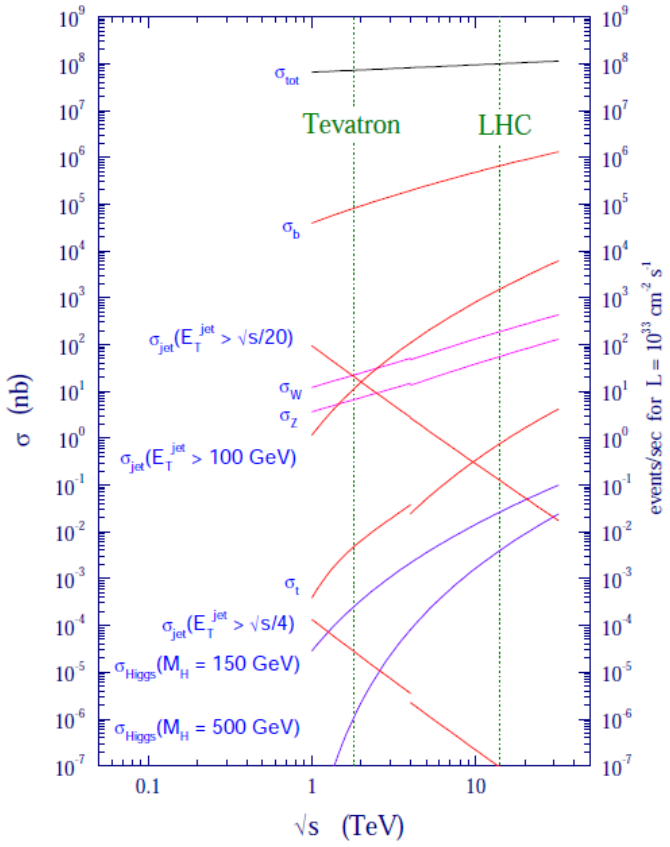

Figure 2.9: *Cross sections of Standard Model processes as a function on the centre-of-mass energy of the proton-proton collisions* [42].

2.3.3 Formation of Hadrons

The evolution of a parton shower stops when the energy of the emitted partons reaches a scale where the coupling constant for the strong interaction cannot be considered small any more and perturbative QCD cannot be employed. At this energy scale, experimentally measured to be $\Lambda_{QCD} \approx 200$ MeV, partons bind to form colourless particles (see Section 1.3). After the recombination of the partons of the shower, a rather collimated collection of hadrons originates, which is called *jet*.

2.3.4 Underlying Event

Besides the hard scattering, there are interactions also among other partons of the protons, typically soft scattering processes. These processes produce the so-called *underlying event* and form a background to the hard scattering processes. The prediction for their magnitude can be made by the use of several non-perturbative and semi-perturbative phenomenological models, whose parameters are constrained by the experimental results (see for example [63]).

Figure 2.10 provides a schematic illustration of the evolution of a proton-proton collision, including all the steps described in this section.

2.4 Monte Carlo Simulations of Physics Processes

In order to study the detector response to different physics processes, detailed simulations are needed. All the different aspects described in the previous section must be taken into account and simulated, together with the interactions between the particles and the detector.

The first step is the *generation* of events using Monte Carlo (MC) methods, where hard and soft interactions are simulated. If the particles produced decay promptly (travel for a distance $c\tau < 10$ mm), the generator handles also the decay, otherwise the decay is handled in the following step. The details of the generation depend on the MC generator adopted:

- *PYTHIA and PYTHIA 8*: The hard scattering process is calculated at LO, then QCD and QED radiation is added in a shower approximation having the best accuracy when the emission angle of the shower particles is small. After the shower, a phenomenological model is used to simulate the hadronisation of quarks and gluons. Soft interactions are then added, to reproduce the underlying events [59] [60].
- *HERWIG and HERWIG++*: The simulation steps are the same as in PYTHIA or PYTHIA 8, the main differences being in the implementation of the parton shower

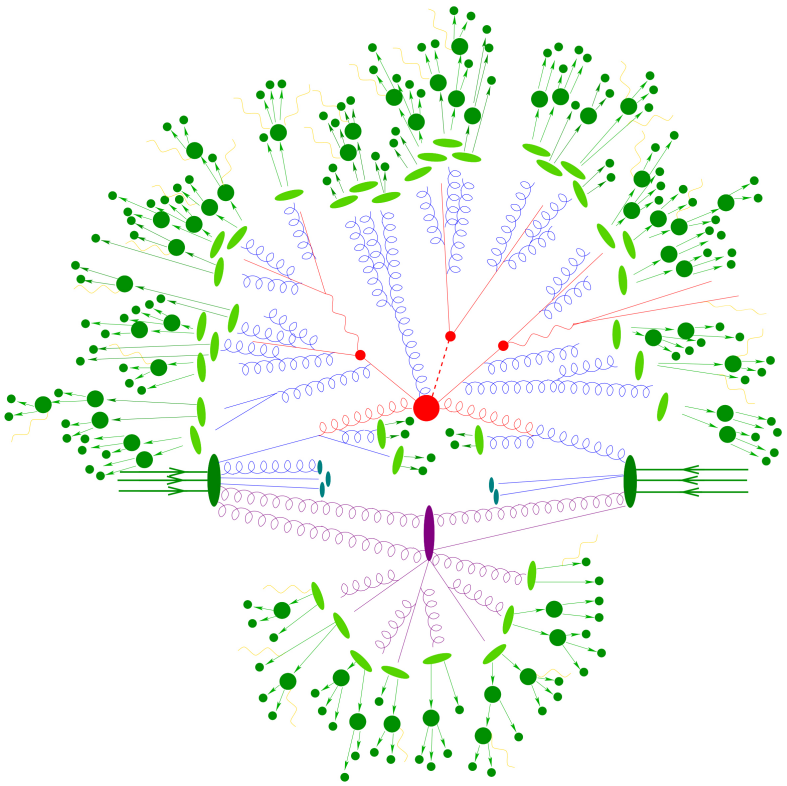

Figure 2.10: *Schematic illustration of a proton-proton collision. The emission of initial and final state radiation is represented in blue, the hard scattering in red, the underlying events in violet and the hadronisation in green* [64].

and hadronisation models. The underlying event is simulated separately with the Jimmy [63] implementation [61] [62].

- *SHERPA*: Matches a fixed-order QCD calculation of the hard scattering to QCD showers. It provides a better description in case of high multiplicity of jets than HERWIG and PYTHIA, and allows the treatment of c and b quarks as massive objects [64] [65].

- *Alpgen*: Targets the generation of final states with many jets, by taking into account the leading order contributions coming from the presence on n additional partons [66]. It is interfaced with HERWIG or PYTHIA for hadronisation and production of initial and final state radiation.

- *McAtNLO*: The evaluation of the hard scattering process is performed at NLO, ensuring better accuracy in cross section evaluation and modelling of the kinematic variables. It is interfaced with HERWIG for the for the simulation of parton shower, underlying event and hadronisation [67].

- *Powheg*: As McAtNLO, Powheg performs NLO QCD computations. It can be interfaced with either PYTHIA or HERWIG for the simulation of the parton shower [68].

- *MadGraph*: Is a leading order generator that can be interfaced with PYTHIA or HERWIG. One of the main advantages of this program is the easy implementation of the processes [70] [71].

- *AcerMC*: Is a generator dedicated to SM background processes critical for the LHC, because their generation was unavailable or not straightforward. It uses an internal library for the matrix element calculation (based on MadGraph), and can be interfaced with PYTHIA or HERWIG for the simulation of the initial and final state radiation and of the hadronisation [69].

- *Whizard*: Is a leading order generator, but matrix elements obtained by alternative methods (for example including loop corrections) may be interfaced as well. It is usually interfaced with HERWIG, and allows to treat the polarisation exactly for both initial and final states [72] [73].

The simulation step takes into account the detector specifications and can be configured to mimic the experimental conditions of a particular data taking period, to get a better agreement between the Monte Carlo simulated events and the real data collected. A full simulation of the detector performed with the simulation program *Geant4* [56] [57] is the default, but is very consuming in terms of computing resources. An alternative simulation method, called *AtlFast-II* [58] is also adopted within the ATLAS experiment.

About 80% of the time taken by the full Geant4 simulation is due to the simulation of the particle showers in the calorimeter, mainly caused by electromagnetic particles. In AtlFast-II rather than fully simulating the development of a shower originated by a particle, a parametrisation of its longitudinal and lateral profile is exploited. This method is intrinsically less accurate, and the parameters have to be tuned against data and full Geant4 simulations.

The output of the generation and simulation processes consist of data, called hits.

The last step is the *digitisation* of the hits. Hits are converted into detector responses, so that Monte Carlo events can be processed as real data, and the final state objects can be identified and reconstructed as elementary particles or jets following the procedures described in Chapter 3.

Chapter 3

Performace of the ATLAS Detector

An efficient reconstruction of the final state objects is a crucial point for any Physics analysis. This chapter briefly describes the trigger and data acquisition system and reports the techniques adopted to reconstruct all final state objects used in this thesis. More details can be found in Ref. [74].

3.1 Trigger and Data Acquisition System

The nominal rate of proton-proton collisions at the LHC is 40 MHz. The resulting volume of data cannot be recorded in its totality. The actual rate of data that can be processed with the available technology and resources is about 200 Hz, therefore a system reducing the initial rate down to this value by selecting only the potentially interesting events is needed. This is achieved by the use of a three-level trigger system:

- *L1*: Reduced granularity information from the calorimeters and from the trigger muon chambers are used to define Regions of Interest (RoI's), i.e. η and ϕ location of the regions where high transverse momentum electrons, muons, taus, photons or jets are likely to have crossed the detector. The events are reduced to a rate of 75 kHz in a time of 2.5 μs per event, stored temporary and sent to the following level.

- *L2*: This level refines the decisions taken at L1 bringing the rate of data down to 3.5 kHz. To achieve this, decisions based on the full granularity and precision of all the sub-detectors are taken in about 40 ms. The selected events are transferred to the event-building system and then passed to the next level for a final selection.

- *Event Filter (EF)*: The EF reduces the event rate to 200 Hz by performing an offline

analysis taking about 4 s per event. Each selected event has an average size of 1.3 Mbyte and is stored permanently on CERN computing facilities.

The data passing the EF are in a format called *raw*. Raw data are further reprocessed in different steps, calibrated and brought to a format suitable to easily perform physics analyses.

3.2 Track and Vertex Reconstruction

The tracks of charged particles with transverse momenta larger than 0.5 GeV and $|\eta| < 2.5$ are reconstructed exploiting the information coming from the ID, described in Subsection 2.2.2. Track reconstruction is performed in three steps:

- *Pre-processing.* The raw data from the pixel and SCT detectors are used to obtain clusters, while the TRT timing information are converted into drift circles. The clusters are then converted into three dimensional space points combining the information from opposite hemispheres of the SCT.

  Pixels traversed by different particles may be merged to form a single cluster, or the same pixel may be traversed my more than one particle. If no attempt to split the clusters is made, these conditions can lead to a loss in reconstruction efficiency. Starting from 2011, artificial neural networks have been used to assess the probability that a cluster is originated from more than one particle, and to split it if possible [75].

- *Track finding.* Three space points from the pixel detector and from the SCT are used as seeds for the default track finding algorithm, the inside-out algorithm. Any hit lying on a helical path compatible with the seeds is added to form a track candidate. Many of the track candidates are fake tracks, originated by combinatorial effects, rather than real tracks, associated to charged particles crossing the ID. An algorithm is employed to discriminate between real and fake tracks, called ambiguity solver. The algorithm associates to each track candidate a score, based on several quality criteria. Track candidates with a score below a certain threshold are rejected. The remaining track candidates are ordered, from the highest to the lowest score, and processed. Track candidates sharing too many clusters with another track candidate higher in the score hierarchy are rejected.

  The next step consist of extending the tracks to the TRT and refitting them exploiting the full information from the three parts of the ID. The refitted tracks are compared to the track candidates obtained without TRT information. Hits on track extensions leading to bad quality tracks are classified as outliers, measurements not belonging to a track.

A different track finding algorithm is used to look for tracks coming from secondary particles from conversions or long lived particles, called back-tracking. Track segments not used by the inside-out algorithm are searched for and then extended in the SCT and pixel detector.

- *Post-processing.* The z coordinates of the reconstructed tracks at the beam line are used as seeds to locate the position of the hard scattering process, called primary vertex. A χ^2 fit of the seeds and the nearby tracks associate a weight to each track depending on its compatibility with the vertex. Tracks more than 7 σ apart from the vertex are used as seeds for a new vertex and the procedure is iterated till no additional vertices can be identified. Among all the vertices found, the hard scattering vertex is the one with the largest sum of squared transverse momentum of its associated tracks.

The track finding efficiency is defined as the fraction of particles matched to reconstructed tracks passing a set of quality cuts, while the fake rate is defined as the fraction of reconstructed tracks passing the same quality cuts but not matched to any particle.

More details on track and vertex reconstruction algorithms and performance can be found in Ref. [76].

3.3 Jet Reconstruction

Jets deposit energy mainly in the cells of the calorimeter system. In order to reconstruct them, it is necessary to find algorithms able to associate the energy deposit in a given cell to the jet it belongs to. This is done by either maximising the energy deposit in a cone of fixed size, or by sequentially recombining objects. The second option has many advantages [1], and is nowadays the preferred technique to define a jet.

The $Anti - k_T$ algorithm

The default jet reconstruction algorithm used in the ATLAS experiment is the $Anti - k_T$ algorithm. It is an algorithm based on the recursive association of pairs of objects, where the objects are usually *topological cell clusters* [2]. Topological cell clusters are groups of neighbouring calorimeter cells, representing the shower development for each particle. The seed for a cluster is chosen based on the energy deposit, that has to be above a threshold

[1] On a theoretical point of view, a good jet definition must be collinear and infrared safe, and order independent (i.e. the result should not depend on the order in which the objects are clustered). The algorithms of the first type are not infrared safe.

[2] Also calorimeter towers can be used as input objects, but since this method is not used for the results of this thesis, no additional details are provided. For a description of calorimeter towers and their clustering procedure see for example Ref. [74]

defined by the noise in the calorimeter. Directly neighbouring cells are added to the cluster, while neighbours of neighbours are added if the energy deposit with respect to the noise is significantly high.

For each pair ij of topological clusters with transverse momentum $p_{T,i}$, $p_{T,j}$ a quantity d_{ij} is defined as:

$$d_{ij} = min(p_{T,i}^{2p}, p_{T,j}^{2p}) \frac{\Delta R_{ij}^2}{R} \tag{3.1}$$

with R controlling the size of the jets (the default choice is $R = 0.4$) and p an integer determining the type of reclustering procedure.

For a given p and R, the minimum d_{ij} and the minimum $d_i = p_{T,i}^{2p}$ are searched for. If d_i is the smallest quantity, it is considered a jet on its own and removed from the list of clusters. If d_{ij} is the smallest quantity, the two clusters are combined in a new object k and the procedure is repeated until all the original input clusters are either combined or form jets on their own.

The $Anti - k_T$ algorithm is obtained taking $p = -1$. This choice ensure a particular resilience of the boundaries of a jet with respect to soft radiation. More details can be found in Ref. [77].

Jet calibration

The electromagnetic and hadronic calorimeters of ATLAS are non compensating, (i.e., the energy scales for the two systems are different), therefore the energy measurements of the jets need to be calibrated.

In this thesis two calibration methods are used: the EM+JES (electromagnetic + jet energy scale) for data collected at a centre-of-mass energy for the proton-proton collisions of 7 TeV, and the LCW+JES (local calibration weighting + jet energy scale), for data collected at 8 TeV.

In the EM+JES calibration the clusters composing the jets are calibrated at the scale of the electromagnetic calorimeter. To obtain the scale of the hadronic calorimeter a multiplicative factor, named JES, is derived from Monte Carlo simulations of truth jets.

In the LCW+JES calibration scheme, the input clusters are already calibrated at the energy scale of the hadronic calorimeter, exploiting simulations of energy deposits of jets. A final JES correction is then applied to the energy value obtained from the calibrated clusters, to account for effects as particles out of acceptance or energy deposits below reconstruction threshold. Figure 3.1 shows the JES correction as a function of η for both calibration procedures. In both schemes a systematic uncertainty is associated to the choice of the JES, derived in bins of p_T and η using in-situ techniques [78]. These techniques are also adopted to evaluate the uncertainty on the resolution of the energy

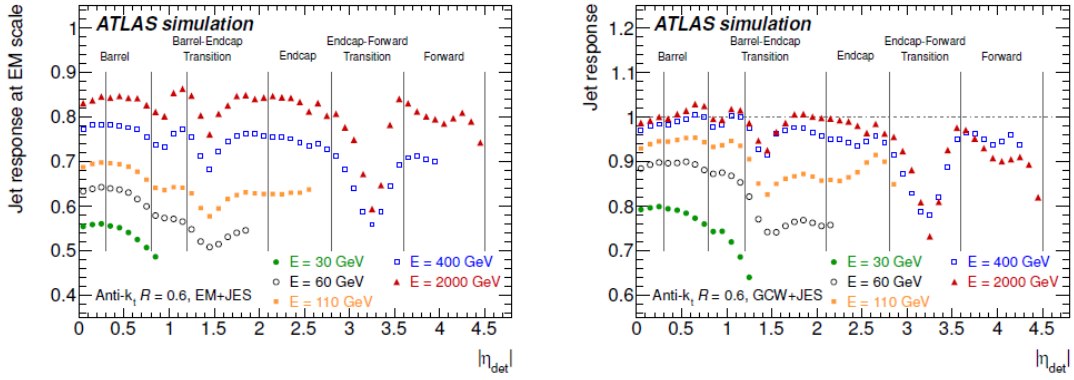

Figure 3.1: *Average energy of jets formed from topo-clusters calibrated at the EM (left) or the LCW scale (right) with respect to the truth jet energy ($E_{jet}^{EM/LCW}/E_{truth}$) as a function of the jet pseudorapidity. Also indicated are the different calorimeter regions. The inverse of the response shown in each bin is equal to the average jet energy scale correction* [78].

measurement of a jet, the JER, derived from measurements of the jet response asymmetry in di-jet events [79].

3.4 b-jet Identification

Jets originating from the hadronisation of a b-quark are called *b-jets*. b-jets can be detected, or tagged, exploiting the properties distinguishing them from jets containing only lighter quarks [80]. The most important feature is the relatively long lifetime of hadrons containing a b-quark, of the order of 1.5 ps, which makes a b-hadron with $p_{\mathrm{T}} = 50$ GeV travel on average about 3 mm in the transverse plane before decaying. The secondary decay vertex is therefore displaced, and can be identified by reconstructing the tracks originating from the b-hadron decay. Its distances in the transverse and longitudinal directions from the primary vertex (transverse and longitudinal impact parameters, d_0 and z_0), can be used to tag the jet. A b-hadron carries a high fraction of the original b-quark transverse momentum and is characterised by high mass (> 5 GeV). As a result, its decay products may have large transverse momentum and opening angles large enough to allow separation. Finally, it is possible to exploit the presence of leptons coming from the semi-leptonic decays of the b-hadrons.

Different b-tagging algorithms have been developed in the ATLAS experiment, exploiting one or more of the features described above (more details can be found in Ref. [80]):

- *IP3D*: It is based on the transverse and longitudinal impact parameter significance, defined as the ratio between the impact parameter and its resolution.

- *SV0*: It tags the secondary vertex of the b-hadrons combining the information on the decay length and its significance.
- *SV1*: In addition to the information on the decay length significance, also the number of tracks, their invariant mass and momentum are used as discriminating variables by this algorithm and combined in a likelihood.
- *JetFitter*: It exploits the topology of the decays of b- and c-hadrons in a jet. The discrimination between b-, c- and light jets is achieved with a likelihood built with similar variables as the ones used in the SV1 tagger.

To achieve higher efficiencies and lower fake rates the taggers listed above can be combined. In this thesis for the data collected at a centre-of-mass energy of 7 TeV a combination of JetFitter and IP3D has been used, called *JetFitterCombNN*. The combination is based on an artificial neural network technique. For the data collected at 8 TeV a combination of JetFitterCombNN, IP3D and SV1 has been adopted. Also this combination has been made with an artificial neural network technique, and is called *MV1* [81].

All these algorithms associate to each jet in an event a weight. A jet is considered a b-jet if its weight is above a certain threshold. For the JetFitterCombNN tagger the threshold adopted in this thesis is 1.8, corresponding to a nominal efficiency of about 60%, and rejection factors 378 and 8 for light and c-jets, respectively. For the MV1 tagger the working point adopted is 0.8, corresponding to a nominal efficiency of about 70%, and rejection factors 150 and 5 for light and c-jets, respectively. Figure 3.2 shows the efficiency of tagging a b-jet, as a function of its transverse momentum. The results obtained on a sample of data containing muons collected at $\sqrt{s} = 7$ TeV are compared to the results obtained on a simulated sample. To account for the discrepancies between the two, correction factors to be applied to the simulated events, called scale factors, have been derived. The rejection power against light and c-jets is very important for background rejection in a physics analysis. Its magnitude as a function of the efficiency for the different taggers is shown in Figure 3.3.

3.5 Electron Reconstruction

Electrons are identified combining the information of the EM and hadronic calorimeters and of the ID, allowing to achieve good rejection against jets and high efficiency.

The first step to reconstruct electrons lying in the pseudorapidity region covered by the ID ($|\eta| < 2.5$) is to create seed clusters of neighbouring EM calorimeter cells with a minimum transverse energy deposition of 2.5 GeV. The direction of the tracks is then compared to the position of the seed clusters. If the extrapolated distance of a track from a seed cluster is below a certain threshold, the track and the energy deposition

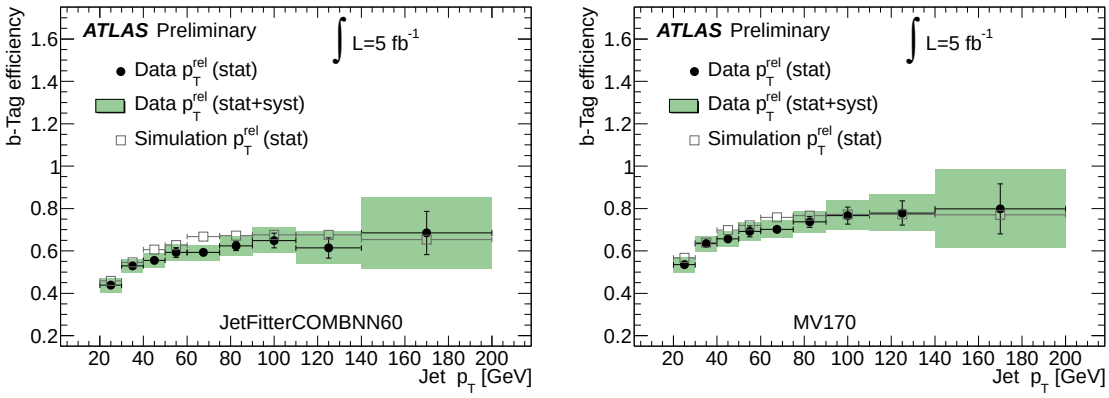

Figure 3.2: *The b-tag efficiency in data and simulation for the JetFitterCombNN tagging algorithms at 60% efficiency (left) and the MV1 tagging algorithms at 70% efficiency (right)* [81].

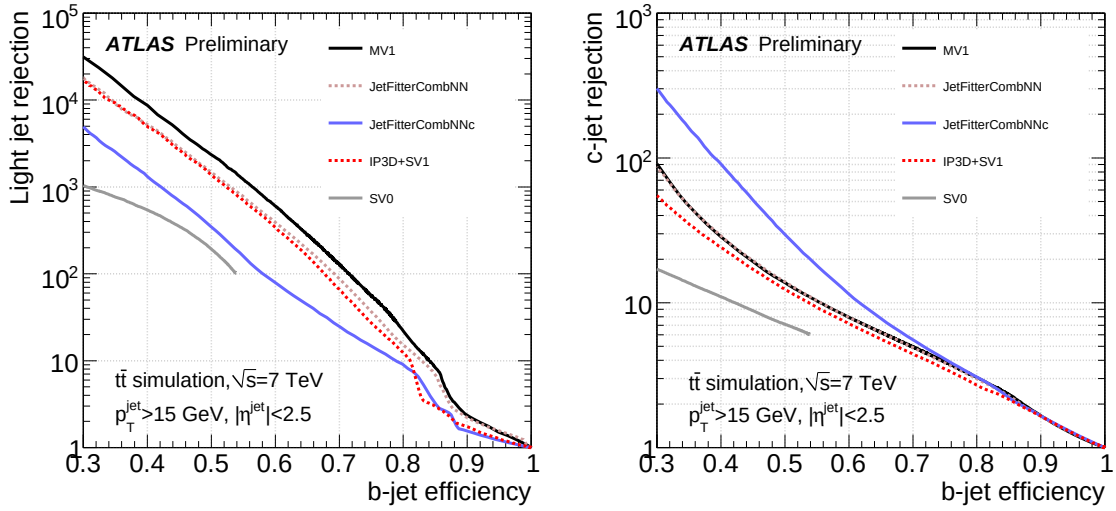

Figure 3.3: *Light-jet (left) and c-jet (right) rejection as a function of the b-tag efficiency for the different b-tagging algorithms, based on simulated $t\bar{t}$ events* [81].

in the calorimeter form a candidate electron. Different identification classes of increasing background rejection power but decreasing efficiency are adopted: *loose*, *medium* and *tight*. In the loose criteria the information on the leakage in the hadronic calorimeter and on the shape of the shower in the second layer of the EM calorimeter are used. The medium criteria includes also shower shape information on the first layer of the calorimeter, plus a requirement on the matching between the clusters and the tracks, which must satisfy some quality criteria. In the tight category the requirement on track matching and quality are more strict, and electrons from photon conversion are rejected.

In the region not equipped with tracking detectors, an electron is reconstructed if there is a cluster with $E_T > 5$ GeV. In this region it is not possible to distinguish between electrons and photons, while it is possible to distinguish electrons originated by hadron decays exploiting the information on the shape of the shower.

In this thesis only electrons falling in the region covered by the ID are used.

The efficiency of tagging an electron can be factorised in different terms:

$$\epsilon_e = \epsilon_{\text{cluster}} \cdot \epsilon_{\text{reco}} \cdot \epsilon_{\text{id}} \cdot \epsilon_{\text{trig}} \cdot \epsilon_{\text{other}} \tag{3.2}$$

$\epsilon_{\text{cluster}}$ is the efficiency to reconstruct an electromagnetic cluster. It has been determined with simulations to be close to unity. ϵ_{reco} is the efficiency of the electron reconstruction algorithm given the presence of a cluster. It has to be determined experimentally on data and compared to Monte Carlo simulations, in order to derive corrections (scale factors) accounting for any discrepancy between the two. ϵ_{id} is the efficiency of the identification criteria (loose, medium or tight) with respect to the reconstructed electron. As the reconstruction efficiency, it has to be derived from data and compared to the expectation from simulated events in order to derive the scale factors. ϵ_{trig} is the efficiency of the trigger with respect to reconstructed electrons satisfying a specific identification criteria, and has to be derived for each electron trigger. Finally, ϵ_{other} is the efficiency of any other selection applied, as for example the requirement of selecting electrons isolated from any other final state object (useful to distinguish electrons originated by a Physics process of interest from electrons originated by hadron decays). This efficiency is process-dependent, therefore has to be measured for each analysis.

The reconstruction and identification efficiencies have been studied on the full dataset collected at a centre-of-mass energy of 7 TeV selecting $Z \to ee$, $W \to e\nu$ and $J/\Psi \to ee$ events [83], and at 8 TeV selecting $Z \to ee$, $Z \to ee\gamma$ and $J/\Psi \to ee$ events [84]. The reconstruction efficiency given the presence of a seed cluster is shown in Figure 3.4 both for the $\sqrt{s} = 7$ TeV and the $\sqrt{s} = 8$ TeV dataset. The efficiency of the different identification criteria is shown in Figure 3.5(a) for the $\sqrt{s} = 7$ TeV dataset and in Figure 3.5(b) for the $\sqrt{s} = 8$ TeV dataset.

Like jets, also the energy measurement of electrons must be calibrated and the energy

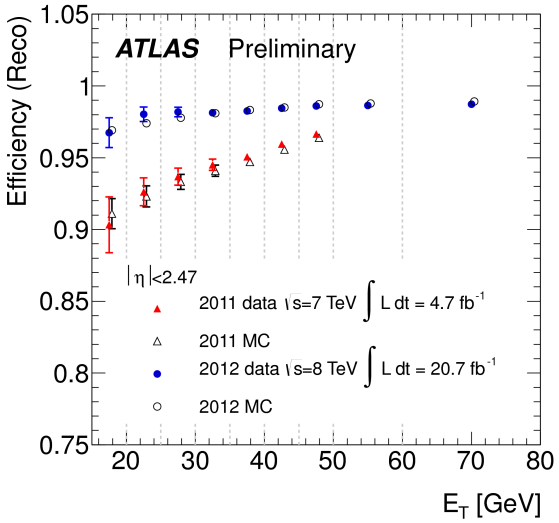

Figure 3.4: *Electron reconstruction efficiency given the presence of a seed cluster as a function of E_T integrated over the full pseudorapidity range for the full dataset collected at a centre-of-mass energy of the proton-proton collisions of $\sqrt{s} = 7$ TeV (triangles) and 8 TeV (circles)* [84].

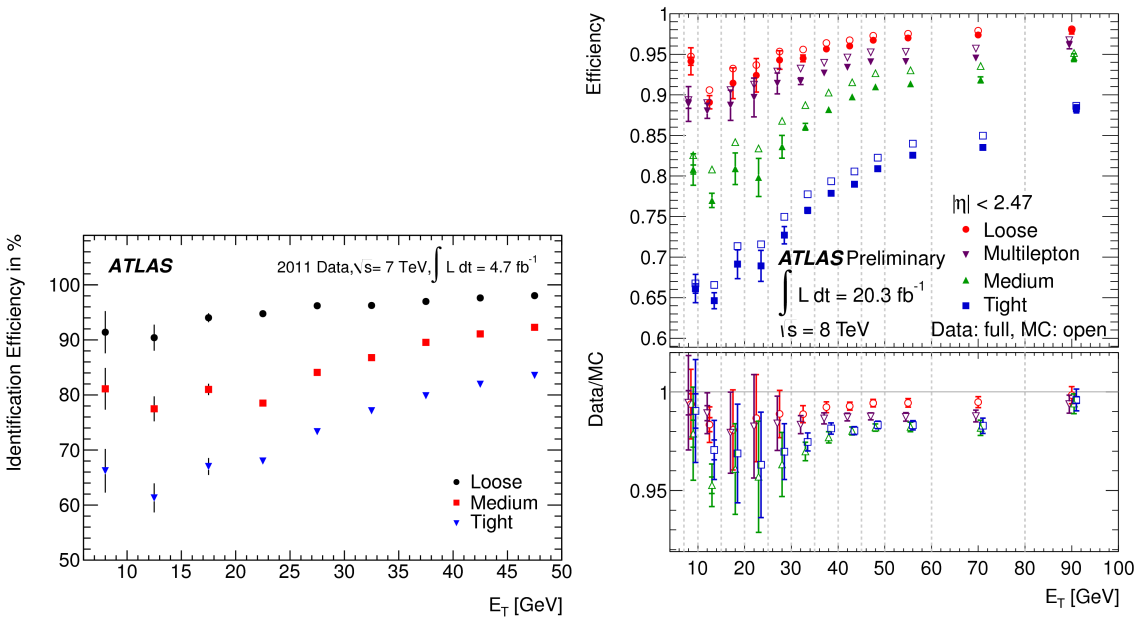

(a) (b)

Figure 3.5: *Efficiencies of the identification criteria as a function of E_T integrated over the full pseudorapidity range for the full dataset collected at a centre-of-mass energy of the proton-proton collisions of (a) 7 TeV,* [83] *and (b) 8 TeV* [84].

response and resolution derived. This is done starting from Monte Carlo simulations of $Z \to ee$ events which are than compared to data collected both at 7 and 8 TeV, as documented in Ref [85].

3.6 Muon Reconstruction

Muons can be reconstructed exploiting only the data from the MS, or combining them with the data from the ID and from the calorimeter system. The different type of muons are [86]:

- *Stand Alone (SA)*: The muon trajectory is reconstructed only with the MS. This identification method is used to extend the geometrical acceptance to the region $2.5 < |\eta| < 2.7$, not covered by the ID.
- *Combined (CB)*: The tracks reconstructed in the MS are combined with the ones reconstructed in the ID. If a pair of tracks is compatible, it forms a combined track and is used as muon candidate. Combined muons are the default type of muons used in the analyses.
- *Segment Tagged (ST)*: A track in the ID is identified as a muon if it can be associated with at least one track segment in the MS. This identification criteria is ideal for muons crossing only one layer of the MS, because of low transverse momentum or because falling in a region of reduced acceptance.
- *Calorimeter Tagged (CaloTag)*: A track in the ID can be associated with an energy deposition in the calorimeter compatible with a minimum ionising particle. The purity of this method is low, but the method can be useful to reconstruct muons falling in non-sensitive regions of the MS.

In this thesis combined and segment tagged muons are used.

The reconstruction performance and the measurements of momentum scale and resolution have been performed on both 7 and 8 TeV data on samples of $Z \to \mu\mu$, $J/\Psi \to \mu\mu$ and $\Upsilon \to \mu\mu$ events. The reconstruction efficiency for the different types of muons is shown in Figure 3.6. The studies on momentum scale and resolution have been used to derive corrections to be applied to the Monte Carlo simulations to improve the data-Monte Carlo agreement [86].

3.7 Missing Transverse Momentum

In a hadron collider, the conservation of the momentum along the z direction cannot be exploited because the momentum of the partons involved in the hard scattering is

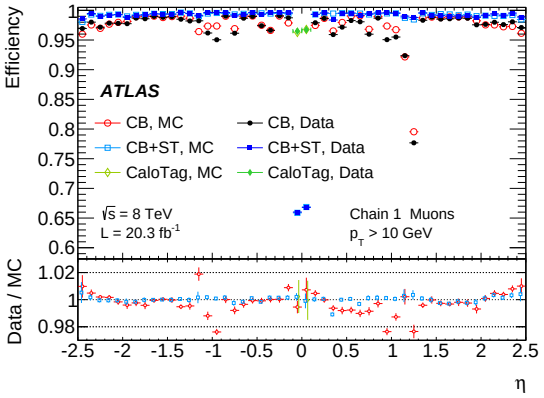

Figure 3.6: *Muon reconstruction efficiency as a function of eta measured in $Z \to \mu\mu$ events for muons with $p_T > 10$ GeV and different muon reconstruction types. CaloTag muons are only shown in the region $|\eta| < 0.1$, where they are used in physics analyses. The error bars on the efficiencies indicate the statistical uncertainty. The panel at the bottom shows the ratio between the measured and predicted efficiencies. The error bars on the ratios are the combination of statistical and systematic uncertainties* [84].

unknown. The conservation of the momentum in the transverse plane can instead be used, as the incoming partons do not carry transverse momentum. If in the final state there is a transverse momentum imbalance, it may signal the presence of weakly interacting particles that crossed the experiment without interacting with the detector material. The momentum imbalance in the transverse plane is called *missing transverse momentum*, $\boldsymbol{E}_{\mathrm{T}}^{\mathrm{miss}}$, and is obtained from the negative vector sum of the transverse momenta of all the particles detected. Its magnitude is denoted with the symbol $E_{\mathrm{T}}^{\mathrm{miss}}$ and referred to as *missing transverse energy*. The two components of $\boldsymbol{E}_{\mathrm{T}}^{\mathrm{miss}}$ are:

$$E_{\mathrm{x(y)}}^{\mathrm{miss}} = E_{\mathrm{x(y)}}^{\mathrm{miss,calo}} + E_{\mathrm{x(y)}}^{\mathrm{miss},\mu} \tag{3.3}$$

and

$$E_{\mathrm{T}}^{\mathrm{miss}} = \sqrt{\left(E_{\mathrm{x}}^{\mathrm{miss}}\right)^2 + \left(E_{\mathrm{y}}^{\mathrm{miss}}\right)^2} \tag{3.4}$$

$E_{\mathrm{x(y)}}^{\mathrm{miss,calo}}$ and $E_{\mathrm{x(y)}}^{\mathrm{miss},\mu}$ in Equation 3.3 are the calorimeter component and the muon component, respectively.

The calorimeter component results from different terms:

$$E_{\mathrm{x(y)}}^{\mathrm{miss,calo}} = E_{\mathrm{x(y)}}^{\mathrm{miss,e}} + E_{\mathrm{x(y)}}^{\mathrm{miss},\gamma} + \left(E_{\mathrm{x(y)}}^{\mathrm{miss},\mu}\right) + E_{\mathrm{x(y)}}^{\mathrm{miss},\tau} + E_{\mathrm{x(y)}}^{\mathrm{miss,jets}} + E_{\mathrm{x(y)}}^{\mathrm{miss,softjets}} + E_{\mathrm{x(y)}}^{\mathrm{miss,CellOut}} \tag{3.5}$$

All these terms are calibrated independently according to their parent objects. Soft jets are jets with $7 < p_T < 20$ GeV. The CellOut term accounts for energy depositions

in calorimeter cells not associated with any object. Energy depositions from muons in the calorimeter are counted only if they cannot be resolved from the calorimetric energy depositions of other objects, as jets. In the opposite case, they are already taken into account when evaluating the muon momentum, and therefore are already included in the second term of Equation 3.3, where:

$$E_{\mathrm{x(y)}}^{\mathrm{miss},\mu} = -\sum_{\mathrm{i}} p_{\mathrm{x(y)}}^{\mu,i} \tag{3.6}$$

with the sum running over the reconstructed muons.

Non-functioning or noisy readout channels of the detector, cosmic-ray and beam-halo muons, can produce fake $E_{\mathrm{T}}^{\mathrm{miss}}$. To avoid this, it is important to apply proper rejection cuts to reduce the impact on $E_{\mathrm{T}}^{\mathrm{miss}}$ of these sources [87].

The performance of the missing transverse momentum reconstruction have been studied on samples of $Z \to \ell\ell$ events, where no genuine source of $E_{\mathrm{T}}^{\mathrm{miss}}$ is expected (apart from a small contribution from semi-leptonic decays of hadrons), and on samples of $W \to \ell\nu$ events, where real $E_{\mathrm{T}}^{\mathrm{miss}}$ is expected. The performance have been assessed on both the 7 TeV and the 8 TeV dataset. For the 8 TeV dataset, additional studies on samples of minimum bias, $H \to \tau\tau$, $t\bar{t}$ and simulated SUSY signal events have been performed.

The distribution of $E_{\mathrm{T}}^{\mathrm{miss}}$ for $Z \to \mu\mu$ events at a centre-of-mass energy of 7 and 8 TeV are shown respectively in Figures 3.7(a) [88] and 3.7(b) [89].

A quantitative evaluation of the performance of the missing transverse momentum reconstruction can be performed studying the $E_{\mathrm{x(y)}}^{\mathrm{miss}}$ *resolution*, $\sigma(E_{\mathrm{x(y)}}^{\mathrm{miss}})$, as a function of the scalar sum of the transverse energy of all the objects in the event, $\sum E_T$. $\sigma(E_{\mathrm{x(y)}}^{\mathrm{miss}})$ is defined as the difference between the reconstructed missing transverse energy and its true value, obtained from the sum of all stable non-interacting particles in the final state (neutrinos and, in case of SUSY, the LSP). $\sigma(E_{\mathrm{T}}^{\mathrm{miss}})$ is found, to a good approximation, to raise linearly with $\sqrt{\sum E_T}$: $\sigma(E_{\mathrm{x(y)}}^{\mathrm{miss}}) = k\sqrt{\sum E_T}$. Figure 3.8 shows the resolution $\sigma(E_{\mathrm{x(y)}}^{\mathrm{miss}})$ as a function of E_T for different MC samples simulated at centre-of-mass energies for the proton-proton collisions of 7 TeV and 8 TeV.

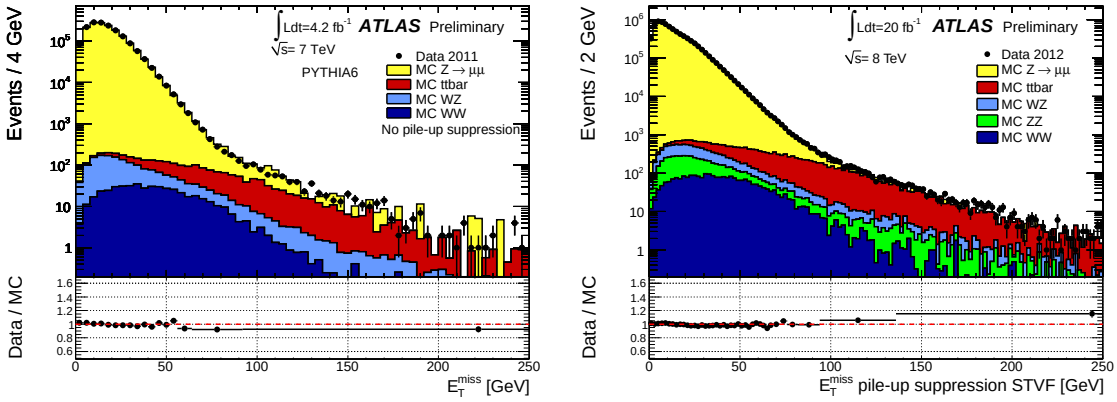

(a) (b)

Figure 3.7: *Distribution of E_T^{miss} as measured in a data sample of $Z \to \mu\mu$ events at a centre-of-mass energy for the proton-proton collisions of 7 TeV (a)* [88] *and 8 TeV (b)* [89]. *The expectation from Monte Carlo simulation is superimposed and normalised to data. The lower parts of the figures show the ratio of data over Monte Carlo. To cope with the harsher pile-up conditions, for the 8 TeV dataset a procedure of pile-up suppression has been used.*

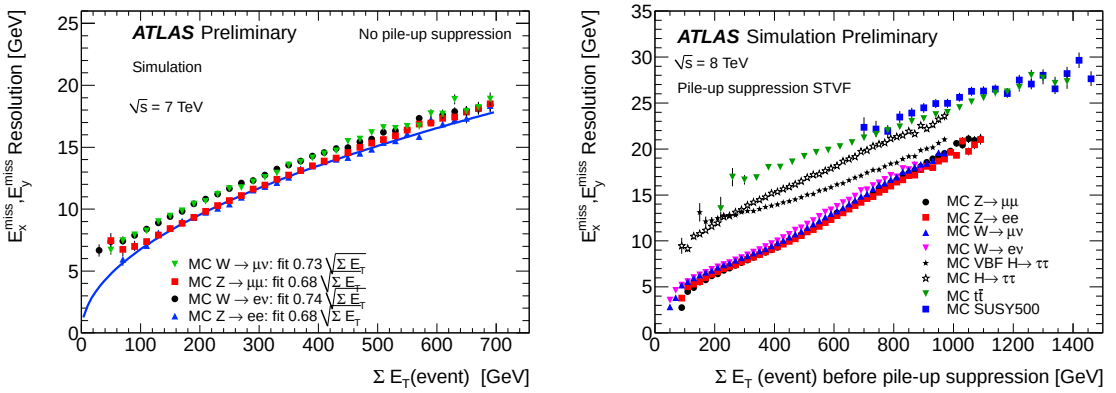

(a) (b)

Figure 3.8: *$E_{x(y)}^{miss}$ resolution as a function of E_T for the MC samples specified in the plots, simulated at a centre-of-mass energy for the proton-proton collisions of 7 TeV (a)* [88] *and 8 TeV (b)* [89]. *To cope with the harsher pile-up conditions, for the 8 TeV dataset a procedure of pile-up suppression has been used.*

Chapter 4

Search for Supersymmetric Particles with the ATLAS Detector

4.1 Program for Supersymmetry Searches

Discovering signals of SUSY particles is one of the main purpose for which the ATLAS detector was built. As already pointed out in Sections 1.7 and 1.8, SUSY extensions of the SM providing a solution to the hierarchy problem favour mass spectra for the SUSY particles in which at least some of them are at the TeV energy scale, and therefore accessible at the LHC.

A large fraction of members of the ATLAS experiment are involved in searches for SUSY signals. The subgroup of the ATLAS collaboration coherently organising this effort is called SUSY group, and its substructure reflects the various research areas.

The first distinction is between searches performed under the hypothesis of R-parity conservation and R-parity violation (see Subsection 1.7.1).

In the context of R-parity conserving SUSY, three classes of signals are targeted, depending on the production cross section and on the topology of the processes of interest: *strong production of gluinos and squarks of the first two generations*, *production of third generation squarks* and *electroweak production*. The expected production cross sections as a function of the average mass of the SUSY particles produced is shown in Figures 4.1(a) and 4.1(b), respectively, at a centre-of-mass energy of proton-proton collisions of 7 and 8 TeV. As can be seen from these figures, the production of gluinos and squarks are the processes characterised by the highest cross sections, followed by the pair production of stops. The cross section for sbottom pair production is not shown in these figures, but its magnitude is only a few percent different from the stop pair production one. The

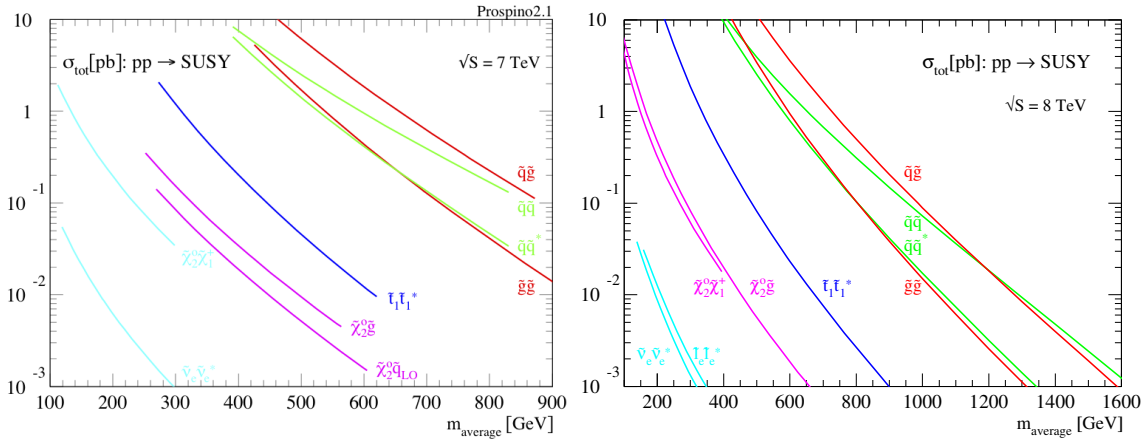

(a) (b)

Figure 4.1: *Production cross sections of the SUSY particles as a function of their average masses, calculated at a centre-of-mass energy of proton-proton collisions of 7 TeV (a) and 8 TeV (b) at NLO+NLL accuracy using the the program NLL-fast* [90].

production of SUSY particles via electroweak interaction is characterised by smaller cross sections, coherently with the magnitude of its coupling constant with respect to the strong interaction one.

Strong production searches targeting gluinos and squarks of first two generations have been the first ones performed within the SUSY group, because of the large production cross section and the topology of the final states. These searches are performed either in the context of specific SUSY models, as for example the mSUGRA and cMSSM models mentioned in Subsection 1.7.2, or in the context of the so called *simplified models*, where only the decay chains of interest are considered in the simulation of the signal and the SUSY particles not involved in them are regarded as not playing any role by setting their masses above the LHC reach.

The final states are characterised by moderate to high $E_{\mathrm{T}}^{\mathrm{miss}}$ because of the presence of the LSP (usually taken to be the $\widetilde{\chi}_1^0$), and a variable number of leptons and jets. Different analyses have been designed and optimised for different scenarios. The collection of all the public results produced by the SUSY group can be found in Ref. [91]. The search which showed the highest sensitivity to a large variety of models requires final states with $E_{\mathrm{T}}^{\mathrm{miss}}$, jets and no leptons. A selection of results obtained with the datasets collected at $\sqrt{s} = 7$ and 8 TeV can be found in Figures 4.2 [92] and 4.3 [93]. Since no excess over the SM expectation was observed, the results were interpreted in terms of 95% confidence level (CL) exclusion limits in the plane defined by the mass parameters of interest, under the conditions specified. The details of the statistical treatment of the results of the SUSY analyses are given in Section 4.4.

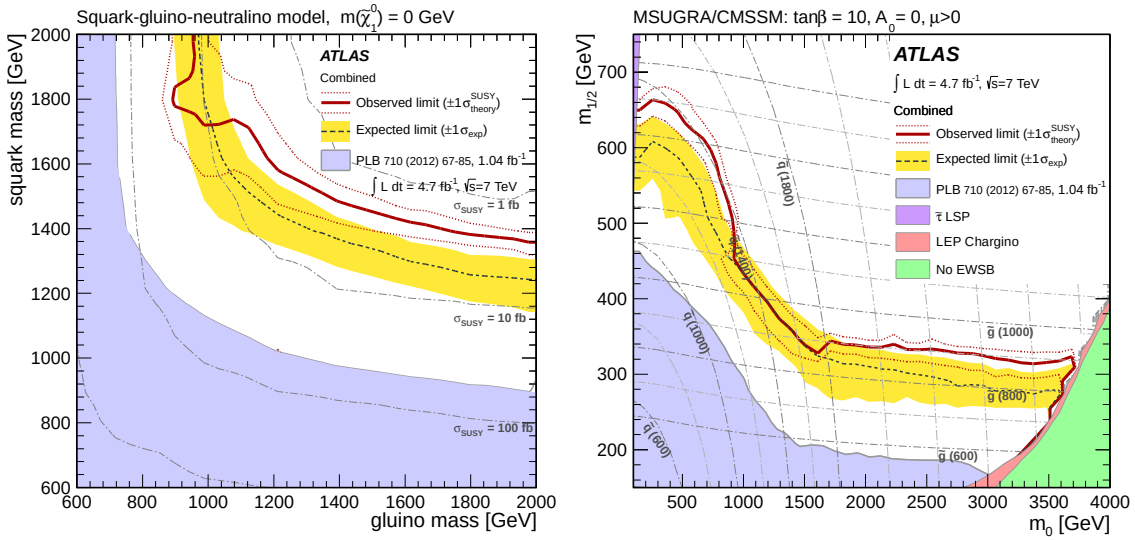

(a) (b)

Figure 4.2: *The 95% CL exclusion limits on (a) the (m_{gluino}, m_{squark}) plane in a simplified MSSM scenario with only strong production of gluinos, first and second generation squarks, with direct decays to jets and massless neutralinos; (b) the (m_0, $m_{1/2}$) plane of MSUGRA/CMSSM for* $\tan\beta = 10$, $A_0 = 0$ *and* $\mu > 0$ *obtained with the full dataset collected at* $\sqrt{s} = 7$ *TeV* [92].

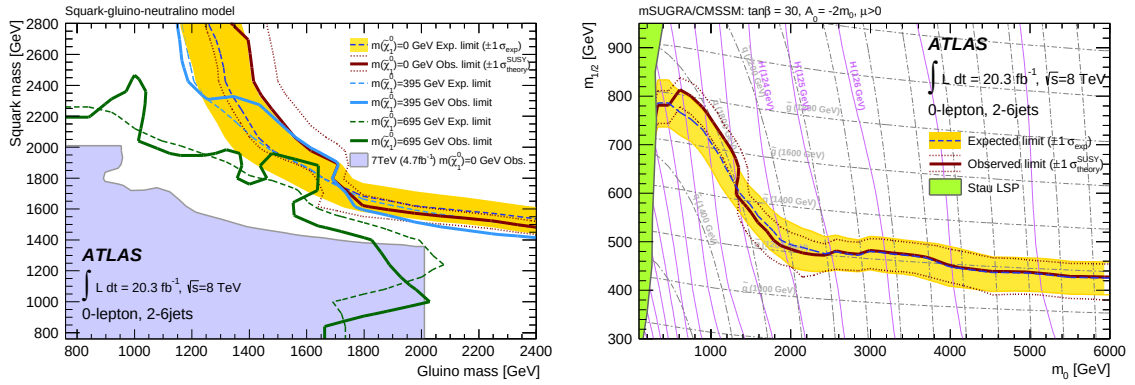

(a) (b)

Figure 4.3: *The 95% CL exclusion limits on (a) the (m_{gluino}, m_{squark}) plane in a simplified MSSM scenario with only strong production of gluinos, first and second generation squarks, with direct decays to jets and neutralinos with different masses; (b) the (m_0, $m_{1/2}$) plane of MSUGRA/CMSSM for* $\tan\beta = 30$, $A_0 = 2m_0$ *and* $\mu > 0$ *obtained with the full dataset collected at* $\sqrt{s} = 8$ *TeV* [93].

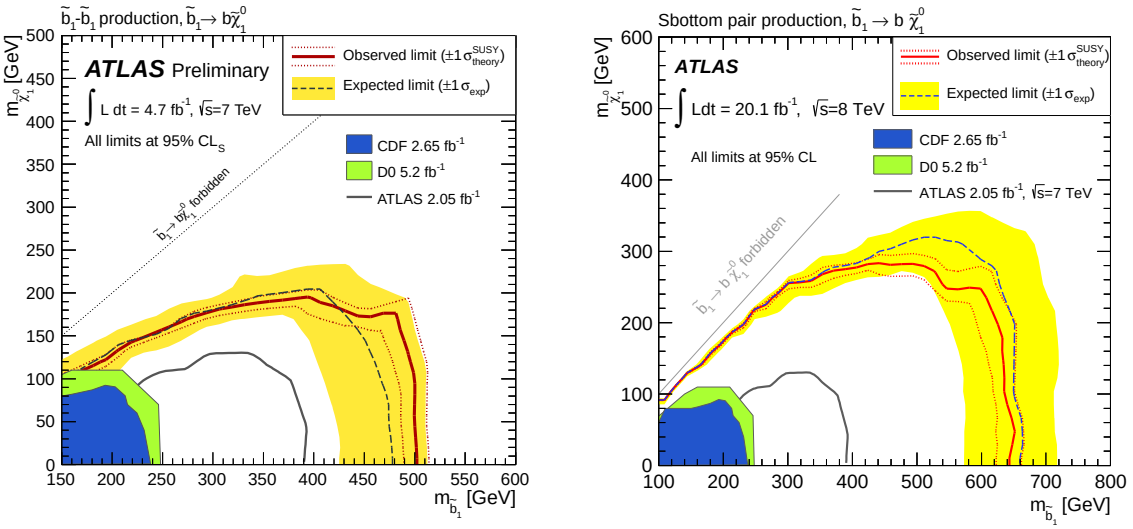

(a) (b)

Figure 4.4: *The 95% CL exclusion limits on the ($m_{\tilde{b}_1}$, $m_{\tilde{\chi}_1^0}$) plane in a simplified MSSM scenario with only the strong production of sbottom pairs, with direct decays to a b-quark and a neutralino. The results are obtained with the full dataset collected at $\sqrt{s} = 7$ TeV (a)* [95] *and $\sqrt{s} = 8$ TeV (b)* [96].

At the time of starting the work of this thesis, the exclusion limits set by the SUSY group of the ATLAS experiment on the masses of gluinos and first two generations of squarks were already approaching and in some cases exceeding the TeV energy scale, starting to create some tension to the traditionally explored SUSY scenarios (see for example the results documented in Ref. [94]). The hypothesis of third generation squarks lying in the sub-TeV range was left relatively unaffected by these results and theoretically promising in the context of naturalness, as explained in Section 1.8. The results obtained by the ATLAS experiment on searches for direct sbottom pair production with the full datasets collected at $\sqrt{s} = 7$ and 8 TeV are shown in Figure 4.4. The results on direct stop pair production searches are the main topic of this thesis and are presented in Chapters 5 and 6.

Electro-weak produced SUSY particles require dedicated searches. In view of their small production cross section, an efficient suppression of the SM backgrounds must be performed, usually requiring the presence of leptons in the final state. The diagrams illustrating the decays of some of the processes addressed are shown in Figure 4.5, while Figure 4.6 shows the status of most of the searches. The complete set of public results can be found in Ref. [91].

In R-parity violating (RPV) scenarios the LSP can decay into SM particles, therefore the presence of $E_{\mathrm{T}}^{\mathrm{miss}}$ in the final state cannot be used as feature to discriminate between

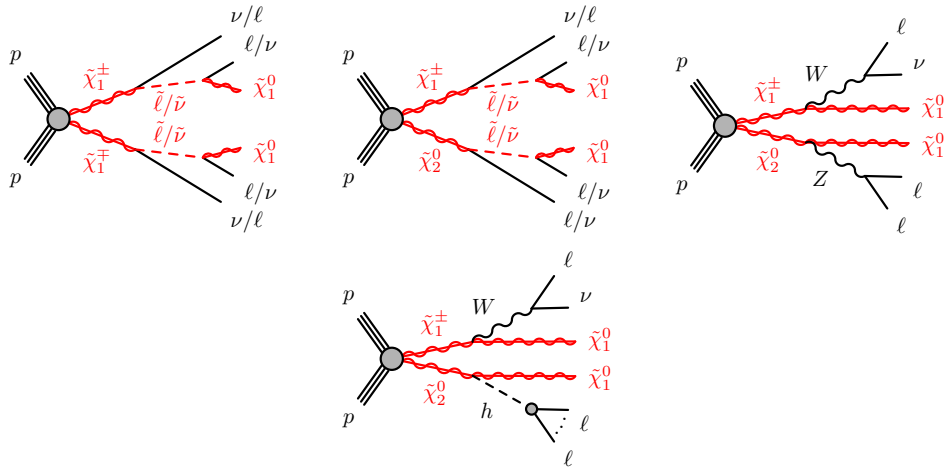

Figure 4.5: *Diagrams illustrating the decays of some of the processes considered by the analyses targeting electro-weak SUSY production.*

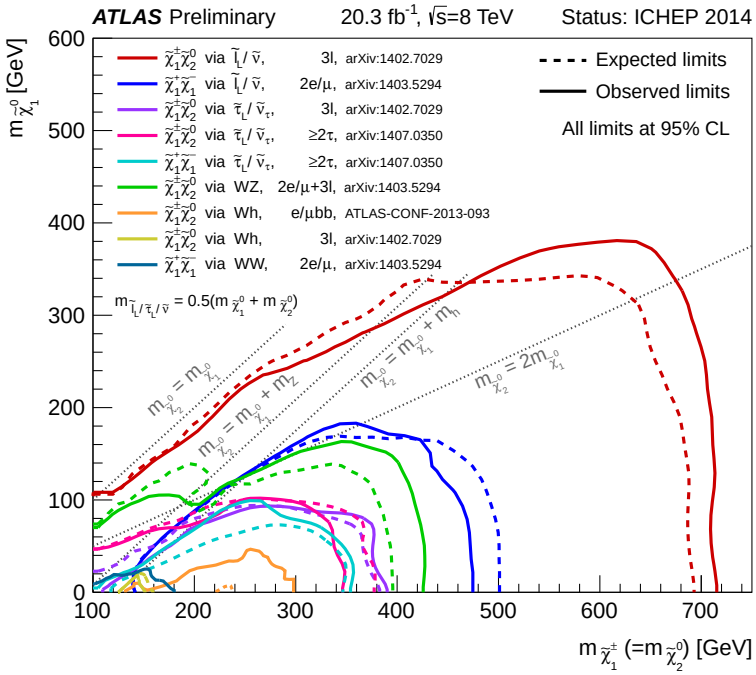

Figure 4.6: *Summary of the ATLAS experiment searches for electro-weak production of charginos and neutralinos based on 20 fb^{-1} of proton-proton collision data at $\sqrt{s} = 8$ TeV. Exclusion limits at 95% CL are shown in the $(m_{\tilde{\chi}_1^{\pm}}, m_{\tilde{\chi}_1^0})$ plane. Different decay modes of the charginos and neutralinos are considered separately with 100% branching ratio, as documented in the references given in the figure.* [91]

signal and background. The lifetime of the SUSY particles in RPV models can be significantly high. In this case, the presence of displaced vertices or disappearing tracks can be exploited to distinguish the expected signal from the SM background. Also in some R-parity conserving SUSY models the superpartners can be long-lived. The features of this kind of signals are more similar to those of RPV scenarios than to those of the most common R-parity conserving models. For this reason, the efforts of searching for RPV or long-lived R-parity conserving SUSY signals are joined. The available results of the searches for RPV and long-lived SUSY signals can be found in Ref. [91].

4.2 Strategy for Supersymmetry Searches

The SUSY signals targeted by the ATLAS experiment are characterised by a particularly low cross section (in the range $10^{-2} - 10$ pb for strong production, see Figures 4.1(a) and 4.1(b)), if compared to the cross sections of the backgrounds from SM processes, shown in Figure 4.7 (for example, the production of top-antitop pairs has a cross section of the order of 100 pb).

The first step in extracting a potential SUSY signal from the SM background is to study the model of interest to understand what are the discriminating variables allowing to distinguish them, and which decay channel serves the scope best. This is done by making use of MC simulations of both signal and background.

Once the decay channel for the signal of interest has been identified and a set of discriminating variables found, the precise values of the cuts for each of the variables must be found. This optimisation procedure is usually performed exploiting different figures of merit, as the ratio of signal over background, S/B, or an approximated formula for the expected discovery significance, $S/\sqrt{B + (\Delta B)^2}$, obtained assuming that signal and backgrounds are distributed according to a Poissonian function [105], and that the estimated value for the background is affected by a systematic uncertainty ΔB. At this stage no use of the data collected by the ATLAS detector is made. This is done to avoid that the data influence the choice of the selections. The kinematic region defined with this procedure is called *Signal Region* (SR).

Usually not a single signal sample but rather a *grid* of samples is considered, obtained performing a scan of the parameter space of the model of interest. In the case of simplified models, for example, a grid is obtained performing a scan in the masses of the SUSY particles involved in the decay chain. An analysis can target more grids with a similar topology. To obtain the best performance, a set of SRs is defined, where each SR targets a group of signals with similar kinematic properties.

The next step is the estimation of the background from SM processes in the different SRs. The backgrounds can be classified in two classes: *reducible* and *irreducible* ones.

Reducible backgrounds are backgrounds characterised by large production cross sections not having the same topology as the signal, but entering a SR because of limitations in the reconstruction of the final state objects. For example, generic multijet QCD events can have a significant amount of fake $E_{\mathrm{T}}^{\mathrm{miss}}$ and therefore pass a selection using this quantity as discriminating variable. The estimation of this kind of backgrounds cannot be performed exploiting MC simulations as these effects cannot be reproduced with enough precision. For this reason, reducible backgrounds are usually estimated directly from data, with techniques called *data-driven*.

On contrast, irreducible backgrounds are those entering the SR because they have the same topology as the signal. Considering again a selection based on $E_{\mathrm{T}}^{\mathrm{miss}}$, SM processes decaying into neutrinos enter the SR if their transverse momentum is high enough. This kind of background sources are usually estimated making a combined use of data and MC simulations, with a technique called *semi data-driven*. Exploiting the same variables defining the SR, a region with similar kinematic properties is defined, called *Control Region* (CR). The CR is used to derive a normalisation factor for the background, and is usually obtained by reverting one or more cuts defining the SR, those more effective in rejecting the source of background under examination. The principle behind this method is that the shape of the variables used as discriminating is well reproduced by the MC simulation, but its normalisation must be extracted from data. Thus, the expected number of background events in the SR for a given process $N_{\mathrm{SR}}^{\mathrm{bg}}$ is:

$$N_{\mathrm{SR}}^{\mathrm{bg}} = N_{\mathrm{SR}}^{\mathrm{bg,MC}} \frac{\left(N_{\mathrm{CR}}^{\mathrm{data}} - N_{\mathrm{CR}}^{\mathrm{others}}\right)}{N_{\mathrm{CR}}^{\mathrm{bg,MC}}} \tag{4.1}$$

where $N_{\mathrm{SR}}^{\mathrm{bg,MC}}$ is the MC prediction of the number of background events in the SR and the second term is the *normalisation factor* $\mu^{\mathrm{bg,MC}}$, obtained by subtracting from the number of data in the CR ($N_{\mathrm{CR}}^{\mathrm{data}}$) the contamination from background processes different from the one of interest ($N_{\mathrm{CR}}^{\mathrm{others}}$, usually taken from MC), and dividing it for the MC expectation of the background in the CR ($N_{\mathrm{CR}}^{\mathrm{bg,MC}}$).

In this equation it is assumed that any contamination from signal in the CR is negligible. When defining a CR, particular attention must be paid to keep the contribution from other backgrounds as low as possible.

Since SRs are often characterised by low numbers of events and therefore large statistical uncertainties, it can be difficult to test if the kinematic properties of a CR are close enough to those of a SR, so that the normalisation factor extracted in CR can be applied to the yield of events $N_{\mathrm{SR}}^{\mathrm{bg,MC}}$. For this purpose another region can be defined, called *validation region* (VR). VRs are typically placed in between CRs and SRs, with the idea of maximising the event yield while minimising the signal contamination. A schematic illustration of the analysis strategy involving CRs, VRs and SRs given two discriminating

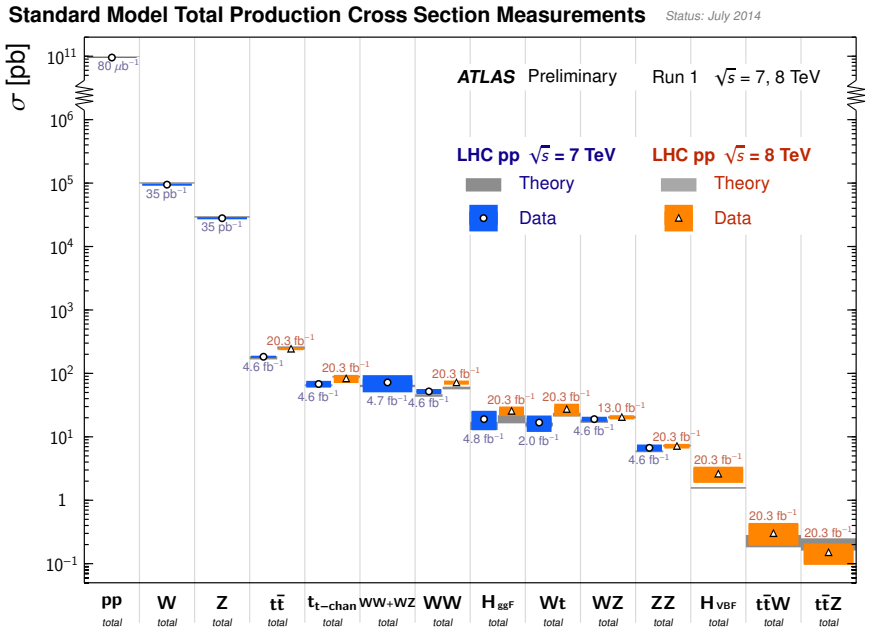

Figure 4.7: *Summary of several SM production cross section measurements, compared to the corresponding theoretical expectations. All theoretical expectations are calculated at NLO or higher order. The W and Z bosons inclusive cross sections were measured with 35 pb^{-1} of integrated luminosity from the 2010 dataset. All other measurements were performed using the 2011 dataset or the 2012 dataset. The luminosity used for each measurement is indicated close to the data point* [97].

variables is shown in Figure 4.8.

Equation 4.1 can be rearranged as:

$$N_{\mathrm{SR}}^{\mathrm{bg}} = (N_{\mathrm{CR}}^{\mathrm{data}} - N_{\mathrm{CR}}^{\mathrm{others}}) \frac{N_{\mathrm{SR}}^{\mathrm{bg,MC}}}{N_{\mathrm{CR}}^{\mathrm{bg,MC}}} = (N_{\mathrm{CR}}^{\mathrm{data}} - N_{\mathrm{CR}}^{\mathrm{others}}) TF_{\mathrm{CR}\to\mathrm{SR}}^{\mathrm{MC}} \tag{4.2}$$

to emphasise the role of the *transfer factor* from the CR to the SR. As already mentioned, good CRs are characterised by similar kinematic conditions as the SR. If this is the case, most of the systematic uncertainties related to the use of MC simulations (see next section) cancel in the ratio $N_{\mathrm{SR}}^{\mathrm{bg,MC}}/N_{\mathrm{CR}}^{\mathrm{bg,MC}}$.

The contribution in the SR from small backgrounds is often taken straight from their MC simulation. In this case, a conservative uncertainty is assigned to the prediction.

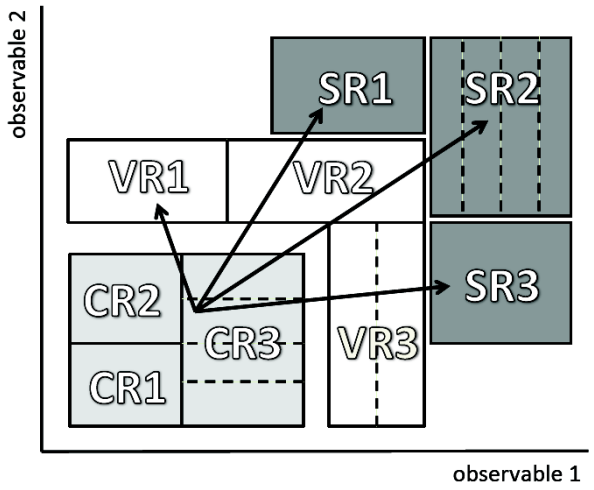

Figure 4.8: *A schematic view of an analysis strategy with CRs, VRs and SRs. The extrapolation from the CRs to the SRs is verified in the VRs* [106].

4.3 Uncertainties

The prediction of all background components and of the expected signal are subject to systematic uncertainties, that can be categorised into two classes: experimental and theoretical uncertainties. These systematic uncertainties impact the event yields in the CRs and the SRs, and therefore also the transfer factors when semi data-driven background estimation techniques are used.

In addition to systematic uncertainties, there are also statistical uncertainties. The finite amount of data collected is a source of statistical uncertainties, as well as the number of events generated in the MC simulation.

4.3.1 Experimental Uncertainties

The experimental uncertainties considered are:

- *Luminosity*
  The uncertainty on the integrated luminosity recorded with the systems described in Subsection 2.2.5 has been estimated to be ±3.9% for the full dataset collected at $\sqrt{s} = 7$ TeV [98] and ±2.8% for the full dataset collected at $\sqrt{s} = 8$ TeV [99].

- *Jet Energy Scale and Resolution (JES and JER)*
  The uncertainty connected to the JES (see Section 3.3) is estimated by shifting the nominal p_T of each jet up and down by a value corresponding to one standard deviation, that depends on the p_T and η of the jet. The uncertainty on the JER is

estimated by smearing the p_{T} of each jet according to a Gaussian distribution with mean value 1 and a p_{T} and η dependent resolution. The software packages used are those recommended in Refs. [100] and [101] for the $\sqrt{s} = 7$ and $\sqrt{s} = 8$ TeV datasets, respectively. The event yields obtained with the nominal p_{T} are compared with the up and down JES variations and with the yields after jet smearing.

- *B-Tagging Uncertainty*
  The uncertainty due to b-tagging is evaluated by varying the b-tagging efficiency and mistag rates of the algorithms described in Section 3.4 within the one sigma up and down uncertainties of the measured values [80].

- *Lepton Identification and Reconstruction Efficiency*
  The identification and reconstruction of electrons and muons has been discussed in Sections 3.5 and 3.6, respectively. The impact on the event yields of the small uncertainties associated with the different steps have been estimated according to the methods described in Refs. [83], [84] and [86].

- *Pile-up*
  The events of the MC simulations have been reweighted to take into account the different pile-up conditions during data taking (see Subsection 2.1.2). An uncertainty has been associated to this procedure, obtained comparing the nominal event yields with the yields obtained assuming that the average number of interactions per bunch crossing μ is off by $\pm 10\%$.

- E_T^{miss} *CellOut and SoftJets*
  The uncertainties on all the terms appearing in Equation 3.5 are taken into account by propagating the uncertainty on the corresponding object to $E_{\mathrm{T}}^{\mathrm{miss}}$ through the `METUtility` tool, with the exception of the CellOut and SoftJets terms. The uncertainty connected with these terms is evaluated separately by varying the calibration scale and resolution of the clustrs, as described in Ref. [102].

4.3.2 Theoretical Uncertainties on SM Background Processes

The simulation of each step leading from proton-proton collisions to final state objects (see Section 2.3) is subject to systematic uncertainties, that are taken into account when performing physics analyses:

- *Parton Distribution Functions*
  The uncertainty connected to the choice of the PDFs is estimated by using different sets.

- *Factorisation and Renormalisation Scales*
  The impact of the choices of the factorisation and renormalisation scales is estimated by considering simulations in which the scales are set to a half and two times their default values.

- *Parton Shower*
  The uncertainty connected to the modelling of the parton showers is estimated by considering different MC generators.

- *Initial and Final State Radiation*
  The amount of ISR and FSR produced is subject to an uncertainty. Its impact is estimated with dedicated samples where ISR and FSR are increased or decreased separately.

- *Matching Scale*
  Some generators, as Alpgen or MadGraph, are interfaced with Pythia or Jimmy for the simulation of the parton shower. The matching between them is done at a given energy scale. To estimate the related uncertainty, the nominal scale is varied and the impact of the change is evaluated.

4.3.3 Theoretical Uncertainties on Signal

The uncertainties on the signal cross sections take into account the PDF uncertainties, the choice of the factorisation and renormalisation scales (see Subsection 4.3.2), and variations of the strong coupling constant, following the PDF4LHC recommendations documented in Ref. [103].

4.4 Interpretation of the Results

Once the definition of the SRs is complete, the SM background modelling is under control and all the sources of uncertainties are taken into account, the results of a physics analysis are derived quantifying the level of agreement of the actual number of events observed in data in the different SRs with different hypotheses [104] [105] [106]. When trying to discover signals of new physics, the level of compatibility of the observed data with the background only hypothesis is tested. To derive exclusion limits on a specific model, the signal plus background hypothesis is tested.

The level of agreement of the observed data with a given hypothesis H is quantified by the p-value, the probability of finding data of equal or greater incompatibility with the predictions of H. If the observed probability is below a certain threshold, H is discarded. The p-value is usually converted in equivalent significance Z: the distance of the observed

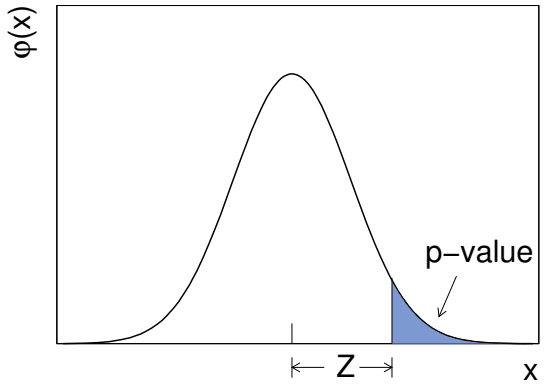

Figure 4.9: *The standard Gaussian distribution* $\varphi(x) = (1/\sqrt{2\pi})\exp(-x^2/2)$*, showing the relation between the significance* Z *and the* p*-value* [105].

value in terms of standard deviations from the mean value of a Gaussian distributed variable such that the upper-tail probability gives p. A schematic representation of the relation between Z and the p-value is shown in Figure 4.9.

The particle physics community has agreed to use a Z-value of 5, corresponding to $p = 2.87 \times 10^{-7}$, to reject the background only hypothesis and thus claim a discovery, and a Z-value of 1.64, corresponding to $p = 0.05$, to reject the signal plus background hypothesis and thus excluding a specific signal model (95 % confidence level, CL, exclusion).

The test statistic used in this thesis (and in most of the particle physics experiments) to determine the significance is the *profile likelihood ratio*. A likelihood function is built as the product of Poisson probabilities for the SR and for each of the CRs, and of the probability distribution functions (pdfs) implementing the constrains on the systematic uncertainties:

$$\begin{gathered} L(\boldsymbol{n}, \boldsymbol{\theta}^0 | \mu, \boldsymbol{b}, \boldsymbol{\theta}) = P_{\mathrm{SR}} \times P_{\mathrm{CR}} \times C_{\mathrm{syst}} = \\ P(n_s | \lambda_s(\mu, \boldsymbol{b}, \boldsymbol{\theta})) \times \prod_{i \in \mathrm{CR}} P(n_i | \lambda_i(\mu, \boldsymbol{b}, \boldsymbol{\theta})) \times C_{\mathrm{syst}}(\boldsymbol{\theta}^0, \boldsymbol{\theta}) \end{gathered} \tag{4.3}$$

where n_s and n_i are the number of observed events in the SR and the CRs, λ_s and λ_i are the Poisson expectations (depending on the predictions for the different background components $\boldsymbol{b}$, the nuisance parameters of the systematic uncertainties $\boldsymbol{\theta}$ and the signal strength μ), and $C_{syst}(\boldsymbol{\theta}^0, \boldsymbol{\theta})$ is a product of Gaussian probabilities having as mean values $\boldsymbol{\theta}^0$, the nominal values of the systematic uncertainties.

The test statistic is given by the ratio:

$$t_\mu = -2 \log \frac{L(\mu, \hat{\hat{\boldsymbol{\theta}}})}{L(\hat{\mu}, \hat{\boldsymbol{\theta}})} \tag{4.4}$$

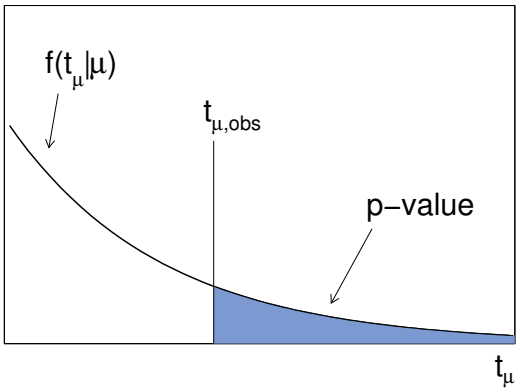

Figure 4.10: *Illustration of the relation between the p-value obtained from an observed value of the test statistic* t_μ [105].

where $\hat{\mu}$ and $\hat{\boldsymbol{\theta}}$ are the values maximising the likelihood, while $\hat{\hat{\boldsymbol{\theta}}}$ maximises the likelihood under the assumption of a specific signal strength μ, taken to be 0 when testing the background only hypothesis and 1 when testing the signal plus background hypothesis. Higher values of t_μ correspond to increasing incompatibility between data and μ.

The p-value is built starting from this test statistic as:

$$p = \int_{t_{\mu,obs}}^{\infty} f(t_\mu|\mu)dt_\mu \tag{4.5}$$

where $t_{\mu,obs}$ is the value as obtained from 4.4 using the data and $f(t_\mu|\mu)$ is the pdf for t_μ under the assumption of μ, built generating pseudo experiments. An illustration of the relation between the p-value and the test statistic t_μ is given in Figure 4.10.

The procedure adopted in this thesis to interpret the results of the analyses follows the default procedure adopted within the SUSY group. The fit procedure is repeated in three different configurations for different purposes, as described in the following. The theory systematic uncertainties described in Subsection 4.3.2 are considered correlated among control regions and signal region, but the different background components are treated as uncorrelated. The experimental systematic uncertainties described in Subsection 4.3.1 are treated as correlated among regions and components. The uncertainty connected to the limited number of events of the Monte Carlo samples used in the background estimation process is treated as completely uncorrelated among regions and components.

Background-only fit

The fit is performed only in the CRs, assuming zero contamination from the signal, with the purpose of estimating the total background in the SRs and the VRs. This allows for an unbiased comparison between the predicted number of events in each region and those

observed in data.

Model-dependent signal fit

In case the background-only fit does not reveal a significant excess of data over the expectation, exclusion limits can be set on the signal models targeted by the analysis. The CRs and a SR are fitted simultaneously, taking into account not only the background components but also the presence of the signal in the different regions. A model is considered excluded at 95% CL if the CL_s is below 0.05:

$$CL_s = \frac{CL_{s+b}}{CL_b} = \frac{p_{s+b}}{1 - p_b} \tag{4.6}$$

where p_{s+b} is the p-value for the signal plus background hypothesis (i.e. μ_{sig}=1) and p_b is the p-value for the background only hypothesis (i.e. μ_{sig}=0)

As explained in Section 4.2 more than one SR can be defined, targeting different choices of the parameters for the signal model of interest. In this case, for the presentation of the results in the plane defined by the parameters, the SR providing the lowest CL_s is chosen and the different points of the grid interpolated. To enhance the sensitivity, orthogonal SRs can be combined.

The curve corresponding to the expected exclusion limit is obtained by replacing the observed number of events from data with the expectation given from the background-only fit. The uncertainty band takes into account all the uncertainties related to the background presented in Subsections 4.3.2 and 4.3.1. The uncertainty band for the observed exclusion limit, obtained making use of the real data, takes into account the theory uncertainties on the signal described in Subsection 4.3.2.

Model-independent Signal fit

The results of a SUSY analysis are also presented in terms of 95% CL upper limits on events from generic non-SM processes. This procedure is particularly useful to recast the results of the search in other scenarios.

The CRs and a SR are fitted simultaneously, neglecting the signal contamination is the CRs (because it is model dependent), and adding the number of signal events as parameter of the fit. The 95% CL upper limits on the number of events can be translated in upper limits on the visible cross section, the production cross section times acceptance and efficiency of the analysis. As in the case of the model-dependent results, the expected numbers are computed by replacing the actual data yield observed with the expectation given by the background-only fit.

Discovery fit

In case the data reveal an excess of events over the SM expectation given by the background-only fit, the significance of the excess is quantified following a procedure very similar to the model-independent signal fit. The main difference is that the hypothesis tested is not the signal plus background one, but the background only, therefore the signal strength μ is set to zero.

Chapter 5

Direct Stop Pair Production Searches at $\sqrt{s} = 7$ TeV

In this chapter one of the first searches for the lightest supersymmetric partner of the top quark is presented. The importance of this particle in the context of natural SUSY has been already pointed out in Section 1.8. This analysis targets direct stop pair production in a mass range close to the top quark mass, well suited to solve the Higgs boson hierarchy problem discussed in Section 1.5.

The results of the analysis presented in this chapter have been published in Ref. [107]. In the context of this thesis were performed the study of the kinematic properties of the signal addressed, the definition of the strategy to separate signal and background, and the optimisation of the signal regions to maximise their sensitivity. Important contributions were also given to the estimation of the main backgrounds to the search (di-leptonic decays of top-antitop pairs and Z bosons decaying into leptons), and to the estimation of the systematic uncertainties.

5.1 Addressed Signal

The addressed signal is direct production of stop-antistop pairs in the context of R-parity conserving MSSM. A diagram illustrating the decay of the process under study is shown in Figure 5.1. The mass hierarchy assumed for the SUSY particles is such that the stop is assumed to be lighter than or have a mass comparable to the top quark, and heavier than the sum of the masses of the chargino and of the b-quark: $m(\tilde{t}_1) \lesssim m(t)$, $m(\widetilde{\chi}_1^{\pm}) + m(b) < m(\tilde{t}_1)$. In this scenario, the favoured decay mode is $\tilde{t}_1 \to b\widetilde{\chi}_1^{\pm}$. The mass of the sleptons are assumed to be very large and the neutralino to be the LSP, so the chargino is expected to decay via real or virtual W boson: $\widetilde{\chi}_1^{\pm} \to W^{(*)}\widetilde{\chi}_1^0$. The subsequent decays of the W boson are the SM ones.

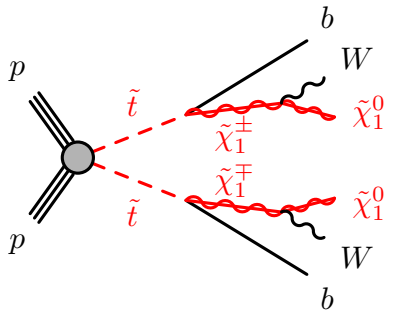

Figure 5.1: *Decay diagram of the signal targeted by this analysis.*

The final state signatures are similar to those of top-antitop pairs production. The decay mode where both W bosons decay into a lepton (electron or muon) and the corresponding neutrino is considered. The final state targeted contains two b-jets, two oppositely-charged electrons or muons and missing transverse energy. Leptonic decays of τ leptons can also pass the selection.

The analysis is sensitive to cases where the mass difference between the $\tilde{t}_1$ and the $\widetilde{\chi}_1^{\pm}$ is sufficient to produce b-jets that are energetic enough to be reconstructed. The addressed mass range for the $\tilde{t}_1$ mass produce leptons and jets that tend to be softer than leptons and jets produced in leptonic decays of $t\bar{t}$ pairs. This feature together with the presence of the $\widetilde{\chi}_1^0$ in the final state can be exploited to distinguish signal and background.

The cross section for stop pair production in the addressed mass range evaluated at NLO+NLL precision is shown in Figure 5.2, together with the associated systematic uncertainties that are discussed in detail in Subsection 5.4.2.

Three sets of simulated signal samples have been used to define and optimise the selections and interpret the results:

- *Varying* $m(\tilde{t}_1)$, $m(\widetilde{\chi}_1^{\pm}) = 2m(\widetilde{\chi}_1^0)$ *(Grid 1).*
  This simplified model is motivated by the assumption of gaugino universality, described in Subsection 1.7.2

- *Fixed* $m(\tilde{t}_1) = 180$ *GeV, varying* $m(\widetilde{\chi}_1^{\pm})$ *and* $m(\widetilde{\chi}_1^0)$ *(Grid 2).*
  In this simplified model the stop mass has been set to a value close to the top quark mass, optimal to solve the Higgs hierarchy problem, and a scan in the chargino and neutralino masses is performed.

- *Fixed* $m(\widetilde{\chi}_1^{\pm}) = 106$ *GeV, varying* $m(\tilde{t}_1)$ *and* $m(\widetilde{\chi}_1^0)$ *(Grid 3).*
  In this simplified model the chargino mass is set just above the exclusion limit for this particle set by the LEP experiments [108], and a scan in the stop and neutralino masses is performed.

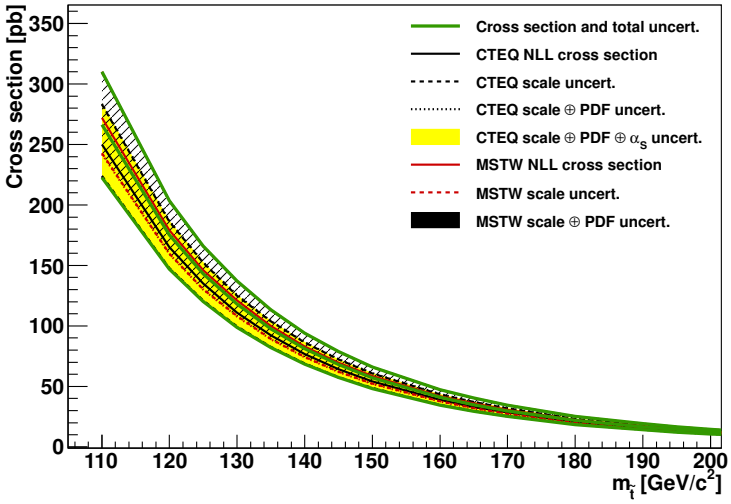

Figure 5.2: *Stop pair production cross section at NLO+NLL accuracy, as a function of the stop mass. The different styled black lines correspond to the cross section predicted using the CTEQ PDF set, and the yellow band to the quadratic sum of all of them. The different styled red lines correspond to the MSTW predictions, with the dashed black region being the quadratic sum of the scale and PDF uncertainties. The green solid lines correspond to the final cross section used and its uncertainty band.*

5.2 Data Samples and Event Selection

5.2.1 Dataset and Triggers

In this analysis all the data collected at a centre-of-mass energy of the proton-proton collisions of 7 TeV have been used, corresponding to the full dataset collected during 2011. The events are required to pass minimum requirements on the quality of the data collected by the detector. After this selection is applied, the data correspond to a total integrated luminosity of 4.7 fb^{-1}.

The trigger used is the lowest p_{T} threshold single electron or muon trigger. Different triggers are adopted depending on the data-taking periods (labelled in alphabetic order from B to M), to cope with the different rate of events due to the increasing instantaneous luminosity. The triggers used in each data-taking period are shown in Table 5.1.

Period	**Electron trigger**	**Muon trigger**
B to I	e20_medium	mu18
J	e20_medium	mu18_medium
K	e22_medium	mu18_medium
L, M	e22vh_medium1 || e45_medium1	mu18_medium

Table 5.1: *Single lepton triggers adopted in the analysis during the different data-taking periods. The name of each trigger is composed of an abbreviation indicating the final state object activating it ("e" for electrons and "mu" for muons), plus its minimum p_{T} (in GeV). The abbreviation "vh" indicates that the trigger has been implemented with different p_{T} thresholds in different η regions, and that a requirement on the hadronic leakage is applied. The last part of the name indicates the identification criteria that the final state object must fulfil to activate the trigger.*

Events with two electrons are selected with the electron trigger and events with two muons are selected with the muon trigger. For events containing one electron and one muon, priority is given to the electron trigger, and the muon trigger is used only if the electron trigger has not been fired.

5.2.2 Preselection: Event Cleaning and Final State Objects

A set of requirements to clean the dataset from low quality events is applied. The same selections are made on the Monte Carlo simulated events to avoid discrepancies.

- The primary vertex of the event must have at least five associated tracks with minimum p_{T} 400 MeV. This selection rejects non collision background events.

- The event is rejected if it contains cosmic muon candidates, selected on the basis of their transverse and longitudinal impact parameters with respect to the primary vertex. This cut brings the background from cosmic rays to a negligible level.

- Events with jets classified as low quality are rejected, because these jets are very likely to be originated by non-collision background or hardware problems. Many parameters are analysed to define the good quality of a jet, as the fraction of energy deposited in the EM calorimeter and in the HEC, the fraction of energy deposited in the different layers of the calorimeter, the quality of the pulse shapes recorded with the calorimeter, the time relation between the bunch crossing and the recorded signal, the ratio between the momentum of the jet and the momentum of the associated tracks, and the calorimeter cells contributing with a negative energy.

- During the 2011 data-taking the signal from several front-end boards of the EM calorimeter was lost for about a month, with the result of not detecting the energy deposited in the second and third layers of the EM calorimeter in the region $0.0 < \eta < 1.4$ and $-0.74 < \phi < 1.64$. This malfunctioning could result in the underestimation of the energy of jets falling in the interested region. The problem affected an amount of data corresponding to 0.86 fb^{-1}, a significant fraction of the dataset collected at $\sqrt{s} = 7$ TeV. Rejecting all events with jets falling in the problematic region would significantly damage the signal acceptance of the analysis, therefore the events are rejected only if the jets falling in the hole significantly contribute to the magnitude of $E_{\text{T}}^{\text{miss}}$. To estimate the energy loss in the non-functioning cells, the information from the neighbouring active cells is exploited.

- Fake muons are most likely to arise from punch through of high p_{T} jets in the MS, or because of a wrong association between tracks in the ID and in the MS. To identify fake muons, a cut on the significance of the ratio between charge and momentum is applied: $\left(\frac{\sigma(\frac{q}{p})}{|\frac{q}{p}|}\right) < 0.2$. If an event contains a fake muon the computation of $E_{\text{T}}^{\text{miss}}$ cannot be trusted, therefore the event is rejected.

After the event quality criteria are applied, the events are required to contain the minimum number of final state objects from the addressed signal decay chain. The events must therefore have:

- A minimum of two jets with p_{T} larger than 20 GeV, out of which at least one must be tagged as a b-jet.

  The jets reconstruction procedure and b-tagging algorithm adopted have been already discussed in Sections 3.3 and 3.4, respectively.

  Since the jets coming from the signal are expected to be soft, the p_{T} threshold has to be as low as possible. To reject jets from pile-up, a cut of 0.75 on the ratio between

the sum of the p_{T} of all jet-matched tracks associated to a given vertex and the sum of the p_{T} of all jet-matched tracks associated to any vertex has been adopted. This choice limits the η range of the jets to the region matching the ID, $|\eta| < 2.5$. If an electron is energetic enough, it is also reconstructed as a jet because it produces a shower in the calorimeter. To avoid double counting the same physical object, a jet is discarded if its distance ΔR from a reconstructed electron is smaller than 0.2.

- Exactly two oppositely charged signal electrons, or muons, or one electron and one muon.

  Baseline electrons, which are for example used to compute the distance from a jet, must satisfy the Medium identification criteria and lie in the region $\eta < 2.47$ (see Section 3.5). The minimum p_{T} threshold is 20 GeV. If a baseline electron has a distance from a jet $\Delta R < 0.4$ the electron is discarded, as it is very likely to be a decay product of a hadron inside a jet. For signal electrons the selections are strengthened. Signal electrons are required to satisfy the Tight identification criteria and to be isolated from other objects, by requiring that the sum of the p_{T} of all the tracks in a cone with size R=0.2 around the electron is less than 10% of the electron p_{T}.

  Combined or segment tagged muons are selected (see Section 3.6). Baseline muons must have $p_{\mathrm{T}} > 10$ GeV, $|\eta| < 2.4$ and satisfy some minimum requirements on the number of hits left in the different parts of the ID, to ensure a good quality of their tracks. As electrons, baseline muons are discarded if their distance ΔR from any jet is smaller than 0.4. Signal muons are required to be isolated from other objects. This is implemented requiring that the sum of the p_{T} of all the tracks in a cone R=0.2 is less than 1.8 GeV.

  When selecting the lepton pair, the minimum p_{T} of the leading lepton is raised to ensure a high efficiency for at least one of the single lepton triggers. For events with two electrons, the leading electron must have p_{T} larger than 25 GeV. For events with two muons, the p_{T} threshold for the leading muon is 20 GeV. For events with one electron and one muon, the thresholds depend on the trigger that fires. If the electron trigger is used, the p_{T} of the electron must be larger than 25 GeV, while if the muon trigger is used, the muon p_{T} must be larger than 20 GeV.

- A minimum amount of $E_{\mathrm{T}}^{\mathrm{miss}}$ of 40 GeV, according to the computation discussed in Section 3.7.

To account for the different electron and muon reconstruction efficiencies in data and MC, weights are applied to the simulated baseline electrons and muons. Weights are also applied for the same reason to b-jets. The distribution of the vertices in MC is re-weighted

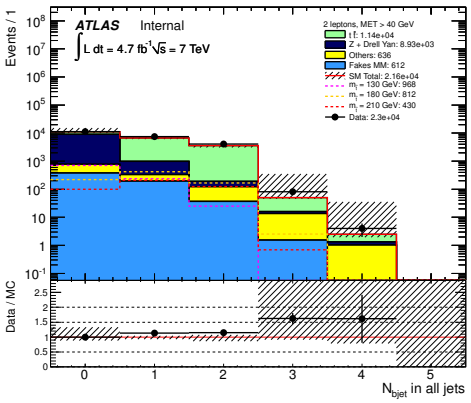

Figure 5.3: *Distribution of the number of b-tagged jets for the events passing the event quality, lepton and jet requirements. The stacked histograms show the Standard Model expectation from simulation compared to the data (points). Simulated signal samples where* $m(\tilde{t}_1) = 130$ *GeV (pink dashed line),* $m(\tilde{t}_1) = 180$ *GeV (yellow dashed line), and* $m(\tilde{t}_1) = 210$ *GeV (red dashed line) are overlaid. The legend reports the count of data and the yields of simulated events for each process. The "Data/MC" plot shows the ratio of data events to the total Standard Model expectation. The hatched uncertainty bands display the total uncertainty on the background expectation .*

to match that of the data, taking into account the different pile-up conditions throughout the data-taking.

Figure 5.3 shows the distribution of the number of b-tagged jets after event quality requirements, lepton and jet selections are applied. From the figure it is evident that requiring two b-jets would significantly reduce the signal acceptance. Figures 5.4 and 5.5 show jet and lepton kinematic properties, respectively, after all the pre-selection requirements (b-tagging included). It can be seen that the data are about 15% higher than the MC prediction, therefore a careful evaluation of the background normalisation factors is needed.

5.2.3 The Subsystem Mass Scale Variable

From Figures 5.4 and 5.5 it can be seen that the dominant source of background is $t\bar{t}$ production, as expected. The kinematic properties of signal and background are similar, with the signal being characterised by softer jets and leptons.

The main discriminating variable used to distinguish between them is the subsystem mass scale variable $\sqrt{s}_{\mathrm{min}}^{(\mathrm{sub})}$ described in Ref. [113], a variation of the mass scale variable $\sqrt{s}_{\mathrm{min}}$ introduced in Ref. [114]. The second variable is the minimum centre-of-mass energy of the partons involved in the hard interaction compatible with the measured values of

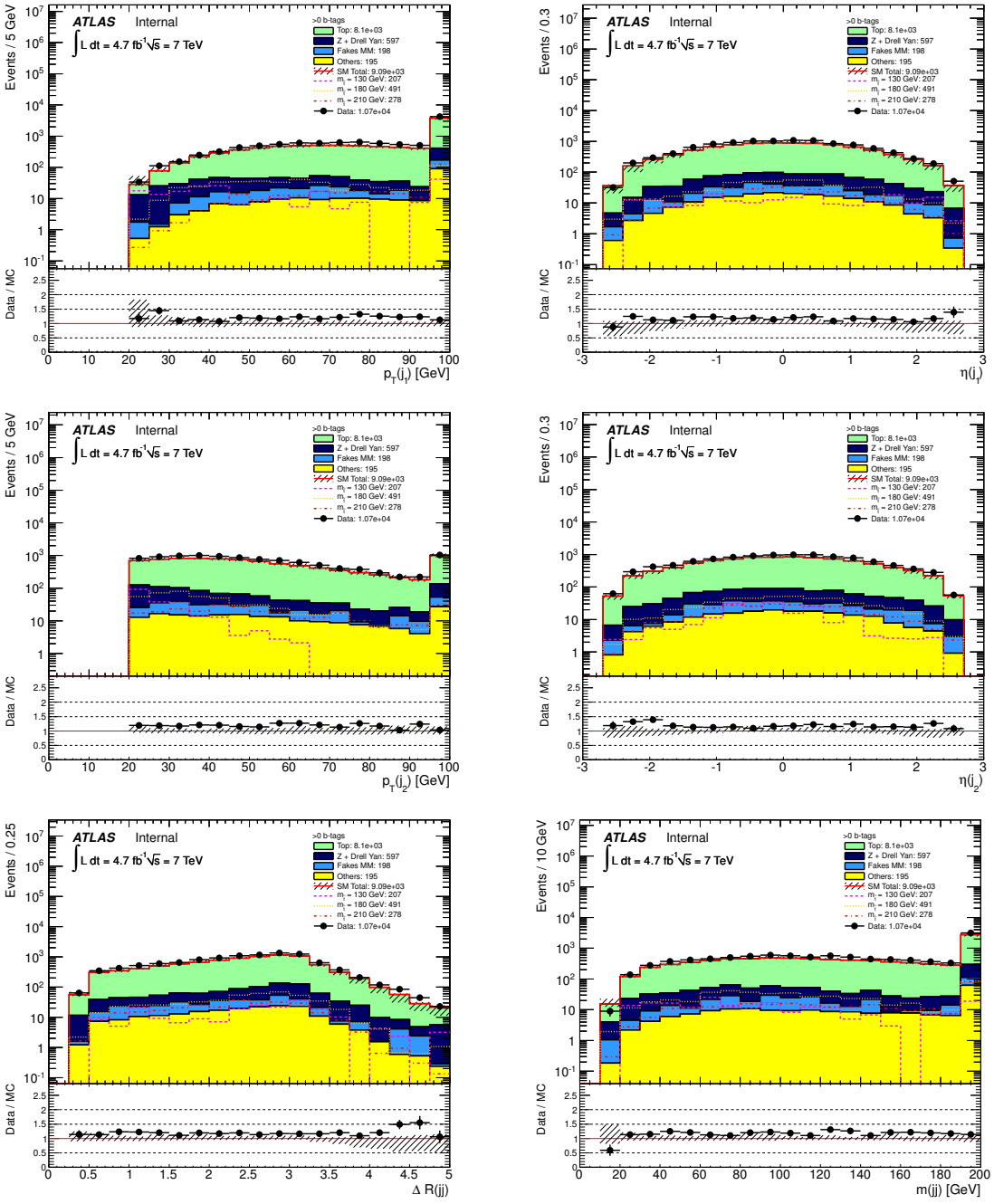

Figure 5.4: *Kinematic distributions of jets after the preselection. From top left to bottom right: leading jet p_{T} and η, subleading jet p_{T} and η, ΔR between the two leading jets, invariant mass of the two leading jets. The stacked histograms show the Standard Model expectation from simulation compared to the data (points). Simulated signal samples where $m(\tilde{t}_1) = 130$ GeV (pink dashed line), $m(\tilde{t}_1) = 180$ GeV (yellow dashed line), and $m(\tilde{t}_1) = 210$ GeV (red dashed line) are overlaid. The legend reports the count of data and the yields of simulated events for each process. The "Data/MC" plots show the ratio of data events to the total Standard Model expectation. The hatched uncertainty bands display the total uncertainty on the background expectation.*

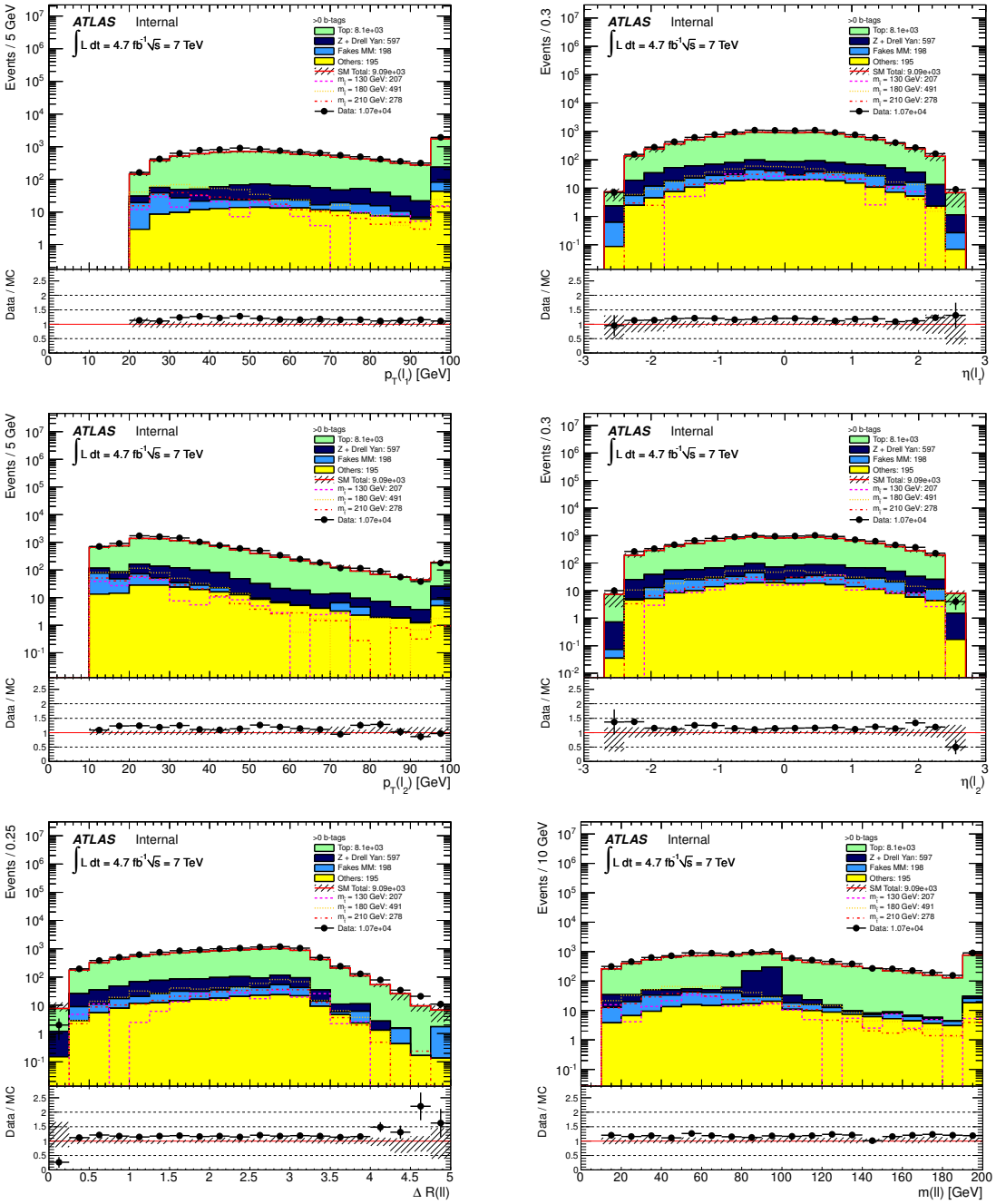

Figure 5.5: *Kinematic distributions of leptons after the preselection. From top left to bottom right: leading lepton p_{T} and η, subleading lepton p_{T} and η, ΔR between the two selected leptons, invariant mass of the two selected leptons. The stacked histograms show the Standard Model expectation from simulation compared to the data (points). Simulated signal samples where $m(\tilde{t}_1) = 130$ GeV (pink dashed line), $m(\tilde{t}_1) = 180$ GeV (yellow dashed line), and $m(\tilde{t}_1) = 210$ GeV (red dashed line) are overlaid. The legend reports the count of data and the yields of simulated events for each process. The "Data/MC" plots show the ratio of data events to the total Standard Model expectation. The hatched uncertainty bands display the total uncertainty on the background expectation.*

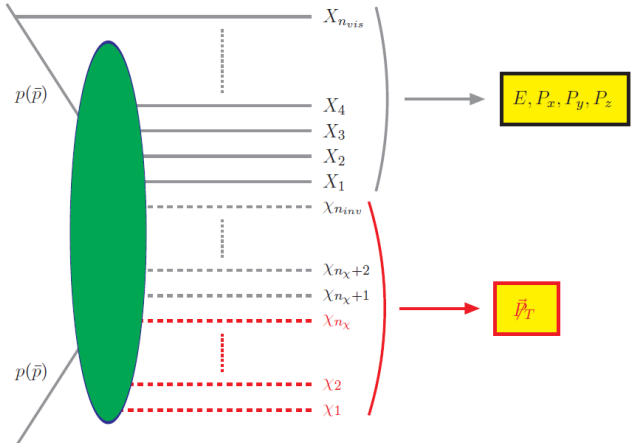

Figure 5.6: *Event topology used to define the $\sqrt{s}_{min}$ variable. The grey (red) lines correspond to SM (SUSY) particles. The solid lines denote SM particles X_i, $i = 1, 2, \ldots, n_{\text{vis}}$ visible in the detector. The SM particles may originate either from ISR, or from the hard scattering and subsequent cascade decays (indicated with the green ellipse). The dashed lines denote neutral stable particles χ_i, $i = 1, 2, \ldots, n_{inv}$ invisible in the detector. The invisible particles consists of n_χ SUSY particles (indicated with the red dashed lines), as well as $n_\nu = n_{inv} - n_\chi$ SM neutrinos (denoted with the black dashed lines). The global event variables describing the visible particles are: the total energy E, the transverse components P_x and P_y and the longitudinal component P_z of the total visible momentum $\vec{P}$. The only experimentally available information regarding the invisible particles is the missing transverse momentum, denoted here with the symbol $\vec{\not{P}}_T$. This figure is taken from Ref.* [114].

energy and momentum of the visible final state objects. Figure 5.6 represents a generic event where n_{vis} visible particles and n_{inv} invisible particles are produced. If E is the total energy of the visible particles, P_z the total longitudinal momentum, $\not{P}_T = E_{\text{T}}^{\text{miss}}$, and $\not{M}$ the sum of the masses of the invisible particles produced in the event, the analytical expression of the variable is:

$$\begin{aligned} \sqrt{s}_{\text{min}}(\not{M}^2) &= \sqrt{E^2 - P_z^2} + \sqrt{\not{M}^2 + \not{P}_T^2} \\ &= \sqrt{M^2 + P_T^2} + \sqrt{\not{M}^2 + \not{P}_T^2} \end{aligned} \tag{5.1}$$

This variable is invariant under longitudinal boosts and does not require any specific reconstruction of the system.

Figure 5.7 shows the distributions of $\sqrt{s}_{\text{min}}$ for a SUSY signal of gluino and $\widetilde{\chi}_1^0$ associated production, in case ISR or multiple partons interactions are absent, and when are present. It is possible to see that the shape of the distribution of the $\sqrt{s}_{\text{min}}$ variable

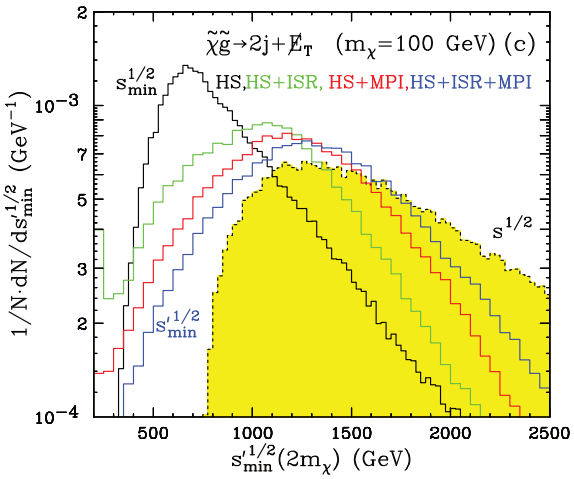

Figure 5.7: *Unit-normalised $\sqrt{s}_{min}$ distributions for a SUSY signal of gluino and $\widetilde{\chi}_1^0$ associated production, with $m_{\widetilde{\chi}_1^0} = 100$ GeV and the gluino decaying in two jets and a $\widetilde{\chi}_1^0$. The black histograms correspond to the idealised case where initial state radiation (ISR) or multiple partons interactions (MPI) are absent, while the green, red and blue histograms include the effect respectively of ISR, MPI, both ISR and MPI. In all these histograms the $\sqrt{s}_{min}$ variable has been evaluated setting $\not{M} = 2m(\widetilde{\chi}_1^0)$ in Equation 5.1. The yellow shaded histograms correspond to the true centre-of-mass energy of the partons involved in the hard interaction. This figure is taken from Ref.* [114].

strongly depends on the presence of final state objects not belonging to the system of interest (as in case of ISR or pile-up from multiple partons interactions), which can spoil the discriminating power of the variable. To recover it, a modified version of the mass scale variable, the subsystem mass scale variable $\sqrt{s}^{(\mathrm{sub})}_{\mathrm{min}}$, has been introduced [113].

As in Figure 5.8, some of the n_{vis} visible particles are supposed to be originating from a well defined subsystem, that is the subsystem of interest, and the others are generated upstream. The n_{inv} invisible particles all belong to the subsystem. If $M_{(sub)}$ and $P_{T(sub)}$ are the mass and transverse momentum of the visible particles of the subsystem, the minimum centre-of-mass energy of the partons compatible with the subsystem is:

$$\sqrt{s}^{(\mathrm{sub})}_{\mathrm{min}}(\not{M}^2) = \left(\sqrt{M^2_{(\mathrm{sub})} + P^2_{T(\mathrm{sub})}} + \sqrt{\not{M}^2 + \not{P}_T^2}\right)^2 - \left(\vec{P}_{T(\mathrm{sub})} + \vec{\not{P}}_T\right)^2 \qquad (5.2)$$

In this analysis, the $\sqrt{s}^{(\mathrm{sub})}_{\mathrm{min}}$ variable is built by identifying the subsystem with the $t\bar{t}$ or $\tilde{t}_1\bar{\tilde{t}}_1$ systems, respectively, for signal and background. $P_{T(\mathrm{sub})}$ and $M_{T(\mathrm{sub})}$ are thus computed with the information of the two selected leptons and the two jets of largest p_{T}. $\not{M}$ is set to zero, that is the case of the neutrinos originating from the $t\bar{t}$ system. The $\sqrt{s}^{(\mathrm{sub})}_{\mathrm{min}}$ variable is expected to peak at $\sim 2m(t)$ for the $t\bar{t}$ background, while for the signal the position of the peak depends on the $\tilde{t}_1$ mass.

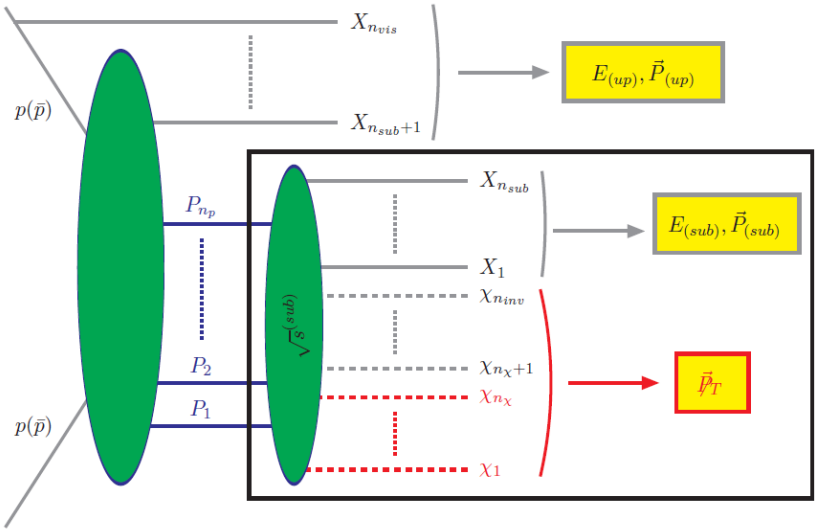

Figure 5.8: *Rearrangement of Figure 5.6 into an event topology with a well defined subsystem (delineated by the black rectangle) with total invariant mass* $\sqrt{s}^{(sub)}$. *There are* n_{sub} *visible particles* X_i, $i = 1, 2, \ldots, n_{sub}$, *originating from the subsystem, while the remaining* $n_{vis} - n_{sub}$ *visible particles* $X_{n_{sub}+1}, \ldots, X_{n_{vis}}$ *are created upstream. All invisible particles* $\chi_1, \ldots, \chi_{n_{inv}}$ *are then assumed to originate from within the subsystem. This figure is taken from Ref.* [113].

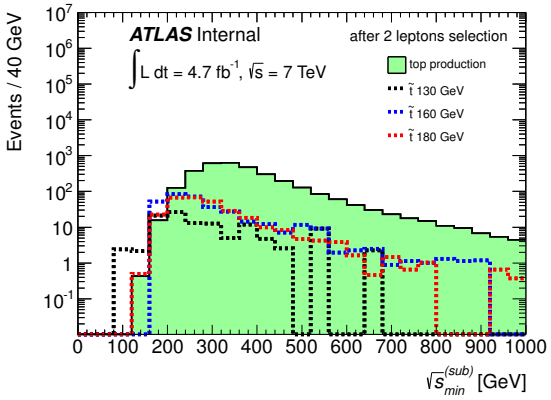

Figure 5.9: *Distribution of the $\sqrt{s}_{min}^{(sub)}$ variable for $t\bar{t}$ background and signal samples with different $\tilde{t}_1$ masses after preselection and the selection of two leptons.*

Figure 5.9 shows the distribution of the $\sqrt{s}_{\text{min}}^{(\text{sub})}$ variable for the $t\bar{t}$ background and three signal samples with different $\tilde{t}_1$ masses, showing how signal and background can be discriminated with an upper cut. The massive neutralinos manifest themselves as an excess in the lower tail of the $\sqrt{s}_{\text{min}}^{(\text{sub})}$ distribution, that gets lower values as the $\tilde{t}_1$ mass decreases.

5.2.4 Event Selection and Optimisation Procedure

After the preselection described in Subsection 5.2.2 is applied, the selection branches to define the CRs for the dominant backgrounds and the SRs. The $\sqrt{s}_{\text{min}}^{(\text{sub})}$ variable described in the previous subsection and the invariant mass of the two leptons $m(ll)$ shown in Figure 5.5 are jointly used for this purpose. A schematic illustration of the SRs and the CRs defined by using these variables is shown in Figure 5.10. Low values of $m(ll)$ and $\sqrt{s}_{\text{min}}^{(\text{sub})}$ are used to define the SRs. The Z boson CR is at low values of $\sqrt{s}_{\text{min}}^{(\text{sub})}$ and in the $m(ll)$ window around its mass, while the $t\bar{t}$ CR is characterised by high $m(ll)$ and $\sqrt{s}_{\text{min}}^{(\text{sub})}$ values. Further discriminating power is given by the invariant mass of the two selected leptons and the two leading jets, $m(lljj)$. Figure 5.11 shows the correlation between $m(lljj)$ and the $\sqrt{s}_{\text{min}}^{(\text{sub})}$ variables for the two main backgrounds and two signal examples with different $\tilde{t}_1$ masses. The variables are correlated, but in a different way for signal and background, therefore a combined use of the two can increase the sensitivity. This can be seen also from Figure 5.12, where the distribution of $m(lljj)$ for signal and background is shown after the preselection cuts, the cut on $m(ll)$ defining the SRs, and an upper cut on $\sqrt{s}_{\text{min}}^{(\text{sub})}$ are applied.

The first SR, SR1, has been defined exploiting only the $\sqrt{s}_{\text{min}}^{(\text{sub})}$ variable, while in the second SR, SR2, both $\sqrt{s}_{\text{min}}^{(\text{sub})}$ and $m(lljj)$ are used. The exact values of the upper cuts have been chosen by maximising the expected discovery significance to signals with stop

SR1	**SR2**
Data Quality, Trigger requirements	
exactly 2 OS leptons:	
e^+e^-: $p_{\mathrm{T}} > 25, 20$ GeV, $\lvert\eta\rvert < 2.47$;	
$\mu^+\mu^-$: $p_{\mathrm{T}} > 20, 10$ GeV, $\lvert\eta\rvert < 2.4$;	
$e^\pm\mu^\mp$: $p_{\mathrm{T}} > 25(e)$ or 20 (μ) GeV, $\lvert\eta\rvert < 2.4(\mu)/2.47(e)$;	
≥ 2 jets, $p_{\mathrm{T}} > 20$ GeV and $\lvert\eta\rvert < 2.5$	
$E_{\mathrm{T}}^{\mathrm{miss}} > 40$ GeV	
≥ 1 b-jets	
$\sqrt{s}_{\mathrm{min}}^{(\mathrm{sub})}$ <225 GeV	$\sqrt{s}_{\mathrm{min}}^{(\mathrm{sub})}$ <235 GeV $m(lljj)$ <140 GeV

Table 5.2: *Summary of the selection criteria to define the two signal regions SR1 and SR2.*

masses ranging from 130 GeV to 180 GeV:

$$s = \frac{sig}{\sqrt{\sigma^2_{bkg,\mathrm{stat}} + \sigma^2_{bkg,\mathrm{syst}}}} \sim \frac{sig}{\sqrt{bkg + \sigma^2_{bkg,\mathrm{syst}}}} \tag{5.3}$$

In this equation sig and bkg denote, respectively, the number of signal and background events as predicted by Monte Carlo simulation. $\sigma_{bkg,\mathrm{stat}}$ is the statistical error associated to the background expectation, approximated as $\sqrt{bkg}$ because the number of background events is sufficient to assume that the Poisson distribution behaves as a Gaussian. $\sigma_{bkg,\mathrm{syst}}$ is the systematic uncertainty on the background prediction. Values between 20% and 30% were considered, to check the impact on the expected results. A summary of the selections obtained can be found in Table 5.2.

Figures 5.13, 5.14 and 5.15 show the numbers of expected events, acceptance, acceptance times efficiency and expected significance obtained on Grid 1, Grid 2 and Grid 3 with the selections of SR1 and SR2. The background expectation in the two SRs as predicted by the Monte Carlo simulation is shown in Table 5.3.

Process	SR1	SR2
$t\bar{t}$	74.1	29.0
Single Top	6.1	3.1
Z+HF	17.8	6.5
W+HF	5.3	2.4
Others	0.9	0.5
Total MC	104.2	41.5

Table 5.3: *Monte Carlo based background estimation for SR1 and SR2. "HF" stands for heavy flavour jets. The "Others" component includes $t\bar{t}$+X (X=W, Z, γ, b, t) and VV (V=Z, W).*

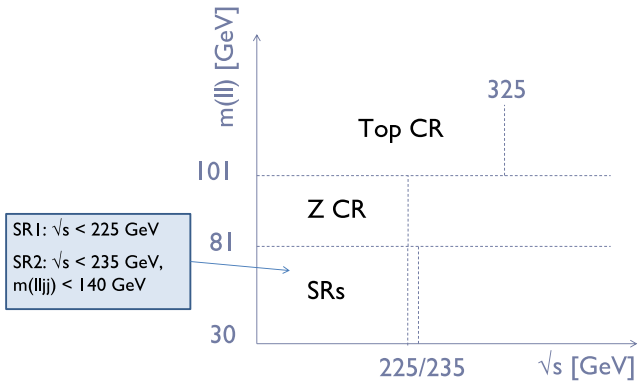

Figure 5.10: *Schematic illustration of the definition of signal and control regions by using the variables $m(ll)$, $m(lljj)$ and $\sqrt{s}_{min}^{(sub)}$.*

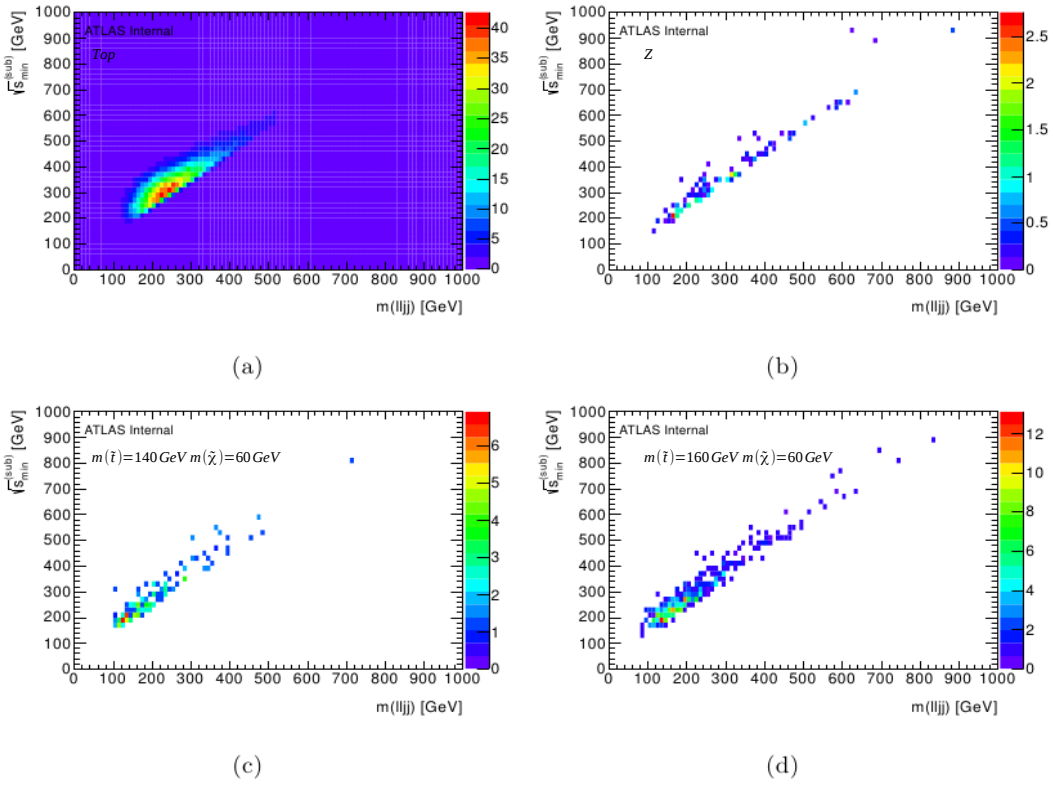

Figure 5.11: *Correlation between the* $\sqrt{s}_{min}^{(sub)}$ *and* $m(lljj)$ *variables for (a)* $t\bar{t}$ *background, (b) Z background, (c) a signal sample with* $m(\tilde{t}_1)$*=140 GeV,* $m(\widetilde{\chi}_1^{\pm})$*=120 GeV,* $m(\widetilde{\chi}_1^0)$*=60 GeV, and (d) a signal sample with* $m(\tilde{t}_1)$*=160 GeV,* $m(\widetilde{\chi}_1^{\pm})$*=120 GeV,* $m(\widetilde{\chi}_1^0)$*=60 GeV.*

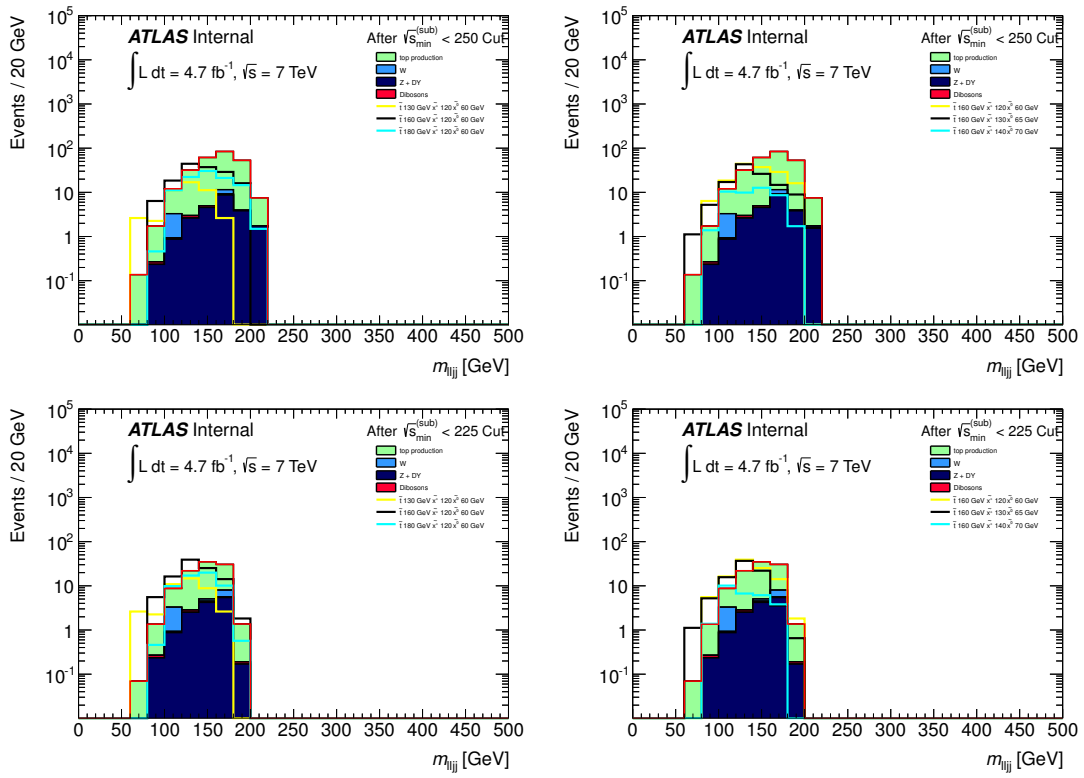

Figure 5.12: *Distributions of $m(lljj)$ for $\sqrt{s}_{min}^{(sub)}$ <250 GeV (top) and $\sqrt{s}_{min}^{(sub)}$ <225 GeV (bottom) for SM backgrounds and signal samples belonging to Grid 1 (left) and Grid 2 (right).*

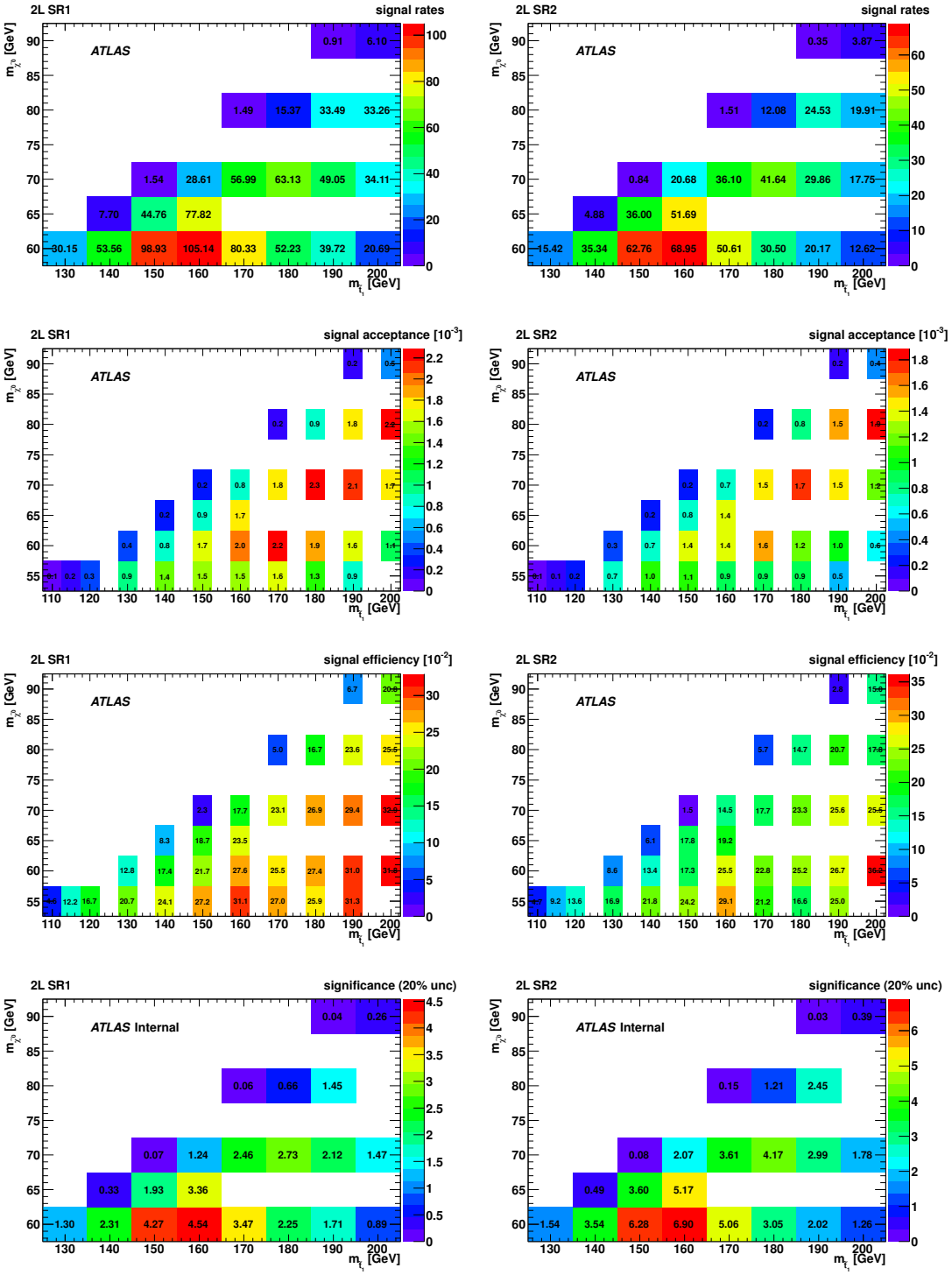

Figure 5.13: *From top to bottom: Signal yields, acceptance, acceptance times efficiency and expected significance for SR1 (left) and SR2 (right) for Grid 1.*

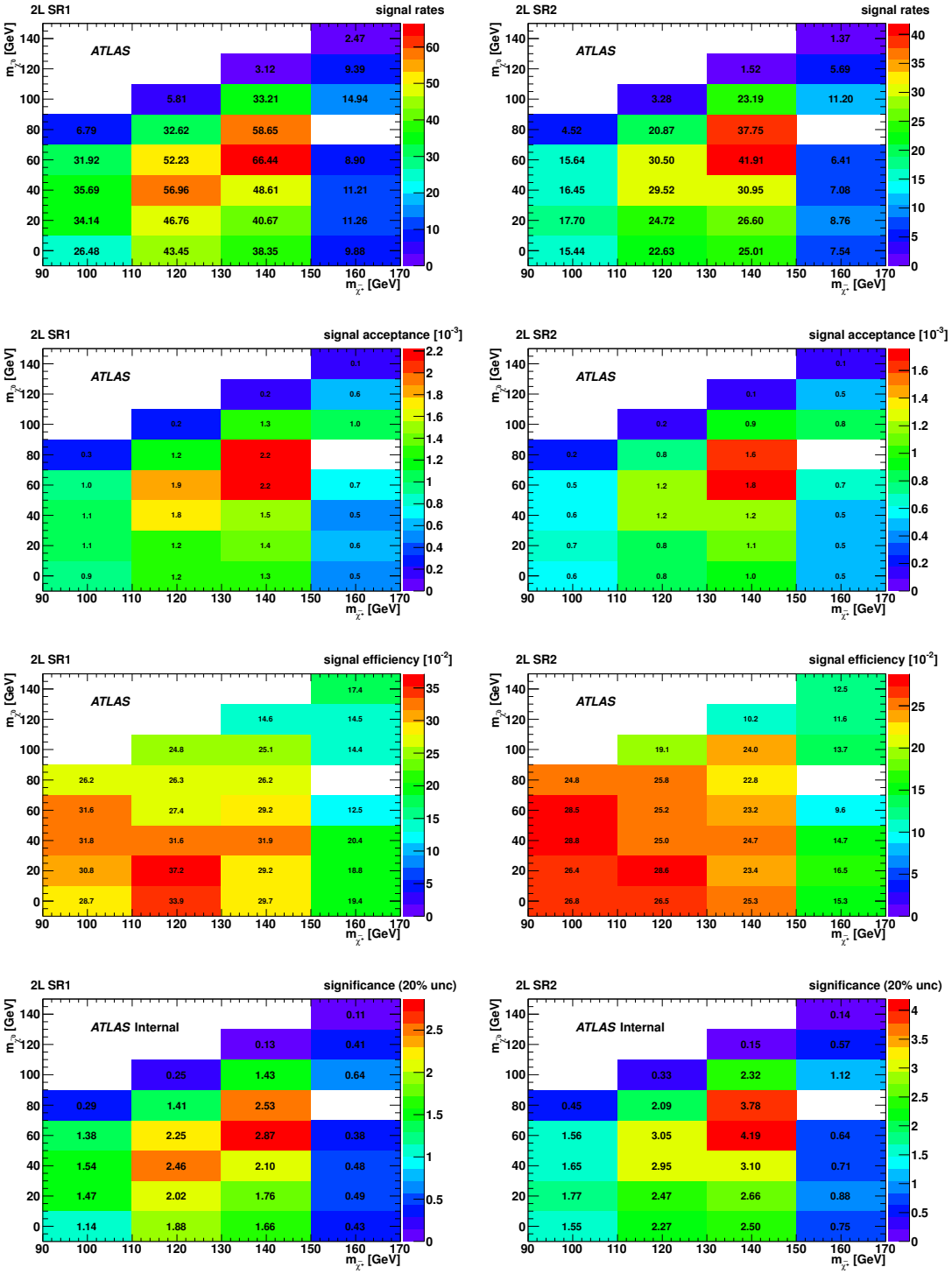

Figure 5.14: *From top to bottom: Signal yields, acceptance, acceptance times efficiency and expected significance for SR1 (left) and SR2 (right) for Grid 2.*

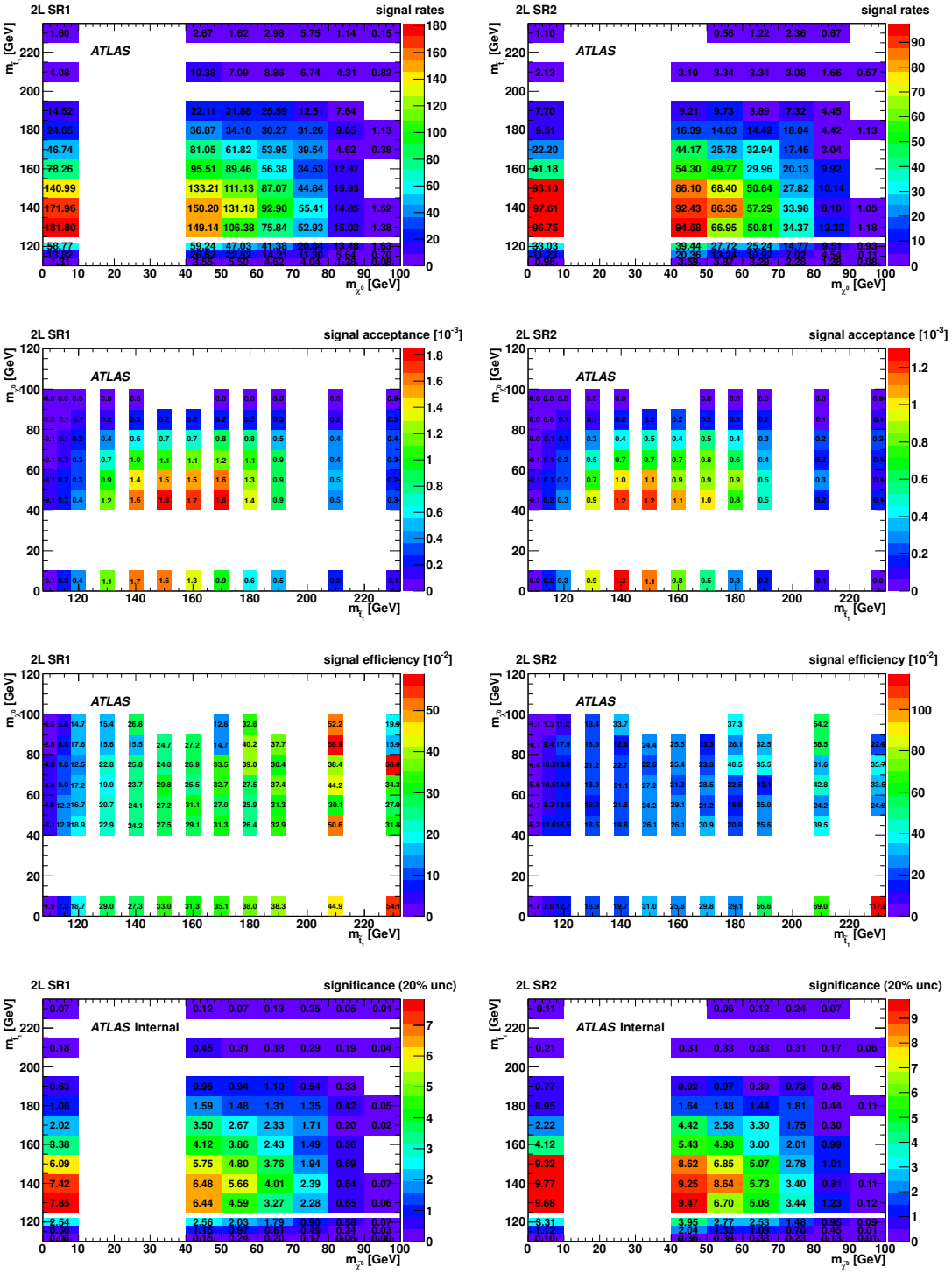

Figure 5.15: *From top to bottom: Signal yields, acceptance, acceptance times efficiency and expected significance for SR1 (left) and SR2 (right) for Grid 3.*

5.3 Background Estimation

As can be seen from Table 5.3, the dominant background in both SR1 and SR2 is $t\bar{t}$ production, followed by Z boson production in association with heavy flavour jets (Z+HF), single top quark production, and W boson plus heavy flavour jets production (W+HF). Minor backgrounds are ZZ, WZ, WW production (VV), and $t\bar{t}$ pairs produced in association with either a W boson, a Z boson, a γ, or a b- or t-quark ($t\bar{t}$+X).

The list of the generators used to simulate each background component can be found in Table 5.3, together with the integrated luminosity representing the number of produced events.

Process	**Generator**	$\mathcal{L}$ [$\mathbf{fb^{-1}}$]
$t\bar{t}$	McAtNLO	164
Single Top	McAtNLO	43
Wt	McAtNLO	57
W + HF	Alpgen+HERWIG	0.4 – 8
Z + HF	Alpgen+HERWIG	8 – 53
Drell-Yan + jets	Alpgen+HERWIG	3 – 15
WW,WZ,ZZ	HERWIG	150
$t\bar{t} + Z$	MadGraph	1050
$t\bar{t} + W$	MadGraph	800
$t\bar{t} + WW$	MadGraph	80000
$t\bar{t} + \gamma$	Whizard+Jimmy	600

Table 5.4: *List of SM Monte Carlo samples used in the analysis. The last column lists the equivalent luminosity for each sample.*

According to the analysis strategy defined in Section 4.2, the main backgrounds ($t\bar{t}$ pairs and Z boson production) are estimated with a semi data-driven technique exploiting the same variables defining the SRs. Events with fake leptons, as QCD multi-jets events, single top and W boson plus jets, are estimated with a data-driven technique. Minor backgrounds, characterised by low cross section or acceptance, account for only few percent of the total SM background and are estimated using Monte Carlo simulation.

5.3.1 QCD Multi-jet Events, W plus Jets and Single Top Production

QCD multi-jet events, W boson produced in association with heavy flavour jets and single top production in the s- and t-channel can enter the SRs if one or two jets originating

from their decays are misidentified as leptons [1].

The number of events with one real and one fake lepton (RF) and the number of events with two fake leptons (FF) are extracted from data with a procedure called *Matrix Method* [115] [116]. Two selection criteria are considered: tight and loose. Tight leptons are signal leptons as defined in Subsection 5.2.2. Loose leptons satisfy all the signal lepton requirements except the isolation cut. Events are split in categories depending on the leptons fulfilling the loose (L) exclusively loose (l) or tight (T) criteria. Only events with two tight leptons enter the SRs. Their total amount $N_{TT}^{FF} + N_{TT}^{FR} + N_{TT}^{RF}$ can be estimated starting from the number of events with two exclusively loose leptons (that are both real, one real and one fake, or both fakes) by measuring the fake rate f and the efficiency r:

$$\begin{pmatrix} N_{TT} \\ N_{Tl} \\ N_{lT} \\ N_{ll} \end{pmatrix} = M \begin{pmatrix} N_{LL}^{RR} \\ N_{LL}^{RF} \\ N_{LL}^{FR} \\ N_{LL}^{FF} \end{pmatrix} \tag{5.4}$$

with:

$$M = \begin{pmatrix} r_1 r_2 & r_1 f_2 & f_1 r_2 & f_1 f_2 \\ r_1(1-r_2) & r_1(1-f_2) & f_1(1-r_2) & f_1(1-f_2) \\ (1-r_1)r_2 & (1-r_1)f_2 & (1-f_1)r_2 & (1-f_1)f_2 \\ (1-r_1)(1-r_2) & (1-r_1)(1-f_2) & (1-f_1)(1-r_2) & (1-f_1)(1-f_2) \end{pmatrix} \tag{5.5}$$

$N_{TT}^{FF} + N_{TT}^{FR} + N_{TT}^{RF}$ is thus extracted from the measurable quantities N_{TT}, N_{Tl}, N_{lT} and N_{ll}, while the values of r_1, r_2, f_1, f_2 and the systematic uncertainties associated with this method have been taken from the analysis documented in Ref. [117], which has a similar preselection as this analysis.

The expected contributions in SR1 and SR2 from events with one fake lepton are reported in Table 5.5 separately for the ee, $\mu\mu$ and $e\mu$ channels. Events with one fake lepton can enter also the top and Z CRs described respectively in Sections 5.3.2 and 5.3.3. Their contribution can be found in Table 5.6.

The contribution from events with two fake leptons has been found to be negligible in all regions, and therefore is not reported.

To avoid double counting, the events with fake leptons are removed from the MC estimate of all the other sources of backgrounds, by exploiting the truth record of the samples. If the reconstructed leptons can be matched to truth leptons originating from a Z boson, a W boson or a t-quark, the leptons are considered as real. Events not containing two real leptons are removed from the sample. For all the background components where

[1] The Wt single top production is dominated by events with real leptons and is therefore estimated with another technique.

	ee	$\mu\mu$	$e\mu$	**Total**
SR1	-0.3 ± 0.1	5.7 ± 2.8	6.4 ± 3.5	12.1 ± 4.9
SR2	0.3 ± 1.5	3.6 ± 2.0	2.5 ± 2.5	6.4 ± 3.6

Table 5.5: *Numbers of fake-lepton events predicted for the two Signal Regions SR1 and SR2 split in the three lepton channels. The associated uncertainties have been estimated as in Ref.* [117].

	ee	$\mu\mu$	$e\mu$	**Total**
Top CR	3.3 ± 3.2	0.2 ± 1.6	1.9 ± 1.4	5.4 ± 5.1
Z CR	-0.1 ± 1.2	-0.2 ± 0.5	-	0.0 ± 1.3

Table 5.6: *Numbers of fake-lepton events predicted for the Top and Z CRs split in the three lepton channels. The associated uncertainties have been estimated as in Ref.* [117].

two real leptons are expected (Z, $t\bar{t}$ and Drell-Yan), 98% of the events have two real leptons. For $t\bar{t}$ produced in association with vector bosons, about the 71% of the events have two real leptons. W boson and single top production in s-channel and t-channel is totally removed. The Wt production is retained in case W and t decay leptonically.

5.3.2 $t\bar{t}$ and Wt Production

To estimate the normalisation factor to be applied to the MC estimate of $t\bar{t}$ and Wt in SR1 and SR2, a CR enriched in these processes has been defined, that will be referred to as Top CR.

The preselection is the one described in Subsection 5.2.2. The $m(ll)$ variable is used to define a pure sample with low signal contamination (at most 10%), by selecting only events with $m(ll) > 101$ GeV (see its distribution in Figure 5.5). The cut on the $\sqrt{s}_{\text{min}}^{(\text{sub})}$ variable is relaxed to 325 GeV, because the correlation between $\sqrt{s}_{\text{min}}^{(\text{sub})}$ and $m(ll)$ forces the first variable to acquire higher values when cutting on the second.

The number of expected events from $t\bar{t}$ and Wt production is, according to Equations 4.1 and 4.2:

$$N_{\text{SR}}^{\text{Top}} = \left(\frac{N_{\text{SR}}}{N_{\text{CR}}}\right)_{\text{MC}}^{\text{Top}} \times [N_{\text{CR}}^{\text{data}} - N_{\text{CR}}^{\text{non-Top,MC}} - N_{\text{CR}}^{\text{Fake}}] \tag{5.6}$$

where $N_{\text{CR}}^{\text{Fake}}$ is the contamination from events with fake leptons, as given in Table 5.6.

The numbers of expected events from simulation and the data count in Top CR are shown in Table 5.7, from which it can be seen that the contribution from $t\bar{t}$ and Wt events (referred to as "Top") is dominant. The resulting normalisation factor is:

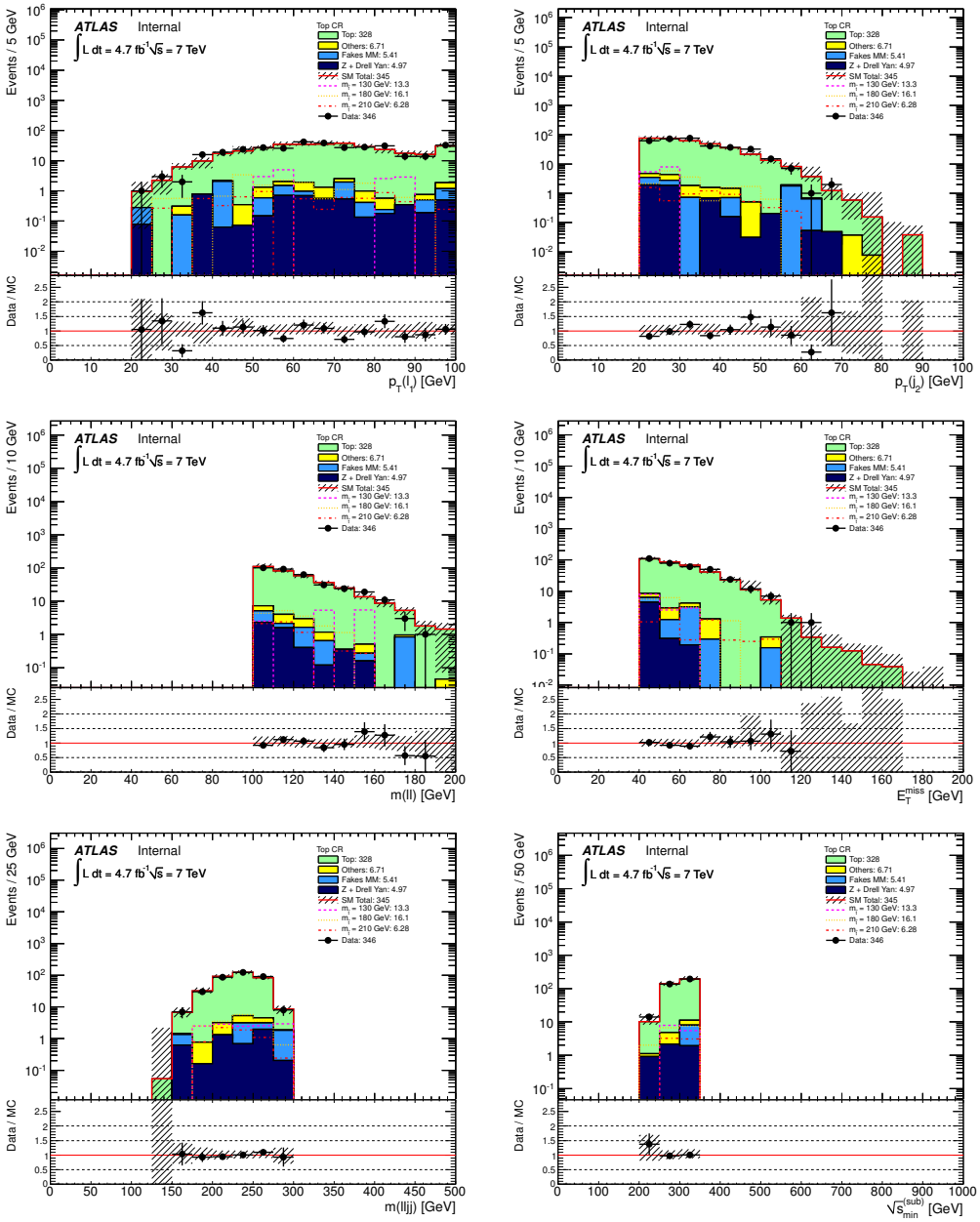

Figure 5.16: *Kinematic distributions for events in the top control region. From top left to bottom right: leading jet* p_{T}*, subleading jet* p_{T}*,* $m(ll)$*,* E_T^{miss}*,* $m(lljj)$*,* $\sqrt{s}_{min}^{(sub)}$*. The stacked histograms show the Standard Model expectation from simulation (normalised with the factors determined from Equations 5.7 and 5.9), compared to the data (points). Simulated signal samples where* $m(\tilde{t}_1) = 130$ *GeV (pink dashed line),* $m(\tilde{t}_1) = 180$ *GeV (yellow dashed line), and* $m(\tilde{t}_1) = 210$ *GeV (red dashed line) are overlaid. The legend reports the count of data and the yields of simulated events for each process. The "Data/MC" plots show the ratio of data events to the total Standard Model expectation. The hatched uncertainty bands display the total uncertainty on the background expectation.*

Process	ee	$\mu\mu$	$e\mu$	Total
Top	$59.1 \pm 1.5 \pm 11.5$	$80.7 \pm 1.8 \pm 15.7$	$145.3 \pm 2.4 \pm 22.3$	$285.1 \pm 3.4 \pm 48.6$
Fakes	$3.3 \pm 3.4 \pm 0.8$	$0.2 \pm 1.6 \pm 0.6$	$1.9 \pm 3.4 \pm 0.7$	$5.4 \pm 5.1 \pm 1.9$
Z+HF	$4.3 \pm 1.3 \pm 1.5$	$2.2 \pm 0.7 \pm 0.8$	$0.0 \pm 0.0 \pm 0.0$	$6.4 \pm 1.4 \pm 2.1$
Others	$1.5 \pm 0.2 \pm 0.2$	$1.8 \pm 0.2 \pm 0.2$	$3.3 \pm 0.3 \pm 0.4$	$6.7 \pm 0.4 \pm 0.7$
Total SM	$68.2 \pm 4.0 \pm 11.6$	$84.9 \pm 2.5 \pm 15.6$	$150.5 \pm 4.2 \pm 22.5$	$303.7 \pm 6.3 \pm 48.8$
Data	75	97	174	346

Table 5.7: *Numbers of expected events from simulation and data count in Top CR. "HF" stands for heavy flavour jets. The "Others" component includes $t\bar{t}$+X (X=W, Z, γ, b, t) and VV (V=Z, W). Both statistical and total systematic uncertainties are displayed.*

$$w_{t\bar{t}} = \frac{N_{\mathrm{CR}}^{\mathrm{data}} - N_{\mathrm{CR}}^{\mathrm{non-top,MC}} - N_{\mathrm{CR}}^{\mathrm{Fake}}}{N_{\mathrm{CR}}^{\mathrm{top,MC}}} = 1.15 \pm 0.21 \tag{5.7}$$

where the uncertainty includes both the statistical and systematic component described in Subection 5.4.1.

Figure 5.16 shows the good data-MC agreement reached after this normalisation factor and the normalisation factor for the Z CR, derived in Section 5.3.3, are applied.

5.3.3 Z plus Jets Production

The CR for the background from Z boson produced in association with heavy flavour jets (Z CR) is defined requiring only same flavour lepton pairs with invariant mass around the Z boson mass value, $81 < m(ll) < 101$ GeV. The selection $\sqrt{s}_{\mathrm{min}}^{(\mathrm{sub})} < 225$ GeV is also applied, to select events with the same kinematic properties as in the SRs and reduce the contamination from $t\bar{t}$ events.

The composition of the Z CR is shown in Table 5.8, compared to the number of events observed in data. The expected number of Z events in SR is obtained as:

$$N_{\mathrm{SR}}^{\mathrm{Z}} = \left(\frac{N_{\mathrm{SR}}}{N_{\mathrm{CR}}}\right)_{\mathrm{MC}}^{\mathrm{Z}} \times [N_{\mathrm{CR}}^{\mathrm{data}} - N_{\mathrm{CR}}^{\mathrm{non-Z,MC}} - N_{\mathrm{CR}}^{\mathrm{Fake}}] \tag{5.8}$$

where again $N_{\mathrm{CR}}^{\mathrm{Fake}}$ can be read from Table 5.6. The resulting normalization factor is:

$$w_{\mathrm{Z}} = \frac{N_{\mathrm{CR}}^{\mathrm{data}} - N_{\mathrm{CR}}^{\mathrm{non-Z,MC}} - N_{\mathrm{CR}}^{\mathrm{Fake}}}{N_{\mathrm{CR}}^{\mathrm{Z,MC}}} = 0.76 \pm 0.48 \tag{5.9}$$

The uncertainty includes both statistic and systematic uncertainties.

Figure 5.17 shows the data-MC comparison for different kinematic distributions in the Z CR, where both the normalisation factor for the Z and the top background are applied.

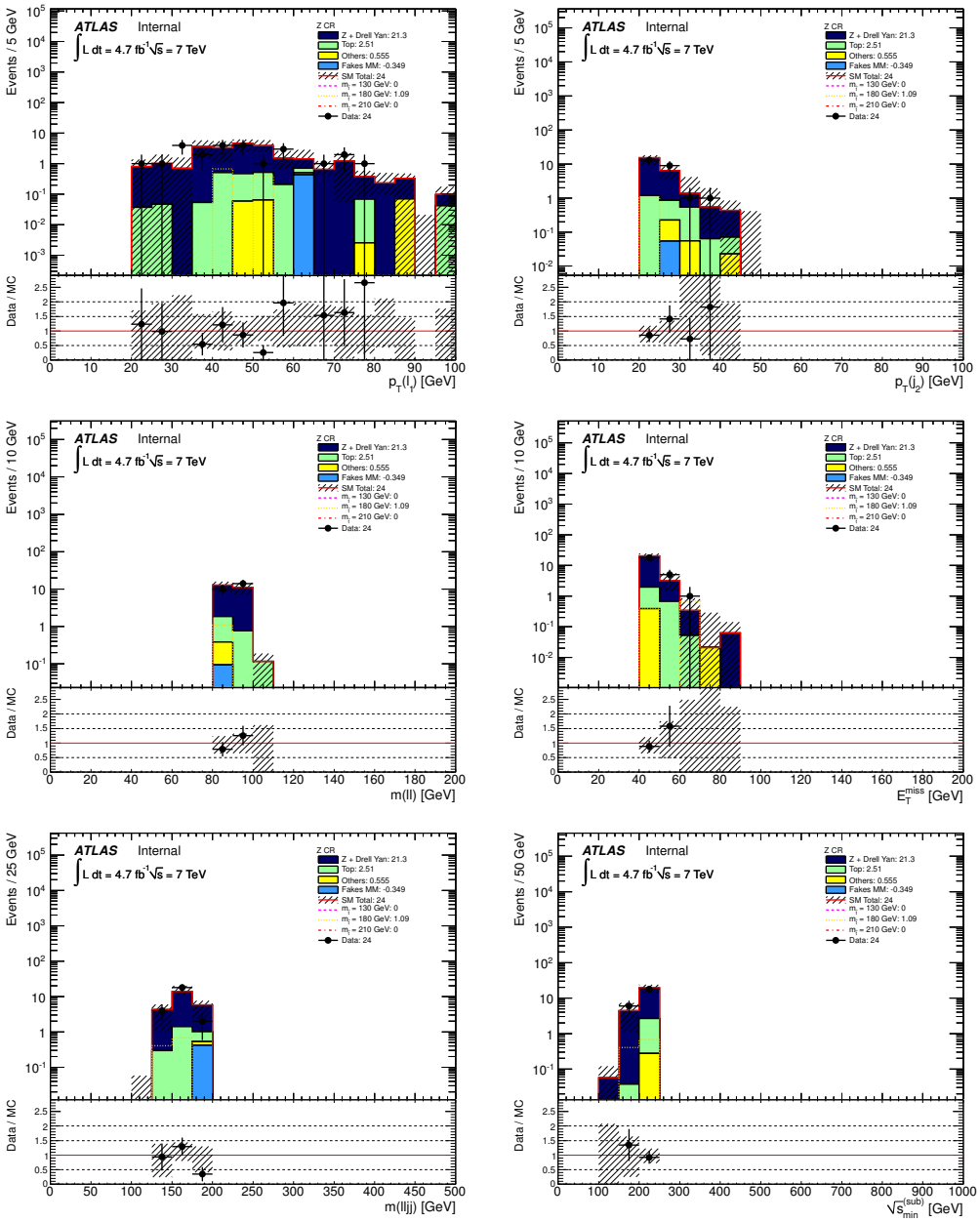

Figure 5.17: *Kinematic distributions for events in the Z control region. From top left to bottom right: leading jet* p_{T}*, subleading jet* p_{T}*,* $m(ll)$*,* E_T^{miss}*,* $m(lljj)$*,* $\sqrt{s}_{min}^{(sub)}$*. The stacked histograms show the Standard Model expectation from simulation (normalised with the factors determined from Equations 5.7 and 5.9), compared to the data (points). Simulated signal samples where* $m(\tilde{t}_1) = 130$ *GeV (pink dashed line),* $m(\tilde{t}_1) = 180$ *GeV (yellow dashed line), and* $m(\tilde{t}_1) = 210$ *GeV (red dashed line) are overlaid. The legend reports the count of data and the yields of simulated events for each process. The "Data/MC" plots show the ratio of data events to the total Standard Model expectation. The hatched uncertainty bands display the total uncertainty on the background expectation.*

Process	ee	$\mu\mu$	**Total**
Top	$0.5 \pm 0.1 \pm 0.8$	$2.0 \pm 0.3 \pm 0.5$	$2.5 \pm 0.3 \pm 0.8$
Fakes	$-0.1 \pm 1.2 \pm 0.4$	$-0.2 \pm 0.5 \pm 0.1$	$0.0 \pm 1.3 \pm 0.5$
Z+HF	$9.5 \pm 1.6 \pm 4.8$	$18.1 \pm 3.2 \pm 7.0$	$27.6 \pm 3.6 \pm 11.5$
Others	$0.3 \pm 0.1 \pm 0.1$	$0.3 \pm 0.1 \pm 0.1$	$0.6 \pm 0.1 \pm 0.1$
Total SM	$10.3 \pm 2.0 \pm 5.0$	$20.4 \pm 3.2 \pm 6.9$	$30.7 \pm 3.8 \pm 11.5$
Data	8	16	24

Table 5.8: *Numbers of expected events from simulation and data count in Z CR. "HF" stands for heavy flavour jets. The "Others" component includes $t\bar{t}$+X (X=W, Z, γ, b, t) and VV (V=Z, W). Both statistical and total systematic uncertainties are displayed.*

5.3.4 Minor Backgrounds: $t\bar{t}$ plus X and VV Production

ZZ, WZ, WW bosons and $t\bar{t}$ pairs produced in association with either a photon, a W or Z boson, a b- or a t-quark are minor backgrounds to this search. The contribution of these processes in SRs is estimated using Monte Carlo simulation. Tables 5.9 and 5.10 show their amount, respectively, in SR1 and SR2.

Process	ee	$\mu\mu$	$e\mu$	**Total**
$t\bar{t} + X$	0.1	0.7	0.6	1.3
VV	0.04	1.0	0.2	1.4
Total Others	0.1 ± 0.1	1.8 ±0.8	0.8 ±0.1	2.7 ±0.9

Table 5.9: *Expected number of events from minor background sources in SR1 as predicted from Monte Carlo. Uncertainties are only statistical.*

Process	ee	$\mu\mu$	$e\mu$	**Total**
$t\bar{t} + X$	0.0	0.3	0.2	0.5
VV	0.06	0.1	0.2	0.4
Total Others	0.1 ± 0.1	0.4 ±0.1	0.4 ±0.1	0.9 ±0.2

Table 5.10: *Expected number of events from minor background sources in SR2 as predicted from Monte Carlo. Uncertainties are only statistical.*

5.4 Systematic Uncertainties

5.4.1 Background Uncertainties

The sources of systematic uncertainties described in Section 4.3 and the statistical uncertainty have been taken into account for each background component.

The detector uncertainties described in Subsection 4.3.1 affect all backgrounds whose estimation rely totally or partially on Monte Carlo simulation. To estimate them, the analysis is re-run from scratch and the yield of events obtained is compared to the nominal event yield. For minor backgrounds this is done by comparing directly the yields in SRs. For $t\bar{t}$, Wt and Z backgrounds the values in Equations 5.6 and 5.8 are recomputed and compared to the nominal ones.

The way the theory uncertainties described in 4.3.2 have been estimated for the different background components depends on the process, the estimation technique and the Monte Carlo generator adopted (if any):

Theory uncertainties for top pair production

The uncertainty on the theoretical production cross section used in this analysis $\sigma_{t\bar{t}} = 166.8^{+11.45}_{-15.78}$ pb is propagated to SR1 and SR2.

For this background a semi data-driven technique has been adopted, therefore the only residual sources of uncertainties are those affecting the shape of the kineamtic distributions. ISR and FSR related uncertainties are evaluated with dedicated AcerMC samples with nominal and modified amount of ISR and FSR. The uncertainty originating from different NLO calculations is evaluated comparing the yield obtained with the default generator McAtNLO to the yield obtained with POWHEG interfaced with HERWIG. The difference between POWHEG samples interfaced to HERWIG or PYTHIA are used to estimate the uncertainty on the parton shower modelling.

Theory uncertainties for single top production

The dominant production channel for single top is Wt, therefore the uncertainty on the theoretical cross section of this channel, that is $\pm 8\%$, is taken as systematic uncertainty. For the other sources of theory systematic uncertainties (ISR and FSR, uncertainty originating from different NLO calculations, parton shower modelling), the values obtained for $t\bar{t}$ have been used.

Theory uncertainties for Z boson production

Similarly to the case of $t\bar{t}$ background, also for the Z background the relevant source of uncertainties are those affecting the shape of the kinematic distributions.

The theoretical uncertainty on the hard scattering cross section and the uncertainty connected to the PS/ME matching scales have been translated in changes in the cross sections of the different NpX (X=0,...,5) components of the Alpgen Monte Carlo samples, corresponding to changes in the cross sections for emission of additional partons.

Uncertainties for fake leptons

The uncertainties related to the multi-jet QCD background have been taken from Ref. [117]. The dominant components are the statistical uncertainties associated with the CRs used do derive the fake rate f, and the uncertainty connected to the extrapolation of the results from the CRs to the SRs.

Tables 5.11 and 5.12 show the impact of each source of uncertainty separately for each background process and for the total background. As expected, the total uncertainty is dominated by the uncertainty on the $t\bar{t}$ background, which is the main source of background.

	stat	**JER**	**JES**	$\boldsymbol{E_T^{miss}}$	**leptons**	***b*-tag**	**pile-up**	**ISR/FSR**	**theory**	
									Top	***Z***
Top	6%	2%	7%	1%	0.1%	1%	0%	4%	10%	0%
Z+HF	32%	1%	25%	5%	0.2%	1%	2%	4%	1%	2%
Others	31%	1%	14%	14%	0.7%	9%	4%	0%	0%	0%
Fakes	41%	84%								
Total	7%	1%	8%	1%	0%	1%	0.3%	3%	7%	0.2%

Table 5.11: *Summary of the systematic uncertainties for each background process of SR1. The "Others" component includes $t\bar{t}$+X (X=W, Z, γ, b, t) and VV (V=Z, W).*

	stat	**JER**	**JES**	$\boldsymbol{E_T^{miss}}$	**leptons**	***b*-tag**	**pile-up**	**ISR/FSR**	**theory**	
									Top	***Z***
Top	7%	4%	5%	0%	0.2%	1%	0%	8%	11%	0%
Z+HF	34%	25%	27%	4%	0.2%	8%	2%	4%	1%	9%
Others	18%	4%	53%	0%	1%	12%	2%	0%	0%	0%
Fakes	55%	67%								
Total	10%	5%	6%	0%	0.1%	1%	0.1%	6%	9	0.2%

Table 5.12: *Summary of the systematic uncertainties for each background process of SR2. The "Others" component includes $t\bar{t}$+X (X=W, Z, γ, b, t) and VV (V=Z, W).*

5.4.2 Signal Uncertainties

The theoretical uncertainties on the signal samples are obtained from an envelope of cross section predictions defined using the 68% CL ranges of the CTEQ6.6 [118] and MSTW2008 [119] PDF sets, together with independent variations of the factorisation and renormalisation scales by factors of two up and down. The numbers have been calculated using the program NN-fast [90]. The nominal cross section value is taken to be the mid-point of the envelope and the uncertainty assigned is half the full width of the envelope, as shown in Figure 5.2. The procedure follows closely the PDF4LHC recommendations [120].

5.5 Results and Interpretation

Figure 5.18 show the $E_{\mathrm{T}}^{\mathrm{miss}}$, $m(lljj)$ and $\sqrt{s}_{min}^{(sub)}$ distributions at different stages of the events selection process. The agreement between the Monte Carlo prediction (normalised according to the normalisation factors from Equations 5.7 and 5.9) and the data is overall good. Figures 5.19 and 5.20 show the same distributions in SR1 and SR2. A candidate event with one electron and one muon passing both SR1 and SR2 selections is shown in Figure 5.21.

The last two columns of Table 5.13 report the predicted and observed numbers of events in SR1 and SR2, with their uncertainties.

In both SRs no significant excess over the SM background expectation has been observed, therefore the results are interpreted in terms of exclusion limits.

The procedure for interpreting the results has been already discussed in detail in Section 4.4. Both model-independent and model-dependent exclusion limits have been derived.

According to Subsection 4.4, The CRs and one SR are fitted simultaneously and the CL_s is evaluated for each signal point of the three grids considered in this analysis.

To derive the final exclusion limits, the results of the analysis presented in this chapter have been combined with the results of an analysis performed in parallel, characterised by the same preselection and definition of the final state objects, the use of the $\sqrt{s}_{\mathrm{min}}^{(\mathrm{sub})}$ variable as main discriminating variable but requiring only one lepton in the final state [107]. Its numerical results for the expected and observed number of events are presented in the "1LSR1" column of Table 5.13.

To maximise the sensitivity, the results of the one-lepton and the two-lepton analyses are combined. The one-lepton and the two-lepton analyses are orthogonal by definition, therefore their combination is straightforward. SR1 and SR2 are not, and the strategy is to combine, for each signal point, the one-lepton results with the two-lepton results among those of SR1 and SR2 providing the lowest expected CL_s.

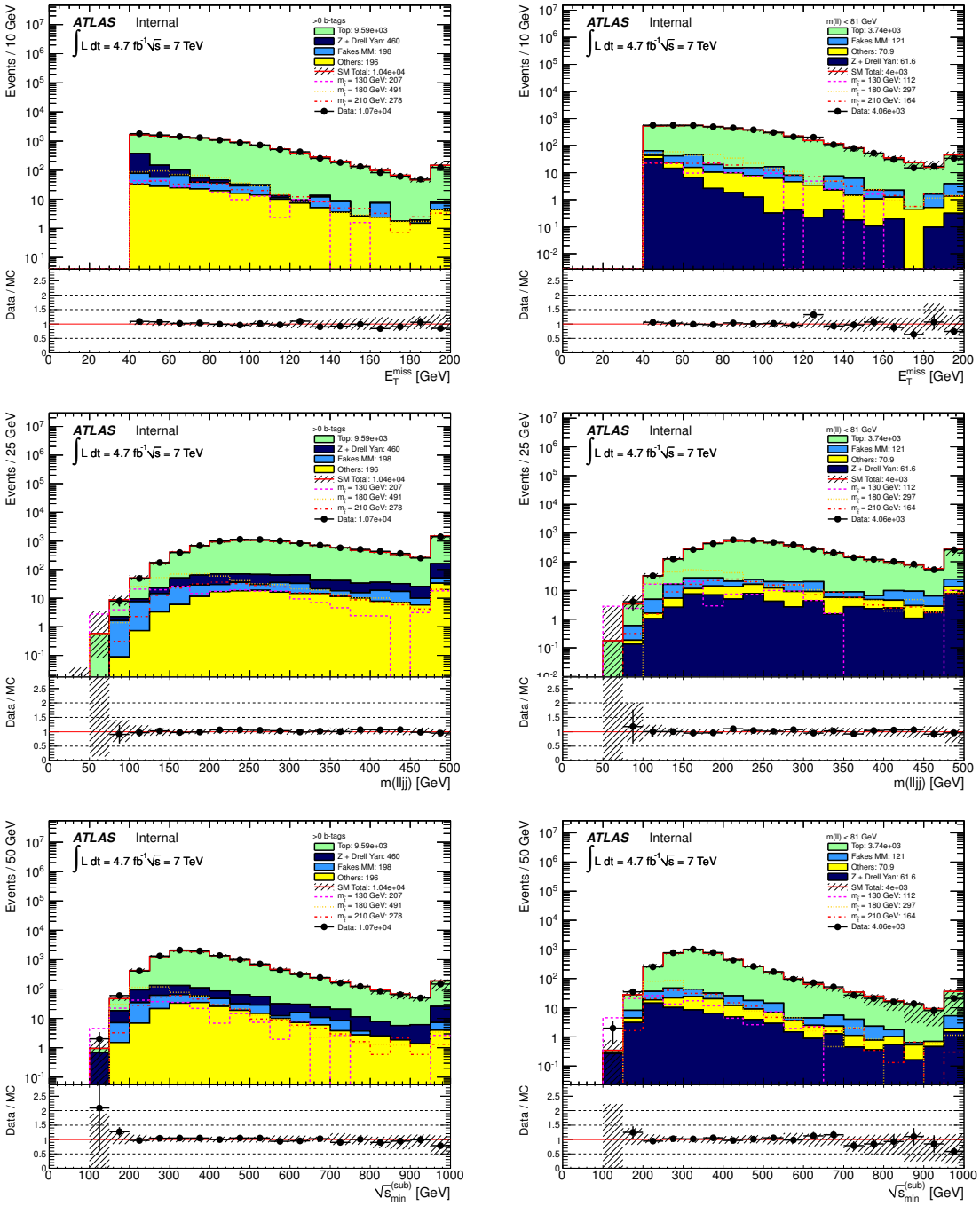

Figure 5.18: *Distributions of E_T^{miss} (top), $m(lljj)$ (middle) and $\sqrt{s}_{min}^{(sub)}$ (bottom) after one b-tag requirement (left) and after the requirement $30 < m_{ll} < 81$ GeV (right). The stacked histograms show the Standard Model expectation from simulation (normalised with the factors determined from Equations 5.7 and 5.9), compared to the data (points). Simulated signal samples where $m(\tilde{t}_1) = 130$ GeV (pink dashed line), $m(\tilde{t}_1) = 180$ GeV (yellow dashed line), and $m(\tilde{t}_1) = 210$ GeV (red dashed line) are overlaid. The legend reports the count of data and the yields of simulated events for each process. The "Data/MC" plots show the ratio of data events to the total Standard Model expectation. The hatched uncertainty bands display the total uncertainty on the background expectation.*

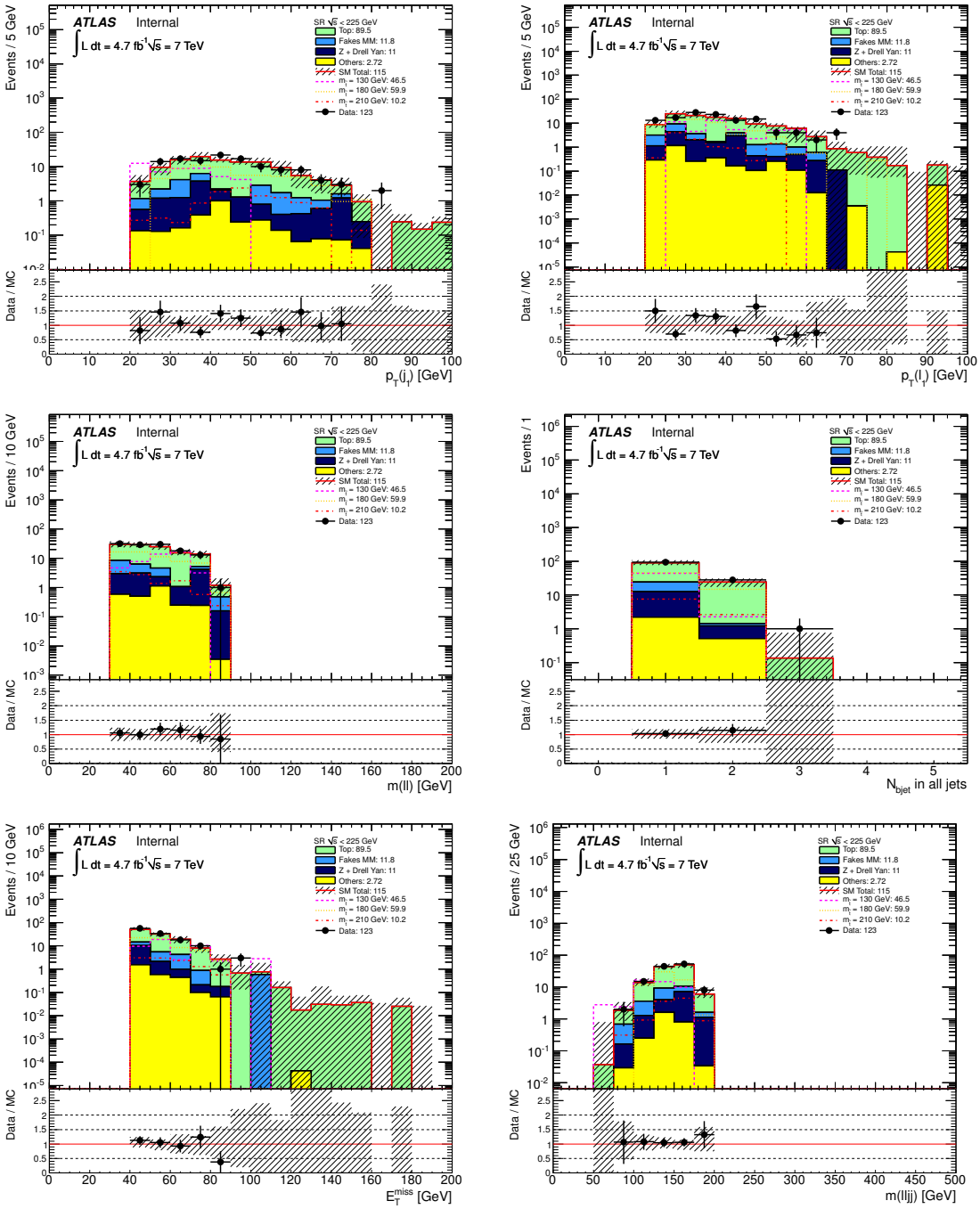

Figure 5.19: *Kinematic distributions for events in SR1. From top left to bottom right: leading jet* p_{T}*, leading lepton* p_{T}*,* $m(ll)$*, number of b-tagged jets,* E_T^{miss}*,* $m(lljj)$*. The stacked histograms show the Standard Model expectation from simulation (normalised with the factors determined from Equations 5.7 and 5.9), compared to the data (points). Simulated signal samples where* $m(\tilde{t}_1) = 130$ *GeV (pink dashed line),* $m(\tilde{t}_1) = 180$ *GeV (yellow dashed line), and* $m(\tilde{t}_1) = 210$ *GeV (red dashed line) are overlaid. The legend reports the count of data and the yields of simulated events for each process. The "Data/MC" plots show the ratio of data events to the total Standard Model expectation. The hatched uncertainty bands display the total uncertainty on the background expectation.*

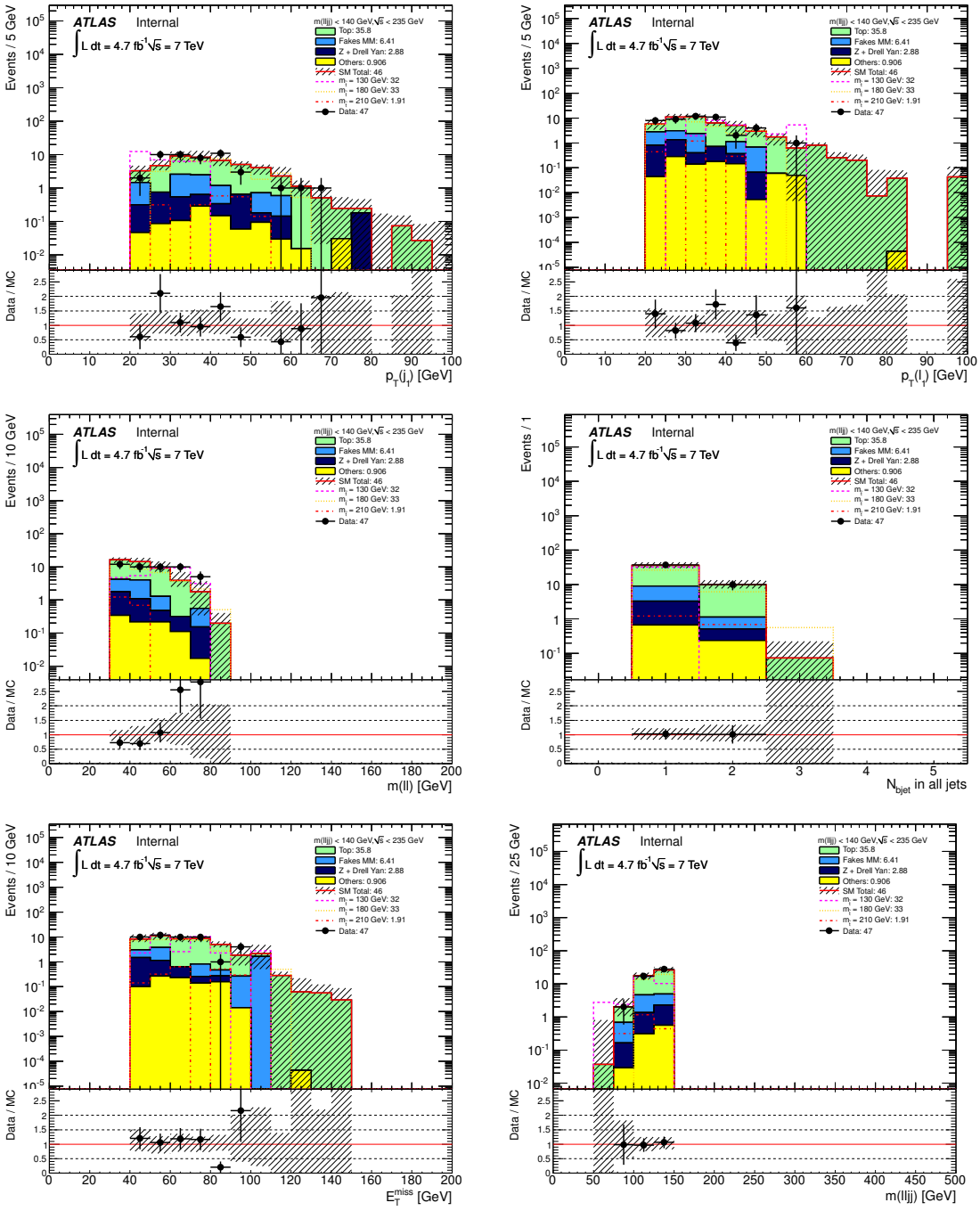

Figure 5.20: *Kinematic distributions for events in SR2. From top left to bottom right: leading jet* p_{T}*, leading lepton* p_{T}*,* $m(ll)$*, number of b-tagged jets,* E_T^{miss}*,* $m(lljj)$*. The stacked histograms show the Standard Model expectation from simulation (normalised with the factors determined from Equations 5.7 and 5.9), compared to the data (points). Simulated signal samples where* $m(\tilde{t}_1) = 130$ *GeV (pink dashed line),* $m(\tilde{t}_1) = 180$ *GeV (yellow dashed line), and* $m(\tilde{t}_1) = 210$ *GeV (red dashed line) are overlaid. The legend reports the count of data and the yields of simulated events for each process. The "Data/MC" plots show the ratio of data events to the total Standard Model expectation. The hatched uncertainty bands display the total uncertainty on the background expectation.*

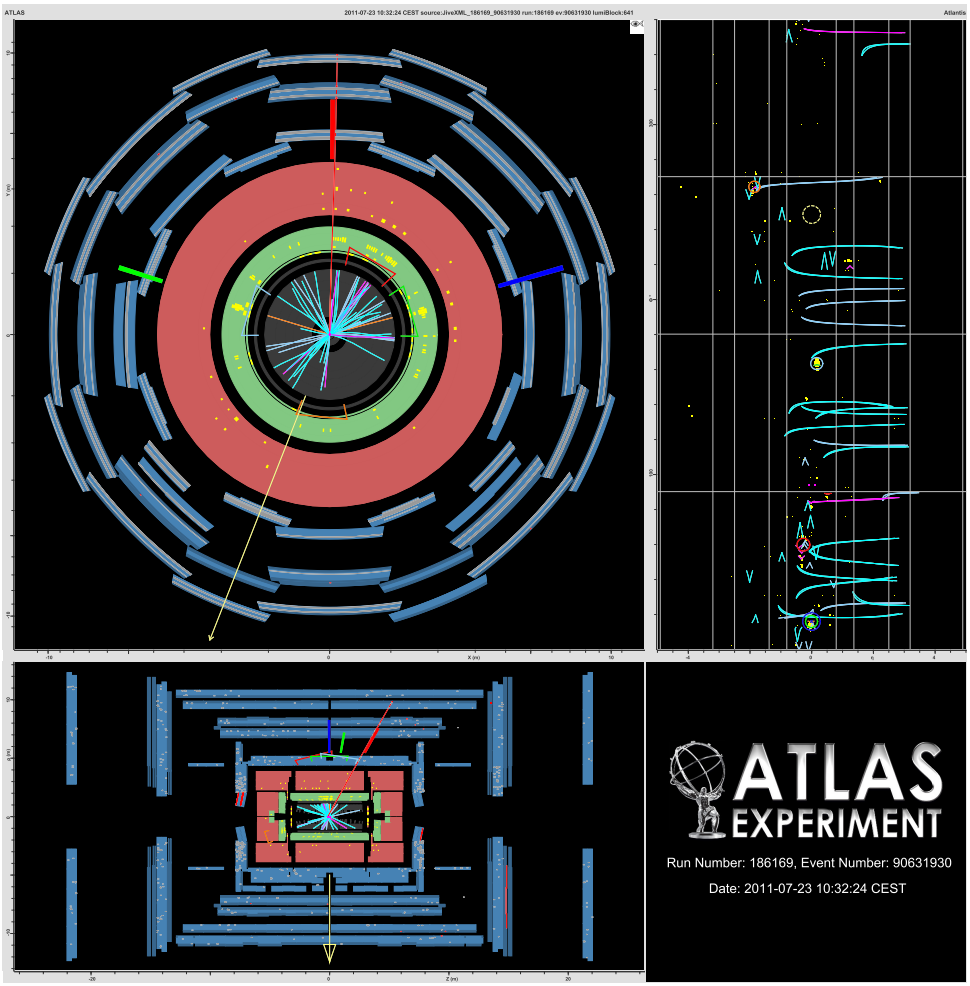

Figure 5.21: *Event display of an electron (green) and muon (red) event with a single b-jet (blue) which passes both SR1 and SR2 requirements. This event has* $m(lljj) = 111\ GeV$ *and* $\sqrt{s}_{\min}^{(\mathrm{sub})} = 209\ GeV$*. The detector is shown in the* $x-y$ *(top-left), the* $y-z$ *(lower-right) planes. The top-right plot shows the* $\eta - \phi$ *map showing calorimeter clusters (yellow), jets (solid circles) and* E_T^{miss} *(dashed red circle), with the turquoise lines representing tracks.*

Process	1LSR	SR1	SR2
Top	$24 \pm 3 \pm 5$	$89 \pm 6 \pm 10$	$36 \pm 2 \pm 5$
W+HF	$6 \pm 1 \pm 2$	n/a	n/a
Z+HF	$0.5 \pm 0.3 \pm 0.3$	$11 \pm 4 \pm 3$	$3 \pm 1 \pm 1$
Fakes	$7 \pm 1 \pm 2$	$12 \pm 5 \pm 11$	$6 \pm 4 \pm 4$
Others	$0.3 \pm 0.1 \pm 0.1$	$2.7 \pm 0.9 \pm 0.7$	$0.9 \pm 0.2 \pm 0.5$
Total SM	$38 \pm 3 \pm 7$	$115 \pm 8 \pm 15$	$46 \pm 4 \pm 7$
Data	50	123	47
$m(\tilde{t}_1) = 170$ GeV, $m(\widetilde{\chi}_1^0) = 70$ GeV	$26 \pm 2 \pm 6$	$57 \pm 3 \pm 6$	$36 \pm 2 \pm 4$
$m(\tilde{t}_1) = 180$ GeV, $m(\widetilde{\chi}_1^0) = 20$ GeV	$20 \pm 2 \pm 4$	$41 \pm 3 \pm 5$	$27 \pm 2 \pm 3$

Table 5.13: *Predicted and observed number of events in the one-lepton SR (1LSR), SR1 and SR2. The "Others" component includes $t\bar{t}$+X (X=W, Z, γ, b, t) and VV (V=Z, W). No values are shown for the W+HF contributions in SR1 and SR2 as these are included in the fake contributions. The expected numbers of events for two signal samples, both with a chargino mass of 140 GeV, are also shown. The uncertainties display statistical and systematic components separately.*

Figure 5.22 shows the 95% CL exclusion limits obtained combining the results of the SRs for the different set of signal samples considered.

The results for Grid 1, the main scenario targeted by this analysis, allow to exclude a large variety of signal points. In particular, $\tilde{t}_1$ masses in the range 120-167 GeV are excluded for $m(\widetilde{\chi}_1^0) = 55$ GeV. The results for Grid 2 allow to exclude a region around $m(\widetilde{\chi}_1^0) = 70$ GeV and $m(\widetilde{\chi}_1^\pm) = 140$ GeV for a fixed $\tilde{t}_1$ mass of 180 GeV. For Grid 3, $\widetilde{\chi}_1^0$ masses of 70 GeV are excluded for $\tilde{t}_1$ masses in the range 125-155 GeV under the assumption of $m(\widetilde{\chi}_1^\pm) = 106$ GeV, extending significantly the limits available on this scenario from searches at the Tevatron [121] and a previous search [122] of the ATLAS collaboration. According to the policy of the ATLAS collaboration, the exclusion limit quoted is the observed limit -1σ signal theoretical uncertainty.

The results have been interpreted also as model-independent exclusion limits, according to the procedure described in Subsection 4.4. The 95% CL upper limit on the numbers of events from a generic beyond the Standard Model signal is shown in Table 5.14. In the same table the upper limit on the events in each SR is translated into an upper limit on the visible cross section $\sigma_{vis} = A \cdot \epsilon \cdot \sigma$, where A and ϵ are the analysis acceptance and efficiency, and σ is the production cross section of a generic signal. To obtain it, the upper limit on the numbers of expected events is divided by the integrated luminosity.

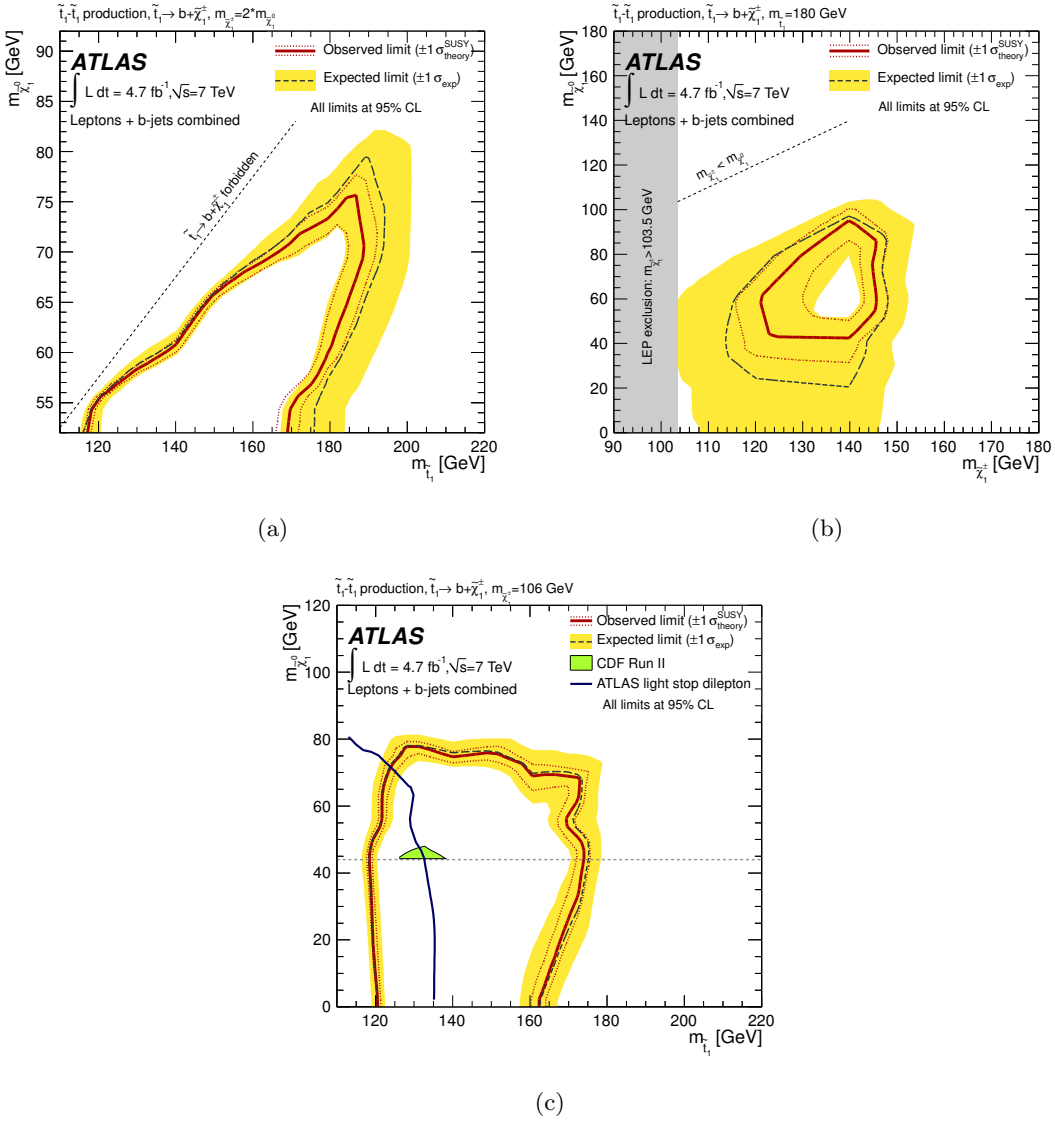

(a) (b)

(c)

Figure 5.22: *Observed and expected exclusion limits at 95% CL on (a) Grid 1 in the* $(\tilde{t}_1 - \tilde{\chi}_1^0)$*-mass plane, (b) Grid 2 in the* $(\tilde{\chi}_1^\pm - \tilde{\chi}_1^0)$*-mass plane, and (c) Grid 3 in the* $(\tilde{t}_1 - \tilde{\chi}_1^0)$*-mass plane. The full combination of the results of the one-lepton analysis with the results of the two-lepton analysis for SR1 or SR2 is shown. The dashed (solid) lines show the expected (observed) limits, including all uncertainties except for the theoretical signal cross section uncertainty. The bands around the expected limits show the* $\pm 1\sigma$ *results. The lines around the observed limits represent the results obtained when moving the nominal signal cross section up or down by the* $\pm 1\sigma$ *theoretical uncertainty. For Grid 3, the results are compared to previous limits from the Tevatron experiments* [121] *and from the ATLAS experiment* [122].

Region	95% CL N events	95% CL σ_{vis}(fb)
one-lepton SR1	52.2 (43.5 exp)	11 fb (9.3 exp.)
two-lepton SR2	24.8 (21.8 exp)	5.2 fb (4.6 exp.)
two-lepton SR	28.6 (20.0 exp)	6.1 fb (4.2 exp.)

Table 5.14: *Model-independent observed and expected upper limits at 95% CL for SR1, SR2 and the one-lepton analysis. Limits are given on the numbers of signal events and in terms of visible cross section. The systematic uncertainties on the SM background estimation are included.*

5.6 Summary of Stop Searches at $\sqrt{s}$=7 TeV

Given the importance of the stop search in the context of natural Supersymmetry, several analyses have been performed with the full dataset collected by the ATLAS experiment at a centre-of-mass energy of the proton-proton collisions of 7 TeV.

The decay mode $\tilde{t}_1 \to b\widetilde{\chi}_1^{\pm}$ with 100% branching ratio under the assumption of gaugino universality has been explored for the first time with the analysis presented in this chapter and the one lepton channel analysis conduced in parallel. As already stated, the $\tilde{t}_1 \to b\widetilde{\chi}_1^{\pm}$ mode have been explored also with the analysis documented in Ref. [122], under the assumption of $m(\widetilde{\chi}_1^{\pm}) = 106$ GeV. No significant excess over the SM prediction has been observed in these analyses, therefore the results have been interpreted in terms of exclusion limits in the $(\tilde{t}_1 - \widetilde{\chi}_1^0)$-mass plane.

In the mass range for the stop masses where $m(\tilde{t}_1) < m(t) - m(\widetilde{\chi}_1^0)$, the favourite decay mode is $\tilde{t}_1 \to t\widetilde{\chi}_1^0$. This scenario has been explored with analyses involving one, two and no leptons (respectively documented in Refs. [123], [124] and [125]). Also in this scenario no significant excess over the SM expectation have been observed and the results have been interpreted as exclusion limits in the $(\tilde{t}_1 - \widetilde{\chi}_1^0)$-mass plane.

A summary of the most relevant 95% CL direct stop pair production exclusion contours can be found in Figure 5.23. The left part of the plot shows the results on $\tilde{t}_1 \to b\widetilde{\chi}_1^{\pm}$ with 100% branching ratio. The excluded area coloured in light green is the exclusion contour presented in the previous section in Figure 5.22(c), together with the exclusion contour that is presented in the summary plot in dark green. The blue area corresponds to the exclusion contour on Grid 1 presented in Figure 5.22(a).

The right part of the figure summarises the results of stop searches in the decay mode $\tilde{t}_1 \to t\widetilde{\chi}_1^0$ with 100% branching ratio.

This figure demonstrates the importance of this analysis in the overall program of searches for direct stop pair production.

5.7 Comparison with the CMS Experiment Results

With the dataset collected at a centre-of-mass energy of the proton-proton collisions of 7 TeV, also the CMS experiment performed direct stop pair production searches in the decay channel $\tilde{t}_1 \to t\widetilde{\chi}_1^0$. No studies of the decay mode $\tilde{t}_1 \to b\widetilde{\chi}_1^{\pm}$ were performed.

All available results are summarised in Figure 5.24. The black line shows the interpretation of the results of the analysis described in Ref. [127], where final states with missing transverse energy and a variable number of b-tagged jets is selected. The main discriminating variable is the kinematic quantity α_T described in Ref. [130], which allows to discriminate events with real and fake missing transverse energy. The red and green lines represent the results documented in Refs. [128] and [129], obtained making or not explicit request of the presence of at least one b-tagged jet. In both analyses signal and background are discriminated with the razor variable described in Ref. [131], which provides the mass scale of pair produced particles.

By comparing the results in Figures 5.24 and 5.23 it is possible to see that the ATLAS experiment set exclusion limits on a wider range of stop masses in the decay mode $\tilde{t}_1 \to t\widetilde{\chi}_1^0$ with respect to the CMS experiment, and provided the only results on the decay mode $\tilde{t}_1 \to b\widetilde{\chi}_1^{\pm}$.

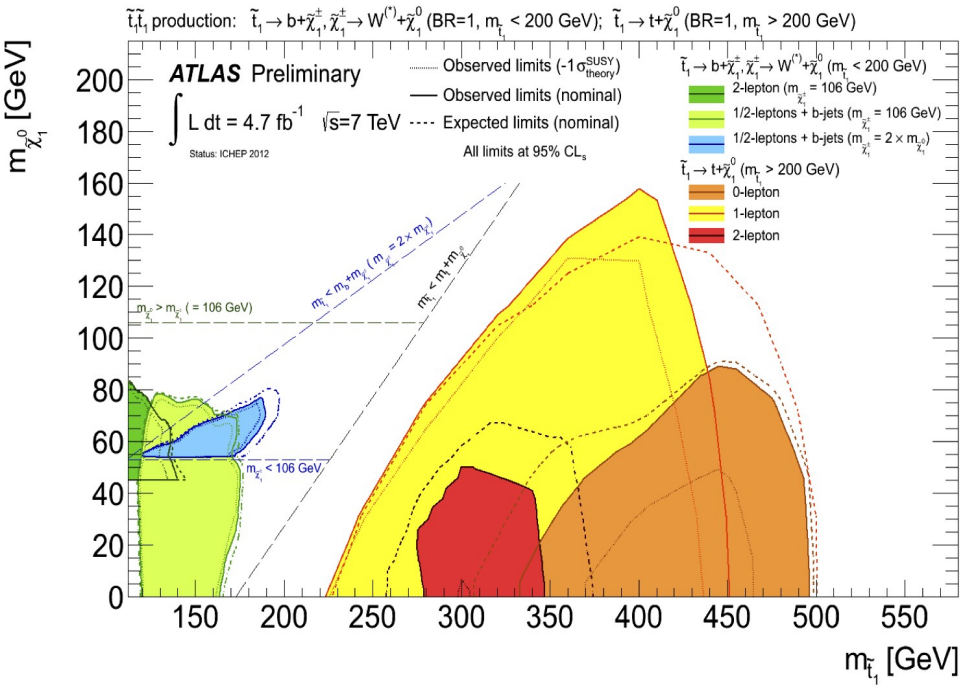

Figure 5.23: *Summary of the searches of the ATLAS experiment for stop pair production based on 4.7 fb^{-1} of proton-proton collision data collected at $\sqrt{s}$ = 7 TeV. Exclusion limits at 95% CL are shown in the $(\tilde{t}_1 - \widetilde{\chi}_1^0)$-mass plane. The dashed and solid lines show the expected and observed limits, respectively, including all uncertainties except the theoretical signal cross section uncertainty. Two decay modes with 100% BR are considered: $\tilde{t}_1 \to b\widetilde{\chi}_1^{\pm}$ (results from the analysis described in this chapter and from the analysis described in Ref. [122]) and $\tilde{t}_1 \to t\widetilde{\chi}_1^0$ (results from the analyses described in Refs. [123], [124] and [125])* [91].

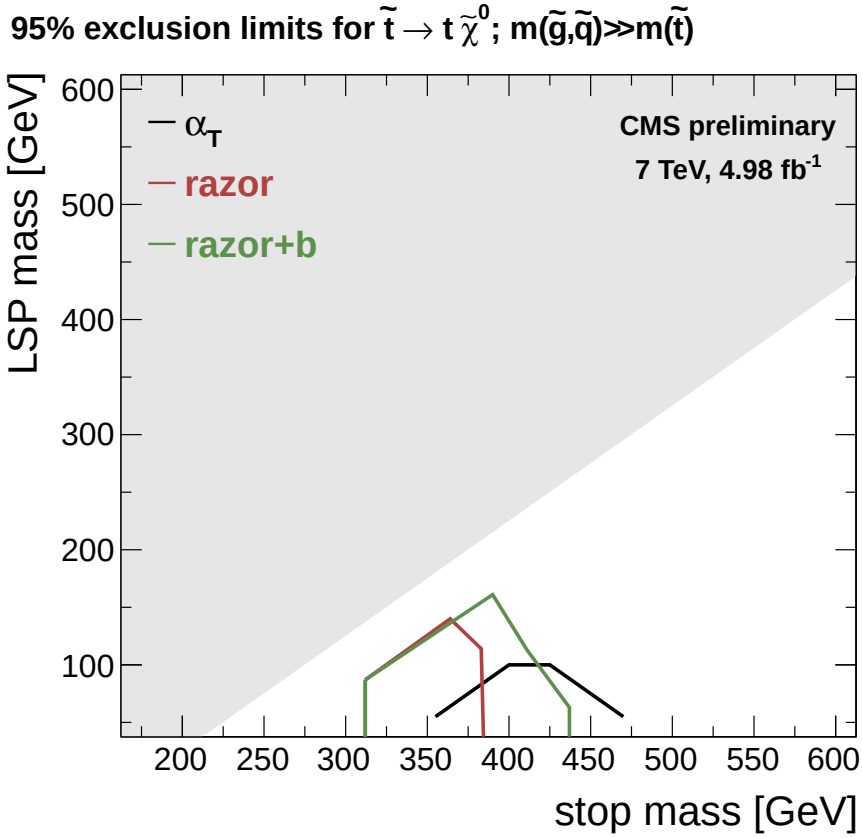

Figure 5.24: *Summary of the searches of the CMS experiment for stop pair production based on 4.98 fb^{-1} of proton-proton collision data collected at $\sqrt{s}$ = 7 TeV. Exclusion limits at 95% CL are shown in the $(\tilde{t}_1 - \tilde{\chi}^0_1)$-mass plane. The lines show the observed limits, including all uncertainties except the theoretical signal cross section uncertainty. The decay mode considered is $\tilde{t}_1 \to t\tilde{\chi}^0_1$ with 100% BR. The results are taken from the analyses described in Ref. [127] (black line), [128] (red line) and [129] (green line).*

Chapter 6

Stop Searches at $\sqrt{s} = 8$ TeV in Final States with Zero Leptons

The rise of the centre-of-mass energy of the proton-proton collisions from 7 to 8 TeV resulted in an increase of the ratio between the cross sections of top squark pair production and Standard Model backgrounds, and higher energy available for the top squarks system. These conditions made higher top squark masses, characterised by small production cross sections, accessible.

In this chapter a search for top squark pair production is presented. The hadronic decay mode is considered, characterised by the largest branching ratio and therefore suitable to address scenarios where the top squark mass is high.

The top squark is assumed to decay via $\tilde{t}_1 \to t\widetilde{\chi}_1^0$ or $\tilde{t}_1 \to b\widetilde{\chi}_1^{\pm}$. In this search, scenarios where both decay modes are present simultaneously with different branching ratios have been considered for the first time. The design and optimization of signal region selections leading to results that are as independent as possible on the decay mode were performed in the context of this thesis, after an extensive study of the kinematic properties of different banchmark signal samples and of the Standard Model backgrounds.

In this analysis the estimation of the Z boson background produced in association with heavy flavour jets, one of the most important backgrounds to this search, is particularly challenging. A novel estimation technique for its evaluation has been established in this thesis.

The results of the analysis presented in this chapter have been published in Ref. [132].

6.1 Addressed Signal

The signal addressed by the analysis described in this chapter is pair production of top squarks (stops), for stop masses in the range 300-700 GeV and therefore larger than the

top quark mass. The production cross section at NLO+NLL as a function of the stop mass at a centre-of-mass energy of the proton-proton collisions of 8 TeV is shown in Figure 6.1.

The branching ratios for the various decay modes depend on the composition of the stop in terms of left and right components, as well as on the mixing parameters and on the masses of the electro-weak gauginos and higgsinos. The decay channels considered are $\tilde{t}_1 \to t\widetilde{\chi}_1^0$ and $\tilde{t}_1 \to b\widetilde{\chi}_1^{\pm}$, as shown in Figure 6.2. The analysis has been designed to have sensitivity under different branching ratio hypotheses.

Final states with no leptons are considered, as the hadronic decays of the top quark and the W boson are characterised by the largest branching ratio. Another advantage of this choice is that, besides semi-leptonic decays of b-hadrons, the only real source of $E_{\mathrm{T}}^{\mathrm{miss}}$ in the signal events are neutralinos, thus allowing the use of $E_{\mathrm{T}}^{\mathrm{miss}}$ as s discriminating variable.

The signal is characterised by the presence of $E_{\mathrm{T}}^{\mathrm{miss}}$ and six jets. The reconstructed events can have a reduced jet multiplicity in case top quarks with significant boost are produced in the decay of high-mass top squarks, or if the mass spectrum in the decay mode $\tilde{t}_1 \to b\widetilde{\chi}_1^{\pm} \to bW^{(*)}\widetilde{\chi}_1^0$ is compressed. The search strategy has been defined to cover all these scenarios, by considering three different signal regions. To design and optimise the signal regions, three sets of simulated signal samples of varying $\tilde{t}_1$ and $\widetilde{\chi}_1^0$ masses were considered.

In the first set of signal samples, referred to as $tN1tN1$ *Grid*, the $\tilde{t}_1\bar{\tilde{t}}_1$ pair decays with 100% BR into a top quark and a $\widetilde{\chi}_1^0$. The $\tilde{t}_1$ is assumed to be mostly the superpartner of the right-handed top quark and the $\widetilde{\chi}_1^0$ to be mostly a bino, to ensure that the dominant decay mode is $\tilde{t}_1 \to t\widetilde{\chi}_1^0$.

In the second set of signal samples, the $tN1bC1$ *Grid*, one stop decays into a top quark and a $\widetilde{\chi}_1^0$ and the other into a b quark and a $\widetilde{\chi}_1^{\pm}$. In this case maximal mixing between the superpartners of the right and left handed top quarks is assumed, to ensure a significant BR in both decay modes. The $\widetilde{\chi}_1^{\pm}$ mass is set to twice the $\widetilde{\chi}_1^0$ mass, as predicted by the gaugino universality hypothesis (see Subsection 1.7.2).

The third set of signal samples, the $bC1bC1$ *Grid*, covers the case in which both stops decay into a b quark and a $\widetilde{\chi}_1^{\pm}$. The stop is chosen to be mostly the superpartner of the left handed top quark, to ensure the addressed decay mode has a significant BR. Also in this case the $\widetilde{\chi}_1^{\pm}$ mass is set to two times the $\widetilde{\chi}_1^0$ mass.

6.2 Data Samples and Events Selection

6.2.1 Dataset and Trigger

In this analysis the full dataset collected by the ATLAS experiment at a centre-of-mass energy of the proton-proton collisions of 8 TeV has been used, for a total integrated

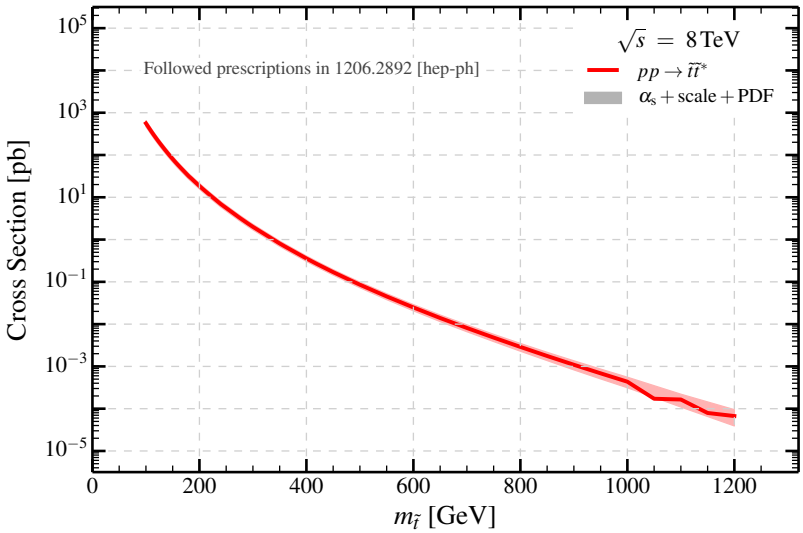

Figure 6.1: *Cross section for stop pair production at NLO+NLL accuracy, as a function of its mass. The ashed area represents the theory uncertainty as described in Subsection 6.5.2. The solid line corresponds to the cross section values used in the analysis.*

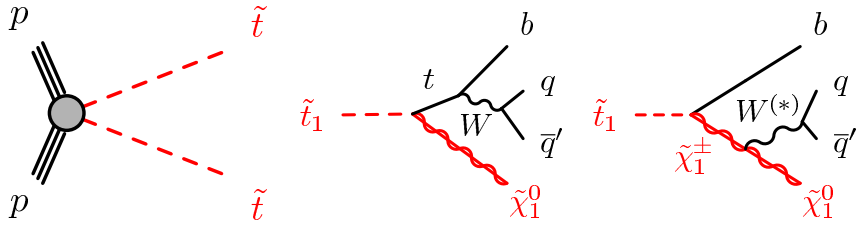

(a) (b) (c)

Figure 6.2: *Direct stop pair production (a) and subsequent decay modes (b), (c) considered in this analysis.*

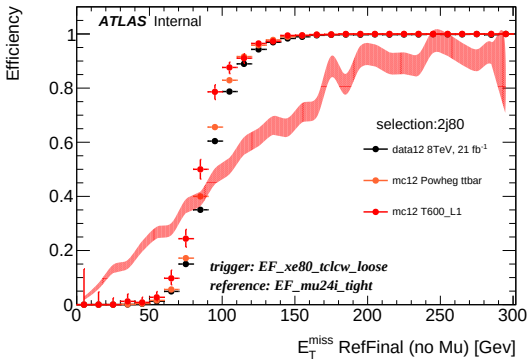

Figure 6.3: *E_T^{miss} trigger efficiency as a function of E_T^{miss}, evaluated on a sample of W bosons decaying into a muon and a neutrino, for a selection requiring at least two jets of $p_{\mathrm{T}} > 80$ GeV and $E_T^{miss} > 150$ GeV. The events with one muon of $p_{\mathrm{T}} > 25$ GeV firing the muon trigger described in the text are used as reference to evaluate the efficiency. The efficiency is plotted for data in black, $t\bar{t}$ in orange, and a signal sample with $(m(\tilde{t}_1),m(\widetilde{\chi}_1^0))=(600,1)$ GeV in red. The red band represents the distribution of E_T^{miss} with its statistical uncertainty in arbitrary units for the signal sample.*

luminosity of 20.3 fb^{-1} after the data quality selections have been applied.

The events are selected using the $E_{\mathrm{T}}^{\mathrm{miss}}$ trigger with the lowest threshold, that is 80 GeV at Event Filter level (see Section 3.1). Its efficiency has been evaluated on a sample of W bosons decaying into a muon and a neutrino, with respect to the lowest threshold muon trigger (requiring a muon with $p_{\mathrm{T}} > 24$ GeV at Event Filter level), for a selection containing one muon of $p_{\mathrm{T}} > 25$ GeV to be in the trigger plateau. Figure 6.3 shows that the $E_{\mathrm{T}}^{\mathrm{miss}}$ trigger is fully efficient for events containing at least two jets of $p_{\mathrm{T}} > 80$ GeV and $E_{\mathrm{T}}^{\mathrm{miss}} > 150$ GeV.

6.2.2 Event Cleaning and Preselection

The events are required to pass a set of selection criteria meant to clean the dataset from low quality events. The selections described in Subsection 5.2.2 are applied, with the only exception of the selection related to the mis-functioning of some of the front-end boards of the EM calorimeter, that was specific to the data-taking conditions of 2011. An additional selection, specific to the 2012 data-taking conditions, had to be applied. One tile calorimeter cell covering the region $-0.2 < \eta < -0.1$ and $2.65 < \phi < 2.75$ was malfunctioning during a small fraction of the data-taking period, and has not been masked during reconstruction. The total amount of data affected corresponds to 0.27 fb^{-1} of integrated luminosity. These events are rejected if any jet falls in the problematic region and the fraction of energy deposited in the second layer is larger than 0.6, to avoid selecting

events characterised by fake $E_{\mathrm{T}}^{\mathrm{miss}}$.

After the cleaning requirements, a preselection of the events compatible with the signal addressed by this analysis is applied:

- Events are vetoed if they contain either an electron or a muon.

  Electrons must satisfy the loose criteria, lie in the region $|\eta| < 2.47$ (see Section 3.5) and have $p_{\mathrm{T}} > 10$ GeV.

  Muons must be combined or segment tagged (see Section 3.6), have $p_{\mathrm{T}} > 10$ GeV and $|\eta| < 2.4$. Muons are also required to satisfy some minimum conditions on the number of hits left in the different parts of the ID, to ensure the good quality of their tracks.

- Events are required to have at least four jets. The two leading jets must have $p_{\mathrm{T}} > 80$ GeV and all other jets $p_{\mathrm{T}} > 35$ GeV. The jets reconstruction procedure and calibration has been already discussed in Section 3.3.

- Among the selected jets, at least two must be b-tagged, according to the definition in Section 3.4.

- $E_{\mathrm{T}}^{\mathrm{miss}} > 150$ GeV, computed as discussed in Section 3.7. The signal is characterised by the presence of neutralinos in the final state, therefore a high amount of $E_{\mathrm{T}}^{\mathrm{miss}}$ is expected.

- To reject events with fake $E_{\mathrm{T}}^{\mathrm{miss}}$, the distance in ϕ between $E_{\mathrm{T}}^{\mathrm{miss}}$ and the same variable built using only track information ($E_{\mathrm{T}}^{\mathrm{miss,track}}$) is required to be smaller than $\pi/3$. In order for the computation to be meaningful, the requirement $E_{\mathrm{T}}^{\mathrm{miss,track}} > 30$ GeV is made.

- To further enforce the rejection of events with fake $E_{\mathrm{T}}^{\mathrm{miss}}$, the distance in ϕ between $E_{\mathrm{T}}^{\mathrm{miss}}$ and the selected jets ($\left|\Delta\phi\left(\mathrm{jet}, E_{\mathrm{T}}^{\mathrm{miss}}\right)\right|$) is also checked and required to be larger than $\pi/5$.

- The transverse mass built with the b-tagged jet closest to $E_{\mathrm{T}}^{\mathrm{miss}}$ and $E_{\mathrm{T}}^{\mathrm{miss}}$ is required to be larger than 175 GeV: $\mathrm{m_T}\left(b_{\min[\Delta\phi\left(b, E_{\mathrm{T}}^{\mathrm{miss}}\right)]}, E_{\mathrm{T}}^{\mathrm{miss}}\right) > 175$ GeV.

  When a particle decays into detectable particles (leptons and jets) and undetectable particles (neutrinos), it is not possible to reconstruct the invariant mass of the system, as no information on the z component of the invisible particle momentum is available. Instead, it is possible to build the transverse mass. Under the assumption that the particle masses are negligible, the transverse mass is defined as $m_T = \sqrt{2p_T^{\mathrm{vis}} E_{\mathrm{T}}^{\mathrm{miss}}(1-\cos\theta)}$, where p_T^{vis} is the transverse momentum of the visible particle, and θ the angle between the direction of p_T^{vis} and $E_{\mathrm{T}}^{\mathrm{miss}}$. The distribution of

this variable is expected to have an endpoint at a value corresponding to the mass of the parent particle. The $\mathrm{m_T}\left(b_{\mathrm{min}[\Delta\phi\left(b,E_{\mathrm{T}}^{\mathrm{miss}}\right)]}, E_{\mathrm{T}}^{\mathrm{miss}}\right)$ distribution for semi-leptonic decays of $t\bar{t}$ pairs is expected to show an endpoint at the top mass. In the signal, the endpoint is exceeded. This selection is therefore useful in rejecting semi-leptonically decaying $t\bar{t}$ pairs without affecting much the acceptance of the signal. The different behaviour of the $\mathrm{m_T}\left(b_{\mathrm{min}[\Delta\phi\left(b,E_{\mathrm{T}}^{\mathrm{miss}}\right)]}, E_{\mathrm{T}}^{\mathrm{miss}}\right)$ variable for some benchmark signal points and for the backgrounds is shown in Figure 6.4.

The procedure to avoid double counting of objects in case electrons or muons overlap with jets is similar to the one described in Subsection 5.2.2. The difference is that a jet with a distance ΔR from a reconstructed electron smaller than 0.2 is discarded, if is not a b-tagged jet. In case it is a b-tagged jet, the electron is discarded. This procedure allows to reject electrons which are likely to come from a leptonic decay of a b-hadron.

A summary of the preselection criteria can be found in Table 6.1.

N_{lep}	0
jets	$\geqslant 4$
b-tagged jets	$\geqslant 2$
$E_{\mathrm{T}}^{\mathrm{miss}}$	> 150 GeV
$\left\lvert\Delta\phi\left(E_{\mathrm{T}}^{\mathrm{miss}}, E_{\mathrm{T}}^{\mathrm{miss,track}}\right)\right\rvert$	$< \pi/3$
$\left\lvert\Delta\phi\left(\mathrm{jet}, E_{\mathrm{T}}^{\mathrm{miss}}\right)\right\rvert$	$> \pi/5$
$\mathrm{m_T}\left(b_{\mathrm{min}[\Delta\phi\left(b,E_{\mathrm{T}}^{\mathrm{miss}}\right)]}, E_{\mathrm{T}}^{\mathrm{miss}}\right)$	> 175 GeV

Table 6.1: *Summary of the preselection criteria.*

6.2.3 Event Selection and Optimisation Procedure

After the preselection, the selection branches in three classes exploiting different discriminating variables. As it has been done for the analyses described in Chapter 5 (see Subsection 5.2.4), the selections have been optimised by maximising the expected discovery significance:

$$s = \frac{sig}{\sqrt{\sigma_{bkg,\mathrm{stat}}^2 + \sigma_{bkg,\mathrm{syst}}^2}} \sim \frac{sig}{\sqrt{bkg + \sigma_{bkg,\mathrm{syst}}^2}} \tag{6.1}$$

For the systematic uncertainty $\sigma_{bkg,\mathrm{syst}}$, values between 20% and 40% were considered.

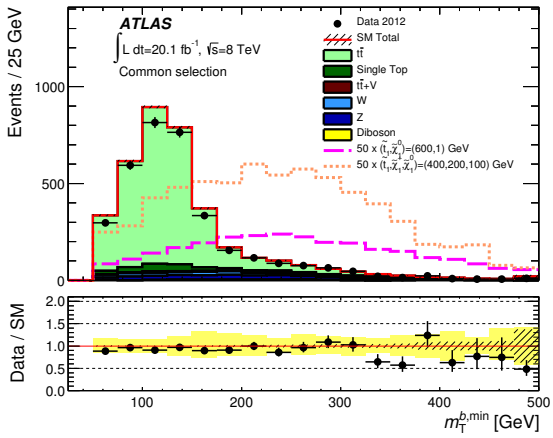

Figure 6.4: *Distribution of* $\mathrm{m_T}\left(b_{\min[\Delta\phi(b,E_T^{miss})]}, E_T^{miss}\right)$ *for the events passing the preselection requirements of Table 6.1, excluding the requirement on* $\mathrm{m_T}\left(b_{\min[\Delta\phi(b,E_T^{miss})]}, E_T^{miss}\right)$. *The stacked histograms show the Standard Model expectation from simulation compared to the data (points). Simulated signal samples where* $m_{\tilde{t}_1} = 600$ *GeV,* $m_{\widetilde{\chi}_1^0} = 1$ *GeV (pink dashed line) and* $m_{\tilde{t}_1} = 400\mathrm{GeV}, m_{\widetilde{\chi}_1^\pm} = 200$ *GeV,* $m_{\widetilde{\chi}_1^0} = 100$ *GeV (orange dotted line) are overlaid; the expected number of signal events is multiplied by a factor of 50 for improved visibility. The "Data/SM" plot shows the ratio of data events to the total Standard Model expectation. The rightmost bin includes all overflows. The hatched uncertainty band around the Standard Model expectation shows the statistical uncertainty and the yellow band (shown only for the "Data/SM" plot) shows the combination of statistical and experimental systematic uncertainties.*

The first class targets the physics scenario $\tilde{t}_1 \to t\widetilde{\chi}_1^0$ with 100% branching ratio, for a wide range of stop masses. The selections of the signal regions, called SRA, have been optimised on the tN1tN1 Grid.

Also the second class, called SRB, has been optimised by using the tN1tN1 Grid and addresses the scenario $\tilde{t}_1 \to t\widetilde{\chi}_1^0$ with 100% branching ratio, but the selections have been chosen to specifically cover stop masses around 700 GeV.

The third and last class is SRC. It has been designed to recover the sensitivity of the analysis in case the $\tilde{t}_1 \to b\widetilde{\chi}_1^\pm$ decay mode competes with the $\tilde{t}_1 \to t\widetilde{\chi}_1^0$ decay mode. The selections of SRC have been optimised on the tN1bC1 Grid, and their performances checked also on the tN1tN1 and the bC1bC1 Grids.

The selections of SRB and SRC are orthogonal to the selection of SRA. To obtain the best performance from this search, the results obtained with SRA are combined with the results of either SRB or SRC, depending on which one is more suitable for the physics case under study.

SRA Selections

In SRA the minimum number of six jets coming from the full hadronic decay of the signal is required.

A natural source of background is top quark pair production ($t\bar{t}$). Due to the requirement on the minimum amount of $E_{\mathrm{T}}^{\mathrm{miss}}$, the decay modes maximally contributing are those where one of the top quarks decays into a lepton and a neutrino, and the other into two quarks (semi-leptonic decays). These events pass the selection if the lepton falls out of the geometric acceptance of the detector or if it is wrongly identified as a jet in the reconstruction procedure. The signal is instead characterised by the presence of two hadronically decaying top quarks. An explicit reconstruction of their masses can be helpful in discriminating the signal from semi-leptonically decaying $t\bar{t}$ and other sources of background. The mass of the two top quark candidates is reconstructed with the following procedure:

1. Among all the light flavour jets, the two closest in ΔR are used to form the first W boson candidate.

2. The closest b-tagged jet is added to the light flavour pair selected in the previous step to form a top quark candidate with mass m^0_{bjj}. No requirements on the masses are applied to define either the W boson or the top candidate.

3. The second W boson candidate is defined with the two closest remaining light jets. The second top quark candidate, with mass m^1_{bjj}, is formed with the second W candidate plus the remaining b-tagged jet.

The mass of both reconstructed top candidates is then considered in the optimisation of the selection criteria, together with the other discriminating variables: $E_{\mathrm{T}}^{\mathrm{miss}}$ and $\min[\mathrm{m_T}\left(\mathrm{jet}^i, E_{\mathrm{T}}^{\mathrm{miss}}\right)]$ (the minimum value of the transverse masses built with $E_{\mathrm{T}}^{\mathrm{miss}}$ and the jets in the event). The selections have been chosen to maximise the sensitivity to signal models of different $\tilde{t}_1$ and $\widetilde{\chi}_1^0$ masses used as benchmark scenarios. As a result, four sets of selections have been chosen, reported in Table 6.2.

The most powerful discriminating variable is $E_{\mathrm{T}}^{\mathrm{miss}}$. For a given $\widetilde{\chi}_1^0$ mass, as the mass of the $\tilde{t}_1$ increases, $E_{\mathrm{T}}^{\mathrm{miss}}$ tends to assume higher values and therefore a higher cut on this variable is more suitable to enhance the significance. The reconstructed hadronic top masses are particularly effective to reduce the non-top background components, as Z and W bosons. $\min[\mathrm{m_T}\left(\mathrm{jet}^i, E_{\mathrm{T}}^{\mathrm{miss}}\right)]$ allows to reject background from semi-leptonically decaying $t\bar{t}$ pairs, already reduced by the selection on $\mathrm{m_T}\left(b_{\min[\Delta\phi\left(b, E_{\mathrm{T}}^{\mathrm{miss}}\right)]}, E_{\mathrm{T}}^{\mathrm{miss}}\right)$ applied during the preselection. Events where a tau lepton is produced in the decay of the $t\bar{t}$ pair are also a potential background. To suppress it, events containing a tau candidate are rejected. Tau candidates are defined as jets with less than four associated tracks and an angular separation $\Delta\phi$ from the direction of $E_{\mathrm{T}}^{\mathrm{miss}}$ smaller than 0.2.

	SRA1	**SRA2**	**SRA3**	**SRA4**
jets	$\geq 6,\ p_{\mathrm{T}} > 80, 80, 35, 35, 35, 35$ GeV			
m^0_{bjj}	< 225 GeV		[50,250] GeV	
m^1_{bjj}	< 250 GeV		[50,400] GeV	
$\min[\mathrm{m_T}\,(\mathrm{jet}^i, E_{\mathrm{T}}^{\mathrm{miss}})]$	–		> 50 GeV	
τ veto	applied			
$E_{\mathrm{T}}^{\mathrm{miss}}$	> 150 GeV	> 250 GeV	> 300 GeV	> 350 GeV

Table 6.2: *Selection criteria for the four sets of selections of SRA.*

SRB Selections

In the benchmark signal model targeted by SRB, $\tilde{t}_1 \to t\tilde{\chi}^0_1$ with 100% BR and $m(\tilde{t}_1) =$ 700 GeV, the jets originating from the hadronic decay of the top quarks can be very close to each other, and potentially not resolvable with the default cone size R adopted in the anti-k_T algorithm, which is 0.4 (see Section 3.3). As a result, such a signal is characterised by a reduced jet multiplicity with respect to the nominal six jets signature. For this reason, and to make the selection of this signal region orthogonal to the selection of SRA, events with four or five jets are considered.

Also in this case the signal is characterised by the presence of two top quarks, but they cannot be reconstructed with the same procedure adopted for SRA. Instead, the jets are re-clustered, using the anti-k_T algorithm of cone size R=1.2. The resulting re-clustered jets are referred to as anti-k_T R=1.2 jets (while the word jet without any specification refers to a jet reconstructed with the anti-k_T algorithm of default cone size R=0.4). The two anti-k_T R=1.2 jets with the highest p_{T} form the hadronic top candidates, and their masses, m^0_{AkT12} and m^1_{AkT12}, are used as discriminating variables. The events are classified according to the value of the mass asymmetry variable:

$$\mathcal{A}_{m_t} = \frac{|m^0_{AKT12} - m^1_{AKT12}|}{m^0_{AKT12} + m^1_{AKT12}} \tag{6.2}$$

Events with two anti-k_T R=1.2 jets with similar masses are characterised by small values of $\mathcal{A}_{m_t}$. For events where the decay products of the two tops are very close it is possible that one of the anti-k_T R=1.2 jets contains decay products from both top quarks, and in this case $\mathcal{A}_{m_t}$ will assume high values. Given the difference between the two topologies, the selections for events with $\mathcal{A}_{m_t} < 0.5$ are optimised separately from the selections for events with $\mathcal{A}_{m_t} \geqslant 0.5$ and are named, respectively, SRB1 and SRB2.

In addition to semi-leptonically decaying $t\bar{t}$ pairs, also Z and W bosons decaying in final states containing neutrinos are an important background. The selections have been

designed to reduce all the sources of background. Together with the mass of the anti-k_T R=1.2 jets, the other discriminating variables considered in the optimisation procedure are:

- $E_{\mathrm{T}}^{\mathrm{miss}}$
- $\mathrm{m_T}\left(b_{\min[\Delta\phi\left(b,E_{\mathrm{T}}^{\mathrm{miss}}\right)]}, E_{\mathrm{T}}^{\mathrm{miss}}\right)$
- $\mathrm{m_T}\left(jet^{untag}_{\min[\Delta\phi\left(jet^{untag},E_{\mathrm{T}}^{\mathrm{miss}}\right)]}, E_{\mathrm{T}}^{\mathrm{miss}}\right)$: Transverse mass between the closest jet to $E_{\mathrm{T}}^{\mathrm{miss}}$ which is not a b-tagged jet and $E_{\mathrm{T}}^{\mathrm{miss}}$, useful to reject background from W and Z bosons.
- $\mathrm{m_T}\left(jet_{lowest-p_{\mathrm{T}}}, E_{\mathrm{T}}^{\mathrm{miss}}\right)$: Transverse mass between the lowest p_{T} jet and $E_{\mathrm{T}}^{\mathrm{miss}}$, for additional discrimination between signal and background from W and Z bosons.
- m^0_{AkT8}: Mass of the leading jet obtained by re-clustering the jets with the anti-k_T algorithm of cone size 0.8 (anti-k_T R=0.8 jets).
- $p^0_{T,AkT12}$: p_{T} of the leading anti-k_T R=1.2 jet.
- $H_T^{sig}(\equiv \frac{E_{\mathrm{T}}^{\mathrm{miss}}}{\sqrt{\sum H_T}})$: $E_{\mathrm{T}}^{\mathrm{miss}}$divided by the scalar sum of the p_{T} of all jets. This variable is effective in rejecting electro-weak backgrounds.

A summary of the selections of SRB1 and SRB2 can be found in Table 6.3.

	SRB1	**SRB2**
jets	4 or 5, $p_{\mathrm{T}} > 80, 80, 35, 35, (35)$ GeV	5, $p_{\mathrm{T}} > 100, 100, 35, 35, 35$ GeV
$\mathcal{A}_{m_t}$	< 0.5	> 0.5
$p^0_{T,AkT12}$	–	> 350 GeV
m^0_{AkT12}	> 80 GeV	$[140, 500]$ GeV
m^1_{AkT12}	$[60, 200]$ GeV	–
m^0_{AkT8}	> 50 GeV	$[70, 300]$ GeV
$\mathrm{m_T}\left(jet^{untag}_{\min[\Delta\phi\left(jet^{untag},E_{\mathrm{T}}^{\mathrm{miss}}\right)]}, E_{\mathrm{T}}^{\mathrm{miss}}\right)$	> 175 GeV	> 125 GeV
$\mathrm{m_T}\left(jet_{lowest-p_{\mathrm{T}}}, E_{\mathrm{T}}^{\mathrm{miss}}\right)$	> 280 GeV for 4-jet case	–
H_T^{sig}	–	$> 17\sqrt{\mathrm{GeV}}$
$E_{\mathrm{T}}^{\mathrm{miss}}$	> 325 GeV	> 400 GeV

Table 6.3: *Selection criteria for the two sets of selections of SRB.*

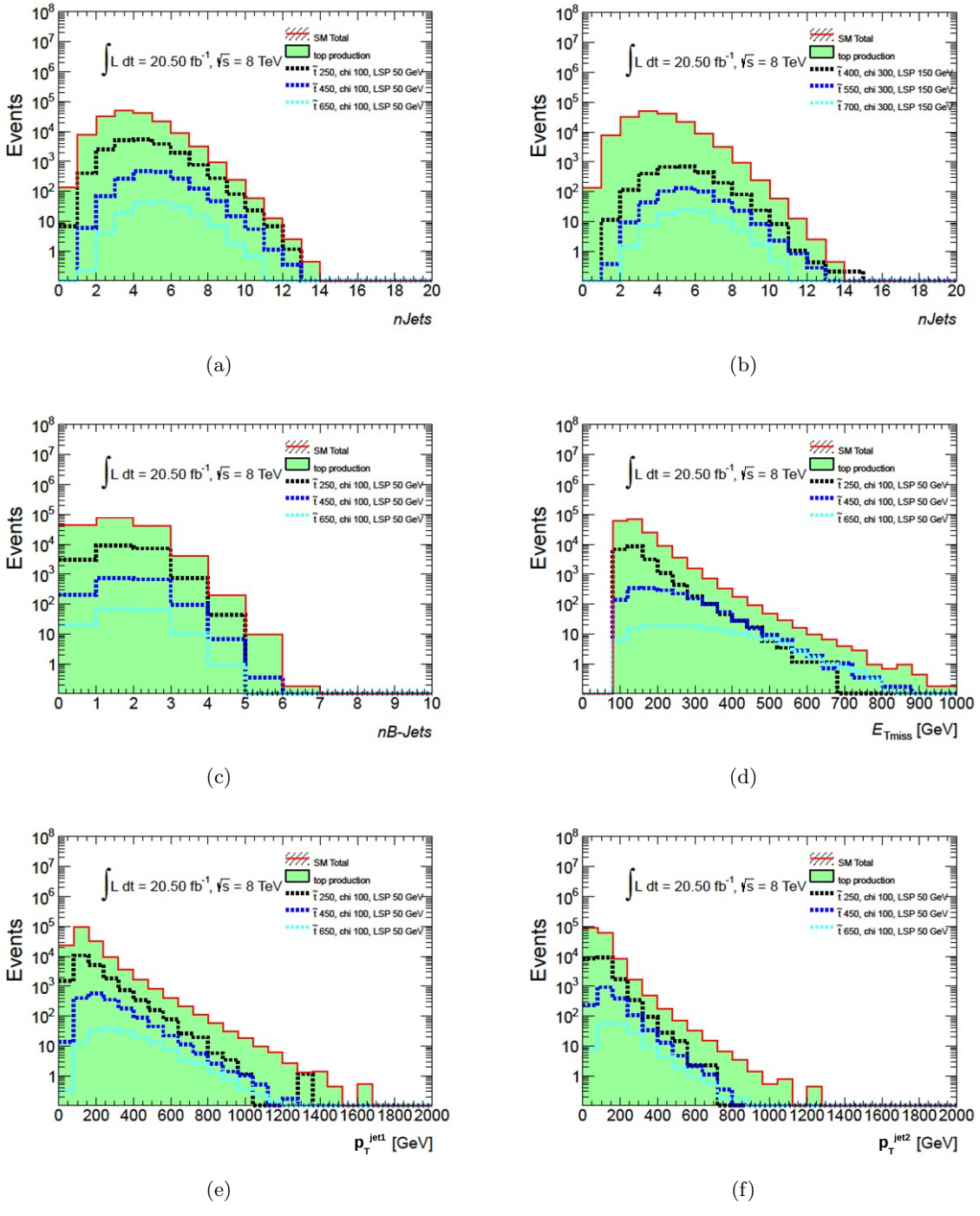

Figure 6.5: *Distributions of kinematic variables for $t\bar{t}$ background (green) and signal samples from the tN1bC1 Grid (dashed lines): (a) and (b) number of jets, (c) number of b-tagged jets, (d) E_T^{miss}, (e) leading jet p_T, (f) sub-leading jet p_T for events with no leptons and $E_T^{miss} > 80$ GeV.*

SRC Selections

The selections of the signal regions described so far have been optimised under the strong assumption that the stop decays into a top quark and a neutralino with 100% BR. Under the hypotheses made on the signal considered in this analysis, the stop is very likely to decay also into a b-quark and a chargino. As the branching ratio in this second decay mode becomes important, the sensitivity of SRA and SRB rapidly decrease. A dedicated selection that recovers the sensitivity in a scenario where both decay modes are possible is therefore needed.

On contrast to SRA and SRB (which have been optimised on the tN1tN1 Grid), SRC has been optimised on the tN1bC1 Grid. The first important distinction between these two cases is that in the latter the signal samples are characterised by the presence of only one top quark decaying into hadrons. Reconstructing two top masses to reject semi-leptonically decaying $t\bar{t}$ pairs is therefore not possible, and different discriminating variables must be found.

In case the mass difference between the $\widetilde{\chi}_1^{\pm}$ and the $\widetilde{\chi}_1^0$ is small, it is very likely that the jet multiplicity expected from a fully hadronic decay of the signal is reduced. Figure 6.5 shows a comparison of the properties of different benchmark signal points and of the $t\bar{t}$ background for a selection vetoing leptons in the final state and requiring a minimum amount of $E_{\mathrm{T}}^{\mathrm{miss}}$ of 80 GeV (compatible with the trigger requirement at Event Filter level). The top row shows the distribution of the number of jets for signals with $m(\widetilde{\chi}_1^{\pm}) =$ 100 GeV and $m(\widetilde{\chi}_1^0) = 50$ GeV (Figure 6.5(a)) or $m(\widetilde{\chi}_1^{\pm}) = 100$ GeV and $m(\widetilde{\chi}_1^0) = 50$ GeV (Figure 6.5(b)), with varying $m(\tilde{t}_1)$. By comparing these figures it is possible to note that for stop masses of similar values, signal samples with smaller mass difference between the $\widetilde{\chi}_1^{\pm}$ and the $\widetilde{\chi}_1^0$ are characterised by a lower jet multiplicity. To increase the acceptance of SRC to the signal, the requirement on the number of jets has been reduced from six to five. This choice allows to retain a high fraction of signal maintaining the amount of background to a tolerable level. Figure 6.5(c) shows the distribution of the number of b-tagged jets. Most of the events have one or two b-tagged jets. Since the ratio between signal and $t\bar{t}$ events is higher in the two b-tagged jets bin, events with two b-tagged jets are selected. Figure 6.5(d) shows that $E_{\mathrm{T}}^{\mathrm{miss}}$ cannot be used as main discriminating variable, on contrast to the tN1tN1 case. Figures 6.5(e) and 6.5(f), displaying the leading and sub-leading jet p_{T}, show that the jets of the signal tend to be softer than the background ones.

Different kinematic quantities have been studied to identify those more suitable in discriminating between signal and background.
As for the other signal regions, $\mathrm{m_T}\left(b_{\min[\Delta\phi(b,E_{\mathrm{T}}^{\mathrm{miss}})]}, E_{\mathrm{T}}^{\mathrm{miss}}\right)$ is a good variable to reject semi-leptonically decaying $t\bar{t}$ pairs. Its distribution for events passing the preselection criteria plus the requirement of exactly five jets is shown in Figure 6.6(a). Further discrimi-

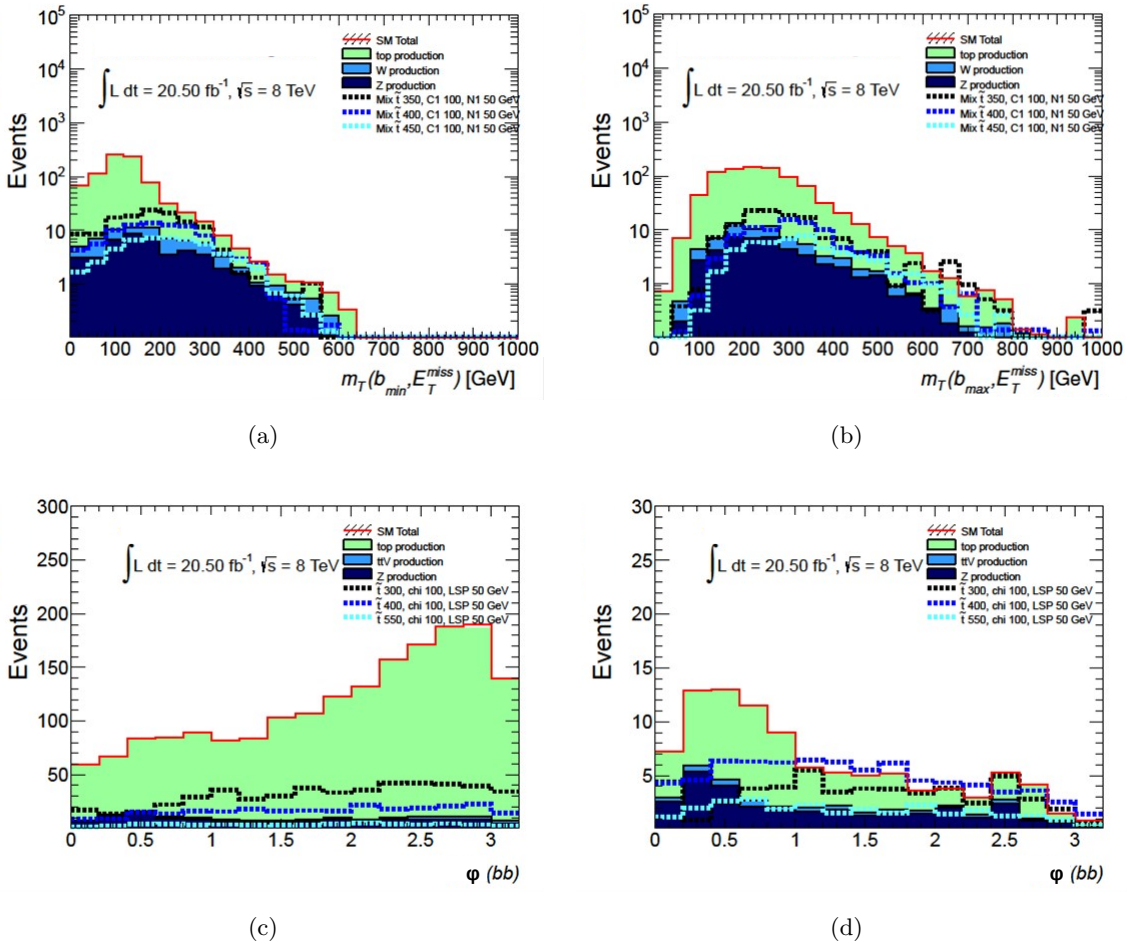

Figure 6.6: *Background and signal distributions of (a)* $\mathrm{m_T}\left(b_{\min[\Delta\phi(b,E_T^{miss})]}, E_T^{miss}\right)$*, (b)* $\mathrm{m_T}\left(b_{\max[\Delta\phi(b,E_T^{miss})]}, E_T^{miss}\right)$*, (c)* $|\Delta\phi(b,b)|$ *for events with no leptons and five jets, and (d)* $|\Delta\phi(b,b)|$ *for events with no leptons, five jets and* $\mathrm{m_T}\left(b_{\min[\Delta\phi(b,E_T^{miss})]}, E_T^{miss}\right) > 175$ *GeV.*

	SRC1	**SRC2**	**SRC3**
jets	5, $p_{\mathrm{T}} > 80, 80, 35, 35, 35\,\mathrm{GeV}$		
$\lvert\Delta\phi\,(b,b)\rvert$	$> 0.2\pi$		
$\mathrm{m_T}\left(b_{\mathrm{min}[\Delta\phi\left(b,E_{\mathrm{T}}^{\mathrm{miss}}\right)]}, E_{\mathrm{T}}^{\mathrm{miss}}\right)$	$> 185\,\mathrm{GeV}$	$> 200\,\mathrm{GeV}$	$> 200\,\mathrm{GeV}$
$\mathrm{m_T}\left(b_{\mathrm{max}[\Delta\phi\left(b,E_{\mathrm{T}}^{\mathrm{miss}}\right)]}, E_{\mathrm{T}}^{\mathrm{miss}}\right)$	$> 205\,\mathrm{GeV}$	$> 290\,\mathrm{GeV}$	$> 325\,\mathrm{GeV}$
τ veto	applied		
$E_{\mathrm{T}}^{\mathrm{miss}}$	$> 160\,\mathrm{GeV}$	$> 160\,\mathrm{GeV}$	$> 215\,\mathrm{GeV}$

Table 6.4: *Selection criteria for the three sets of selections of SRC.*

nation is provided by the variable $\mathrm{m_T}\left(b_{\mathrm{max}[\Delta\phi\left(b,E_{\mathrm{T}}^{\mathrm{miss}}\right)]}, E_{\mathrm{T}}^{\mathrm{miss}}\right)$ shown in Figure 6.6(b), the transverse mass built with $E_{\mathrm{T}}^{\mathrm{miss}}$ and the furthest b-tagged jet from $E_{\mathrm{T}}^{\mathrm{miss}}$, that acquires higher values as the mass of the $\tilde{t}_1$ increases.

Z bosons decaying into neutrinos produced in association with heavy flavour jets is also a potentially relevant background. To reject it, the ϕ separation between the b-tagged jets can be exploited. Unlike the b-jets of the signal or of the $t\bar{t}$ background, which are produced in the decay chain, the b-jets produced in association with Z bosons are mainly produced via splitting of an ISR gluon into a $b\bar{b}$ pair. These b-jets are close to each other, as can be seen from Figure 6.6(c), showing the ϕ separation between the b-tagged jets ($\lvert\Delta\phi\,(b,b)\rvert$) for events with five jets passing the preselection. Figure 6.6(d) shows the same variable for a selection including $\mathrm{m_T}\left(b_{\mathrm{min}[\Delta\phi\left(b,E_{\mathrm{T}}^{\mathrm{miss}}\right)]}, E_{\mathrm{T}}^{\mathrm{miss}}\right) > 175$ GeV. Comparing the two distributions it is possible to note that the selection on $\mathrm{m_T}\left(b_{\mathrm{min}[\Delta\phi\left(b,E_{\mathrm{T}}^{\mathrm{miss}}\right)]}, E_{\mathrm{T}}^{\mathrm{miss}}\right)$ forces both signal and background towards lower values, but the discriminating power of the variable remains high. The selection $\lvert\Delta\phi\,(b,b)\rvert > 0.2\pi$ has been found to be the best compromise between background rejection and signal efficiency.

The final optimisation of the selections has been carried out by considering the variables $\mathrm{m_T}\left(b_{\mathrm{min}[\Delta\phi\left(b,E_{\mathrm{T}}^{\mathrm{miss}}\right)]}, E_{\mathrm{T}}^{\mathrm{miss}}\right)$, $\mathrm{m_T}\left(b_{\mathrm{max}[\Delta\phi\left(b,E_{\mathrm{T}}^{\mathrm{miss}}\right)]}, E_{\mathrm{T}}^{\mathrm{miss}}\right)$ and $E_{\mathrm{T}}^{\mathrm{miss}}$. The selections reported in Table 6.4 have been identified. The different signal regions target signals of increasing stop masses in the range 250-550 GeV, getting more stringent as the addressed stop mass increases.

Figure 6.7 shows the distribution of the discriminating variables at different stages of SRC2 selection. All the background components are shown together with two benchmark signal points.

A comparison between the background expectation as predicted by Monte Carlo simulation and the data for events passing the preselection requirement, jet and $\lvert\Delta\phi\,(b,b)\rvert$ selection is shown in Figure 6.8.

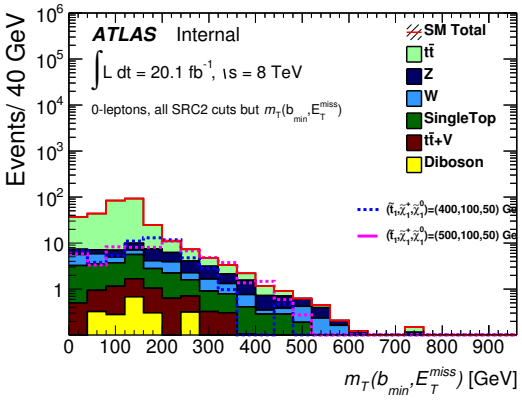

(a)

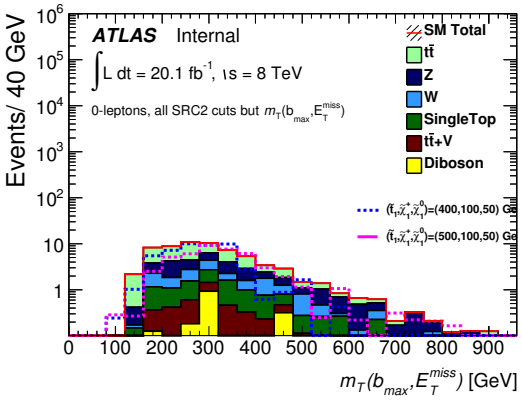

(b)

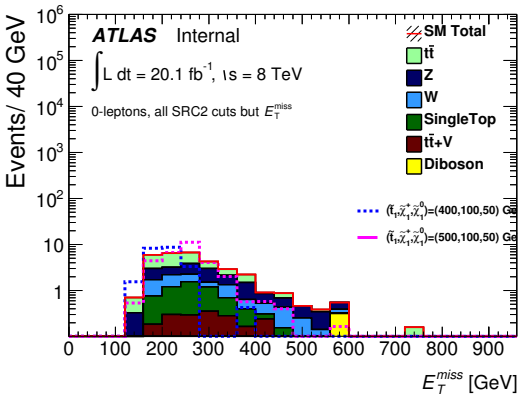

(c)

Figure 6.7: *Background and signal distributions of (a)* $\mathrm{m_T}\left(b_{\min[\Delta\phi(b,E_T^{miss})]}, E_T^{miss}\right)$*, (b)* $\mathrm{m_T}\left(b_{\max[\Delta\phi(b,E_T^{miss})]}, E_T^{miss}\right)$*, (c)* E_T^{miss} *at different stages of the SRC2 selection, specified in the plots.*

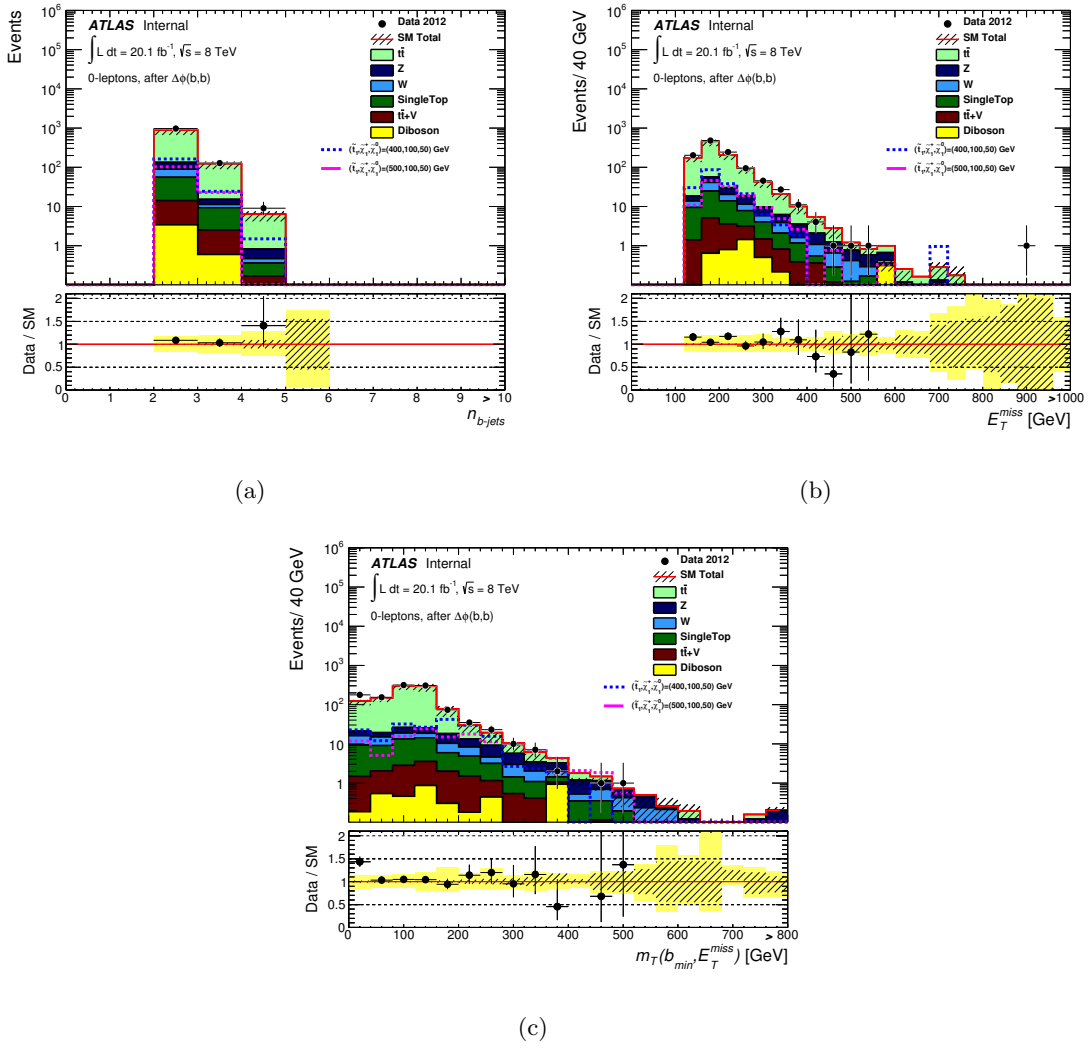

(a)

(b)

(c)

Figure 6.8: *Distribution of (a) the number of b-tagged jets, (b) E_T^{miss}, (c) $\mathrm{m_T}\left(b_{\min[\Delta\phi(b,E_T^{miss})]}, E_T^{miss}\right)$ for the events passing the jets and $|\Delta\phi\,(b,b)|$ selections of SRC. The stacked histograms show the Standard Model expectation from simulation compared to the data (points). Simulated signal samples of the tN1bC1 Grid, where $m_{\tilde{t}_1} = 400$ GeV, $m_{\widetilde{\chi}_1^0} = 50$ GeV (blue dashed line) and $m_{\tilde{t}_1} = 500$ GeV, $m_{\widetilde{\chi}_1^0} = 50$ GeV (pink line), are overlaid. The "Data/SM" plot shows the ratio of data events to the total Standard Model expectation. The rightmost bin includes all overflows. The hatched uncertainty band around the Standard Model expectation shows the statistical uncertainty and the yellow band (shown only for the "Data/SM" plot) shows the combination of statistical and experimental systematic uncertainties.*

6.3 Background Estimation

The most relevant background sources are top pairs decaying semi-leptonically ($t\bar{t}$), Z bosons produced in association with heavy flavour jets decaying into neutrinos (Z+HF), W bosons produced in association with heavy flavour jets (W+HF). Minor backgrounds are $t\bar{t}$ pairs produced in association with a Z or a W boson ($t\bar{t}$+V), associated production of Z and W bosons (VV), single top production (single top), and production of QCD multi-jets events.

Top quarks pair production is simulated with POWHEG [68]. POWHEG is used also to simulate single top production in the s- and Wt-channels, while AcerMC [69] is used for the t-channel. SHERPA [65] is used to simulate single and associate production of W and Z bosons. $t\bar{t}$ produced in association with a W or a Z boson is simulated with MadGraph [71].

All the background components have been normalised to the highest order calculation available of their cross section.

The relative importance of the background components depends on the type of signal region considered. Tables 6.5, 6.6 and 6.7 show the yield of background events as predicted by Monte Carlo in SRA, SRB and SRC, together with some benchmark signal models targeted by each signal region.

According to the analysis strategy described in Section 4.2, the most relevant backgrounds are estimated with semi-data-driven techniques, minor backgrounds are evaluated with Monte Carlo simulation, while the contribution from QCD multi-jet events is determined with a data-driven technique.

Process	**SRA1**	**SRA2**	**SRA3**	**SRA4**
Z+HF	1.5 ± 0.3	0.68 ± 0.15	0.82 ± 0.21	0.72 ± 0.15
W+HF	0.95 ± 0.24	0.46 ± 0.17	0.67 ± 0.20	0.06 ± 0.05
$t\bar{t}$	10.4 ± 0.8	1.9 ± 0.3	2.6 ± 0.4	0.54 ± 0.16
single top	1.0 ± 0.2	0.3 ± 0.1	0.36 ± 0.10	0.31 ± 0.10
$t\bar{t}+V$	1.8 ± 0.1	0.85 ± 0.06	0.98 ± 0.07	0.50 ± 0.05
VV	0.00 ± 0.00	0.00 ± 0.00	0.00 ± 0.00	0.32 ± 0.32
Total SM	16.0 ± 0.9	4.2 ± 0.4	5.5 ± 0.5	2.1 ± 0.3
$(m(\tilde{t}_1), m(\tilde{\chi}_1^0)) = (400, 1)$ GeV	39.9 ± 2.0	22.2 ± 1.5	25.0 ± 1.6	4.0 ± 0.7
$(m(\tilde{t}_1), m(\tilde{\chi}_1^0)) = (600, 1)$ GeV	8.1 ± 0.2	6.9 ± 0.1	6.3 ± 0.1	6.8 ± 0.1
$(m(\tilde{t}_1), m(\tilde{\chi}_1^0)) = (700, 1)$ GeV	3.0 ± 0.2	2.8 ± 0.2	2.5 ± 0.2	3.3 ± 0.2

Table 6.5: *Background and signal yields from Monte Carlo simulation in SRA, normalised to an integrated luminosity of 20.3 fb^{-1}. The signal samples belong to the tN1tN1 Grid.*

Process	**SRB1**	**SRB2**	**Combined**
Z+HF	0.69 ± 0.11	0.46 ± 0.08	1.2 ± 0.1
W+HF	0.40 ± 0.15	0.07 ± 0.05	0.47 ± 0.16
$t\bar{t}+V$	0.32 ± 0.04	0.15 ± 0.03	0.47 ± 0.05
$t\bar{t}$	0.00 ± 0.00	0.10 ± 0.06	0.10 ± 0.06
single top	0.02 ± 0.02	0.06 ± 0.04	0.08 ± 0.05
VV	0.02 ± 0.02	0.00 ± 0.00	0.02 ± 0.02
Total SM	1.5 ± 0.2	0.84 ± 0.13	2.3 ± 0.2
$(m(\tilde{t}_1), m(\tilde{\chi}_1^0)) = (700, 1)$ GeV	1.8 ± 0.1	1.1 ± 0.1	2.9 ± 0.2

Table 6.6: *Background and signal yields from Monte Carlo simulation in SRB, normalised to an integrated luminosity of 20.3 fb^{-1}. The signal samples belong to the tN1tN1 Grid.*

6.3.1 $t\bar{t}$ Background Estimation

Semi-leptonically decaying $t\bar{t}$ pairs are a relevant background in SRA and SRC, up to about 65% and 45%, respectively. This Standard Model background passes the signal selection if the lepton is either an electron or a muon misidentified as a jet, or a tau decaying into hadrons. A negligible fraction of events has the electron or the muon falling out of the detector acceptance. $t\bar{t}$ pairs decaying into hadrons are a minor source of background, due to the strong requirements on the presence of $E_{\mathrm{T}}^{\mathrm{miss}}$ in the final state.

To estimate the background from $t\bar{t}$ pairs, a CR with either one electron or one muon has been defined. This choice allows to derive the normalisation factor specific to one of the main components of the $t\bar{t}$ background entering the signal regions, thus allowing to reduce the impact of the systematic uncertainties. The selected lepton is treated as a jet in the control sample selection process, as it were misidentified.

Events containing an electron are required to fire the electron trigger with the lowest p_{T} threshold. Similarly, the events containing a muon are required to fire the muon trigger with the lowest p_{T} threshold. As jets, electrons and muons must have $p_{\mathrm{T}} > 35$ GeV. This minimum value also ensures a high efficiency of the triggers. Muons and electrons must be isolated from other final state objects. In addition, electrons must satisfy the Tight identification criteria described in Section 3.5.

Three control regions with different jet multiplicities have been defined, reflecting the jet multiplicities of each of the signal regions. The selection criteria for each of them have been chosen to resemble as much as possible the signal region for which the $t\bar{t}$ background normalisation must be derived, while ensuring the minimum contamination from signal and other background components. Table 6.8 summarises the selections applied to define the control regions, denoted as CRTopA, CRTopB and CRTopC.

Process	**SRC1**	**SRC2**	**SRC3**
Z+HF	14.8 ± 0.9	8.5 ± 0.7	5.7 ± 0.5
W+HF	8.5 ± 0.9	4.8 ± 0.8	2.8 ± 0.4
$t\bar{t}$	30.4 ± 1.2	12.2 ± 0.8	6.3 ± 0.6
single top	7.3 ± 0.6	4.5 ± 0.4	2.8 ± 0.3
$t\bar{t}+V$	3.3 ± 0.1	1.9 ± 0.1	1.3 ± 0.1
VV	1.1 ± 0.6	0.42 ± 0.33	0.42 ± 0.33
Total SM	65.3 ± 2.0	32.3 ± 1.4	19.4 ± 1.0
$(m(\tilde{t}_1, \tilde{\chi}_1^0)) = (300, 50)$ GeV	57.1 ± 7.7	26.1 ± 3.4	9.2 ± 3.1
$(m(\tilde{t}_1, \tilde{\chi}_1^0)) = (400, 50)$ GeV	52.3 ± 5.2	32.2 ± 4.0	18.5 ± 3.0
$(m(\tilde{t}_1, \tilde{\chi}_1^0)) = (500, 50)$ GeV	26.1 ± 3.4	16.1 ± 2.6	12.6 ± 2.4

Table 6.7: *Background and signal yields from Monte Carlo simulation in SRC, normalised to an integrated luminosity of 20.3 fb^{-1}. The signal samples belong to the tN1bC1 Grid.*

	CRTopA	**CRTopB**	**CRTopC**
Trigger	electron or muon		
N_{lep}	1		
p_T^{lep}	$> 35\,\text{GeV}$		
N_{jet}	$\geqslant 6$	4 or 5	5
$N_{\text{b-jet}}$	$\geqslant 2$		
$\lvert\Delta\phi\left(\text{jet}, E_{\text{T}}^{\text{miss}}\right)\rvert$	$> \pi/10$		
$\text{m}_{\text{T}}\left(b_{\min[\Delta\phi\left(b, E_{\text{T}}^{\text{miss}}\right)]}, E_{\text{T}}^{\text{miss}}\right)$	$> 125\,\text{GeV}$	–	$> 150\,\text{GeV}$
$\text{m}_{\text{T}}\left(b_{\min[\Delta\phi\left(b, E_{\text{T}}^{\text{miss}}\right)]}, E_{\text{T}}^{\text{miss}}\right)$	–	–	$> 125\,\text{GeV}$
$\text{m}_{\text{T}}\left(\ell, E_{\text{T}}^{\text{miss}}\right)$	$[40, 120]\,\text{GeV}$		
$\lvert\Delta\phi\left(b, b\right)\rvert$	–	–	$> 0.2\pi$
Top reconstruction	m_{bjj}^0 or $m_{bjj}^1 < 600\,\text{GeV}$	$\geqslant 2$ $R = 1.2$ RC jets	–
$E_{\text{T}}^{\text{miss}}$	$> 150\,\text{GeV}$	$> 150\,\text{GeV}$	$> 100\,\text{GeV}$

Table 6.8: *Summary of the selection criteria of the three control regions CRTopA, CRTopB and CRTopC for the $t\bar{t}$ background.*

The composition of the control regions as predicted by Monte Carlo simulation is given in Table 6.9, together with the number of events observed in data. The signal contamination has been checked and found to be below 1%, therefore it can be considered to be negligible. The resulting normalisation factors are $N_{\text{CRTopA}} = 1.23 \pm 0.10$, $N_{\text{CRTopB}} = 0.99 \pm 0.04$ and $N_{\text{CRTopC}} = 1.06 \pm 0.08$, where the uncertainties include only the statistical

component.

Figure 6.9 shows different kinematic distributions for data and Monte Carlo in the different top control regions, with the normalisation factors for the $t\bar{t}$ background and for the Z and W bosons backgrounds (see Sections 6.3.4 and 6.3.2) applied. The agreement observed between data and simulation is overall good for all the control regions.

	CRTopA	**CRTopB**	**CRTopC**
Data	247	205	313
$t\bar{t}$	160.7 ± 2.8	153.6 ± 2.8	226.0 ± 3.5
single top	24.6 ± 1.0	22.4 ± 1.3	40.5 ± 1.3
W+HF	20.0 ± 1.1	13.5 ± 1.6	28.4 ± 1.5
$t\bar{t}$	1.4 ± 0.5	1.7 ± 0.7	2.5 ± 0.8
$t\bar{t}+V$	3.6 ± 0.1	0.56 ± 0.06	2.2 ± 0.1
Z+HF	0.31 ± 0.15	0.01 ± 0.01	0.17 ± 0.08
Total MC	213.1 ± 3.4	191.7 ± 3.5	299.9 ± 4.1

Table 6.9: *Event yields in the different control regions CRTop for the $t\bar{t}$ background normalised to a luminosity of 20.3 fb^{-1} and summed over electrons and muons.*

6.3.2 *W* Boson Background Estimation

Similarly to the case of $t\bar{t}$, also the W boson produced in association with jets and decaying into a lepton and a neutrino can enter the signal regions if the lepton is misidentified with a jet. Due to its reduced jet multiplicity, this background source is particularly important in SRB and therefore a control region to check the correct normalisation of the MC simulation must be defined.

The requirements to define the control region for the W boson (CRW) are similar to those of the $t\bar{t}$ control region: an electron or muon is selected, that is treated as a jet in the selection process. The b-tagged jet multiplicity is reduced to one in order to enhance the W boson contribution over $t\bar{t}$. Other requirements meant to reduce the $t\bar{t}$ contamination are applied: only the region $\mathcal{A}_{m_t} < 0.5$ is selected, and the mass of the leading anti-k_T $R = 1.2$ re-clustered jet is required to be less than 40 GeV. The full list of selection criteria is summarised in Table 6.10.

Table 6.11 shows the yield of events for each background component in CRW as predicted by Monte Carlo simulation, together with the number of events observed in data. The contamination from $t\bar{t}$ is relevant, but the normalisation factor for the W boson has been computed taking into account the normalisation factor for the $t\bar{t}$ background (which is very close to one). The resulting factor is $N_{\mathrm{CRW}} = 1.03 \pm 0.24$.

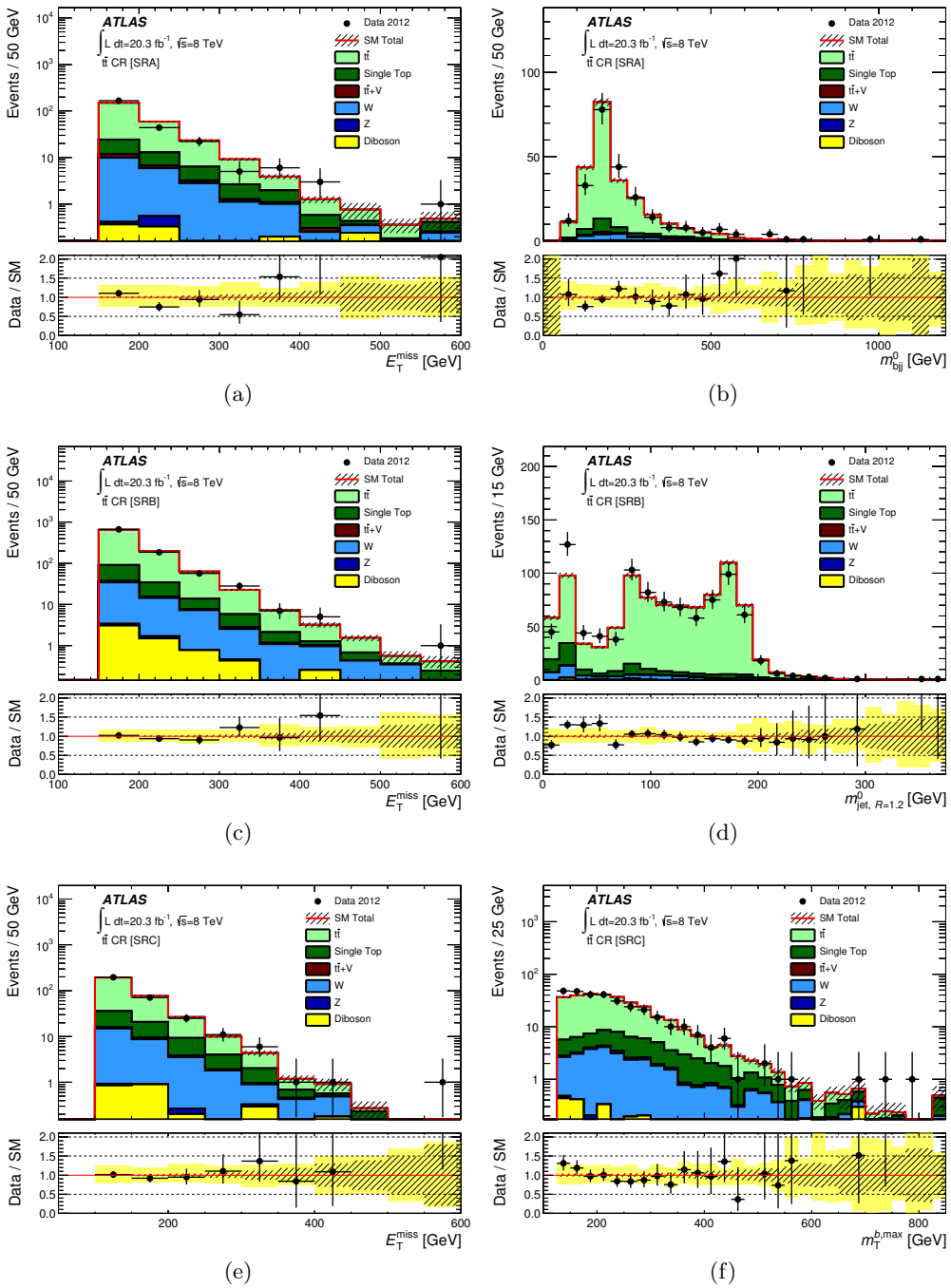

Figure 6.9: *Distributions of (a) E_T^{miss} and (b) m^0_{bjj} in CRTopA, (c) E_T^{miss} and (d) m^0_{AkT12} in CRTopB, and (e) E_T^{miss} and (f) $\mathrm{m_T}\left(b_{\max[\Delta\phi(b,E_T^{miss})]}, E_T^{miss}\right)$ in CRTopC. All kinematic quantities were recalculated after treating the lepton as a jet. The stacked histograms show the Standard Model expectation, normalised using the factors summarised in Table 6.28. The "Data/SM" plots show the ratio of data events to the total Standard Model expectation. The rightmost bin includes all overflows. The hatched uncertainty band around the Standard Model expectation shows the statistical uncertainty and the yellow band (shown only for the "Data/SM" plots) shows the combination of statistical and detector-related systematic uncertainties.*

	CRW
Trigger	electron or muon
N_{lep}	1
p_T^{lep}	$> 35\,\text{GeV}$
N_{jet}	4 or 5
$N_{\text{b-jet}}$	$\geqslant 2$
$\lvert\Delta\phi\left(\text{jet}, E_{\text{T}}^{\text{miss}}\right)\rvert$	$> \pi/10$
$\text{m}_{\text{T}}\left(\ell, E_{\text{T}}^{\text{miss}}\right)$	$[40, 120]\,\text{GeV}$
Top reconstruction	$\geqslant 2$ $R = 1.2$ RC jets
$E_{\text{T}}^{\text{miss}}$	$> 150\,\text{GeV}$
$\mathcal{A}_{m_t}$	< 0.5
$m^0_{AkT12}[\,\text{GeV}\,]$	< 40

Table 6.10: *Summary of the selection criteria of the control region CRW for the W boson background.*

	CRW
Data	340
VV	10.6 ± 1.7
$t\bar{t}$+V	0.8 ± 0.1
W+HF	182.9 ± 6.3
single top	39.9 ± 2.1
$t\bar{t}$	189.5 ± 3.0
Z+HF	1.3 ± 0.4
Total MC	435.1 ± 7.5

Table 6.11: *Event yields in the control region CRW for the W boson, normalised to a luminosity of 20.3 fb^{-1} and summed over electrons and muons.*

Figure 6.10 shows the distribution of two of the discriminating variables of SRB in CRW.

6.3.3 Multi-jet Background Estimation

The background from generic multi-jet QCD events (including fully hadronic decaying $t\bar{t}$) enters the signal regions mainly because of mis-measurements of the jet energies resulting in high values of $E_{\mathrm{T}}^{\mathrm{miss}}$. These effects cannot be predicted with a Monte Carlo simulation, therefore a data-driven technique must be employed (see the discussion in Section 4.2). The method adopted in this analysis is the jet-smearing technique described in Ref. [134]. A sample of well measured multi-jet events is selected in data by requiring low values of $E_{\mathrm{T}}^{\mathrm{miss}}/\sqrt{\sum E_T}$ (being $\sum E_T$ the scalar sum of the transverse energy of all the objects in the event). The momentum and ϕ direction of the jets are then smeared by separate response functions for light and heavy flavour jets determined with PYTHIA, emulating the calorimeter response. The sample of smeared events is used to estimate the background after normalizing it to data in a control region dominated by multi-jet events.

The control region (CRQCD) is characterised by the same jet multiplicity as the signal regions, the same number of b-tagged jets and the same $E_{\mathrm{T}}^{\mathrm{miss,track}}$ requirement. The selection applied to the signal regions to reject multi-jet QCD events are reverted to enhance their contribution: the events are required to have either $\min\left|\Delta\phi\left(\mathrm{jet}^{0-2}, E_{\mathrm{T}}^{\mathrm{miss}}\right)\right| < 0.2\pi$ or $\left|\Delta\phi\left(E_{\mathrm{T}}^{\mathrm{miss}}, E_{\mathrm{T}}^{\mathrm{miss,track}}\right)\right| > \pi/3$. The selections of each control region are summarised in Table 6.12.

	CRQCDA	**CRQCDB**	**CRQCDC**
N_{jet}	$\geqslant 6$	4 or 5	5
$N_{\mathrm{b-jet}}$	$\geqslant 2$		
$E_{\mathrm{T}}^{\mathrm{miss,track}}$	$> 30\,\mathrm{GeV}$		
QCD Selection	$\left\|\Delta\phi\left(\mathrm{jet}, E_{\mathrm{T}}^{\mathrm{miss}}\right)\right| > \pi/10$ or $\min\left\|\Delta\phi\left(\mathrm{jet}^{0-2}, E_{\mathrm{T}}^{\mathrm{miss}}\right)\right| < 0.2\pi$		
$E_{\mathrm{T}}^{\mathrm{miss}}$	$> 150\,\mathrm{GeV}$	$> 150\,\mathrm{GeV}$	$> 100\,\mathrm{GeV}$

Table 6.12: *Summary of the selection criteria of the control region CRQCD for the QCD multi-jet background.*

Figure 6.11 shows the good agreement between data and simulations obtained on the distributions of $\min\left|\Delta\phi\left(\mathrm{jet}^{0-2}, E_{\mathrm{T}}^{\mathrm{miss}}\right)\right|$ and $\left|\Delta\phi\left(E_{\mathrm{T}}^{\mathrm{miss}}, E_{\mathrm{T}}^{\mathrm{miss,track}}\right)\right|$ in CRQCD before applying the cut on these variables.

The estimation of multi-jet and fully hadronic $t\bar{t}$ background contributions in the signal regions is made applying all the signal region requirements to the sample of smeared events after normalisation. Table 6.13 shows the estimated yield of multi-jet and all-hadronic $t\bar{t}$

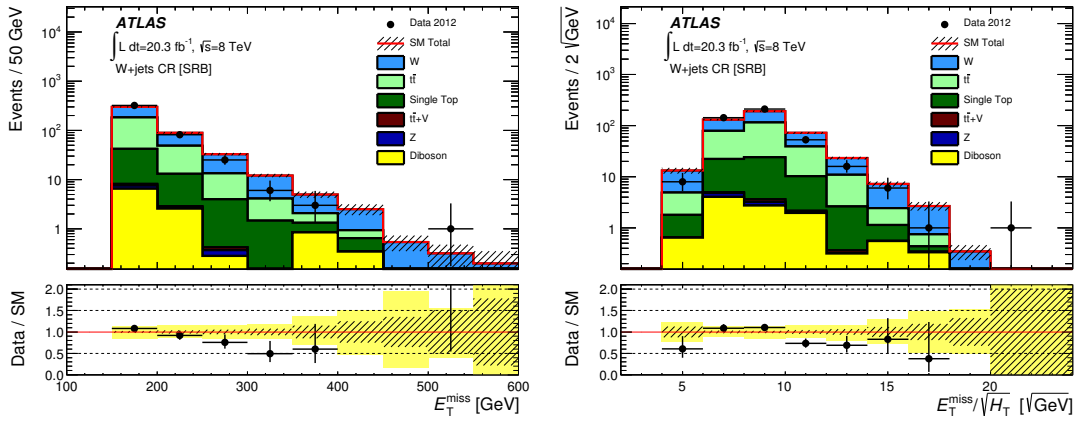

(a) (b)

Figure 6.10: *The (a) E_T^{miss} and (b) H_T^{sig} distributions in CRW. All kinematic quantities were recalculated after treating the lepton as a jet. The stacked histograms show the Standard Model expectation, normalised using the factors summarised in Table 6.28. The "Data/SM" plots show the ratio of data events to the total Standard Model expectation. The rightmost bin includes all overflows. The hatched uncertainty band around the Standard Model expectation shows the statistical uncertainty and the yellow band (shown only for the "Data/SM" plots) shows the combination of statistical and detector-related systematic uncertainties.*

events in the different signal regions.

Signal region	Estimated background
SRA1	0.005 ± 0.001
SRA2	< 0.0006
SRA3	< 0.0006
SRA4	< 0.0006
SRB1	< 0.001
SRB2	< 0.001
SRC1	0.24 ± 0.01
SRC2	0.06 ± 0.001
SRC3	0.009 ± 0.002

Table 6.13: *Estimated background from QCD multi-jets and all-hadronic $t\bar{t}$ in all signal regions. The uncertainties shown are statistical only.*

6.3.4 *Z* Boson Background Estimation

Estimation Technique

Z bosons produced in association with heavy flavour jets and decaying into neutrinos are a natural background to this search. This source of background becomes more relevant as the selection on $E_{\mathrm{T}}^{\mathrm{miss}}$ or other discriminating variables is tightened.

A possible normalisation bias can be estimated by the use of a $Z \to \ell\ell$ control sample (where the lepton ℓ can be either an electron or a muon). This decay mode has the advantage of making easy the selection of pure samples of Z bosons by computing the invariant mass of the two leptons. However, it is characterised by a lower branching fraction than the relevant background.

In this analysis the number of Z boson events is reduced by the following signal regions requirements:

- The $E_{\mathrm{T}}^{\mathrm{miss}}$ selection (which is effectively the Z boson p_{T}).
- The high jet multiplicity requirement.
- The requirement on the number of b-tagged jets.

These selections make any attempt of building a control sample of $Z \to \ell\ell$ have very few events in it. To mitigate this problem, the $Z \to \ell\ell$ control regions (one for each jet multiplicity) have been defined by dropping the requirement on the number of b-tagged

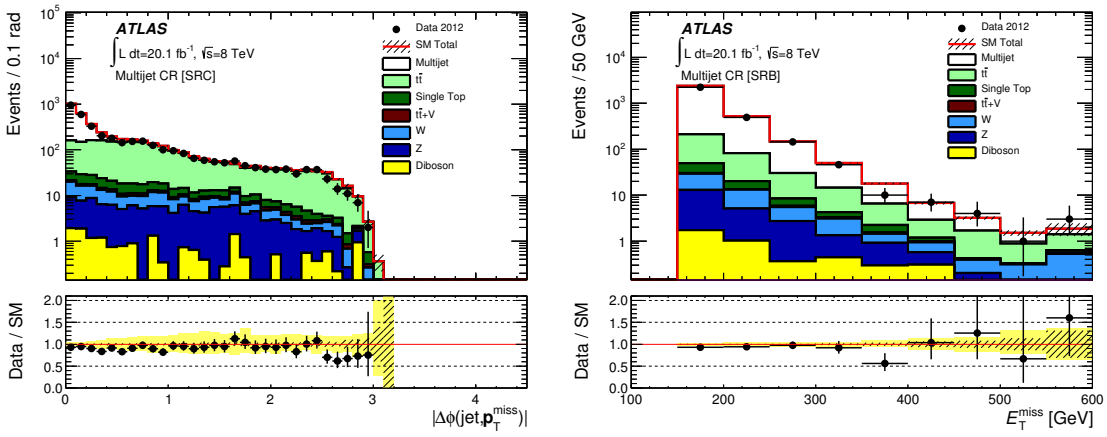

(a) (b)

Figure 6.11: *Distributions of (a) $\left|\Delta\phi\left(\text{jet}, E_T^{miss}\right)\right|$ in the multi-jet control region for SRC and (b) E_T^{miss} in the multi-jet control region for SRB. The stacked histograms show the Standard Model expectations, normalised using the factors summarised in Table 6.28. The "Data/SM" plots show the ratio of data events to the total Standard Model expectation. The rightmost bin includes all overflows. The hatched uncertainty band around the Standard Model expectation shows the statistical uncertainty and the yellow band (shown only for the "Data/SM" plots) shows the combination of statistical and detector-related systematic uncertainties.*

jets. The fraction of events with two b-tagged jets are then predicted by the use of a fitting procedure described later in this section. The advantage of this method is a reduced uncertainty with respect to the uncertainty that would result from using a control sample with a low number of events, as shown at the end of this section.

Since the b-tagging requirement is not applied directly to the control regions, it is not possible to apply all the selection cuts defining the signal regions and thus carry on a fully data-driven estimation. Instead, a semi data-driven method is employed. Once the fraction of events with two b-tagged jets has been derived both for data and Z boson Monte Carlo prediction, the factors are applied to the yield in the control regions and the residual normalisation bias evaluated.

The exact definition of the Z boson control sample, CRZ, is as follows:

1. Either the electron or the muon trigger with the lowest p_{T} threshold must be fired.

2. Exactly two electrons or muons with opposite charge are selected, with p_{T} of the leading lepton larger than 25 GeV and p_{T} of the sub-leading lepton larger than 10 GeV. The electron and muon definitions are the same adopted for CRTop (see

Subsection 6.3.1).

3. To reduce the contamination from $t\bar{t}$ pairs, an upper cut on $E_{\mathrm{T}}^{\mathrm{miss}}$ of 50 GeV is applied.

4. The transverse momentum of the selected leptons is removed from the computation of $E_{\mathrm{T}}^{\mathrm{miss}}$ in order to treat them as if they were neutrinos (and therefore not interacting with the detector material). The new quantity obtained, called $E_{\mathrm{T}}^{\mathrm{miss}\prime}$, is required to have values larger than 70 GeV, to get as close as possible to the signal regions, while maintaining enough events in the control region.

5. The di-lepton invariant mass must be in the range 86-96 GeV, to bring the contamination from non Z boson backgrounds and signal to a negligible level (crucial requirement for the fitting procedure discussed below).

The selected events are then split based on their jet multiplicity. The events with exactly four, five and six jets are labelled respectively as CRZ4, CRZ5 and CRZ6. They are used to predict the Z boson background in SRB1 (CRZ4), SRB1, SRB2 and SRC (CRZ5) and SRA (CRZ6).

A summary of the selections to define CRZ and of the subsequent categorisation in CRZ4, CRZ5 and CRZ6 is given in Table 6.14.

	CRZ		
Trigger	electron or muon		
N_{lep}	2		
p_T^{lep1}	$> 25\,\mathrm{GeV}$		
p_T^{lep2}	$> 10\,\mathrm{GeV}$		
$m(\ell\ell)$	$[86, 96]\,\mathrm{GeV}$		
$E_{\mathrm{T}}^{\mathrm{miss}}$	$< 50\,\mathrm{GeV}$		
$E_{\mathrm{T}}^{\mathrm{miss}\prime}$	$> 70\,\mathrm{GeV}$		
	CRZ4	**CRZ5**	**CRZ6**
N_{jet}	4	5	6

Table 6.14: *Summary of the CRZ selections and categorisation in CRZ4, CRZ5 and CRZ6.*

Before deriving the normalisation factors by comparing the Z boson Monte Carlo prediction to the data in CRZ4, CRZ5 and CRZ6, the fraction of events with two b-tagged jets must be derived.

A study based on simulation of Z boson events entering the signal regions showed that the b-tagged jets originate mainly from gluons radiated by quarks splitting into $b\bar{b}$ pairs. A

linear increase of their number with the jet multiplicity is therefore expected and has been confirmed. This feature is exploited to extract the fraction of events in CRZ4, CRZ5 and CRZ6 with two b-tagged jets. First, the events passing the CRZ selections are retained. The events are categorised based on their jet multiplicity, from two to six. The number of events falling in each jet multiplicity bin is shown in Tables 6.15 and 6.16, respectively, for the electron and muon channels. Among the selected events in each bin, the sub-sample of the events with at least two b-tagged jets is then considered. The information on the population of each category are given in Tables 6.15 (electrons) and 6.16 (muons). The ratio between the events with at least two b-tagged jets and all the events in each bin is the quantity rising linearly, and is referred to as $b\bar{b}$-fraction.

The $b\bar{b}$-fraction as a function of the number of jets is fitted with a linear function, separately for data and Z boson Monte Carlo simulation. The results of the fit in the four, five and six jets bins represent the fraction of events, respectively, in CRZ4, CRZ5 and CRZ6 having at least two b-tagged jets. The factors obtained with the fit are therefore multiplied for the rate of events in the relevant control region to obtain the predicted numbers of events with two b-tagged jets.

The estimation then follows the semi data-driven technique described in Section 4.2: the normalisation factor is derived as the ratio between the predicted yield of data events with two b-tagged jets in each control region (after subtracting the residual small contamination from non-Z boson backgrounds as predicted by Monte Carlo simulation) and the predicted yield of Z Monte Carlo events with two b-tagged jets in the same control region.

The linear fits for data, data after subtracting the contamination from non-Z boson backgrounds as predicted by Monte Carlo simulation, and Z boson Monte Carlo simulation have been performed separately for electrons and muons, using the jet multiplicity bins from two to six. Higher jet multiplicity bins have been excluded from the fit because of the low number of events.

Figures 6.12 and 6.13 show separately for electrons and muons the $b\bar{b}$-fraction as a function of the number of jets and the results of the fits with their 1-sigma error lines. The results on data and on data minus the contamination from non-Z boson backgrounds are compatible both for electrons and for muons, showing that the small contamination has no impact on the results of the method. In the right bottom plots of these figures Z Monte Carlo and data minus the contamination from non Z backgrounds are overlaid, to show that the difference in the slopes of the two fitting functions is covered by the uncertainties on the fits.

The electron and muon channels are summed together in Figure 6.14. The figure reports in the higher panel the number of events in data and Monte Carlo simulation, with and without the b-tagging requirement, for each jet multiplicity bin. In the lower panel the $b\bar{b}$ fraction for data and Monte Carlo are shown.

Figures 6.15 and 6.16 show the data-Monte Carlo comparison of the $E_{\mathrm{T}}^{\mathrm{miss}\prime}$ variable for different jet multiplicities. The selections applied correspond to the steps from 1 to 4 defining CRZ. The range for the invariant mass of the two leptons has been enlarged to 81-101 GeV, to allow the comparison in a more populated sample.

N Jets	**2**	**3**	**4**	**5**	**6**
Data	5311	2955	975	250	42
Z	5146.6 ± 34.9	2976.1 ± 25.1	1073.1 ± 14.9	287.4 ± 7.3	60.2 ± 3.3
$t\bar{t}$	15.8 ± 0.9	18.1 ± 1.0	8.3 ± 0.7	2.3 ± 0.3	0.90 ± 0.23
$t\bar{t}+V$	0.23 ± 0.04	1.3 ± 0.1	2.3 ± 0.1	2.0 ± 0.1	1.1 ± 0.1
VV	2.5 ± 0.4	2.4 ± 0.4	0.46 ± 0.17	0.20 ± 0.12	0.00 ± 0.00
single top	1.0 ± 0.2	0.84 ± 0.18	0.07 ± 0.04	0.04 ± 0.04	0.00 ± 0.00

Table 6.15: *Expected and observed numbers of events in the electron channel passing the CRZ requirements, split by jet multiplicity.*

N Jets	**2**	**3**	**4**	**5**	**6**
Data	5925	3110	965	249	59
Z	5626.3 ± 37.0	3277.8 ± 27.3	1123.2 ± 15.9	310.9 ± 8.0	59.0 ± 3.5
$t\bar{t}$	15.2 ± 0.6	18.0 ± 0.7	8.3 ± 0.7	2.5 ± 0.4	0.7 ± 0.1
VV	4.1 ± 0.4	2.2 ± 0.3	0.69 ± 0.15	0.05 ± 0.03	0.00 ± 0.00
$t\bar{t}+V$	0.22 ± 0.04	0.92 ± 0.09	2.1 ± 0.1	2.0 ± 0.1	0.57 ± 0.05
single top	1.1± 0.2	0.95 ± 0.19	0.09 ± 0.06	0.12 ± 0.06	0.00 ± 0.00

Table 6.16: *Expected and observed numbers of events in the muon channel passing the CRZ requirements, split by jet multiplicity.*

Results

Tables 6.19 and 6.20 show the numbers of predicted events with two b-tagged jets in the different CRZ. The uncertainties on Z boson Monte Carlo and data predictions include both the statistical uncertainty and the uncertainty deriving from the fit, which is ±17%. The prediction for the contamination from other backgrounds has been taken from Monte Carlo. To derive the normalisation factors, the electron and muon channels have been added together. The normalisation factor derived in CRZ6 is 0.96 ± 0.21, the normalisation factor derived in CRZ5 is 1.06 ± 0.17, and the normalisation factor derived in CRZ4 is 1.13 ± 0.16.

N Jets	**2**	**3**	**4**	**5**	**6**
Data	43	65	49	17	5
Z	33.5 ± 1.8	53.8 ± 2.7	27.7 ± 2.0	12.6 ± 1.3	3.3 ± 0.5
$t\bar{t}$	6.0 ± 0.6	7.9 ± 0.7	3.7 ± 0.5	1.2 ± 0.2	0.45 ± 0.15
$t\bar{t}+V$	0.05 ± 0.02	0.37 ± 0.04	0.77 ± 0.06	0.74 ± 0.06	0.53 ± 0.05
VV	0.08 ± 0.08	0.00 ± 0.00	0.05 ± 0.05	0.00 ± 0.00	0.00 ± 0.00
single top	0.13 ± 0.06	0.14 ± 0.07	0.04 ± 0.03	0.03 ± 0.03	0.00 ± 0.00

Table 6.17: *Expected and observed numbers of events in the electron channel passing the CRZ requirements and containing at least two b-tagged jets, split by jet multiplicity.*

N Jets	**2**	**3**	**4**	**5**	**6**
Data	50	59	43	14	8
Z	40.2 ± 3.4	49.6 ± 2.1	29.8 ± 1.7	10.6 ± 1.4	3.9 ± 0.8
$t\bar{t}$	5.8 ± 0.4	7.6 ± 0.5	3.7 ± 0.3	1.4 ± 0.2	0.28 ± 0.09
$t\bar{t}+V$	0.04 ± 0.02	0.31 ± 0.04	0.68 ± 0.06	0.82 ± 0.07	0.57 ± 0.05
VV	0.00 ± 0.00	0.02 ± 0.01	0.07 ± 0.05	0.00 ± 0.00	0.00 ± 0.00
single top	0.23 ± 0.08	0.29 ± 0.10	0.01 ± 0.01	0.07 ± 0.05	0.00 ± 0.00

Table 6.18: *Expected and observed numbers of events in the muon channel passing the CRZ requirements and containing at least two b-tagged jets, split by jet multiplicity.*

	CRZ6	**CRZ5**	**CRZ4**
Data	3.3 ± 0.7	15.1 ± 2.5	41.8 ± 6.6
Z	3.0 ± 0.6	11.3 ± 2.2	30.5 ± 5.9
other bg	0.98 ± 0.16	2.0 ± 0.2	4.5 ± 0.5

Table 6.19: *Numbers of events with two b-tagged jets in the electron channel as predicted applying the relevant $b\bar{b}$ fraction to the different CRZ yields of data and Z boson Monte Carlo, and contamination from other backgrounds taken from Monte Carlo.*

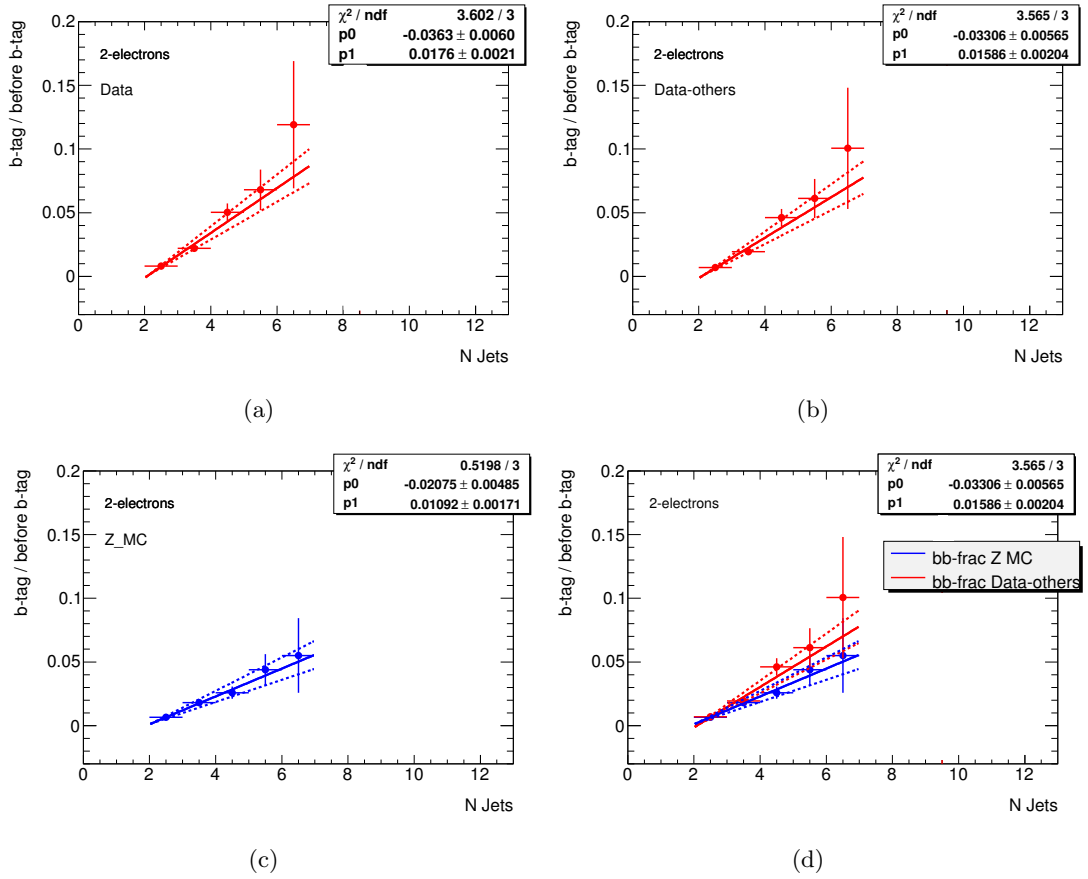

Figure 6.12: *$b\bar{b}$ fraction in the electron channel as a function of the jet multiplicity and results of the linear fits for (a) data, (b) data minus contamination from non-Z boson backgrounds, (c) Z boson Monte Carlo simulation and (d) Z boson Monte Carlo simulation overlaid to data minus contamination from non-Z boson backgrounds.*

	CRZ6	**CRZ5**	**CRZ4**
Data	3.9 ± 0.7	12.2 ± 1.6	35.5 ± 3.7
Z	2.6 ± 0.4	10.6 ± 1.4	28.2 ± 3.3
other bg	0.9 ± 0.1	2.2 ±0.2	4.4 ± 0.3

Table 6.20: *Numbers of events with two b-tagged jets in the muon channel as predicted applying the relevant $b\bar{b}$ fraction to the different CRZ yields of data and Z boson Monte Carlo, and contamination from other backgrounds taken from Monte Carlo.*

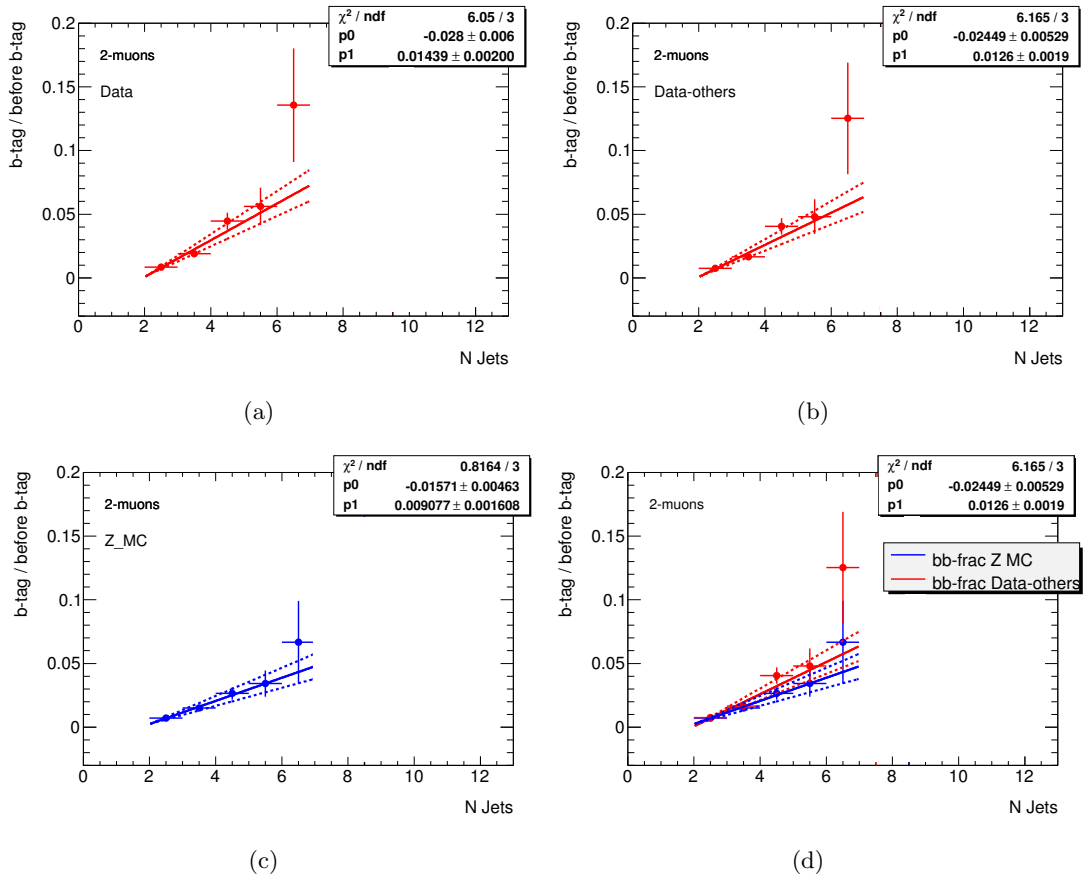

Figure 6.13: *$b\bar{b}$ fraction in the electron channel as a function of the jet multiplicity and results of the linear fits for (a) data, (b) data minus contamination from non-Z boson backgrounds, (c) Z boson Monte Carlo simulation and (d) Z boson Monte Carlo simulation overlaid to data minus contamination from non-Z boson backgrounds.*

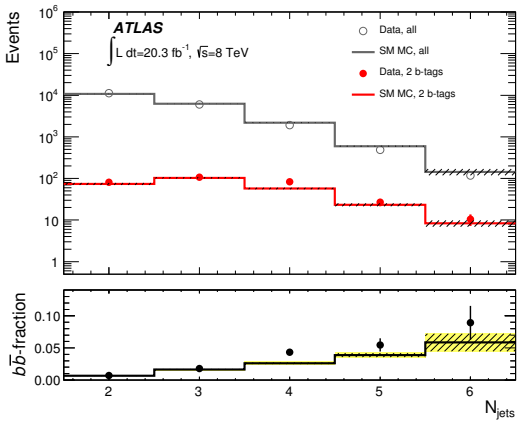

Figure 6.14: *Number of events in data and simulation passing the CRZ selections summarised in Table 6.14, as a function of the jet multiplicity. The open (solid) points show all events (events with two or more b-tagged jets) in data, while the grey (red) line indicates the Standard Model expectation for all events (events with two or more b-tagged jets). The $b\bar{b}$-fraction in data (simulation) is shown in the bottom panel, as indicated by the points (line). The hatched areas indicate Monte Carlo statistical uncertainties and the yellow band (shown only for the $b\bar{b}$-fraction) includes the b-tagging systematic uncertainty. The rightmost bin includes all overflows.* .

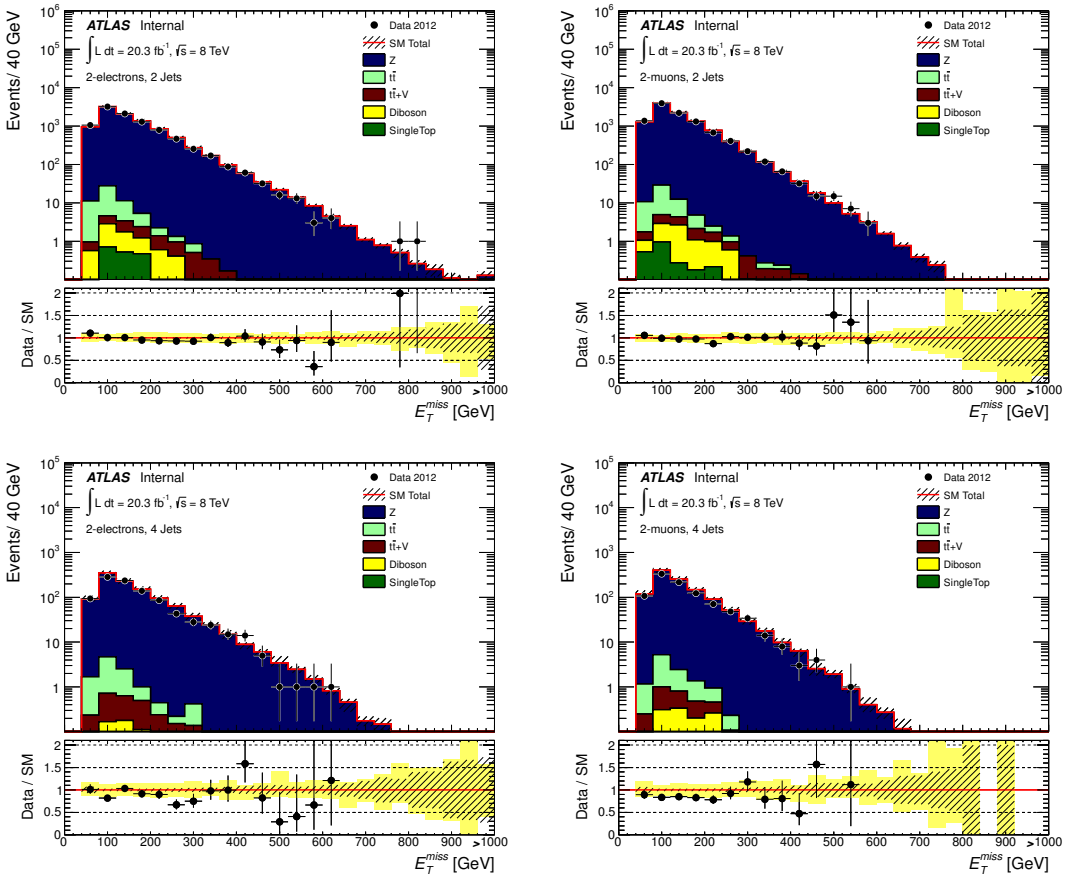

Figure 6.15: $E_{\mathrm{T}}^{\mathrm{miss}\prime}$ *distributions for data and Monte Carlo simulation for events passing the CRZ selections summarised in Table 6.14, with the exception of the selection on the invariant mass which is required to be between 81 and 101 GeV. The plots are done after selecting events with at least two jets (top row) and four jets (bottom row). The left column shows the electron channel, the right column the muon channel. The "Data/SM" plots show the ratio of data events to the total Standard Model expectation. The hatched uncertainty bands around the Standard Model expectations show the statistical uncertainty and the yellow bands (shown only for the "Data/SM" plot) show the combination of statistical and experimental systematic uncertainties .*

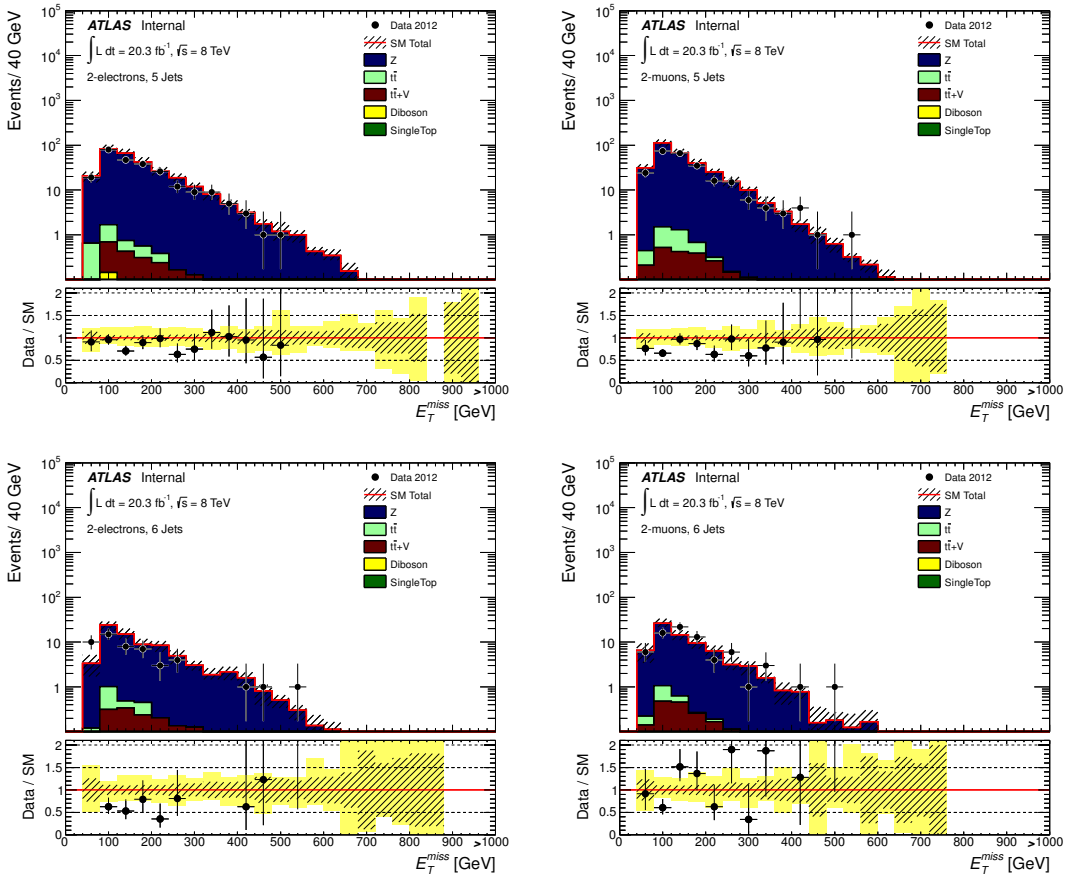

Figure 6.16: $E_{\mathrm{T}}^{\mathrm{miss}\prime}$ *distributions for data and Monte Carlo simulation for events passing the CRZ selections summarised in Table 6.14, with the exception of the selection on the invariant mass which is required to be between 81 and 101 GeV. The plots are done after selecting events with five jets (top row) and six jets (bottom row). The left column shows the electron channel, the right column the muon channel. The "Data/SM" plots show the ratio of data events to the total Standard Model expectation. The hatched uncertainty bands around the Standard Model expectations show the statistical uncertainty and the yellow bands (shown only for the "Data/SM" plot) show the combination of statistical and experimental systematic uncertainties.*

The normalisation factor derived in CRZ6 is effectively the normalisation factor for SRA (which includes events with at least six jets), as the normalisation factor derived in CRZ5 is the normalisation factor for SRB2 and SRC (both requiring the presence of five jets).

In SRB1, 28% of the events have four jets and the remaining 72% have five jets. The normalisation factor built considering the relative population of these two classes of events is 1.11 ± 0.17. Due to the small difference between this value and the normalisation factor obtained using CRZ5, only the last control region has been considered to derive the normalisation factor for the Z boson background for both SRB1 and SRB2. The 4.5 % difference between the two values is considered as an additional uncertainty.

Uncertainty of the Prediction

In addition to the statistical uncertainty and the uncertainty deriving from the linear fit, also the following sources of systematic uncertainties have been considered and taken into account:

- All the systematic uncertainties connected with the detector, as described in Subsection 4.3.1. To take them into account, the linear fit of the $b\bar{b}$-fraction for Z boson Monte Carlo is repeated after applying each of the different detector systematic variations. This procedure ensures the cancellation of the detector systematic uncertainties when evaluating the transfer factor. Tables 6.21 and 6.22 show the comparison between the $b\bar{b}$ fractions obtained in CRZ4, CRZ5 and CRZ6 (respectively in the electrons and muons channel) for the most relevant detector uncertainties.

- The theoretical uncertainty on Z boson production. A large uncertainty due to the heavy flavour component can be expected if no control region for the Z boson background produced in association with heavy flavour quarks is defined, and the prediction for this background is taken straight from the Monte Carlo prediction. With the method described above, this source of uncertainty largely cancels because the ratio between $Z \to \nu\nu$ and $Z \to \ell\ell$ Monte Carlo events is considered in the transfer factor. The treatment of any residual theoretical uncertainty is discussed in Subsection 6.5.1.

- A possible systematic uncertainty on the assumption of the linear behaviour of the $b\bar{b}$-fraction with the number of jets has also been considered. For this purpose, the fit of the Z boson Monte Carlo $b\bar{b}$-fraction have been repeated in different ranges. The results of the $b\bar{b}$-fraction obtained with the default option (fit on the jet multiplicity bins from 2 to 6) have been compared with the results obtained performing the fit on the bins from 2 to 5 and from 3 to 6. Tables 6.23 and 6.24 show that the results

are compatible. The uncertainty evaluated as the maximum difference between the nominal result and the results obtained with different fit ranges is lower than the uncertainty on the prediction arising from the limited number of events of the control sample and the fit uncertainty, therefore no further uncertainty has been added.

	base	*b*-up	*b*-down	c-up	c-down	JES-up	JES-down	JER	data	data-bg
CRZ4	2.84	3.04	2.64	2.97	2.71	2.74	2.89	2.81	4.29	3.83
CRZ5	3.93	4.21	3.66	4.11	3.76	3.79	4.01	3.88	6.05	5.42
CRZ6	5.02	5.38	4.68	5.26	4.80	4.83	5.12	4.95	7.81	7.00

Table 6.21: *Comparison of the $b\bar{b}$-fraction (in %) in the electron channel for Z Monte Carlo (base) and the variations connected to the detector systematic uncertainties: b-tag up, b-tag down, c-tag up, c-tag down, JES-up, JES-down and JER. The values obtained for data and data minus the contamination from non Z backgrounds are also shown.*

	base	*b*-up	*b*-down	c-up	c-down	JES-up	JES-down	JER	data	data-bg
CRZ4	2.51	2.70	2.33	2.60	2.43	2.49	2.60	2.55	3.68	3.22
CRZ5	3.42	3.69	3.16	3.54	3.31	3.41	3.56	3.46	5.11	4.48
CRZ6	4.33	4.67	4.00	4.47	4.19	4.32	4.50	4.38	6.55	5.74

Table 6.22: *Comparison of the $b\bar{b}$-fraction (in %) in the muon channel for Z Monte Carlo (base) and the variations connected to the detector systematic uncertainties: b-tag up, b-tag down, c-tag up, c-tag down, JES-up, JES-down and JER. The values obtained for data and data minus the contamination from non Z backgrounds are also shown.*

Potential Biases

The CRZ has been defined applying a reverted $E_{\mathrm{T}}^{\mathrm{miss}}$ cut meant to reduce the background from di-leptonically decaying $t\bar{t}$ pairs, and a cut on $E_{\mathrm{T}}^{\mathrm{miss}\prime}$ at a lower value with respect to the $E_{\mathrm{T}}^{\mathrm{miss}}$ cuts applied in the different signal regions, to reduce the statistical uncertainty.

Both these conditions can potentially lead to a bias in the prediction of the $b\bar{b}$-fraction and therefore their effect have been investigated. Samples with a larger number of events have been selected applying a looser invariant mass cut for the lepton pair (between 81 and 101 GeV) with respect to the CRZ one.

The fitting procedure has been repeated with and without reverted $E_{\mathrm{T}}^{\mathrm{miss}}$ cut and with different $E_{\mathrm{T}}^{\mathrm{miss}\prime}$ cuts. In all cases no significant impact on the $b\bar{b}$-fraction have been

	Fit 2-6	Fit 2-5	Fit 3-6
CRZ4	0.028 ± 0.003	0.028 ± 0.003	0.028 ± 0.004
CRZ5	0.039 ± 0.005	0.039 ± 0.005	0.038 ± 0.007
CRZ6	0.050 ± 0.006	0.050 ± 0.007	0.049 ± 0.011

Table 6.23: *Results of the $b\bar{b}$-fraction in the electron channel for the various CRZ considering different ranges for the fit: the nominal one (jet multiplicity bins from 2 to 6), compared with the results obtained fitting the bins from 2 to 5 and from 3 to 6.*

	Fit 2-6	Fit 2-5	Fit 3-6
CRZ4	0.025 ± 0.003	0.025 ± 0.003	0.026 ± 0.003
CRZ5	0.034 ± 0.004	0.034 ± 0.004	0.037 ± 0.007
CRZ6	0.043 ± 0.006	0.042 ± 0.006	0.049 ± 0.010

Table 6.24: *Results of the $b\bar{b}$-fraction in the muon channel for the various CRZ considering different ranges for the fit: the nominal one (jet multiplicity bins from 2 to 6), compared with the results obtained fitting the bins from 2 to 5 and from 3 to 6.*

observed. The tests have been conduced on Z boson Monte Carlo and not on data, as the enlarged range for the lepton pair invariant mass results in a significant contamination from non Z boson backgrounds, which spoils the linear behaviour of the $b\bar{b}$-fraction. Figure 6.17 shows the effect on the $b\bar{b}$-fraction slope of the reverted $E_{\mathrm{T}}^{\mathrm{miss}}$ cut, while Figure 6.18 shows the effect on the fit of different $E_{\mathrm{T}}^{\mathrm{miss}\prime}$ cuts. It is seen that the slope is rather independent on all these variations of the selection.

Cross Check Estimation Method and Performance Comparison

In order to cross check the results obtained with the fitting procedure to estimate the Z boson background, another estimation method has been considered. Control regions with not only the same jet multiplicity but also the same number of b-tagged jets as the signal regions are defined as follows:

1. Either the electron or the muon trigger with the lowest p_{T} threshold must be fired.

2. Exactly two electrons or muons with opposite charge are selected, with p_{T} of the leading lepton larger than 25 GeV and p_{T} of the sub-leading lepton larger than 10 GeV. The electron and muon definitions are the same adopted for CRTop (see Subsection 6.3.1).

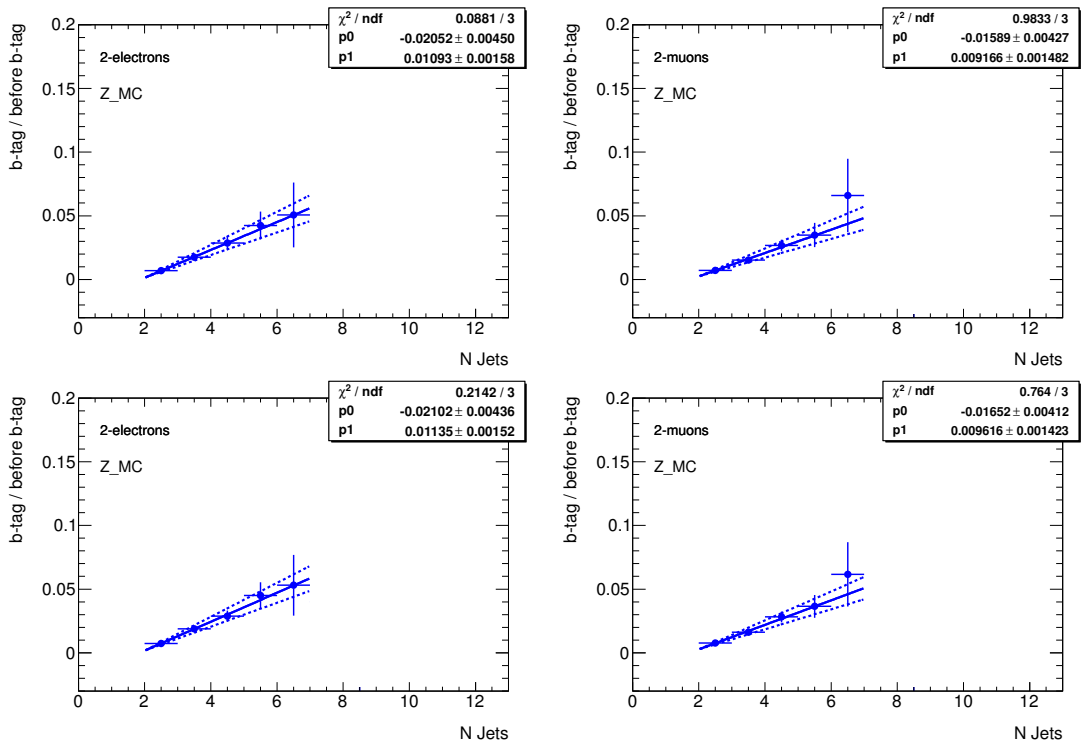

Figure 6.17: *$b\bar{b}$ fraction as a function of the jet multiplicity and results of the linear fits for the electron (left column) and the muon (right column) channels, for Z boson Monte Carlo events passing the nominal CRZ selection (top row) and for a selection where the reverted E_T^{miss} cut is dropped (bottom row).*

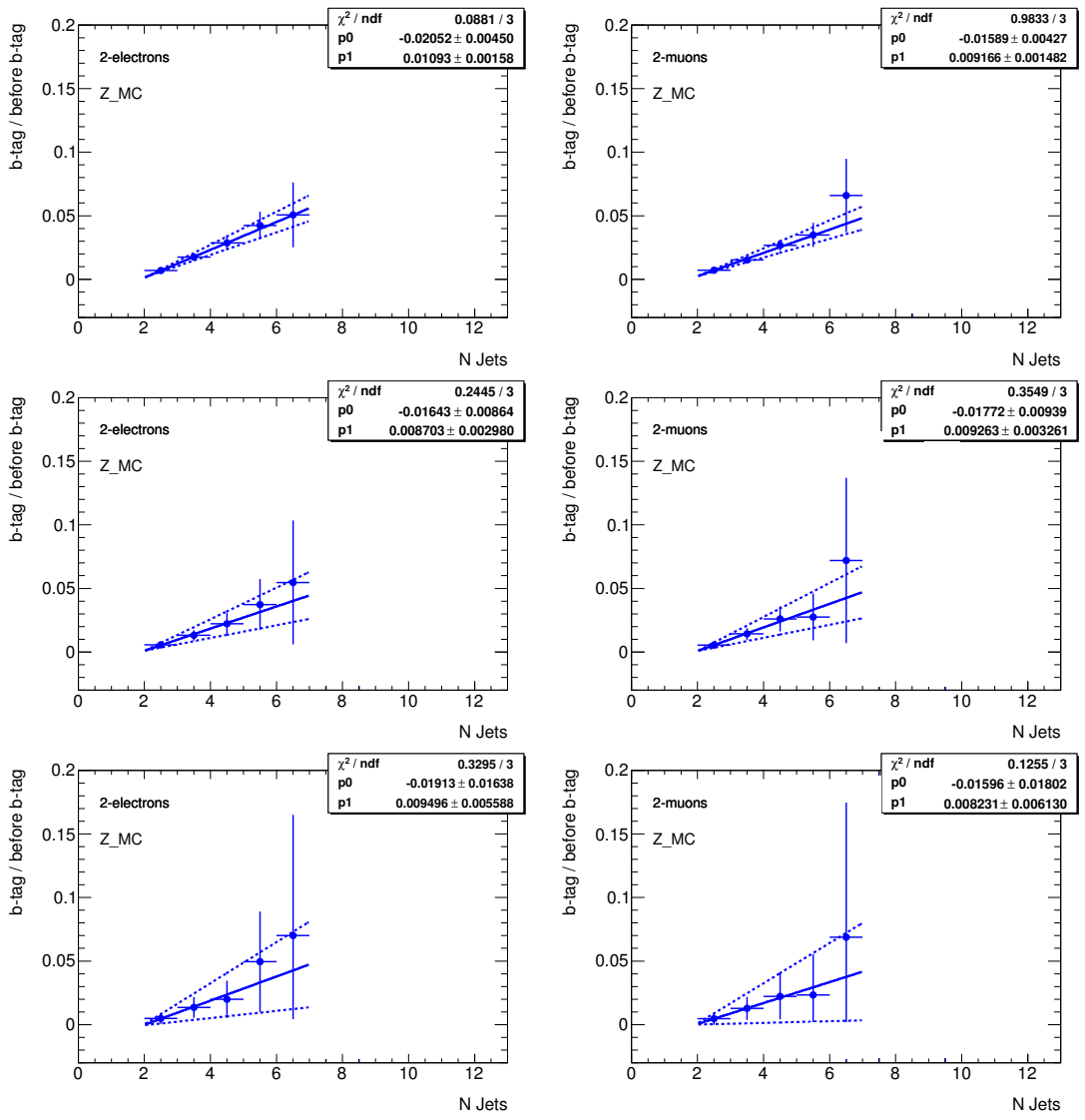

Figure 6.18: *$b\bar{b}$ fraction as a function of the jet multiplicity and results of the linear fits for the electron (left column) and the muon (right column) channels, for Z boson Monte Carlo events passing the nominal CRZ selection (top row) and for a selection where the $E_{\mathrm{T}}^{\mathrm{miss}\prime}$ cut is enhanced to 200 GeV (middle row) and to 300 GeV (bottom row).*

3. To reduce the contamination from $t\bar{t}$ pairs, an upper cut on $E_{\mathrm{T}}^{\mathrm{miss}}$ of 50 GeV is applied.

4. The transverse momentum of the selected leptons is removed from the computation of $E_{\mathrm{T}}^{\mathrm{miss}}$ in order to treat them as if they were neutrinos (and therefore not interacting with the detector material). The new quantity obtained, called $E_{\mathrm{T}}^{\mathrm{miss}\prime}$, is required to have values larger than 70 GeV, to get as close as possible to the signal regions, while maintaining enough events in the control region.

5. The di-lepton invariant mass must be in the range 81-101 GeV, to bring the contamination from non Z boson backgrounds and signal to a negligible level (crucial requirement for the fitting procedure discussed below).

6. The events are required to satisfy the same condition on the number of b-tagged jets as the signal regions: a minimum of two.

7. The events are then split based on their jet multiplicity. The events with exactly four, five and six jets are employed as CR events to predict the Z background, respectively in SRB1 (CRZ4_2), SRB1, SRB2 and SRC (CRZ5_2) and SRA (CRZ6_2). The events with two b-tagged jets and exactly four, five and six jets are employed as CR events to predict the Z background respectively in SRB1 (CRZ4_2), SRB1, SRB2 and SRC (CRZ5_2) and SRA (CRZ6_2).

A summary of the selections to define CRZ4_2, CRZ5_ and CRZ6_ is given in Table 6.25.

	CRZ4_2	**CRZ5_2**	**CRZ6_2**
Trigger	electron or muon		
N_{lep}	2		
p_T^{lep1}	$> 25\,\mathrm{GeV}$		
p_T^{lep2}	$> 10\,\mathrm{GeV}$		
$m(\ell\ell)$	$[81, 101]\,\mathrm{GeV}$		
$E_{\mathrm{T}}^{\mathrm{miss}}$	$< 50\,\mathrm{GeV}$		
$E_{\mathrm{T}}^{\mathrm{miss}\prime}$	$> 70\,\mathrm{GeV}$		
$N_{\mathrm{b-jet}}$	$\geqslant 2$		
N_{jet}	4	5	6

Table 6.25: *Summary of the selections to define the control regions CRZ4_2, CRZ5_2 and CRZ6_2.*

The Monte Carlo prediction and the data yields in CRZ4_2, CRZ5_2 and CRZ6_2 can be found in Tables 6.26 and 6.27 for electrons and muons, respectively.

	CRZ6_2	**CRZ5_2**	**CRZ4_2**
Data	5	21	56
Z	4.3 ± 0.5	14.5 ± 1.3	36.5 ± 2.4
Top	1.0 ± 0.2	2.5 ± 0.4	7.0 ± 0.6
single top	0.00 ± 0.00	0.03 ± 0.03	0.12 ± 0.05
ttV	0.87 ± 0.06	0.82 ± 0.06	0.86 ± 0.07
VV	0.00 ± 0.00	0.00 ± 0.00	0.05 ± 0.05
Tot MC	6.2 ± 0.6	17.8 ± 1.4	44.5 ± 2.5

Table 6.26: *Background composition of CRZ6_2, CRZ5_2, CRZ4_2 and yield of data in the electron channel. Only statistical uncertainties are shown.*

	CRZ6_2	**CRZ5_2**	**CRZ4_2**
Data	9	18	53
Z	5.7 ± 0.9	13.0 ± 1.4	35.5 ± 1.8
Top	0.769 ± 0.13	2.86 ± 0.27	7.09 ± 0.42
single top	0.00 ± 0.00	0.11 ± 0.07	0.07 ± 0.04
ttV	0.92 ± 0.06	0.92 ± 0.07	0.80 ± 0.07
VV	0.00 ± 0.00	0.00 ± 0.00	0.09 ± 0.07
Tot MC	7.3 ± 0.9	16.8 ± 1.5	43.5 ± 1.9

Table 6.27: *Background composition of CRZ6_2, CRZ5_2, CRZ4_2 and yield of data in the muon channel. Only statistical uncertainties are shown.*

As for the main estimation method, the normalisation factors have been derived adding together electron and muon channels. The normalisation factors derived in CRZ4_2, CRZ5_2 and CRZ6_2 have been estimated to be 1.29 ± 0.16, 1.16 ± 0.21 and 1.05 ± 0.39, respectively. These results are compatible with the normalisation factors obtained with the other estimation technique. The uncertainties for the four and five jets bin obtained with the two methods are comparable, while the main estimation technique provides a significantly lower uncertainty on the normalisation factor for the six jets bin (±22% versus ±37%) because of the lower statistical uncertainty.

6.4 Validation Regions

Validation regions dominated by $t\bar{t}$ have been defined for all signal regions, orthogonal to both the control regions and the signal regions.

For SRA, two validation regions have been defined. The first validation region, VRA1, has all the SRA1 requirements applied but the selections on the top candidates mass and the tau veto, that is reverted. This validation region allows to test that the normalisation factor derived in CRTop by selecting samples containing electrons or muons is suitable also for the normalisation of a sample enriched in taus. In the second validation region, VRA2, the SRA1 requirements are applied with the exception of those on the top candidates mass and the selection on $\mathrm{m_T}\left(b_{\mathrm{min}[\Delta\phi(b,E_{\mathrm{T}}^{\mathrm{miss}})]}, E_{\mathrm{T}}^{\mathrm{miss}}\right)$, that is required to be between 125 and 175 GeV.

For the validation region for SRB, VRB, the logical or between SRB1 and SRB2 is considered, with the $E_{\mathrm{T}}^{\mathrm{miss}}$ cut lowered to 150 GeV, $\mathrm{m_T}\left(b_{\mathrm{min}[\Delta\phi(b,E_{\mathrm{T}}^{\mathrm{miss}})]}, E_{\mathrm{T}}^{\mathrm{miss}}\right)$ that is required to be between 100 and 175 GeV and no further selection on the other transverse mass variables applied.

For SRC, two validation regions are defined. The SRC1 selections are considered, but $\mathrm{m_T}\left(b_{\mathrm{min}[\Delta\phi(b,E_{\mathrm{T}}^{\mathrm{miss}})]}, E_{\mathrm{T}}^{\mathrm{miss}}\right)$ is required to be between 150 and 185 GeV, and the cut on $\mathrm{m_T}\left(b_{\mathrm{max}[\Delta\phi(b,E_{\mathrm{T}}^{\mathrm{miss}})]}, E_{\mathrm{T}}^{\mathrm{miss}}\right)$ is lowered to 125 GeV. The tau veto is reverted to form VRC1 (to test the normalisation factor for the $t\bar{t}$ background on a tau enriched sample), or applied to form VRC2.

6.5 Systematic Uncertainties

6.5.1 Background Uncertainties

The theory and detector uncertainties described in Subsections 4.3.2 and 4.3.1 have been taken into account together with the statistical uncertainty connected to the use of Monte Carlo simulation.

The impact of theory and detector uncertainties is mitigated by the use of control regions kinematically similar to the signal regions for the estimation of the major backgrounds.

Due to the high jet multiplicity considered in this analysis, the dominant detector uncertainties are jet energy resolution (±6-15% in SRA, ±16% in SRB, ±3-6% in SRC) and jet energy scale (±5-9% in SRA, ±6% in SRB, ±8-11% in SRC). The other sources of detector uncertainties are negligible if compared to these two.

The theory uncertainties on the background modelling have been estimated with different methods depending on the component considered.

Theory uncertainties for top pair production

The $t\bar{t}$ background is estimated with a semi data-driven technique, therefore the systematic uncertainties connected with the modeling of this background have been evaluated considering their impact on the transfer factor.

The uncertainties connected to the choice of the factorisation and renormalisation scales have been estimated with dedicated Monte Carlo samples with the scales varied up and down by a factor of two.

The uncertainty connected to the choice of the parton shower have been evaluated comparing the results obtained for the default option of the Monte Carlo simulation (POWHEG interfaced to HERWIG) with the results obtained using POWHEG interfaced to PYTHIA.

The impact of the ISR and FSR settings have been evaluated through the use of AcerMC generated samples with different tunings of the shower parameters.

The uncertainty related to the choice of the PDF set is evaluated considering both the results obtained varying the PDF within the envelope of the CT10 set [135] and the results obtained by using a different set of PDF, the HERA PDFs [136]. The variations of the results with respect to the default option are added in quadrature to form the total PDF uncertainty.

The total theory uncertainties for $t\bar{t}$ is less than 10% both in SRA and SRC, the signal regions where this background component is relevant.

Theory uncertainties for W boson production

As the $t\bar{t}$ background, also the W boson background is estimated with a semi data-driven technique and therefore the uncertainty is evaluated on its transfer factor from the control region to the signal region.

The uncertainty on the choice of renormalisation and factorisation scales is estimated with the usual procedure of varying them by a factor two up and down. The resulting uncertainty is summed in quadrature with the uncertainties deriving from the choice of

the matching scale and the PDF set used in the Monte Carlo samples generated with SHERPA.

A ±38% uncertainty on the production cross section of the W boson in association with heavy flavour jets has been derived from the measurement documented in Ref. [137] and taken into account.

Possible uncertainties related to the use of the parton shower to simulate extra jets have also been evaluated comparing the results obtained with Alpgen samples simulated with the matrix element taking care of producing up to 4 or up to 5 partons.

The fractions of $W+c$, $W+b\bar{b}$ and $W+c\bar{c}$ events in CRW and signal regions is different because of the different b-tagged jet multiplicity required in CRW. An additional uncertainty of ±20% has been considered accounting for a possible bias in the normalisation factor resulting from this difference.

The total theoretical uncertainties on the W boson background are ±1–2% in SRA, ±10% in SRB and ±5% in SRC.

Theory uncertainties for Z boson production

The uncertainty on the modelling of the Z boson background has been evaluated comparing the transfer factors obtained with the default option for the Monte Carlo generator (SHERPA) and the results obtained using Alpgen.

The uncertainty on the event generation with a finite number of partons have been assessed as for the W boson background, while the uncertainty connected to the choice of the PDF set has been evaluated following the same procedure adopted for $t\bar{t}$.

The resulting total uncertainty is ±1–2% in SRA, ±9% in SRB, and ±4–5% in SRC. These uncertainties have to be added to the systematic uncertainty of ±17% on the $b\bar{b}$-fraction discussed in Subsection 6.3.4.

Theory uncertainties for $t\bar{t}+V$ production

The uncertainty on the $t\bar{t}+W/Z$ background is dominated by the uncertainty on the production cross section, which is ±22% [138], [139]. Other sources of theoretical uncertainties are the choices of renormalisation, factorisation and matching scale, and the amount of ISR and FSR. All these uncertainties have been assessed making use of dedicated MadGraph samples with appropriate changes in the settings. The uncertainty arising from a finite number of additional partons in the matrix element has been evaluated comparing the yields obtained on samples with one additional parton to the yields obtained on samples with two additional partons in the matrix element.

The resulting uncertainty is ±3-6% in SRA, ±6% in SRB, and at the per cent level in SRC.

Theory uncertainties for single top production

The dominating single top sub-process in the signal regions is Wt, therefore the $\pm 6.8\%$ theoretical uncertainty on its production cross section has been considered [140].

The effect of the interference between single-top and $t\bar{t}$ production has been evaluated comparing the difference in total yields from these two background components obtained with POWHEG and AcerMC.

Additional uncertainties taken into account are the choice of the generator (estimated comparing the yields obtained with the default option, POWHEG interfaced to HERWIG, to the yields ontained with MCAtNLO), the choice of the parton shower (estimated comparing the yields obtained with POWHEG interfaced to HERWIG or PYTHIA), ISR and FSR settings (estimated with dedicated AcerMC samples), and the PDF set choice.

The total uncertainty for this background is between $\pm 1\%$ and $\pm 5\%$, depending on the signal region considered.

Theory uncertainties for dibosons production

The diboson production is a small background. A conservative uncertainty of $\pm 50\%$ has been assigned to it, which results in an uncertainty below the percent level on the total background.

Uncertainties for QCD multi-jet events

An uncertainty of $\pm 100\%$ has been assigned to the estimated yield of QCD multi-jet events, which has a negligible impact on the total background uncertainty.

6.5.2 Signal Uncertainties

The procedure for estimating the theoretical uncertainty on the signal cross section follows the the PDF4LHC recommendations [120]: the uncertainty due to the choice of the PDF set, the variations of the factorisation and renormalisation scales of a factor two up and down and and strong coupling constant variations have been taken into account. These uncertainties have all been found to be below the percent level. The impact of different settings for the amount of ISR have been also tested and found to be negligible.

The most important sources of uncertainties are the detector related ones. The dominating uncertainty is the JES, resulting in a variation of the signal yields between ± 4 and $\pm 16\%$ in SRA, $\pm 3\%$ in SRB, ± 4 to $\pm 10\%$ in SRC. The b-tagging uncertainty is also relevant, accounting for a variation of the yields of $\pm$7-8% in all signal regions, as well as JER, determining a yield variation from ± 2 to $\pm 10\%$ in SRA, $\pm 10\%$ in SRB and from ± 2 to $\pm 3\%$ in SRC.

Background Source	SRA	SRB	SRC
$t\bar{t}$	1.24 ± 0.13	$1.00^{+0.10}_{-0.05}$	1.07 ± 0.11
W	–	1.0 ± 0.4	–
Z	$0.94^{+0.16}_{-0.15}$	1.07 ± 0.07	1.07 ± 0.07

Table 6.28: *Normalisation factors for the backgrounds from $t\bar{t}$, W and Z bosons, as obtained from the background-only fits (see text) for SRA, SRB and SRC.*

6.6 Results and Interpretation

The procedure for extracting the results has been described in Section 4.4. First, a background-only profile likelihood fit of the control regions is performed, treating the normalisation factors as free parameter. To predict the background composition of SRA and SRC, CRTop and CRZ are fitted simultaneously. For the prediction of the background in SRB also CRW is taken into account, since W plus heavy flavour jets production constitutes an important background in this signal region. The contributions from minor backgrounds are fixed to their Monte Carlo predictions. The sample of smeared events used to predict the QCD multi-jet background are normalised to data prior to performing the fit. Table 6.28 shows the normalisation factors as obtained with the background-only fit. Their validity has been tested by applying them to the Monte Carlo predictions of the backgrounds in the validation regions described in Section 6.4 and comparing the results to the observed data yields. As shown in Table 6.29, agreement within one standard deviation has been observed in all regions, confirming the robustness of the background estimation methods.

The fit is then repeated taking into account together with the control regions, also one signal region at a time. The distributions of $E_{\mathrm{T}}^{\mathrm{miss}}$ for the different signal regions are shown in Figure 6.19 with the normalisation factors shown in Table 6.28 applied to the relevant background components. SRA1 and SRA2, as well as SRA3 and SRA4, differ only for the $E_{\mathrm{T}}^{\mathrm{miss}}$ requirement, therefore combined distributions are shown. Two events with $E_{\mathrm{T}}^{\mathrm{miss}} = 585$ GeV and $E_{\mathrm{T}}^{\mathrm{miss}} = 746$ GeV have been observed in SRA4 and SRA5, and one event with $E_{\mathrm{T}}^{\mathrm{miss}} = 896$ GeV has been observed in SRB1 and all SRC. A careful investigation of these events showed that such high values of $E_{\mathrm{T}}^{\mathrm{miss}}$ are unlikely to have been generated by malfunctioning of the ATLAS experiment. Displays of these events, showing the different final state objects, are shown in Figure 6.20.
The background expectation for the different signal regions as obtained with the fitting procedure is shown in Table 6.30 together with the observed data yields. No significant

	VRA1	VRA2	VRB	VRC1	VRC2
Observed events					
	158	51	69	103	24
Fitted background events					
Total SM	188.7 ± 26.4	49.5 ± 5.8	70.4 ± 19.0	110.2 ± 12.2	21.1 ± 2.9
$t\bar{t}$	170.1 ± 27.3	33.9 ± 7.0	59.6 ± 18.9	92.6 ± 12.0	17.3 ± 2.8
Z	4.0 ± 1.1	1.5 ± 0.4	1.5 ± 0.5	6.9 ± 1.5	0.24 ± 0.20
W	2.8 ± 1.2	4.8 ± 2.2	2.1 ± 1.4	3.9 ± 1.8	1.1 ± 0.5
Others	11.8 ± 3.1	9.1 ± 2.2	7.2 ± 2.5	6.7 ± 2.0	2.4 ± 0.7

Table 6.29: *Event yields in the validation regions described in Section 6.4 compared to the background estimates obtained from the fit. Statistical and systematic uncertainties in the number of fitted background events are shown. Smaller background contributions from multi-jets, single-top, $t\bar{t}+W/Z$, and diboson production are included in "Others".*

excess over the Standard Model expectation has been observed, therefore the results have been interpreted in terms of 95% CL upper limits on the number of events from non Standard Model processes, as shown in the table. The exclusion limits on the number of events are also converted into limits on the visible cross section of a generic non Standard Model process.

Finally, model-dependent limits on direct stop pair production are set. The simultaneous fit of control and signal regions is performed taking into account the signal presence in the different regions. To enhance the sensitivity of the analysis, the results of the signal regions are combined. SRA is orthogonal to both SRB and SRC, but SRB and SRC are not orthogonal to each other. To derive the exclusion limits, for each simulated signal point in the $(\tilde{t}_1 - \widetilde{\chi}_1^0)$-mass plane the combination of one of the SRA with either SRB or one of the SRC providing the lowest 95% CL_s is considered. The results are derived for different BR of the decay mode $\tilde{t}_1 \to t\widetilde{\chi}_1^0$ (corresponding to 1-BR($\tilde{t}_1 \to b\widetilde{\chi}_1^{\pm}$)). Figure 6.21 shows the combinations of signal regions which results provide the lowest CL_s, for each $\tilde{t}_1$-$\widetilde{\chi}_1^0$ mass combination and for different branching ratios. For high values of the $\tilde{t}_1$ mass the SRA performing better are those characterised by stringent cuts on the discriminating variables. These signal regions are combined with SRB when high BR($\tilde{t}_1 \to t\widetilde{\chi}_1^0$) and high $\tilde{t}_1$ masses are considered. As the BR($\tilde{t}_1 \to t\widetilde{\chi}_1^0$) or the $\tilde{t}_1$ mass considered decreases, SRC is the preferred signal region to be combined. This behaviour is coherent with the analysis strategy.

Figure 6.22 shows the exclusion limits corresponding to the combination of the signal

regions of Figure 6.21, plus a plot summarizing all the exclusion contours. For a BR($\tilde{t}_1 \rightarrow t\widetilde{\chi}_1^0$) of 100% (the top left plot), $\tilde{t}_1$ masses between 270 and 645 GeV are excluded for $\widetilde{\chi}_1^0$ masses below 30 GeV. This result can be compared to the exclusion limit represented by the orange area of Figure 5.23, which has been obtained with the full dataset collected at a centre-of-mass energy of the proton-proton collisions of 7 TeV with an analysis addressing a similar final state. By comparing the plots it is possible to see how the analysis presented in this chapter performed on the full 8 TeV dataset significantly extends the exclusion contour. For the intermediate case BR($\tilde{t}_1 \rightarrow t\widetilde{\chi}_1^0$)=50%, $\tilde{t}_1$ masses between 250 and 550 GeV are excluded for $\widetilde{\chi}_1^0$ masses below 60 GeV. No previous results targeting mixed branching ratios in $\tilde{t}_1 \rightarrow t\widetilde{\chi}_1^0$ and $\tilde{t}_1 \rightarrow b\widetilde{\chi}_1^{\pm}$ are available, since signal regions targeting this scenario were developed for the first time for this analysis.

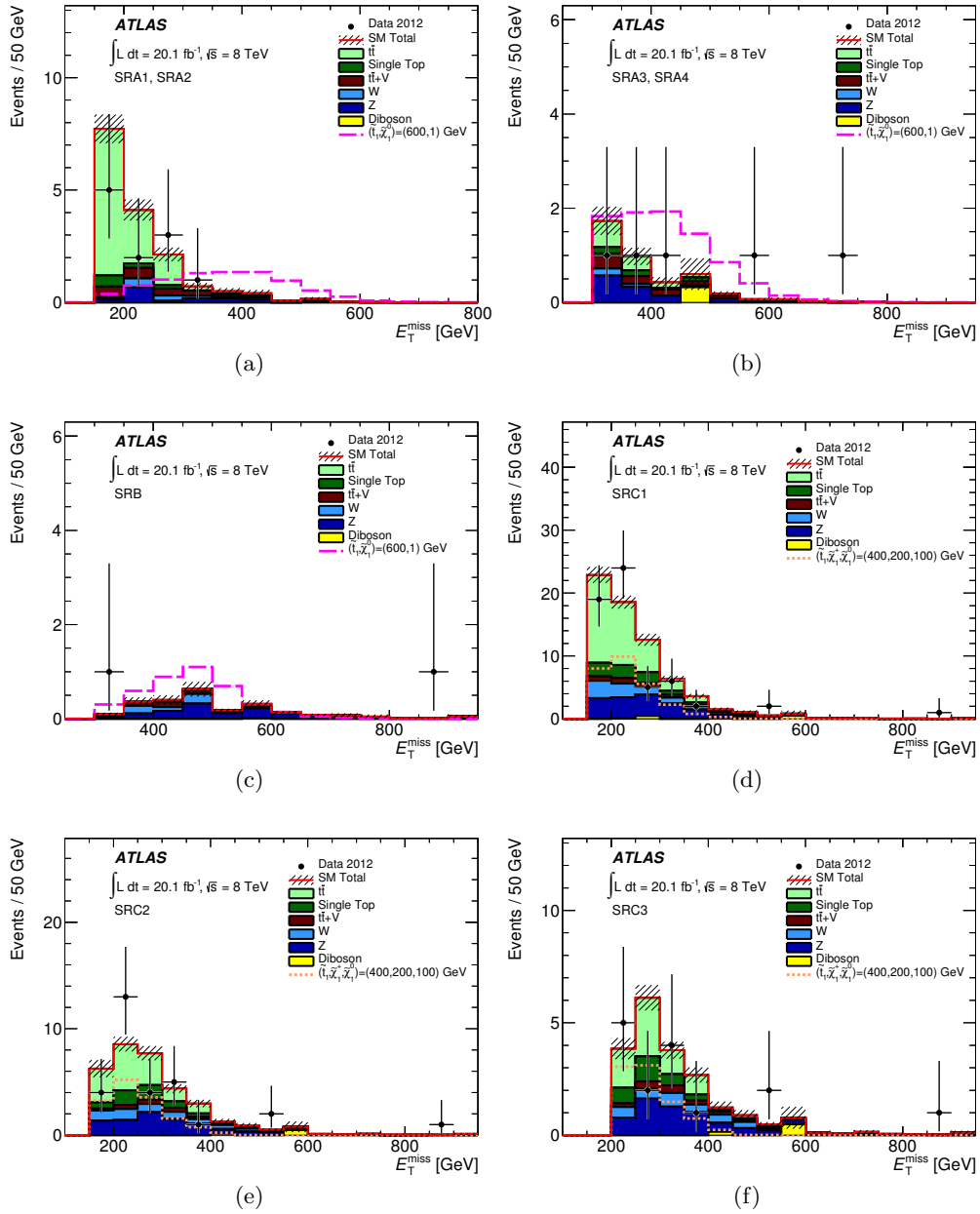

Figure 6.19: *E_T^{miss} distributions for (a) SRA1 and SRA2, (b) SRA3 and SRA4, (c) SRB, (d) SRC1, (e) SRC2, and (f) SRC3. SRA1 and SRA2, as well as SRA3 and SRA4, differ only for the E_T^{miss} requirement. The background expectation (data) are represented by the stacked histograms (black points). For SRA and SRB, the simulated signal distribution for $m_{\tilde{t}_1} = 600$ GeV, $m_{\tilde{\chi}_1^0} = 1$ GeV of the tN1tN1 Grid is overlaid (pink dashed line), while for SRC the simulated signal distribution for $m_{\tilde{t}_1} = 400$ GeV, $m_{\tilde{\chi}_1^\pm} = 200$ GeV, and $m_{\tilde{\chi}_1^0} = 100$ GeV of the tN1bC1 Grid is overlaid (orange dotted line). The hatched band on the Standard Model total histogram represents the Monte Carlo statistical uncertainty only.*

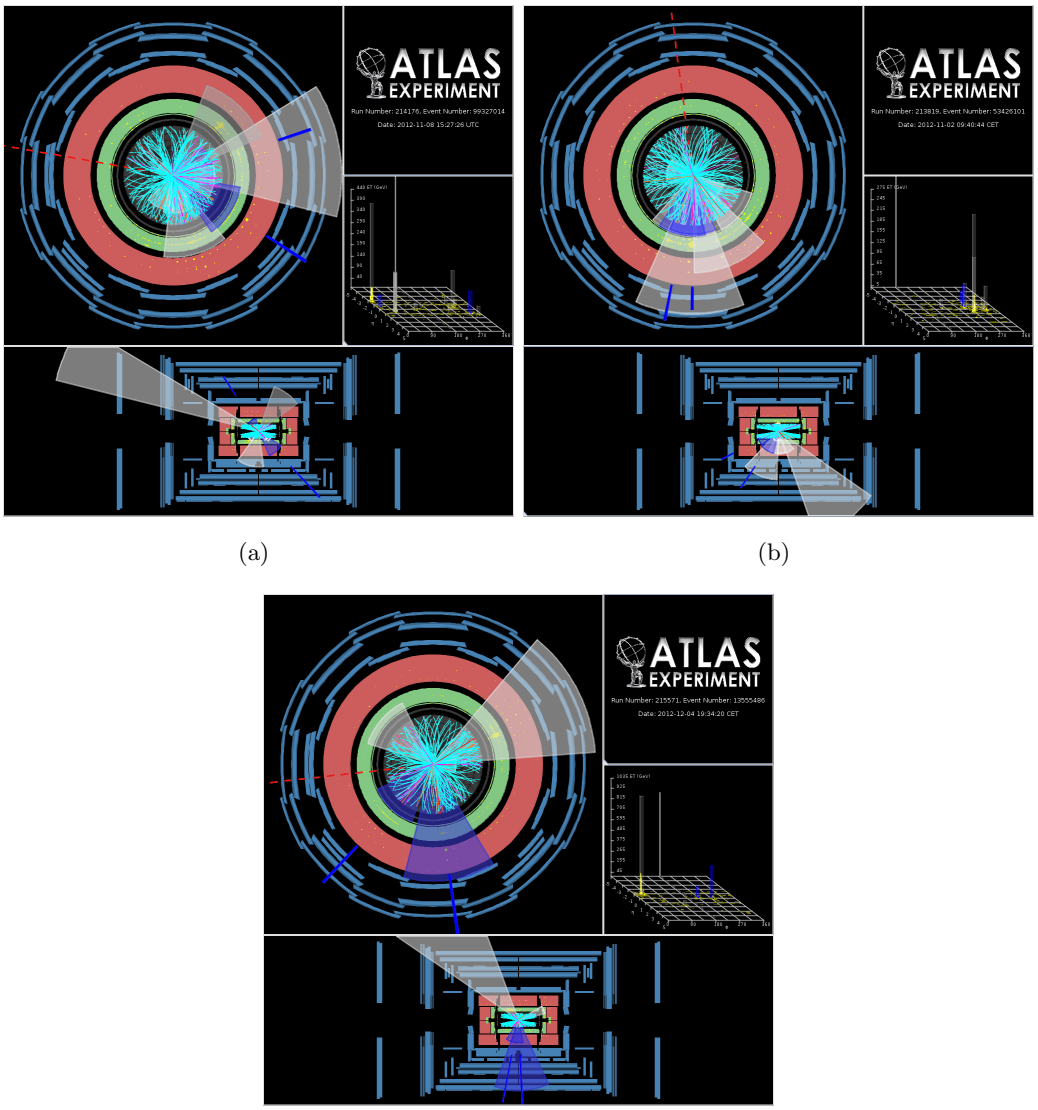

(a) (b)

(c)

Figure 6.20: *Event displays of the three high E_T^{miss} events observed after all signal selections are applied. The E_T^{miss} is indicated by a red dashed line, jets are indicated by white cones, and b-tagged jets are indicated by blue cones. The colour spectrum (blue to red) for the inner detector tracks indicates the relative p_{T} (low to high). (a) Event 99327014 in Run 214176 has seven jets, two of which are b-tagged, $E_T^{miss} = 746$ GeV, $m_{\mathrm{T}}\left(b_{\min[\Delta\phi(b,E_T^{miss})]}, E_T^{miss}\right) = 407$ GeV, and two top candidates with $m^0_{bjj} = 244$ GeV and $m^1_{bjj} = 197$ GeV. The highest p_{T} jet has $p_{\mathrm{T}} = 422$ GeV and is not contained in either top candidate. This event appears in both SRA3 and SRA4. (b) Event 53426101 in Run 213819 has six jets, two of which are b-tagged, $E_T^{miss} = 585$ GeV, $m_{\mathrm{T}}\left(b_{\min[\Delta\phi(b,E_T^{miss})]}, E_T^{miss}\right) = 374$ GeV, and two top candidates with $m^0_{bjj} = 107$ GeV and $m^1_{bjj} = 304$ GeV. The highest p_{T} jet has $p_{\mathrm{T}} = 250$ GeV. This event appears in both SRA3 and SRA4. (c) Event 13555486 in Run 215571 has five jets, two of which are b-tagged, $E_T^{miss} = 896$ GeV, $m_{\mathrm{T}}\left(b_{\min[\Delta\phi(b,E_T^{miss})]}, E_T^{miss}\right) = 212$ GeV, $H_T^{sig} = 23\sqrt{GeV}$, and two re-clustered top candidates with $m^0_{AkT12} = 167$ GeV and $m^1_{AkT12} = 170$ GeV. The highest p_{T} jet has $p_{\mathrm{T}} = 995$ GeV. This event appears in SRB and all SRC.*

	SRA1	**SRA2**	**SRA3**	**SRA4**	**SRB**	**SRC1**	**SRC2**	**SRC3**
Observed events	11	4	5	4	2	59	30	15
Total SM	15.8 ± 1.9	4.1 ± 0.8	4.1 ± 0.9	2.4 ± 0.7	2.4 ± 0.7	68.2 ± 7.3	33.8 ± 4.6	20.3 ± 3.0
$t\bar{t}$	10.6 ± 1.9	1.8 ± 0.5	1.1 ± 0.6	0.49 ± 0.34	0.10 ± 0.14	32.2 ± 4.4	12.9 ± 2.0	6.7 ± 1.2
$t\bar{t} + W/Z$	1.8 ± 0.6	0.85 ± 0.29	0.82 ± 0.29	0.50 ± 0.17	0.47 ± 0.17	3.2 ± 0.8	1.9 ± 0.5	1.3 ± 0.4
Z	1.4 ± 0.5	0.63 ± 0.22	1.2 ± 0.4	0.68 ± 0.27	1.2 ± 0.3	15.7 ± 3.5	9.0 ± 1.9	6.1 ± 1.3
W	1.0 ± 0.5	0.46 ± 0.21	0.21 ± 0.19	0.06 ± 0.06	0.49 ± 0.33	8.5 ± 3.7	4.8 ± 2.2	2.8 ± 1.2
Single top	1.0 ± 0.4	0.30 ± 0.17	0.44 ± 0.14	0.31 ± 0.16	0.08 ± 0.06	7.2 ± 2.9	4.5 ± 1.8	2.9 ± 1.4
Diboson	< 0.4	< 0.13	0.32 ± 0.17	0.32 ± 0.18	0.02 ± 0.01	1.1 ± 0.8	0.6 ± 0.6	0.6 ± 0.6
Multi-jets	< 0.001	< 0.001	< 0.001	< 0.001	< 0.001	0.24 ± 0.24	0.06 ± 0.06	0.01 ± 0.01
σ_{vis} (obs) [fb]	0.33	0.29	0.33	0.32	0.21	0.78	0.62	0.40
σ_{vis} (exp) [fb]	0.48 ± 0.14	0.29 ± 0.09	0.29 ± 0.09	0.25 ± 0.07	0.24 ± 0.06	1.03 ± 0.29	0.73 ± 0.21	0.55 ± 0.15
N_{obs}^{95}	6.6	5.7	6.7	6.5	4.2	15.7	12.4	8.0
N_{exp}^{95}	9.7 ± 3.0	5.8 ± 1.8	5.9 ± 1.9	5.0 ± 1.4	4.7 ± 1.2	20.7 ± 5.8	14.7 ± 4.2	11.0 ± 3.1

Table 6.30: *Event yields in each signal region (SRA, SRB, and SRC) are compared to the background estimate from the profile likelihood fit. Statistical, detector, and theoretical systematic uncertainties are included; the total systematic uncertainty in the background estimate includes all correlations. For each signal region, the* 95% *CL upper limits on the expected (observed) visible cross sections* $\sigma_{vis}\,(exp)$ *(*$\sigma_{vis}\,(obs)$*) and the expected (observed) event yields* N_{exp}^{95} *(*N_{obs}^{95}*) are summarised.*

6.7 Summary of Stop Searches at $\sqrt{s} = 8$ TeV

The search for direct stop pair production decaying into top and neutralino with 100% BR with the dataset collected by the ATLAS experiment at a centre-of-mass energy of the proton-proton collisions of 8 TeV has been performed not only in the zero lepton channel, but also with analyses involving one [141] and two leptons [142]. No significant excess over the Standard Model expectation was observed, and the results were interpreted in terms of 95% CL exclusion limits. The exclusion contours obtained are summarised in Figure 6.23 in orange, yellow and red. The same figure shows the exclusion contours already presented in Figure 5.23 obtained with the dataset collected at a centre-of mass-energy of 7 TeV with analyses targeting the same final states. By comparing the contours it is possible to appreciate how the increase of energy and the advancement in the analysis techniques allowed to extend the reach of each search.

The plot reports also the exclusion contours obtained for decay modes explored for the first time analysing the 8 TeV dataset. The light and dark violet areas are the exclusion limits obtained with the one and two-lepton analyses already mentioned, when considering the direct three body decay $\tilde{t}_1 \rightarrow Wb\widetilde{\chi}_1^0$ with 100% BR (an important decay mode when the mass spectrum of the particles is such that $m(W) + m(b) + m(\widetilde{\chi}_1^0) < m(\tilde{t}_1)$ and $m(\tilde{t}_1) < m(t) + m(\widetilde{\chi}_1^0)$). For $m(b/c) + m(\widetilde{\chi}_1^0) < m(\tilde{t}_1)$ and $m(\tilde{t}_1) < m(t) + m(\widetilde{\chi}_1^0)$, the decay modes $\tilde{t}_1 \rightarrow bff'\widetilde{\chi}_1^0/c\widetilde{\chi}_1^0$ can dominate. The exclusion limits obtained under the assumptions of 100% BR decays are shown in light [141] or dark grey [145] and pink [145].

The region where the stop mass is close to the top quark mass is left uncovered by the analyses presented so far. The reason for this is that the decay products of the expected signal and of the $t\bar{t}$ background have very similar kinematic properties, therefore an effective discrimination between them is not possible with the discriminating variables considered. An alternative approach is to exploit a precise measurement of the $t\bar{t}$ pair production cross section to set limits on stop pair production. The stop pair production cross section for stop mass values close to the top mass is about 15% of the $t\bar{t}$ pair production one. The analysis documented in Ref. [143] allowed to measure the cross section for $t\bar{t}$ production with an experimental uncertainty of $\pm 4\%$. The theoretical uncertainty is $\pm 5\%$, thus allowing to have a sensitivity of the order of $\pm 10\%$ to any contribution to the cross section from a stop close in mass to the top quark. The resulting exclusion limit at 95% CL ranges from the top mass to 177 GeV under the assumption that the stop is mostly the superpartner of the right-handed top quark and that decays with 100% BR into a top quark and an LSP with a mass of 1 GeV. This exclusion limit is extended to 191 GeV by the analysis documented in Ref. [144] which select events with two leptons. The angular correlation between the leptons is studied, which allows to extract information about the spin of the particle originating them.

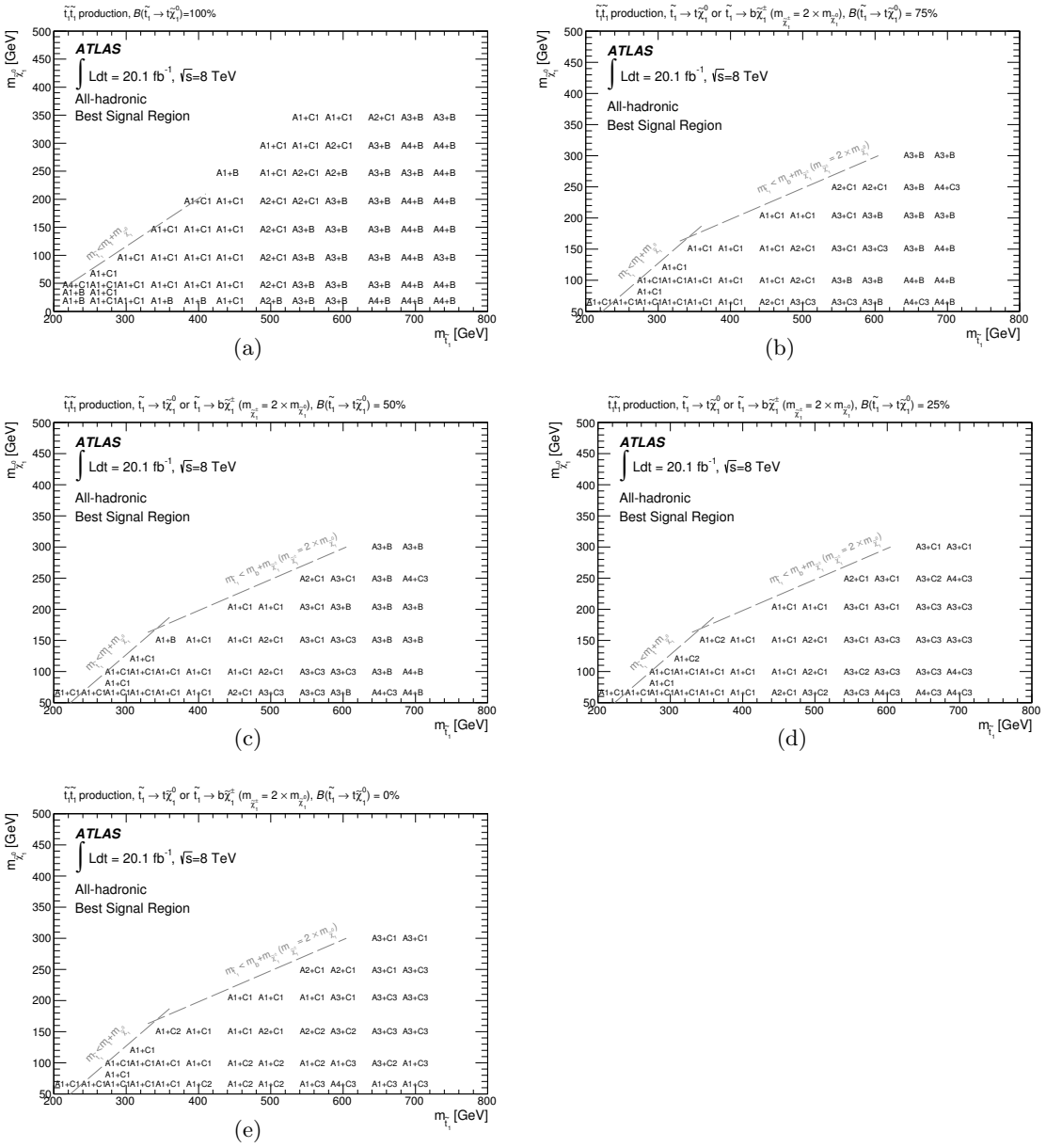

Figure 6.21: *Combination of SRA and SRB or SRA and SRC providing the lowest CL_s for different branching ratios $BR(\tilde{t}_1 \to t\tilde{\chi}_1^0)$=1-$BR(\tilde{t}_1 \to b\tilde{\chi}_1^{\pm})$ of (a) 100%, (b) 75%, (c) 50%, (d) 25%, and (e) 0%.*

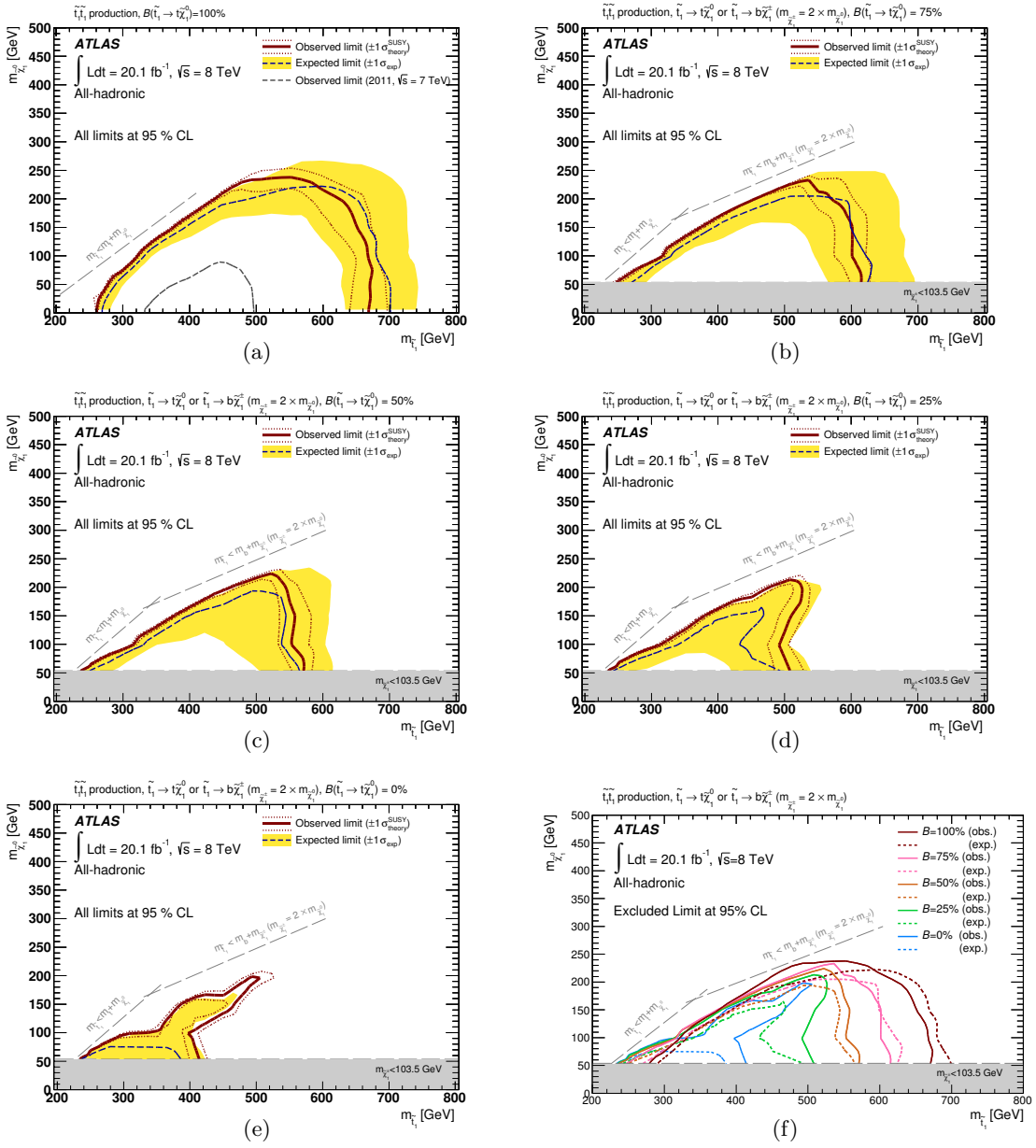

Figure 6.22: *Exclusion contours at 95 % CL for different branching ratios BR($\tilde{t}_1 \to t\tilde{\chi}_1^0$)=1-BR($\tilde{t}_1 \to b\tilde{\chi}_1^\pm$) of (a) 100%, (b) 75%, (c) 50%, (d) 25%, and (e) 0%. The $\tilde{\chi}_1^\pm$ mass is fixed to twice the $\tilde{\chi}_1^0$ mass, and the gray filled areas correspond to the LEP limit of 103.5 GeV on the mass of the lightest chargino [108, 109, 110, 111, 112]. The observed (expected) exclusion limit is shown with a red solid line (blue dashed line). The yellow band around the expected limit shows the $\pm 1\sigma$ variations on the expected limit, including all uncertainties except theoretical uncertainties in the signal. The dotted red lines around the observed limit indicate the sensitivity to $\pm 1\sigma$ variations of the signal theoretical uncertainties. (f) summarises the expected and observed exclusion limits for the different options of BR($\tilde{t}_1 \to t\tilde{\chi}_1^0$).*

As the 7 TeV dataset, also the 8 TeV dataset has been exploited to search for direct stop pair production decaying into a b-quark and a chargino with 100% BR, with a subsequent decay of the chargino into a W boson and a neutralino. The exclusion limits have been set under different assumptions for the chargino and neutralino masses. Figure 6.24 shows the different exclusion contours obtained under the assumptions specified in the figure with the analyses described in Refs. [96], [141] and [142]. The figure reports also the results obtained with the 7 TeV dataset and documented in Refs. [122] and [107]. The last result cited corresponds to the analyses described in Chapter 5. Finally, Figure 6.25 shows the exclusion limits for a stop mass of 300 GeV in the $(\widetilde{\chi}_1^{\pm} - \widetilde{\chi}_1^0)$-mass plane, obtained with the analyses documented in Refs. [96], [141] and [142].

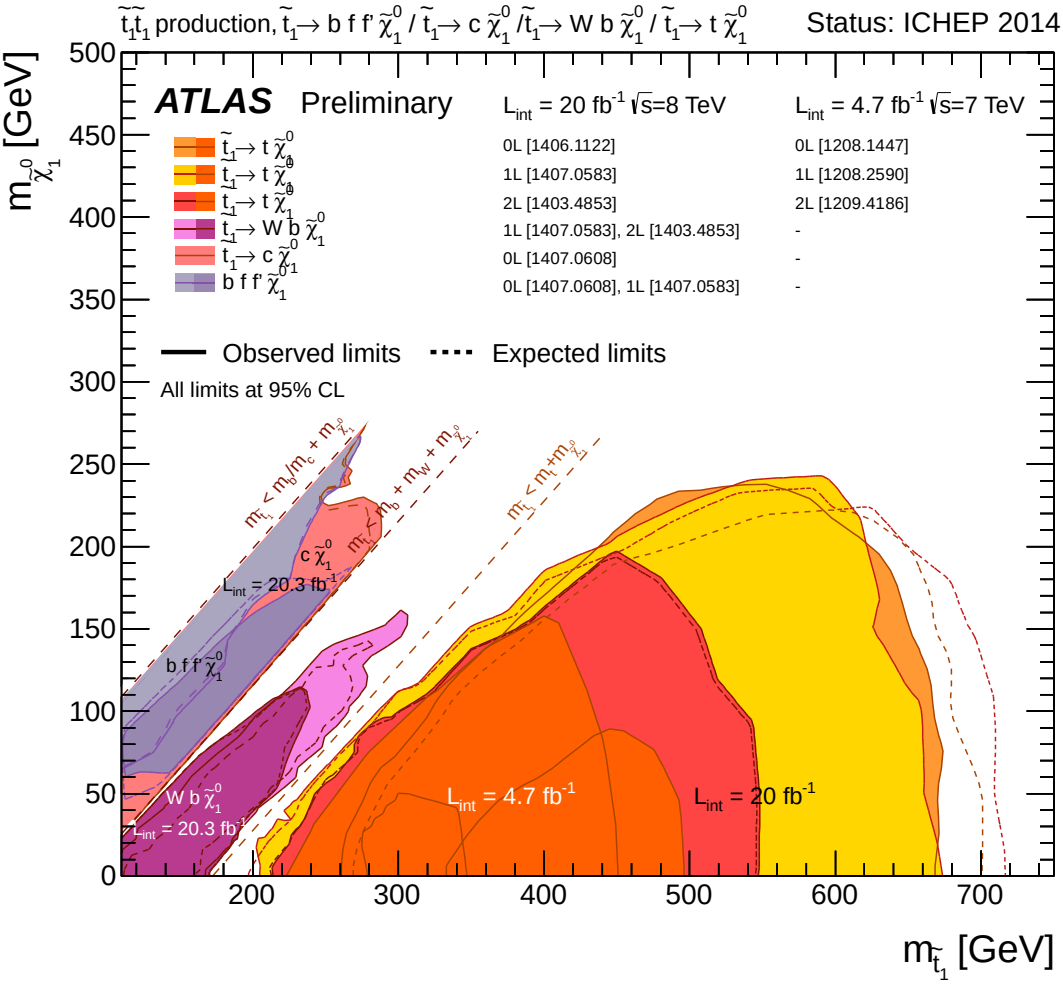

Figure 6.23: *Summary of the searches of the ATLAS experiment for stop pair production based on 20 fb^{-1} of proton-proton collision data taken at $\sqrt{s} = 8$ TeV, and 4.7 fb^{-1} of proton-proton collision data taken at $\sqrt{s} = 7$ TeV. Exclusion limits at 95% CL are shown in the $(\tilde{t}_1 - \tilde{\chi}_1^0)$-mass plane. The dashed and solid lines show the expected and observed limits, respectively, including all uncertainties except the theoretical signal cross section uncertainty. Four decay modes are considered separately with 100% BR: $\tilde{t}_1 \to t\tilde{\chi}_1^0$ (7 TeV: [125] (1208.1447), [123] (1208.2590) and [124] (1209.4186), 8 TeV: [132] (1406.1122), [141] (1407.0583) and [142] (1403.4853), where the $\tilde{t}_1$ is mostly the superpartner of the right-handed top quark), $\tilde{t}_1 \to Wb\tilde{\chi}_1^0$ (3-body decay for $m(\tilde{t}_1) < m(t) + m(\tilde{\chi}_1^0)$, 8 TeV [141] (1407.0583) and [142] (1403.4853)), $\tilde{t}_1 \to c\tilde{\chi}_1^0$ [145] (1407.0608) and $\tilde{t}_1 \to ff'b\tilde{\chi}_1^0$ (4-body decay, 8 TeV [145] (1407.0608) and [141] (1407.0583). The latter two decay modes are superimposed. The region $\tilde{t}_1$ mass below 100 GeV has not been considered in [141] (1407.0583) for the 4-body decay* [146].

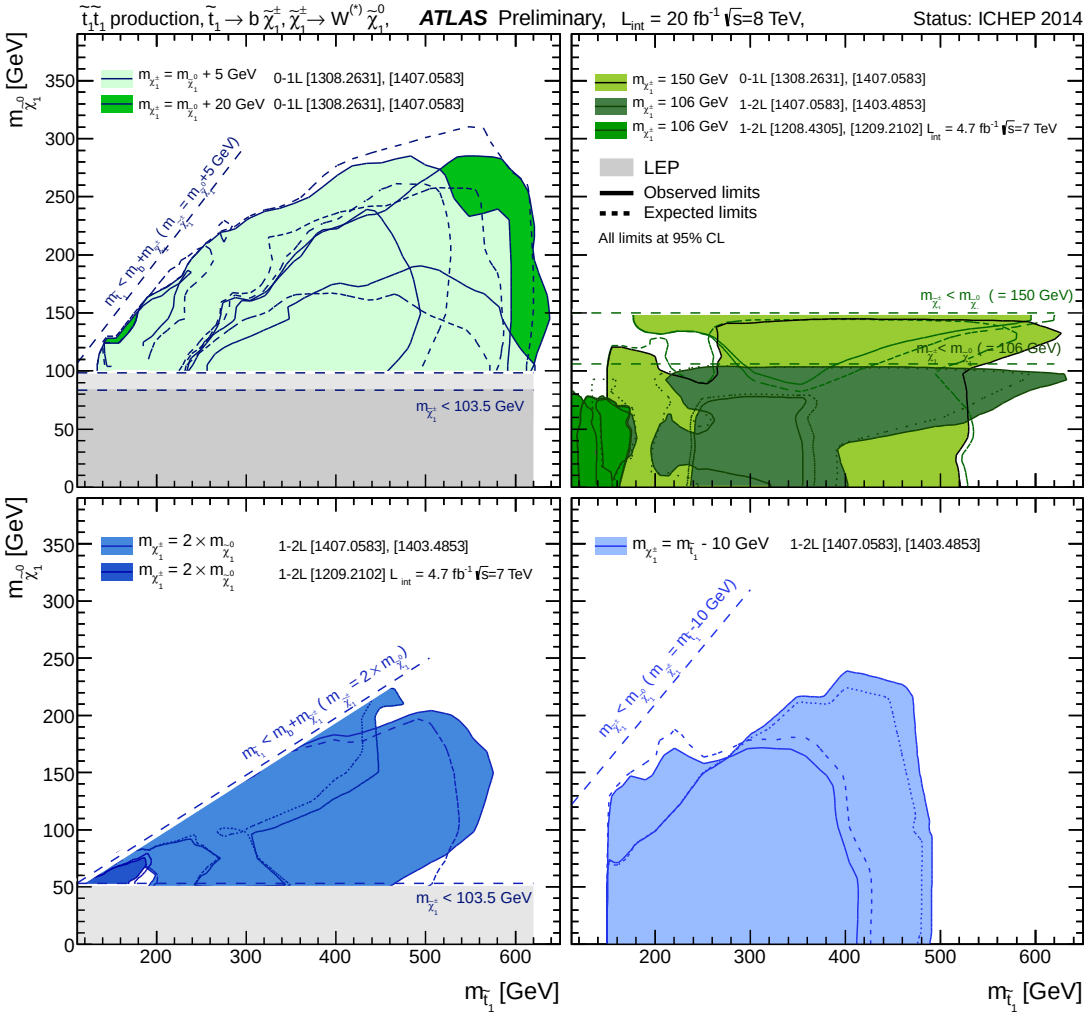

Figure 6.24: *Summary of the searches of the ATLAS experiment for $\tilde{t}_1 \to b\tilde{\chi}_1^{\pm}$ based on 20 fb^{-1} of proton-proton collision data taken at $\sqrt{s} = 8$ TeV, and 4.7 fb^{-1} of proton-proton collision data taken at $\sqrt{s} = 7$ TeV. Exclusion limits at 95% CL are shown in the $(\tilde{t}_1 - \tilde{\chi}_1^0)$-mass plane. The dashed and solid lines show the expected and observed limits, respectively, including all uncertainties except the theoretical signal cross section uncertainty. Different assumptions on the $\tilde{\chi}_1^{\pm}$ and $\tilde{\chi}_1^0$ masses are made, specified in the plots. (7 TeV: [122] (1208.4305) and [107] (1209.2102). 8 TeV: [96] (1308.2631), [141] (1407.0583) and [142] (1403.4853))* [146].

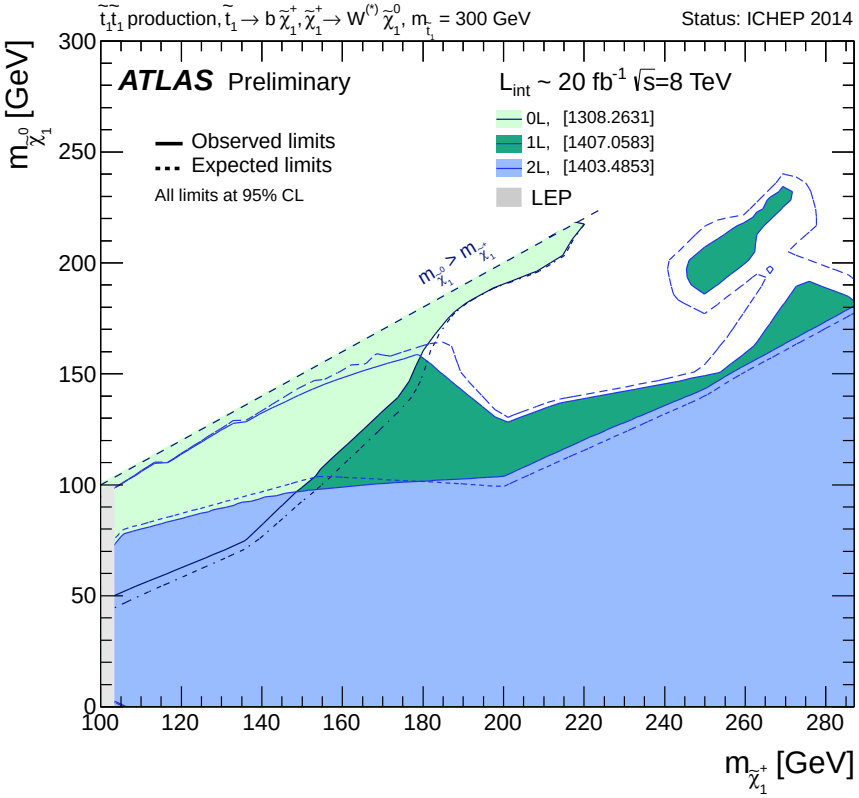

Figure 6.25: *Summary of the searches of the ATLAS experiment for* $\tilde{t}_1 \to b\tilde{\chi}_1^\pm$ *with* $m(\tilde{t}_1) = 300$ *GeV, based on 20* fb^{-1} *of proton-proton collision data taken at* $\sqrt{s} = 8$ *TeV. Exclusion limits at 95% CL are shown in the* $(\tilde{\chi}_1^\pm - \tilde{\chi}_1^0)$*-mass plane. The dashed and solid lines show the expected and observed limits, respectively, including all uncertainties except the theoretical signal cross section uncertainty ([96] (1308.2631), [141] (1407.0583) and [142] (1403.4853))* [146].

6.8 Comparison with the CMS Experiment

The CMS experiment also performed direct stop pair production searches with the 8 TeV dataset in many of the decay modes considered by the ATLAS experiment, without observing any significant deviation of the data with respect to the Standard Model expectation.

The decay mode $\tilde{t}_1 \to t\widetilde{\chi}_1^0$ with 100% BR has been investigated with analyses targeting final states with zero, one and two leptons. Analyses considering orthogonal set of events were combined when appropriate to enhance the sensitivity. The right part of Figure 6.26 shows the 95% CL exclusion limits obtained with the different analyses. By comparing the contours to the corresponding ones in Figure 6.23 it can be noted that the expected exclusion limits obtained by the two experiments are similar, while the observed limit of the CMS experiment analysis targeting high stop masses reaches larger values, due to a deficit of data with respect to the Standard Model expectations in the signal regions driving the result.

The left part of Figure 6.26 shows the 95% CL exclusion limits obtained on the decay mode $\tilde{t}_1 \to c\widetilde{\chi}_1^0$ and the three body decay $\tilde{t}_1 \to Wb\widetilde{\chi}_1^0$. For the first decay mode, the ATLAS and CMS experiments have a similar reach in the region close to the kinematic boundary determined by $m(\tilde{t}_1) = m(W) + m(\widetilde{\chi}_1^0)$, while the ATLAS experiment has a better reach in the region close to the other kinematic boundary, determined by the relation $m(\tilde{t}_1) = m(t) + m(\widetilde{\chi}_1^0)$. For the second decay mode, the reach of the analysis of the CMS experiment is larger, allowing to exclude higher stop and neutralino masses. No results are available on the four body decay $\tilde{t}_1 \to ff'b\widetilde{\chi}_1^0$.

A selection of exclusion limits on $\tilde{t}_1 \to b\widetilde{\chi}_1^\pm$ with 100% BR and varying BR in $\tilde{t}_1 \to b\widetilde{\chi}_1^\pm$ and $\tilde{t}_1 \to t\widetilde{\chi}_1^0$ are shown in Figures 6.27 and 6.28, respectively. A direct comparison of these results to the results produced by the ATLAS experiment and shown in Figures 6.24 and 6.22 is not always easy, as the assumptions on the $\widetilde{\chi}_1^\pm$ and $\widetilde{\chi}_1^0$ masses are different in most cases. In the scenario where the $\widetilde{\chi}_1^\pm - \widetilde{\chi}_1^0$ mass difference is 5 GeV, the reach of the CMS experiment extends towards higher stop masses, while the ATLAS experiment covers a region characterised by low stop masses left uncovered by the CMS experiment.

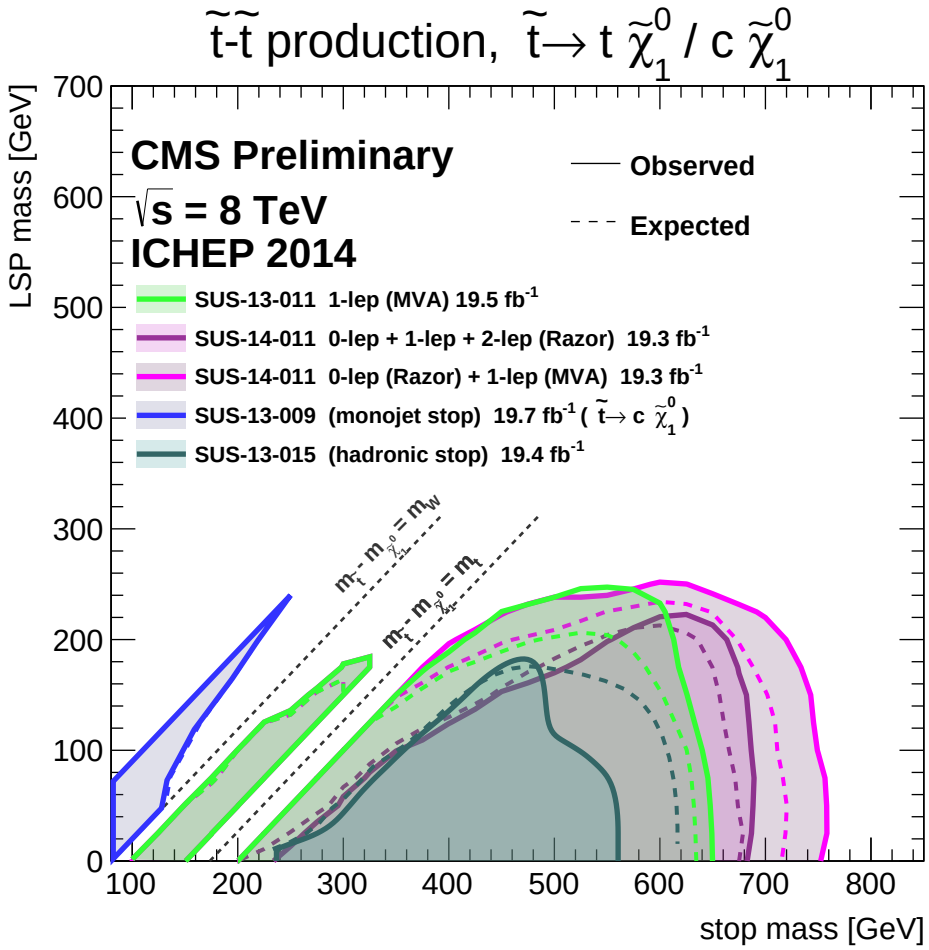

Figure 6.26: *Summary of the searches of the CMS experiment for stop pair production based on about 20 fb^{-1} of proton-proton collision data taken at $\sqrt{s}$ = 8 TeV. Exclusion limits at 95% CL are shown in the $(\tilde{t}_1 - \widetilde{\chi}_1^0)$-mass plane. The dashed and solid lines show the expected and observed limits, respectively, including all uncertainties except the theoretical signal cross section uncertainty. Three decay modes are considered separately with 100% BR: $\tilde{t}_1 \to t\widetilde{\chi}_1^0$ ([148] (SUS-13-011), [150] (SUS-14-011) and [149] (SUS-13-015)), $\tilde{t}_1 \to Wb\widetilde{\chi}_1^0$ (3- body decay for $m(\tilde{t}_1) < m(t) + m(\widetilde{\chi}_1^0)$, [148] (SUS-13-011)) and $\tilde{t}_1 \to c\widetilde{\chi}_1^0$ [147] (SUS-13-009)* [151].

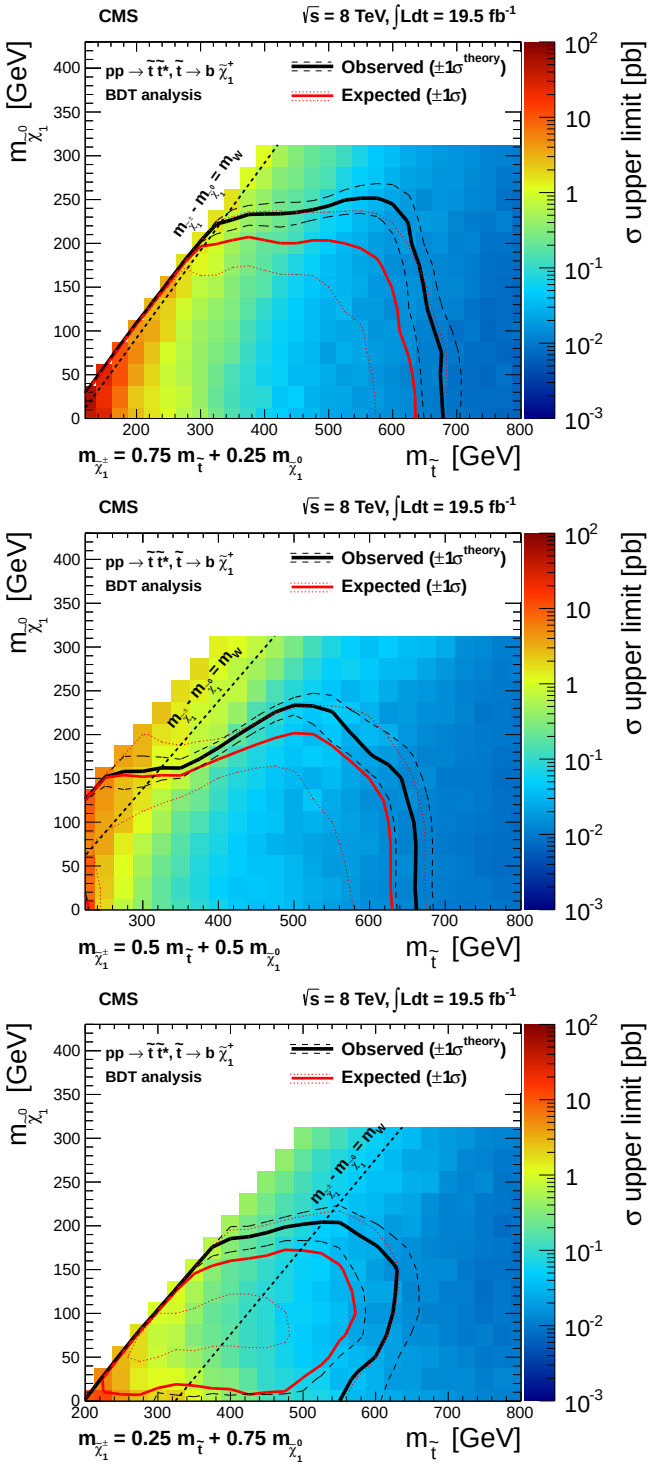

Figure 6.27: *Result of the CMS experiment search for* $\tilde{t}_1 \to b\widetilde{\chi}_1^{\pm}$ *in one lepton final states. The analysis is based on about 20* fb^{-1} *of proton-proton collision data taken at* $\sqrt{s} = 8$ *TeV. Exclusion limits at 95% CL are shown in the* $(\tilde{t}_1 - \widetilde{\chi}_1^0)$*-mass plane. The red and black lines show the expected and observed limits, respectively, The results are shown for* $m(\widetilde{\chi}_1^{\pm} = 0.75m(\tilde{t}_1) + 0.25m(\widetilde{\chi}_1^0))$ *(top),* $m(\widetilde{\chi}_1^{\pm} = 0.50m(\tilde{t}_1) + 0.50m(\widetilde{\chi}_1^0))$ *(middle),* $m(\widetilde{\chi}_1^{\pm} = 0.25m(\tilde{t}_1) + 0.75m(\widetilde{\chi}_1^0))$ *(bottom)* [148].

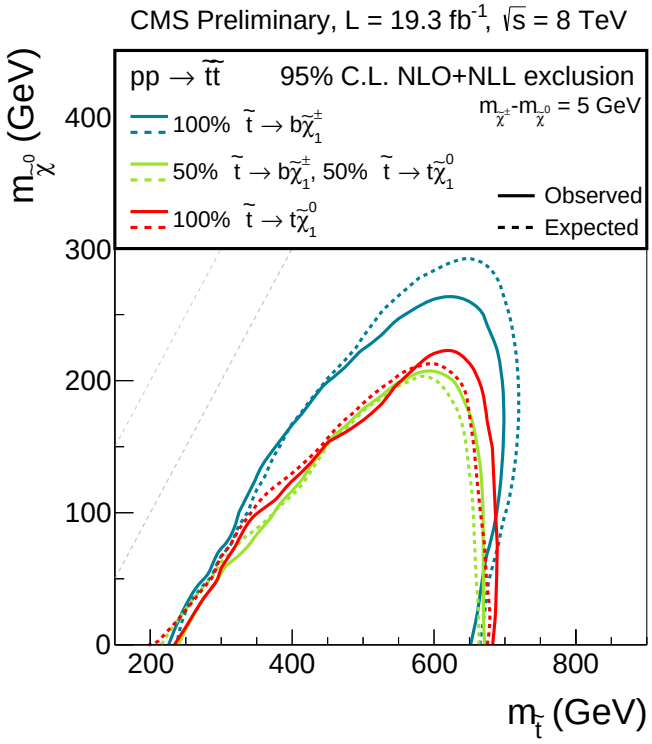

Figure 6.28: *Result of the CMS experiment search for stop pair production decaying into top neutralino and b-quark chargino. The analysis is based on about 20 fb^{-1} of proton-proton collision data taken at $\sqrt{s}$ = 8 TeV. Exclusion limits at 95% CL are shown in the $(\tilde{t}_1 - \tilde{\chi}_1^0)$-mass plane. The dashed and solid lines show the expected and observed limits, respectively, including all uncertainties except the theoretical signal cross section uncertainty. The results are shown for a chargino-neutralino mass difference of 5 GeV separately for $BR(\tilde{t}_1 \to t\tilde{\chi}_1^0)$=100%, $BR(\tilde{t}_1 \to b\tilde{\chi}_1^{\pm})$=100% and $BR(\tilde{t}_1 \to t\tilde{\chi}_1^0)$=$BR(\tilde{t}_1 \to b\tilde{\chi}_1^{\pm})$=50%* [150].

Chapter 7

Preparation for ATLAS Run-2

7.1 Stop Pair Production Searches in Run-2

This year the ATLAS experiment will restart collecting data at a centre-of-mass energy of the collisions of 13 TeV, opening the Run-2.

The search for SUSY particles and in particular for pair production of top squarks will continue to be an important part of the physics program of the experiment. The idea of natural Supersymmetry, driving many searches, has been challenged by the limits set during Run-1, but not ruled out. Even under the strong assumptions of 100% branching ratio decays, the exclusion limits are still in the sub-TeV range, below 700 GeV in all the cases considered. These limits get weaker when the assumptions on the branching ratio in a single decay mode is loosened. Furthermore, some regions of the parameter space of the scenarios considered were left uncovered by the Run-1 analyses.

The searches for direct stop pair production during Run-2 need to be designed to explore all the possibilities not excluded in Run-1. Closing the gaps and expanding the reach of the searches towards higher masses are important goals. Considering the scenario $\tilde{t}_1 \to t\widetilde{\chi}_1^0$ with 100% branching ratio, it will be possible to have sensitivity to a 700 GeV $\tilde{t}_1$ for an almost massless $\widetilde{\chi}_1^0$ with about 3.5 fb^{-1} of data collected at $\sqrt{s} = 13$ TeV. Also continuing the effort started during Run-1 of designing analyses sensitive to scenarios where more than one decay mode is possible is a priority. In this context, in addition to the simplified models used to optimise the searches and interpret the results during Run-1, the use of more physics inspired models, as for example the phenomenological MSSM models introduced in Ref. [152] (where the MSSM parameter space is reduced with a set of experimentally motivated assumptions and constraints), is a crucial point.

7.2 Tracking in Dense Environment

7.2.1 Track Reconstruction Efficiency

Because of the increase in the centre-of-mass energy of the proton-proton collisions foreseen for Run-2, many interesting physics processes will be characterised by very collimated and energetic final state objects.

For direct stop pair production searches, and in general for searches for third generation squarks, the capability of tagging energetic b-jets in environments characterised by a high density of particles is a crucial requirement. Among the aspects concurring to this goal, an important point is a tracking algorithm able to resolve tracks close to each other.

The work performed in the context of this thesis allowed to understand which modification to the track reconstruction algorithm can lead to higher reconstruction efficiency when the separation between the tracks at the first layer of the pixel detector approaches the size of the pixel sensors.

A sample of 500000 Monte Carlo simulated events of single B^0 mesons with p_{T} between 20 GeV and 1 TeV and $|\eta| < 1$ has been used as benchmark scenario of an environment characterised by close-by tracks and highly energetic particles. The tracks of the sample have been reconstructed applying the neural network based clustering algorithm introduced in Section 3.2, meant to split the clusters formed in the pre-processing stage of the track reconstruction algorithm which are likely to be produced by more than one particle.

To perform the study, different objects have been considered: particles, pseudo-tracks and tracks.

The particles considered are the decay products of the B^0 mesons. Only charged particles have been selected, as these are the particles which can be reconstructed exploiting the ID information. The particles are required to be produced before the last layer of the pixel detector. In particular, only particles originated within a distance of 10 cm from the interaction point are retained. Secondary particles originated from interactions with the detector material have been excluded from the study.

The concept of pseudo-tracks, or truth tracks, was introduced in Ref. [153]. Pseudo tracks are tracks built starting from the information on the hits left in the different layers of the ID by the simulated particles, rather than reconstructed with the procedure described in Section 3.2. Pseudo-tracks represent the ideal limit of the track reconstruction algorithm, therefore are a good tool to study the track reconstruction efficiency.

Figures 7.1(a) and 7.1(b) show the p_{T} and η distributions for all the reconstructed tracks, for all the pseudo-tracks, and for all the particles in each event.

To understand the performance of the track reconstruction algorithm in environments characterised by a high density of particles, tracks and pseudo-tracks have been matched to the charged particles they originate from by exploiting the information of the Monte

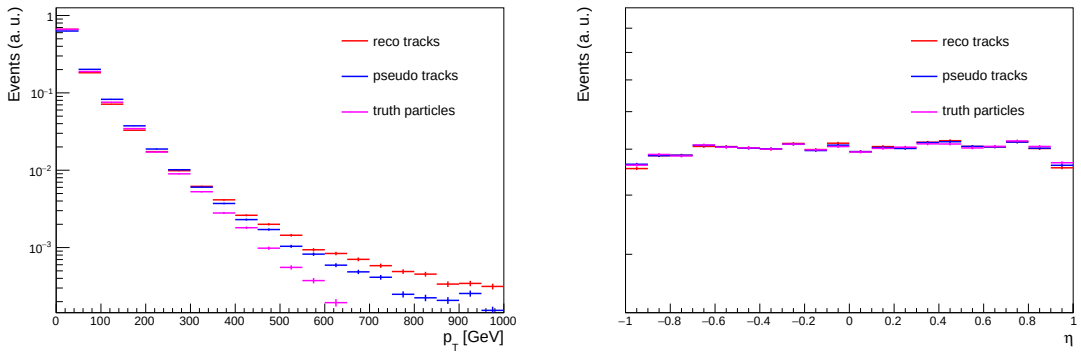

(a) (b)

Figure 7.1: *Distributions of (a) p_{T}, and (b) η for the reconstructed tracks, the pseudo-tracks and the particles in each event, normalised to unit area.*

Carlo simulation, and the matching efficiency for different quantities and for different p_{T} ranges of the B^0 meson studied.

Figures 7.2, 7.3 and 7.4 show the efficiency of matching the pseudo-tracks and the reconstructed tracks to the particles they originate from (from now on denoted as *truth efficiency* and *reconstruction efficiency*), as a function of p_{T} and η of the particles, and as a function of the distance from the interaction point at which the particle was generated. Since pseudo-tracks are formed exploiting the record of the interactions of the particles with the detector, the truth efficiency represents the efficiency of an ideal track reconstruction algorithm, able to identify the tracks in an event without fake rate. The loss of efficiency becomes relevant for events with B^0 mesons of p_{T} larger than 200 GeV. It is independent on the η coordinate of the objects and increases with the distance from the interaction point at which the particle was generated.

To determine how the density of tracks impacts the performance of the tracking algorithm, the efficiency of matching the pseudo-tracks to the reconstructed tracks as a function of their distance from the closest pseudo-track is evaluated. Only pseudo-tracks which are matched to particles are considered for this study. Figure 7.5 shows how the efficiency significantly decreases as the distance between the tracks evaluated at the first layer of the pixel detector approaches the pixel size and how, on contrast, it is close to one when the tracks are separated enough to leave hits on two different pixel sensors.

The reconstruction efficiency has been further studied considering different variables. Figure 7.6(a) shows the efficiency of matching pseudo-tracks to tracks, as a function of the amount of charge deposited in the first layer of the pixel detector. This quantity is expected to increase with the number of particles from which the tracks originate. The figure shows

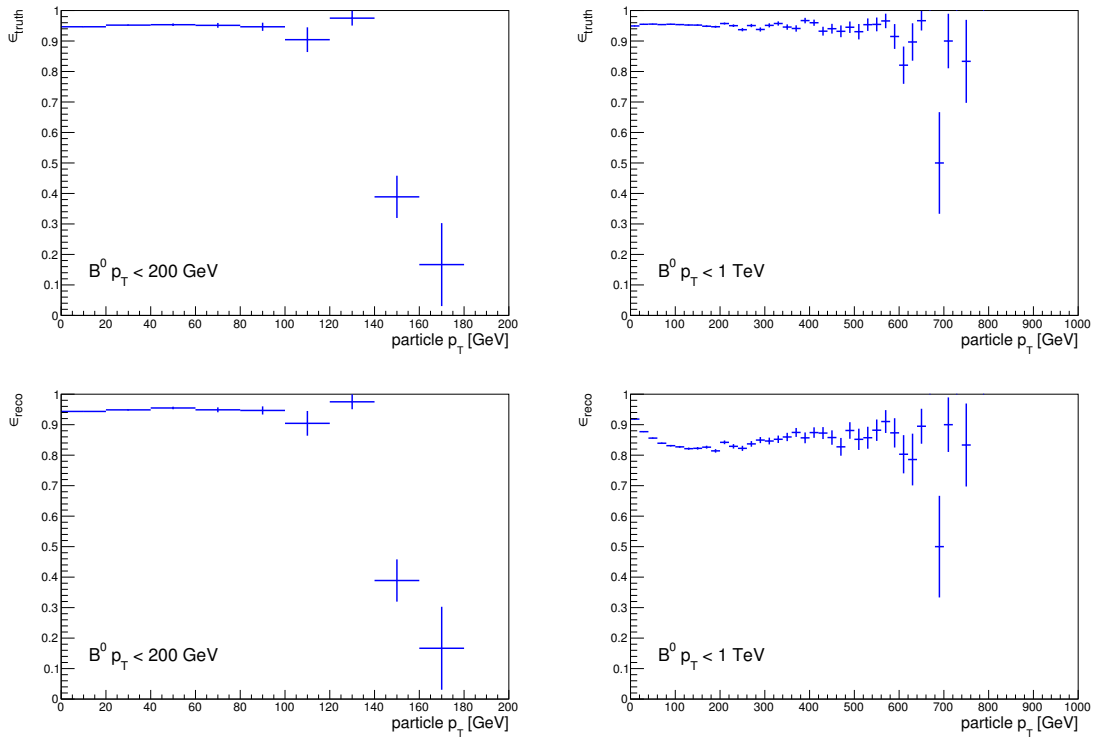

Figure 7.2: *Truth (top row) and reconstruction (bottom row) efficiency, as defined in the text, for events with B^0 $p_{\mathrm{T}} < 200$ GeV (left column) and B^0 $p_{\mathrm{T}} < 1$ TeV (right column), as a function of the p_{T} of the particles associated to the tracks.*

that the efficiency decreases as the amount of charge deposited increases, hinting towards an inefficiency in splitting the clusters as the number of particles gets higher. To test this hypothesis, the same efficiency curve has been produced for a sample obtained by replacing the default neural network algorithm splitting the clusters with an algorithm which exploits the information of the Monte Carlo simulation about the particles crossing the ID, and therefore not subject to any ambiguity on how to split clusters originated from two or more particles. The result is shown in Figure 7.6(b). The figure shows that the efficiency is rather independent on the amount of charge collected when there is no ambiguity about how to split the clusters and associate them to the corresponding tracks.

7.2.2 Modification to the Track Reconstruction Algorithm

In the previous section it has been shown that tracks originated from energetic particles, as B^0 mesons with transverse momenta up to 1 TeV, can have a distance smaller than the size of the pixel sensors of the ID. This condition leads to a loss of reconstruction efficiency, which can reduce the performance of the b-tagging algorithms.

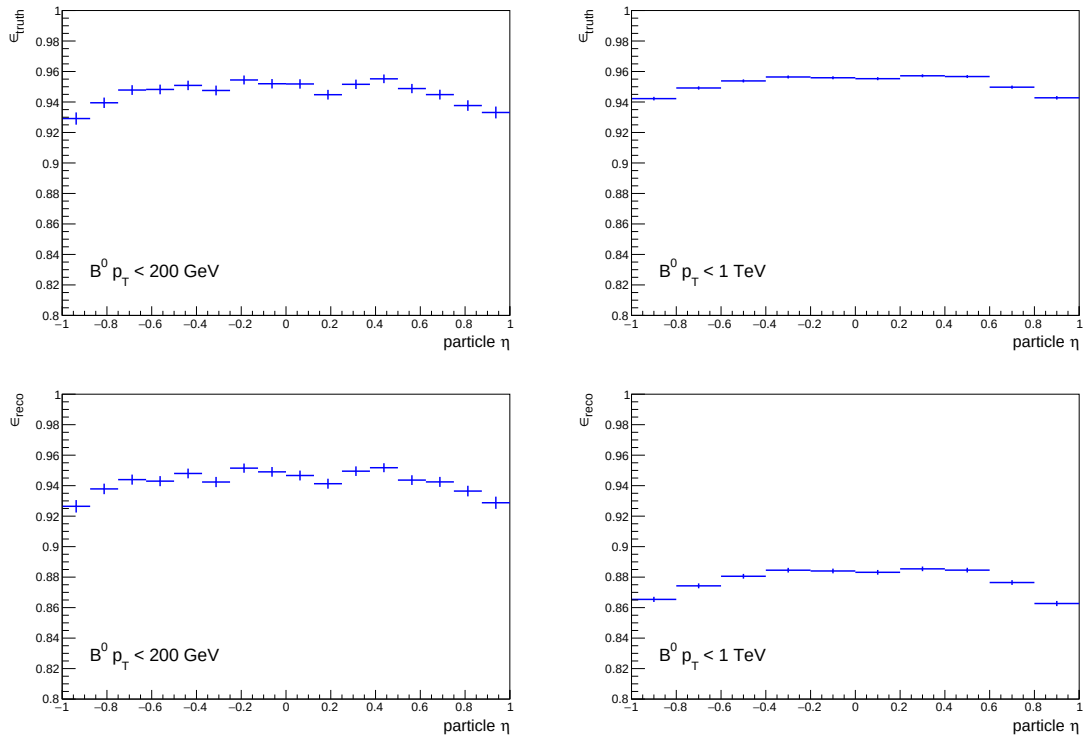

Figure 7.3: *Truth (top row) and reconstruction (bottom row) efficiency, as defined in the text, for events with B^0 $p_{\mathrm{T}} < 200$ GeV (left column) and B^0 $p_{\mathrm{T}} < 1$ TeV (right column), as a function of the η of the particles associated to the tracks.*

A source of inefficiency has been identified in the cluster splitting stage. In the default reconstruction procedure, the clusters are split before the track-finding algorithm is run and track candidates are formed. As a consequence, important information, as the information on the track incident angle, cannot be exploited by the splitting algorithm. On contrast, if the track candidates are formed before the splitting of the clusters is performed, a more precise determination of which hits to assign to a track is possible, because the information on the fitted trajectories are available. This choice has also the advantage of requiring less computational time because the cluster splitting algorithm is run on a smaller collection of inputs.

The study presented in this chapter served as a basis to identify which step of the track reconstruction algorithm could be modified to obtain good performance in environments characterised by a high density of tracks, a condition that will characterise many interesting physics processes during Run-2. Moving the neural network splitting algorithm from cluster formation to within the ambiguity resolving stage is the core of the modification to the track reconstruction procedure that has been shown to lead to higher reconstruction

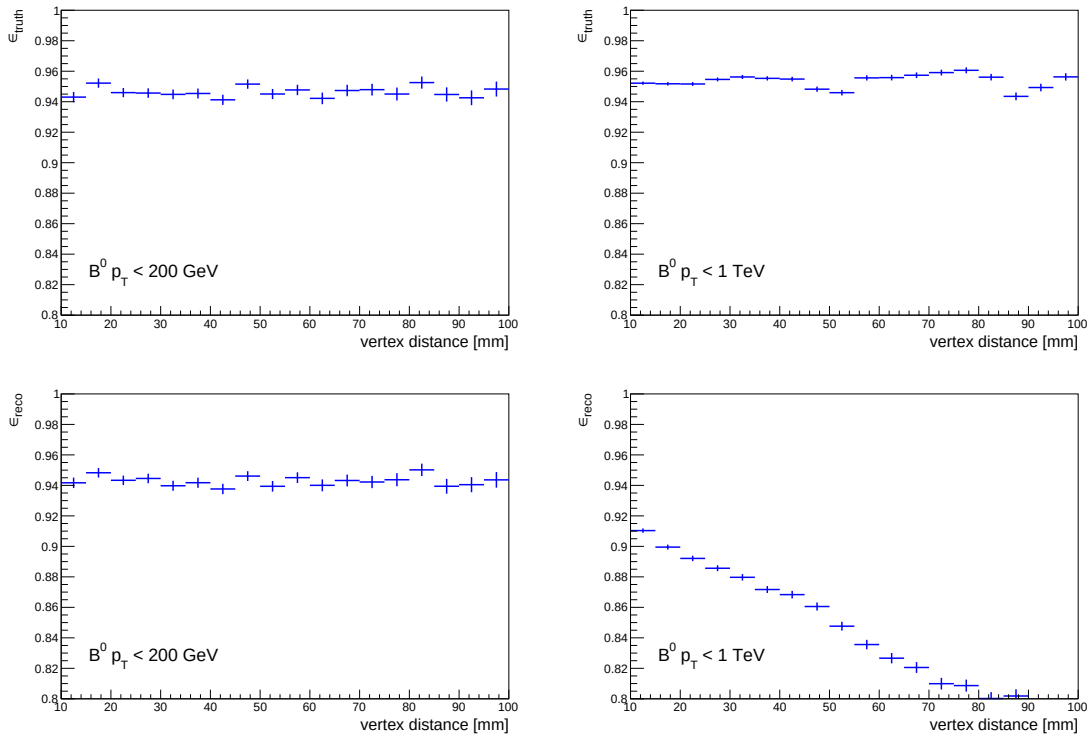

Figure 7.4: *Truth (top row) and reconstruction (bottom row) efficiency, as defined in the text, for events with B^0 $p_T < 200$ GeV (left column) and B^0 $p_T < 1$ TeV (right column), as a function of the distance from the interaction point at which the particle was generated.*

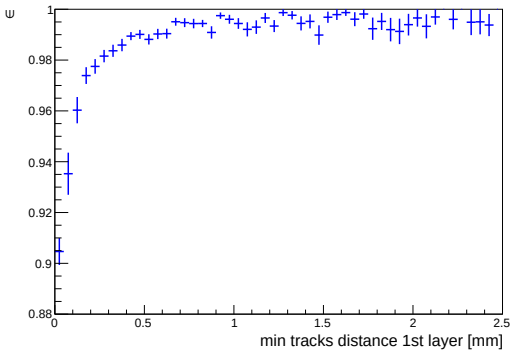

Figure 7.5: *Efficiency of matching pseudo-tracks to tracks as a function of their distance evaluated at the firsst layer of the pixel detector from the closest pseudo-track.*

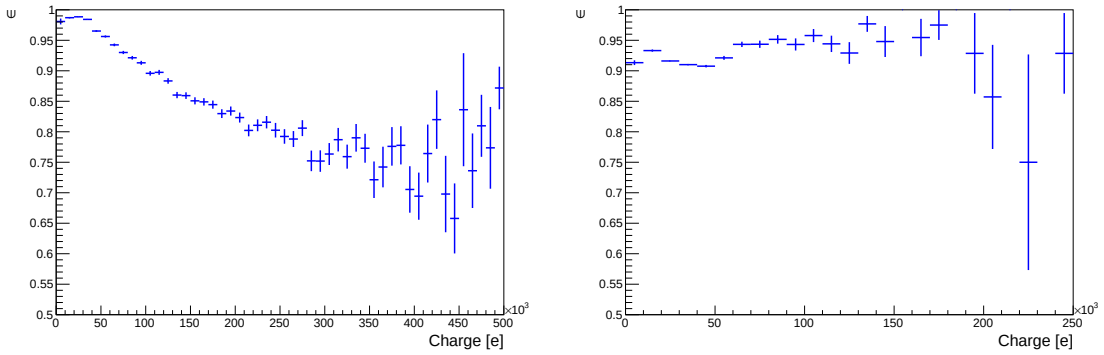

(a) (b)

Figure 7.6: *Efficiency of matching pseudo-tracks to tracks as a function of the charge deposited in the first layer of the pixel detector (a) for a sample where the clusters are split with the neural network clustering algorithm, and (b) for a sample where the clusters are split with an alogorithm exploiting the information on the particles from which the tracks originate.*

efficiency and lower fake rate, and will be adopted in the official track reconstruction procedure for Run-2.

Chapter 8

Summary

The LHC (Large Hadron Collider), is a hadron collider able to accelerate protons to unprecedented energies. Between 2010 and 2012 it operated at a centre-of-mass energy of the proton-proton collisions of 7 and 8 TeV. Its general-purpose experiments, ATLAS (A Toroidal LHC Apparatus) and CMS (Compact Muon Spectrometer) collected data corresponding to about 5 fb^{-1} at $\sqrt{s} = 7$ TeV and 20 fb^{-1} at $\sqrt{s} = 8$ TeV. The LHC and its experiments have been built with the main motivations of searching for the Higgs boson, discovered by the ATLAS and CMS experiments in 2012, and searching for signals of Supersymmetry. There are strong theoretical reasons to expect the supersymmetric particles to lie at the TeV energy scale, which would make them accessible at the LHC.

In the Minimal Supersymmetric Standard Model, the lightest superpartner of the top quark, light stop (symbol $\tilde{t}_1$) is very likely to be lighter than the superpartners of the other quarks. This thesis focuses on the search for direct stop pair production with the data collected by the ATLAS experiment. Two analyses have been performed, addressing different final states and decay modes.

The first analysis targets stop masses close to the mass of the top quark, ideal to solve the hierarchy problem. The mass spectrum assumed is such that $m(\tilde{t}_1) \lesssim m(t)$ and $m(\widetilde{\chi}_1^{\pm}) + m(b) < m(\tilde{t}_1)$ (where t and b indicate the top and bottom quarks, respectively, and the symbol $\widetilde{\chi}_1^{\pm}$ represents the lightest chargino). Under this assumption, the decay mode $\tilde{t}_1 \to b\widetilde{\chi}_1^{\pm}$ is favoured. The chargino is assumed to further decay via $\widetilde{\chi}_1^{\pm} \to W^{(*)}\widetilde{\chi}_1^0$. The analysis targets scenarios in which both W bosons are assumed to decay leptonically. The expected final state is therefore composed of two b-jets, two leptons of opposite charge, and missing transverse energy ($E_{\text{T}}^{\text{miss}}$) due to the presence of the $\widetilde{\chi}_1^0$, which is assumed to be the LSP. To enhance the acceptance of the analysis to the signal, in the event selection process only one of the jets is required to be b-tagged. The same final state is expected from di-leptonic decays of top-antitop ($t\bar{t}$) pairs, that is therefore the main background to this search. To discriminate signal and background, the final state objects are used

to construct the $\sqrt{s}_{\mathrm{min}}^{(\mathrm{sub})}$ variable, providing the minimum energy compatible with the mass scale of the subsystem of interest. This variable is expected to peak at $\sim 2m(t)$ for the $t\bar{t}$ background, while for the signal the position of the peak depends on the $\tilde{t}_1$ mass. Further discriminating power is given by the different masses of the invisible particles in signal and background. Two regions where the presence of the signal is enhanced have been defined, called signal regions. A careful estimation of the background from Standard Model processes has been performed, and the background prediction compared to the number of events observed in data. No significant excess of data over the Standard Model expectation, hinting towards the presence of signals from new physics processes, has been observed. The results have been interpreted in terms of 95% CL exclusion limits. Both model-independent exclusion limits on the number of signal events from new physics processes and model-dependent exclusion limits have been derived. The model-dependent limits are given in the $(\tilde{t}_1 - \widetilde{\chi}_1^0)$-mass plane, under different hypotheses on the masses of the supersymmetric particles. They have been derived combining the results of the two-lepton analysis briefly described above with the results of an analysis performed in the one-lepton channel conduced in parallel, optimised on the same scenarios and showing a similar sensitivity. A wide range of stop masses around and below the top mass have been excluded. In particular, in the scenario where the chargino mass is set to twice the neutralino mass, that has been explored for the first time with this analysis, stop masses between 120 GeV and the top mass have been excluded for a neutralino mass of 55 GeV. For a chargino mass just above the experimental limit of 106 GeV set by LEP, stop masses between 120 GeV and the the top mass are excluded for a neutralino mass of 55 GeV, and masses between 130 and 155 GeV are excluded for a neutralino mass of 75 GeV. These results significantly extend the limits available on this scenario from searches at the Tevatron and from a previous search of the ATLAS collaboration.

The rise of the centre-of-mass energy of the proton-proton collisions from 7 to 8 TeV made possible the exploration of higher stop masses. An analysis targeting stop masses between 300 and 700 GeV has been performed in the hadronic channel, characterised by the largest branching ratio and therefore suitable to address scenarios where the top squark mass is high.

The stop is assumed to decay via $\tilde{t}_1 \to t\widetilde{\chi}_1^0$ and $\tilde{t}_1 \to b\widetilde{\chi}_1^{\pm}$. Scenarios where both decay modes are present simultaneously with different branching ratios have been considered for the first time. Three different signal regions optimised for different values of the stop mass and different assumptions on the branching ratios in the two decay modes have been defined. The nominal signature of the signal is six jets, out of which two are b-jets, and $E_{\mathrm{T}}^{\mathrm{miss}}$. The number of jets can be reduced if the mass spectrum is compressed, or if the top quarks produced in the decay of the stop have significant boost, and therefore its decay products are very collimated.

The main backgrounds to this search are $t\bar{t}$ production, W and Z boson production in association with heavy flavour jets. The estimation of this last source of background is particularly challenging, because the signal regions requirements make any control sample have a few events in it. To overcome this problem, a technique has been developed to measure the fraction of Z boson plus four to six jets events having at least two b-tagged jets. This technique allows to define the control sample without any requirement on the number of b-tagged jets, and thus to significantly reduce the uncertainty on the estimation of this background.

The numbers of events observed in data in the different signal regions have been compared to the background prediction. No significant excess has been observed, therefore exclusion limits have been set. To derive model-dependent limits, the results of the signal regions have been combined. The results are given in the $(\tilde{t}_1 - \widetilde{\chi}_1^0)$-mass plane for different values of the branching ratio BR($\tilde{t}_1 \to t\widetilde{\chi}_1^0$)=1-BR($\tilde{t}_1 \to b\widetilde{\chi}_1^{\pm}$). For BR($\tilde{t}_1 \to t\widetilde{\chi}_1^0$)=100%, stop masses between 270 and 546 GeV are excluded for a neutralino lighter than 30 GeV. These limits significantly extend the previous results. For BR($\tilde{t}_1 \to t\widetilde{\chi}_1^0$)=50%, stop masses between 250 and 550 GeV are excluded for a neutralino lighter than 60 GeV.

The searches performed in the context of this thesis and other results from the ATLAS and CMS collaborations allowed to exclude a large variety of stop masses under different assumptions on the decay modes and on the mass spectra. Nevertheless, even under the strong assumptions of 100% branching ratio decays, the exclusion limits are still in the sub-TeV range.

This year the ATLAS experiment will restart collecting data at the increased centre-of-mass energy of the proton-proton collisions of 13 TeV. The searches for direct stop pair production will continue to be of primary importance in the physics program of ATLAS, and need to be designed to explore all the possibilities not covered so far.

Due to the increase in the centre-of-mass energy, many interesting final states will be characterised by very collimated and energetic decay products. The capability of tagging energetic b-jets in environments characterised by a high density of particles will therefore be an important requirement for stop searches. Among the aspects concurring to this goal, a tracking algorithm able to resolve tracks close to each other is of crucial importance. In view of this, the reconstruction efficiency of the track reconstruction algorithm of the ATLAS experiment has been studied on a simulated sample of B^0 mesons. This study contributed to the identification of a step of the track reconstruction procedure that needs to be modified to achieve good performance in case the tracks originate from particles which have a separation below the size of the pixel sensors of the tracker of the ATLAS experiment.

Bibliography

[1] UA1 Collaboration, "Experimental Observation of Isolated Large Transverse Energy Electrons with Associated Missing Energy at $\sqrt{s}$ = 540 GeV", Phys. Lett. B 122 (1983) 103-116.

[2] UA2 Collaboration, "Observation of Single Isolated Electrons of High Transverse Momentum in Events with Missing Transverse Energy at the CERN $\overline{p}p$ Collider", Phys. Lett. B 122 (1983) 476-485.

[3] UA1 Collaboration, "Experimental Observation of Lepton Pairs of Invariant Mass Around 95 GeV/c^2 at the CERN SPS Collider", Phys. Lett. B 126 (1983) 398-410.

[4] UA2 Collaboration, "Evidence for $Z^0 \to e^+e^-$ at the CERN $\overline{p}p$ Collider", Phys. Lett. B 129 (1983) 130-140.

[5] CDF Collaboration, "Observation of Top Quark Production in $\overline{p}p$ Collisions", Phys. Rev. Lett. 74 (1995) 2626.

[6] D0 Collaboration, "Observation of the Top Quark", Phys. Rev. Lett. 74 (1995) 2632.

[7] The ATLAS Collaboration, "Observation of a New Particle in the Search for the Standard Model Higgs Boson with the ATLAS Detector at the LHC", Physics Letters B 716 (2012) 1-29.

[8] The CMS collaboration, "Observation of a new boson at a mass of 125 GeV with the CMS experiment at the LHC". Physics Letters B 716 (2012) 30-61.

[9] M. E. Peskin, Daniel V. Schroeder, "An Introduction to Quantum Field Theory", Westview Press, 1995.

[10] D. Griffith, "Introduction to elementary Particles", Wiley-VCH, 2004.

[11] F. Halzen and A. D. Martin, "Quarks and Leptons: An Introductory Course in Modern Particle Physics", John Wiley & Sons, Inc., 1984.

[12] S. P. Martin, "A Supersymmetry primer", arXiv:9709356.

[13] M. Papucci, J. T. Ruderman and A. Weiler, "Natural SUSY Endures", JHEP 1209 (2012) 035.

[14] ALEPH Collaboration, "Determination of the number of light neutrino species", Phys. Lett. B231(4) 519-529 (1989).

[15] C. S. Wu, E. Ambler, R. W. Hayward, D. D. Hoppes, "Experimental Test of Parity Conservation in Beta Decay". Physical Review 105 (4): 1413-1415 (1957).

[16] R. L. Garwin, L. M. Lederman, M. Weinrich, "Observations of the Failure of Conservation of Parity and Charge Conjugation in Meson Decays: The Magnetic Moment of the Free Muon", Physical Review 105 (4): 1415â1417 (1957).

[17] The ALEPH Collaboration, the DELPHI Collaboration, the L3 Collaboration, the OPAL Collaboration, the SLD Collaboration, the LEP Electroweak Working Group, the SLD electroweak, heavy flavour groups, "Precision Electroweak Measurements on the Z Resonance", Phys. Reports 427, 257 (2006).

[18] A.V. Artamonov et al., "New Measurement of the $K^+ \to \pi^+\nu\bar{\nu}$ Branching Ratio", Phys. Rept. 427: 257-454 (2006).

[19] K.A. Olive et al. (Particle Data Group), Chin. Phys. C, 38, 090001 (2014).

[20] Nambu, Y. "Quasiparticles and Gauge Invariance in the Theory of Superconductivity". Physical Review 117: 648-663 (1960).

[21] J. Goldstone, A. Salam, S. Weinberg, "Broken Symmetries". Physical Review 127: 965-970 (1962).

[22] The ATLAS Collaboration, "Measurement of the Higgs boson mass from the $H \to \gamma\gamma$ and $H \to ZZ^*4\ell$ channels with the ATLAS detector using 25 fb^{-1} of pp collision data", Phys. Rev. D 90, 052004 (2014).

[23] The CMS Collaboration, "Precise determination of the mass of the Higgs boson and studies of the compatibility of its couplings with the standard model", CMS-PAS-HIG-14-009 (2014).

[24] G. Dissertori, I.G. Knowles, M. Schmelling, "Quantum Chromodynamics, High Energy Experiments and Theory" International Series of Monographs on Physics 115.

[25] Planck Collaboration, "Planck 2013 results. I. Overview of products and scientific results", Astron.Astrophys. 571 (2014) A1.

[26] Georgi, H., Glashow, S.L., "Unity of All Elementary Particle Forces", Physical Review Letters 32: 438-441 (1974).

[27] M. C. Gonzalez-Garcia, M. Maltoni, "Phenomenology with Massive Neutrinos", Physics Reports 460: 1-129 (2008).

[28] R. Haag, J. Lopuszanski, and M. Sohnius, Nucl. Phys. B 88, 257 (1975).

[29] S. Coleman and J. Mandula, Phys. Rev. 159 (1967) 1251.

[30] L. J. Hall, J. D. Lykken and S. Weinberg, "Supergravity as the Messenger of Supersymmetry Breaking", Phys. Rev. D27 (1983) 2359-2378.

[31] M.L. Brooks et al. [MEGA Collaboration], Phys. Rev. Lett. 83, 1521 (1999), Phys. Rev. D 65, 112002 (2002).

[32] M. Ciuchini et al., JHEP 9810, 008 (1998).

[33] J. Ellis, S. Ferrara and D.V. Nanopoulos, Phys. Lett. B 114, 231 (1982); W. Buchmeuller and D. Wyler, Phys. Lett. B 121, 321 (1983); J. Polchinski and M.B. Wise, Phys. Lett. B 125, 393 (1983); F. del Aguila, M.B. Gavela, J.A. Grifols and A. Mendez, Phys. Lett. B 126, 71 (1983) [Erratum-ibid. B 129, 473 (1983)]; D.V. Nanopoulos and M. Srednicki, Phys. Lett. B 128, 61 (1983).

[34] M. Carena, S. Heinemeyer, O. Stål, C.E.M. Wagner, G. Weiglein, "MSSM Higgs Boson Searches at the LHC: Benchmark Scenarios after the Discovery of a Higgs-like Particle", Eur. Phys. J. C73 (2013) 2552.

[35] The ATLAS Collaboration, "Search for the neutral Higgs bosons of the Minimal Supersymmetric Standard Model in pp collisions at $\sqrt{s}$=7 TeV with the ATLAS detector", JHEP02 (2013) 095.

[36] L. Evans and P. Bryant, "LHC Machine", JINST 3 (2008) S08001.

[37] https://espace.cern.ch/acc-tec-sector/default.aspx

[38] The ATLAS Collaboration, "The ATLAS Experiment at the CERN Large Hadron Collider", JINST 3 (2008) S08003.

[39] The CMS Collaboration, "The CMS Experiment at the CERN LHC", JINST 3 (2008) S08004.

[40] The LHCb Collaboration, "The LHCb Detector at the LHC", JINST 3 (2008) S08005.

[41] The ALICE Collaboration, "The ALICE Experiment at the CERN LHC", JINST 3 (2008) S08002.

[42] J. M. Campbell, J. W. Huston, W. J. Stirling, "Hard Interactions of Quarks and Gluons: a Primer for LHC Physics", Rept.Prog.Phys.70 (2007):89.

[43] https://twiki.cern.ch/twiki/bin/view/AtlasPublic/LuminosityPublicResults

[44] S. D. Drell and T. M. Yan, Ann. Phys. 66 (1971) 578.

[45] J. C. Collins and D. E. Soper, Ann. Rev. Nucl. Part. Sci. 37 (1987) 33.

[46] V. Sudakov, Zh. Eksp. Teor. Fiz. 30, 87 (1956); (Eng. trans) Sov. Phys. JETP 3, 65 (1956).

[47] Y. L. Dokshitzer, "Calculation of the Structure Functions for Deep Inelastic Scattering and e^+e^- Annihilation by Perturbation Theory in Quantum Chromodynamics", Sov. Phys. JETP 46 (1977) 641-653.

[48] V. Gribov and L. Lipatov, "Deep inelastic e p scattering in perturbation theory", Sov. J. Nucl. Phys. 15 (1972) 438-450.

[49] G. Altarelli and G. Parisi, "Asymptotic Freedom in Parton Language", Nucl. Phys. B 126 (1977) 298.

[50] J, Gao, M. Guzzi, J. Huston, H.-L. Lai, Z. Li, P. Nadolsky, J. Pumplin, D. Stump , C.-P. Yuan, "CT10 next-to-next-to-leading order global analysis of QCD", Phys. Rev. D 89 (2014) 3, 033009.

[51] A.D. Martin, W.J. Stirling, R.S. Thorne, G. Watt, "Parton distributions for the LHC", Eur. Phys. J. C 63 (2009): 189-285.

[52] A.D. Martin, R. G. Roberts, W.J. Stirling, R.S. Thorne, "Physical Gluons and High E_T Jets", Phys. Lett. B 604 (2004), 61.

[53] https://nnpdf.hepforge.org

[54] A. M. Cooper-Sarkar on behalf of ZEUS and H1 collaborations, "PDF Fits at HERA", Proceedings of the 2011 Europhysics Conference on High Energy Physics, HEP 2011, July 2011.

[55] The ATLAS Collaboration, "The ATLAS Simulation Infrastructure", Eur.Phys.J.C70 (2010): 823-874.

[56] S. Agostinelli et al., "Geant4 - a simulation toolkit", Nucl. Instr. Methods Phys. Res. A 506 (2003) 250-303.

[57] J. Allison et al., "Geant4 Developments and Applications", IEEE Transactions on Nuclear Science 53 (2006) 270-278.

[58] W. Lukas on behalf of The ATLAS Collaboration, "Fast Simulation for ATLAS: Atlfast-II and ISF", ATL-SOFT-PROC-2012-065, ATL-COM-SOFT-2012-137.

[59] T. Sjoestrand, S. Mrenna and P. Skands, "PYTHIA 6.4 physics and manual", JHEP 05 (2006) 026.

[60] T. Sjostrand, S. Mrenna, P. Skands, "A Brief Introduction to PYTHIA 8.1", Comput. Phys. Commun. 178 (2008): 852-867.

[61] G. Corcella et al., "HERWIG 6: An event generator for hadron emission reactions with interfering gluons (including supersymmetric processes)", JHEP 01 (2001) 010.

[62] M. Bahr, S. Gieseke, M. Gigg, D. Grellscheid, K. Hamilton et al., "Herwig++ Physics and Manual", EPJ C 58 (2008) 639-707.

[63] J. Butterworth, J. Forshaw and M. Seymour, "Multiparton interactions in photoproduction at HERA", Z. Phys. C72 (1996) 637-646.

[64] T. Gleisberg et al., "SHERPA 1.alpha, a proof-of-concept version", JHEP 02 (2004) 056.

[65] T. Gleisberg et al., Event generation with SHERPA 1.1, JHEP 02 (2009) 007.

[66] M. Mangano et al., "ALPGEN, a generator for hard multiparton processes in hadronic collisions", JHEP 07 (2003) 001.

[67] S. Frixione, P. Nason and B.R. Webber, "Matching NLO QCD and parton showers in heavy flavour production", JHEP 08 (2003) 007.

[68] S. Frixione, P. Nason and C. Oleari, "Matching NLO QCD computations with Parton Shower simulations: the POWHEG method", JHEP 11 (2007) 070.

[69] B. P. Kersevan and E. Richter-Was, "The Monte Carlo event generator AcerMC version 2.0 with interfaces to PYTHIA 6.2 and HERWIG 6.5", arXiv:hep-ph/0405247.

[70] T. Stelzer and W. F. Long, "Automatic Generation of Tree Level Helicity Amplitudes", Comput. Phys. Commun. 81 (1994), 357.

[71] J. Alwall et al., "MadGraph 5 : Going Beyond", JHEP 06 (2011) 128.

[72] W. Kilian, T. Ohl, J. Reuter, "WHIZARD: Simulating Multi-Particle Processes at LHC and ILC", Eur.Phys.J.C71 (2011) 1742.

[73] M. Moretti, T. Ohl, J. Reuter, O'Mega, "An Optimizing matrix element generator", LC-TOOL-2001-040-rev.

[74] The ATLAS Collaboration, "Expected Performance of the ATLAS Experiment:Detector, Trigger and Physics", CERN-OPEN-2008-020.

[75] The ATLAS Collaboration, "A neural network clustering algorithm for the ATLAS silicon pixel detector", JINST 9 (2014) P09009.

[76] The ATLAS Collaboration, "Performance of the ATLAS Inner Detector Track and Vertex Reconstruction in the High Pile-Up LHC Environment", ATLAS-CONF-2012-042.

[77] M. Cacciari, G. P. Salam, G. Soyez, "The anti-k_T jet clustering algorithm", JHEP 04 (2008) 005.

[78] The ATLAS Collaboration, "Jet energy measurement with the ATLAS detector in proton-proton collisions at $\sqrt{s} = 7$ TeV", Eur. Phys. J. C 73 (2013) 2304.

[79] The ATLAS Collaboration, "Jet Energy Resolution and Selection Efficiency Relative to Track Jets from In-situ Techniques with the ATLAS Detector Using Proton-Proton Collisions at a Center of Mass Energy $\sqrt{s} = 7$ TeV", ATLAS-CONF-2010-054.

[80] The ATLAS Collaboration, "Commissioning of the ATLAS high-performance b-tagging algorithms in the 7 TeV collision data", ATLAS-CONF-2011-102.

[81] The ATLAS Collaboration, "Measurement of the b-tag Efficiency in a Sample of Jets Containing Muons with 5 fb^{-1} of Data from the ATLAS Detector", ATLAS-CONF-2012-043.

[82] The ATLAS Collaboration, "Expected electron performance in the ATLAS experiment, ATL-PHYS-PUB-2011-006.

[83] The ATLAS Collaboration, "Electron reconstruction and identification efficiency measurements with the ATLAS detector using the 2011 LHC proton-proton collision data", E.P.J. C 74 (2014) 2941.

[84] The ATLAS Collaboration, "Electron efficiency measurements with the ATLAS detector using the 2012 LHC proton-proton collision data ", ATLAS-CONF-2014-032.

[85] The ATLAS Collaboration, "Electron and photon energy calibration with the ATLAS detector using LHC Run 1 data", Eur. Phys. J. C (2014) 74:3071.

[86] The ATLAS Collaboration, "Measurement of the muon reconstruction performance of the ATLAS detector using 2011 and 2012 LHC protonâproton collision data", Eur. Phys. J. C74 (2014) 3130.

[87] The ATLAS Collaboration, "Performance of Missing Transverse Momentum Reconstruction in Proton-Proton Collisions at $\sqrt{s} = 7$ TeV with ATLAS", Eur.Phys.J. C72 (2012) 1844.

[88] The ATLAS Collaboration, "Performance of Missing Transverse Momentum Reconstruction in ATLAS with 2011 Proton-Proton Collisions at $\sqrt{s} = 7$ TeV", ATLAS-CONF-2012-101.

[89] The ATLAS Collaboration, "Performance of Missing Transverse Momentum Reconstruction in ATLAS studied in Proton-Proton Collisions recorded in 2012 at $\sqrt{s} = 8$ TeV", ATLAS-CONF-2013-082.

[90] http://web.physik.rwth-aachen.de/service/wiki/bin/view/Main/SquarksandGluinos

[91] https://twiki.cern.ch/twiki/bin/view/AtlasPublic/SupersymmetryPublicResults

[92] The ATLAS Collaboration,"Search for squarks and gluinos with the ATLAS detector in final states with jets and missing transverse momentum using 4.7 fb^{-1} of $\sqrt{s} = 7$ TeV proton-proton collision data", Phys. Rev. D 87 (2013), 012008.

[93] The ATLAS Collaboration,"Search for squarks and gluinos with the ATLAS detector in final states with jets and missing transverse momentum using $\sqrt{s} = 8$ TeV proton-proton collision data ", JHEP 09 (2014) 176.

[94] The ATLAS Collaboration,"Search for squarks and gluinos using final states with jets and missing transverse momentum with the ATLAS detector in $\sqrt{s} = 7$ TeV proton-proton collisions", ATLAS-CONF-2011-086.

[95] The ATLAS Collaboration,"Search for scalar bottom pair production in final states with missing transverse momentum and two b-jets in pp collisions at $\sqrt{s} = 7$ TeV with the ATLAS detector", ATLAS-CONF-2012-106.

[96] The ATLAS Collaboration,"Search for direct third-generation squark pair production in final states with missing transverse momentum and two b-jets in $\sqrt{s} = 8$ TeV pp collisions with the ATLAS detector", .

[97] https://twiki.cern.ch/twiki/bin/view/AtlasPublic/StandardModelPublicResults

[98] The ATLAS Collaboration, "Luminosity Determination in pp Collisions at $\sqrt{(s)} = 7$ TeV Using the ATLAS Detector at the LHC" , Eur.Phys.J. C71 (2011) 1630, 1101.2185.

[99] The ATLAS Collaboration, "Improved luminosity determination in pp collisions at $\sqrt{(s)} = 7$ TeV using the ATLAS detector at the LHC", Eur. Phys. J. C 73 (2013) 2518.

[100] https://twiki.cern.ch/twiki/bin/viewauth/AtlasProtected/JetEtmissRecommendations2011

[101] https://twiki.cern.ch/twiki/bin/viewauth/AtlasProtected/JetEtmissRecommendations2012

[102] The ATLAS Collaboration Collaboration, "Performance of missing transverse momentum reconstruction in proton-proton collisions at 7 TeV with ATLAS", Eur.Phys.J. C72 (2012) 1844.

[103] M. Kramer et al., "Supersymmetry production cross sections in pp collisions at $\sqrt{s}$ = 7 TeV", arXiv:1206.2892.

[104] A. Read, "Presentation of search results: the CL_s technique", Journal of Physics G: Nuclear and Particle Physics 28, 2693 (2002).

[105] G. Cowan, K. Cranmer, E. Gross and O. Vitells, Eur.Phys.J. C71, 1554 (2011).

[106] M. Baak, G.J. Besjes, D. Cote, A. Koutsman, J. Lorenz, D. Short, "HistFitter software framework for statistical data analysis", arXiv:1410.1280.

[107] The ATLAS Collaboration, "Search for light top squark pair production in final states with leptons and b-jets with the ATLAS detector in $\sqrt{s}$=7 TeV proton-proton collisions", Phys. Lett. B 720 (2013) 13-21.

[108] LEP SUSY Working Group (ALEPH, DELPHI, L3 and OPAL experiments), Notes LEPSUSYWG/01-03.1 and 04-01.1, http://lepsusy.web.cern.ch/lepsusy/Welcome.html.

[109] ALEPH Collaboration, A. Heister et al., "Absolute mass lower limit for the lightest neutralino of the MSSM from e+e- data at $\sqrt{s}$ up to 209 GeV", Phys. Lett. B 583 (2004) 247-263.

[110] DELPHI Collaboration, J. Abdallah et al., "Searches for supersymmetric particles in e+e- collisions up to 208 GeV and interpretation of the results within the MSSM", Eur. Phys. J. C 31 (2003) 421-479.

[111] L3 Collaboration, M. Acciarri et al., "Search for charginos and neutralinos in e+e- collisions at $\sqrt{s}$= 189 GeV", Phys. Lett. B 472 (2000) 420-433.

[112] OPAL Collaboration, G. Abbiendi et al., "Search for chargino and neutralino production at $\sqrt{s}$ 192 GeV to 209 GeV at LEP", Eur. Phys. J. C 35 (2004) 1-20.

[113] P. Konar, K. Kong, K. T. Matchev and M. Park, "RECO level $\sqrt{s}_{min}$ and subsystem $\sqrt{s}_{min}$: improved global inclusive variables for measuring the new physics mass scale in $E_{\rm T}^{\rm miss}$ events at hadron colliders", JHEP 1106 (2011), 041.

[114] P. Konar, K. Kong and K. T. Matchev, "$\sqrt{\hat{s}}_{min}$: A Global inclusive variable for determining the mass scale of new physics in events with missing energy at hadron colliders", JHEP 0903 (2009), 085.

[115] The ATLAS Collaboration, "Measurement of the top quark-pair production cross section with ATLAS in pp collisions at $\sqrt{s} = 7$ TeV", Eur. Phys. J. C 71 (2011) 1577.

[116] The ATLAS Collaboration, "Measurement of the top quark pair production cross section in pp collisions at $\sqrt{s} = 7$ TeV in dilepton final states with ATLAS", Phys. Lett. B 707 (2012).

[117] The ATLAS Collaboration, "Search for a heavy top-quark partner in final states with two leptons with the ATLAS detector at the LHC", JHEP 1211 (2012) 094.

[118] P. M. Nadolsky, H.-L. Lai, Q.-H. Cao, J. Huston, J. Pumplin, D. Stump, W.-K. Tung, C.-P. Yuan, "Implications of CTEQ global analysis for collider observables", Phys. 1168 Rev. D78 (2008) 013004.

[119] A. D. Martin, W. J. Stirling, R. S. Thorne, G. Watt, "Parton distributions for the LHC", Eur. Phys. J. C63 (2009) 189.

[120] A. C.-S. M. Botje, J. Butterworth et al., "The PDF4LHC Working Group Interim Recommendations", arXiv:1101.0538.

[121] CDF Collaboration, "Search for Pair Production of Supersymmetric Top Quarks in Dilepton Events from $p\overline{p}$ Collisions at $\sqrt{s} = 1.96$ TeV", Phys. Rev. Lett. 104, 251801 (2010).

[122] The ATLAS Collaboration, "Search for light scalar top quark pair production in final states with two leptons with the ATLAS detector in $\sqrt{s} = 7$ TeV proton-proton collisions", Eur.Phys.J. C72 (2012) 2237.

[123] The ATLAS Collaboration, "Search for direct top squark pair production in final states with one isolated lepton, jets, and missing transverse momentum in $\sqrt{s} = 7$ TeV pp collisions using 4.7 fb^{-1} of ATLAS data", Phys. Rev. Lett. 109, 211803 (2012).

[124] The ATLAS Collaboration, "Search for a heavy top-quark partner in final states with two leptons with the ATLAS detector at the LHC", JHEP 1211 (2012) 094.

[125] The ATLAS Collaboration, "Search for a supersymmetric partner to the top quark in final states with jets and missing transverse momentum at $\sqrt{s} = 7$ TeV with the ATLAS detector", Phys.Rev.Lett. 109, 211802 (2012).

[126] https://twiki.cern.ch/twiki/bin/view/CMSPublic/SUSYSMSSummaryPlots7TeV

[127] The CMS Collaboration, "Search for supersymmetry in final states with missing transverse energy and 0, 1, 2, or $\geq$ 3 b jets in 7 TeV pp collisions ", JHEP 1301 (2013) 077.

[128] The CMS Collaboration, "Search for supersymmetry with the razor variables at $\sqrt{s}$ = 7 Tev", CMS-PAS-SUS-12-005.

[129] The CMS Collaboration, "Search for supersymmetry in final states with b-jets using the razor variables at $\sqrt{s} = 7$ Tev", CMS-PAS-SUS-11-024.

[130] L. Randall and D. Tucker-Smith, "Dijet Searches for Supersymmetry at the Large Hadron Collider", Phys. Rev. Lett. 101, 221803 (2008).

[131] The CMS Collaboration, "Search for Supersymmetry at the LHC in Events with Jets and Missing Transverse Energy", Phys. Rev. Lett. 107, 221804 (2011).

[132] The ATLAS Collaboration, "Search for direct pair production of the top squark in all-hadronic final states in protonâproton collisions at $\sqrt{s} = 8$ TeV with the ATLAS detector", JHEP 09 (2014) 015.

[133] The ATLAS Collaboration, "Measurements of top quark pair relative differential cross-sections with ATLAS in pp collisions at $\sqrt{s} = 7$ TeV", Eur. Phys. J. C 73 (2013) 2261.

[134] The ATLAS Collaboration, "Search for squarks and gluinos with the ATLAS detector in final states with jets and missing transverse momentum using 4.7 fb^{-1} of $\sqrt{s}$ = 7 TeV proton-proton collision data", Phys. Rev. D 87 (2013) 012008.

[135] The ATLAS Collaboration, "Measurement of $t\bar{t}$ production with a veto on additional central jet activity in pp collisions at $\sqrt{s} = 7$ TeV using the ATLAS detector, Eur. Phys. J. C 72 (2012) 2043.

[136] H1 and ZEUS Collaborations, "Combined Measurement and QCD Analysis of the Inclusive e^+p Scattering Cross Sections at HERA", JHEP 01 (2010) 109.

[137] The ATLAS Collaboration, "Measurement of the cross-section for W boson production in association with b-jets in pp collisions at $\sqrt{s} = 7$ TeV with the ATLAS detector", JHEP 06 (2013) 084.

[138] J. M. Campbell and R. K. Ellis, "$t\bar{t}W^{+-}$ production and decay at NLO", JHEP 07 (2012) 052.

[139] M. Garzelli, A. Kardos, C. Papadopoulos, and Z. Trocsanyi, "$t\bar{t}W^{\pm}$ and $t\bar{t}Z$ Hadroproduction at NLO accuracy in QCD with Parton Shower and Hadronization effects", JHEP 11 (2012) 056.

[140] N. Kidonakis, "NNLL resummation for s-channel single top quark production", Phys. Rev. D 81 (2010) 054028.

[141] The ATLAS Collaboration, "Search for top squark pair production in final states with one isolated lepton, jets, and missing transverse momentum in $\sqrt{s}$= 8 TeV pp collisions with the ATLAS detector", JHEP 11 (2014) 118.

[142] The ATLAS collaboration, "Search for direct top-squark pair production in final states with two leptons in pp collisions at $\sqrt{s}$=8TeV with the ATLAS detector", JHEP 06 (2014) 124.

[143] The ATLAS Collaboration, "Measurement of the $t\bar{t}$ production cross-section using $e\mu$ events with b-tagged jets in pp collisions at $\sqrt{s}$=7 and 8 TeV with the ATLAS detector", Eur. Phys. J. C74 (2014) 3109.

[144] The ATLAS Collaboration, "Measurement of Spin Correlation in Top-Antitop Quark Events and Search for Top Squark Pair Production in pp Collisions at $\sqrt{s}$=8 TeV Using the ATLAS Detector", Submitted to PRL (arXiv:1412.4742).

[145] The ATLAS collaboration, "Search for pair-produced third-generation squarks decaying via charm quarks or in compressed supersymmetric scenarios in pp collisions at $\sqrt{s}$=8TeV with the ATLAS detector", Phys. Rev. D 90, 052008 (2014).

[146] https://atlas.web.cern.ch/Atlas/GROUPS/PHYSICS/CombinedSummaryPlots/SUSY

[147] The CMS Collaboration, "Search for direct production of stops decaying to a charm and LSP using the monojet + $E_{\mathrm{T}}^{\mathrm{miss}}$ final state", CMS-PAS-SUS-13-009.

[148] The CMS Collaboration, "Search for direct top squark pair production in the single lepton final state at $\sqrt{s}$=8 TeV", CMS-PAS-SUS-13-011.

[149] The CMS Collaboration, "Search for top squarks in multijet events with large missing momentum in proton-proton collisions at 8 TeV", CMS-PAS-SUS-13-015.

[150] The CMS Collaboration, "Exclusion limits on gluino and top-squark pair production in natural SUSY scenarios with inclusive razor and exclusive single-lepton searches at $\sqrt{s}$ = 8 TeV", CMS-PAS-SUS-14-011.

[151] https://twiki.cern.ch/twiki/bin/view/CMSPublic/SUSYSMSSummaryPlots8TeV

[152] M. W. Cahill-Rowley, J. L. Hewett, S. Hoeche, A. Ismail, and T. G. Rizzo, "SUSY Without Prejudice at the 7 and 8 TeV LHC: Gravitino LSPs", Eur.Phys.J. C72 (2012) 2156.

[153] R. Jansky, "Truth seeded reconstruction for fast simulation in the ATLAS experiment", CERN-THESIS-2013-194.

Acknowledgments

I would like to thank Prof. Karl Jakobs for the possibility of working as a PhD student in the ATLAS experiment on such an interesting topic.

Thanks to Iacopo Vivarelli for the support and guidance he provided throughout my PhD work, and to my colleague and friend Claudia Giuliani, who literally shared with me these last years, for the fruitful collaboration.

Thanks also to all the members of the Freiburg ATLAS group for creating such a stimulating and pleasant environments where to work.

A big thanks goes to Christina Skorek, for her extensive help with all the administrative tasks going well beyond her responsibilities.

Finally, thanks to my family, to Alessandro and to my friends for their love, constant presence and support.